

**Dynamic Proton Exchange Membrane Fuel Cell System
Synthesis/Design and Operation/Control Optimization under
Uncertainty**

KIHYUNG KIM

Dissertation submitted to the Faculty of the
Virginia Polytechnic Institute and State University
in partial fulfillment of the requirements for the degree of

DOCTOR OF PHILOSOPHY

in

Mechanical Engineering

Dr. Michael von Spakovsky, Chair

Dr. Douglas J. Nelson, Co-chair

Dr. Michael W. Ellis

Dr. Marty Johnson

Dr. Diego Rancruel

January 10th 2008

Blacksburg, Virginia

Keywords: optimization, PEM fuel cell, dynamic simulation, transient,
uncertainty analysis, decomposition

Copyright 2008, Kihyung Kim

Dynamic Proton Exchange Membrane Fuel Cell System Synthesis/Design and Operation/Control Optimization under Uncertainty

by Kihyung Kim

Abstract

Proton exchange membrane fuel cells (PEMFCs) are one of the leading candidates in alternative energy conversion devices for transportation, stationary, and portable power generation applications. PEMFC systems with their own fuel conversion unit typically consist of several subsystems: a fuel processing subsystem, a fuel cell stack subsystem, a work recovery-air supply subsystem, and a power electronics subsystem. Since these subsystems have different physical characteristics, their integration into a single system/subsystem level unit make the problems of dynamic system synthesis/design and operation/control highly complex. Typically, the synthesis/design optimization of energy systems is based on a single full load condition at steady state. However, a more comprehensive synthesis/design and operation/control optimization requires taking into account part as well as full load conditions for satisfying an optimal efficiency/cost/environmental effect objective. Optimal couple of these various aspects of system development requires dynamic system/subsystem/component modeling and a multi-disciplinary approach which results in an integrated set of diverse types of models and highly effective optimization strategies such as decomposition techniques (e.g., Dynamic Iterative Local-Global Optimization: DILGO).

In energy system synthesis/design and operation/control problems, system/component models are typically treated deterministically, even though input values, which include the specific load profile for which the system or subsystem is developed, can have significant uncertainties that inevitably propagate through the system to the outputs. This deficiency can be overcome by treating the inputs and outputs

probabilistically. In this work, various uncertainty analysis methodologies are applied; and among these traditional probabilistic approaches (e.g., Monte Carlo simulation) and the response sensitivity analysis (RSA) method are examined to determine their applicability to energy system development. In particular, these methods are used for the probabilistic (non-deterministic) modeling, analysis, and optimization of a residential 5 kWe PEMFC system, and uncertainty effects on the energy system synthesis/design and operation/control optimization have been assessed by taking the uncertainties into account in the objectives and constraints. Optimization results show that there is little effect on the objective (the operating cost and capital cost), while the constraints (e.g., on the CO concentration) can be significantly affected during the synthesis/design and operation/control optimization.

Acknowledgements

Although this dissertation work took a lot of hard work and dedication on my part, it would not have been possible without the help and contributions of various people. First, I would like to thank my advisor Dr. Michael von Spakovsky for providing me the opportunity to work on this research and keeping faith in my capabilities and giving valuable suggestions. I also thank and appreciate Dr. Michael von Spakovsky for persevering with me as my advisor through out the time it took me to complete this research and write the dissertation.

Many thanks to Drs. Doug Nelson, Michael Ellis, Martin Johnson, and Diego Rancruel for serving on my committee and providing valuable inputs. They have generously given their time and expertise to better my work. I thank them for their contribution and their good-natured support.

I must acknowledge as well the colleagues and computer support group who assisted, advised, and supported my research and writing efforts over the years. I would also like to thank my friends who were always there for me during the tough times. During the past three years I had the opportunity to work with people from different countries and backgrounds and learnt a lot about various cultures, and I am really grateful for that.

I cannot end without thanking my family, on whose constant encouragement and love I have relied throughout my time at the university. I am grateful for all the sacrifices they have made for me. They have always been the source of inspiration and have encouraged me to achieve my goals and be successful in life. It is to them that I dedicate this work.

Kihyung Kim

Table of Contents

ABSTRACT	ii
ACKNOWLEDGEMENTS	iv
TABLE OF CONTENTS	v
LIST OF FIGURES	ix
LIST OF TABLES	xvi
ACRONYMS INDEX	xix
NOMENCLATURE	xx
CHAPTER 1 INTRODUCTION	1
1.1 Overview of Fuel Cell Technologies	2
1.1.1 Fuel Cell Types and Applications.....	4
1.1.2 PEMFC System Characteristics	7
1.1.3 Challenges in Fuel Cell Technologies	9
1.2 Energy System Synthesis/Design and Operation/Control	12
1.3 Reliability and Uncertainty in Simulation	14
1.4 Proposed Comprehensive Paradigm for Energy System Synthesis/Design and Operation/Control Optimization under Uncertainty	15
1.5 Thesis Objectives, Original Contributions, and Practical Impacts	19
CHAPTER 2 LITERATURE REVIEW	22
2.1 Energy System Synthesis/Design and Operation/Control	22
2.1.1 Synthesis/Design and Operation/Control Optimization of Energy Systems	23
2.1.2 Multi-objective Optimization	29
2.2 Probabilistic Approach: Uncertainty and Optimization	31
2.2.1 Monte Carlo Simulation (MCS) Approach.....	33
2.2.2 Response Sensitivity Analysis (RAS) Approach.....	34
2.2.3 Fast Probability Integration (FPI) Approach	35
2.2.4 Uncertainty and Optimization.....	35

2.3	Some Comments	36
CHAPTER 3	PEMFC SYSTEM DESCRIPTION AND MODELING	39
3.1	PEMFC System	39
3.1.1	PEMFC System Definition	42
3.1.2	Conceptual Design of a PEMFC System	43
3.2	Stack Subsystem (SS)	46
3.2.1	Description of the SS	46
3.2.2	Mathematical Model of a Single PEMFC and the Stack	47
3.2.2.1	Cathode Gas Diffusion and Catalyst Layer	48
3.2.2.2	Proton Concentration	51
3.2.2.3	Electrochemical Reaction	52
3.2.2.4	Cell Voltage	55
3.2.2.5	Gross Stack Output	56
3.3	Fuel Processing Subsystem (FPS)	56
3.3.1	Description of the FPS	56
3.3.2	Steam Methane Reformer (SMR)	59
3.3.2.1	Reaction Kinetics	61
3.3.2.2	Diffusional Limitation	62
3.3.2.3	Governing Equations for the SMR Modeling	64
3.3.3	CO Removal Unit	67
3.3.3.1	High-/Low-Temperature Water-Gas Shift Reactors (HTSR/LTSR)	67
3.3.3.2	Preferential Oxidation (PrOx) Reactor	70
3.3.4	Steam Generator (SG)	71
3.3.5	Heat Exchangers (HXs)	76
3.4	Work-Recovery Air-Supply Subsystem (WRAS)	78
3.4.1	Description of the WRAS	78
3.4.2	Compressor and Expander	80
3.4.2.1	Compressor	80
3.4.2.2	Expander	84
3.4.3	Electrical Motor	85
3.4.4	Coupling of the Compressor, Expander, and Motor	87
3.5	Cost Models for the PEMFC System	88
3.5.1	Cost Models of the FPS	90
3.5.2	Cost Models of the WRAS	94
3.5.3	Cost Models of the SS.....	94

CHAPTER 4	UNCERTAINTY ANALYSIS METHODS FOR DYNAMIC SYSTEM ANALYSIS	96
4.1	Monte Carlo Simulation (MCS)	98
4.2	Response Sensitivity Analysis (RSA) Based on Taylor Series Expansion (TSE)	100
4.3	Fast Probability Integration (FPI) Methods	106
4.3.1	Fundamental Concept of Reliability Analysis	107
4.3.2	First-Order FPI Method	108
4.3.2.1	Advanced First-Order Second-Moment Method (AFOSM)	109
4.3.2.2	Response Surface Methodology (RSM)	113
4.4	Validation of Uncertainty Analysis Methodologies	113
4.4.1	Determining the System Performance Function	113
4.4.2	Comparison the MCS, FPI, and RSA Methods	115
CHAPTER 5	OPTIMIZATION STRATEGY FOR DYNAMIC PEMFC SYSTEM SYNTHESIS/DESIGN AND OPERATION/CONTROL OPTIMIZATION UNDER UNCERTAINTY	119
5.1	Optimization Algorithms	119
5.2	Single/Multi-Objective Optimization	123
5.3	Single/Multi-Level Optimization Approach for Energy System Synthesis/Design and Operation/Control	126
5.3.1	General Concepts of Decomposition Techniques	126
5.3.2	Physical Decomposition Techniques for Large-Scale Energy System Optimization Problems	128
5.3.2.1	Local-Global Optimization (LGO) Approach	129
5.3.2.2	Iterative Local-Global Optimization (ILGO) Approach	130
5.3.3.3	Dynamic Iterative Local-Global Optimization (DILGO) Approach ...	132
5.4	Applying DILGO to the Dynamic PEMFC System Synthesis/Design and Operation/Control Optimization under Uncertainties	133
5.4.1	System-Level Dynamic Synthesis/Design and Operation/Control Optimization Problem	133
5.4.2	Uncertainty Consideration in System-Level Dynamic Synthesis/Design and Operation/Control Optimization	134
5.4.3	Decomposition and Coupling Function Definition for the Dynamic PEMFC System Synthesis/Design and Operation/Control Optimization under Uncertainty.....	137
5.4.3.1	FPS System-Level, Unit-Based Optimization	139

5.4.3.2	SS System-Level, Unit-Based Optimization	143
5.4.3.3	WRAS System-Level, Unit-Based Optimization	146
5.4.4	Solution Approach: Modeling and Applying DILGO	148
5.4.4.1	System Model and Computational Framework Development	148
5.4.4.2	Applying DILGO to the PEMFC System Synthesis/Design and Operation/Control Optimization	150
5.5	Residential Load Profile Development	154
CHAPTER 6 RESULTS AND DISCUSSIONS.....		156
6.1	Validation and Characteristics of each Subsystem	156
6.1.1	SS Model.....	157
6.1.2	FPS Model	161
6.1.2.1	Validation of the FPS	161
6.1.2.2	Characteristics of the FPS	164
6.1.3	WRAS Model	170
6.2	FPS Synthesis/Design and Operation/Control Optimization under Uncertainty	171
6.2.1	RSA Method Evaluation	171
6.2.2	Multi-Objective Optimization	175
6.2.3	Uncertainty Effects on the FPS Synthesis/Design and Operation/Control Optimization	183
6.3	Dynamic Synthesis/Design and Operation/Control Optimization of the PEMFC System Using DILGO	186
6.3.1	Optimization Results	187
6.3.2	Cost Evaluation	196
6.3.3	Sensitivity Analysis	199
6.3.4	Dynamic Responses	204
6.3.4.1	FPS	204
6.3.4.2	SS	208
6.3.4.3	WRAS	208
6.3.5	System Efficiencies	213
6.3.6	Comparison with Gradient-based Optimization Results of Wang (2008)	215
CHAPTER 7 CONCLUSIONS		218
REFERENCES		222
VITA		234

List of Figures

Figure 1.1	Diagram of a single cell	3
Figure 1.2	Comparison of full and partial load efficiencies of power generation systems (von Spakovsky et al. 2006)	8
Figure 1.3	Gravimetric energy density of fuels based on the lower heating value (LHV)	10
Figure 1.4	Volumetric energy density of fuels.	10
Figure 1.5	Proposed paradigm for the energy system synthesis/design and operation/control optimization under uncertainty	18
Figure 2.1	Schematic of the 1.5 MW hybrid SOFC-GT system ((Reprinted from “Single-level optimization of a hybrid SOFC-GT power plant”, Vol. 159, pp 1169-1185, Calise et al., Journal of Power Sources, 2006, with permission from Elsevier)	24
Figure 2.2	Schematic of the 5 kWe PEMFC system (Reprinted from “Technical design and economic evaluation of a PEM fuel cell system”, Kamarudin et al., Journal of Power Sources, Vol. 157, pp 641-649, 2006a, with permission from Elsevier)	25
Figure 2.3	Sechematic of the 5 kWe cogeneration PEMFC system (Reprinted from “Study of a small heat and power PEMFC system generator”, Hubert, Achard, and Metkemeijer, Journal of power sources, Vol.156, pp 64-70, 2006, with permission from Elsevier).....	25
Figure 2.4	Schematic of the optimum 5 kWe SOFC system resulting from synthesis/ design and operation/control optimization (Rancruel, 2005)	27
Figure 2.5	Electric load profiles of a peak cooling day (a) and a peak heating day (b) in Atlanta. (Rancruel, 2005)	27
Figure 2.6	Schematic of the 13 kW PEMFC system with gasoline reformer (Reprinted from “Modeling and dynamic simulation of a fuel cell system with an	

	autothermal gasoline reformer”, Sommer et al., Journal of Power Sources, Vol. 127, pp 313-318, 2004, with permission from Elsevier)	28
Figure 2.7	Transient behavior of the system for different load changes (Reprinted from “Modeling and dynamic simulation of a fuel cell system with an autothermal gasoline reformer”, Sommer et al., Journal of Power Sources, Vol. 127, pp 313-318, 2004, with permission from Elsevier)	28
Figure 2.8	Schematic of the 50 kWe SOFC system (Reprinted from “A methodology for thermo-economic modeling and optimization of solid oxide fuel cell systems”, Palazzi et al., Applied Thermal Engineering, Vol. 27, pp 2703-2712, 2007, with permission from Elsevier)	30
Figure 2.9	Schematic of the hybrid SOFC-PEMEC system (Reprinted from “Multi-objective optimization for hybrid fuel cells power system under uncertainty”, Subramanyan, Diwekar, and Goyal, Journal of Power Sources, Vol. 132, pp 99-112, 2004, with permission from Elsevier).....	31
Figure 2.10	Comparison of deterministic stochastic capital cost values (Subramanyan and Diwekar, 2005).....	33
Figure 3.1	Schematic of a general PEMFC system for stationary applications	39
Figure 3.2	Diagram of system definition and synthesis/design procedure	42
Figure 3.3	Proposed non-optimized 5 kWe PEMFC system configuration at the beginning stage of system development	44
Figure 3.4	Schematic of the Stack Subsystem (SS).....	47
Figure 3.5	Description of species diffusion through the electrode and membrane and the electrochemical reactions of a single PEMFC	48
Figure 3.6	Configuration of the initially proposed fuel processing subsystem	58
Figure 3.7	Schematic of the proposed SMR	59
Figure 3.8	Fundamental description of the heat transfer mechanism in a reactor model	60

Figure 3.9	Schematic of the horizontal type of steam generator	72
Figure 3.10	Compact heat exchanger spatial discretization	77
Figure 3.11	Schematic of the WRAS	79
Figure 3.12	Developed compressor performance map for simulation (Wang, 2008).....	82
Figure 3.13	Selecting a compressor	83
Figure 3.14	Computationally regenerated 50RM230 DC motor	85
Figure 3.15	Schematic of linkages between components of the WRAS	88
Figure 4.1	Basic concept of MCS coupled with system modeling	99
Figure 4.2	Basic ideas of RSA for a non-linear system	104
Figure 4.3	AFOSM for a linear/nonlinear system depicted in the reduced coordinate frame	110
Figure 4.4	Optimization procedure for the AFOSM method	112
Figure 4.5	Comparison of the output response from the actual model and the approximate model	114
Figure 4.6	Comparison of the uncertainty analysis results for the MCS, AFOSM, and RSA methods	117
Figure 5.1	Optimization algorithm of the SEQOPT algorithm	123
Figure 5.2	Pareto set and domain in a multi-objective function space	125
Figure 5.3	Schematic of the general deterministic single- and multi-level optimization process	127
Figure 5.4	Physical decomposition of a two-subsystem or two-unit energy system ..	129
Figure 5.5	Subsystem boundaries and coupling functions	138
Figure 5.6	Proposed non-optimized PEMFC system configuration for the dynamic synthesis/design and operation/control optimization	140
Figure 5.7	Schematic of general optimization under uncertainty	149

Figure 5.8	Configuration of the developed interface framework	150
Figure 5.9	Parallel computational scheme for the DILGO (or ILGO) strategy applied to the PEMFC system	151
Figure 5.10	Sequential computational scheme for the DILGO (or ILGO) strategy applied to the PEMFC system.	153
Figure 5.11	Electricity demand per day from December to February in Southern California in 2006	155
Figure 5.12	Electricity demand per day from June to August in Southern California in 2006	155
Figure 5.13	Approximated electricity demand profile and the variance of the demand profile over a 48 hours, winter-summer period in Southern California area in 2006	155
Figure 6.1	Comparison of the simulated and measured cell performance at steady-state	158
Figure 6.2	Comparison of the simulated and measured cell dynamic response	158
Figure 6.3	Influence of the cell temperature on the polarization curve	159
Figure 6.4	Influence of the operating pressure on the polarization curve	159
Figure 6.5	Voltage response due to a change of current density from 0.5 A/cm ² to 0.35 A/cm ²	160
Figure 6.6	Conversion of methane according to variation in space time; the temperature (isothermal) is 848 K and the pressure at 10 bar	161
Figure 6.7	Comparison of predicted CO conversion with those of Choi and Stenger (2005): flow CO/H ₂ ratio of 1/2, pressure of 1 atm, and operating temperature of 523 K	163
Figure 6.8	Comparison of the predicted CO conversion of the model with those of Choi and Stenger (2004) for different catalyst loadings; a O ₂ /CO flow ratio of 1.2, a pressure of 1 bar, and an operating temperature of 473 K ..	163

Figure 6.9	Comparison of the predicted heat transfer performance with those of Kim (2002).	164
Figure 6.10	Steam-to-carbon (S/C) ratio, pressure, and reforming temperature effects on the steam reforming	166
Figure 6.11	Steam-to-carbon (S/C) ratio and temperature effects on CO generation in the SMR	166
Figure 6.12	Effectiveness factors for each of the reaction mechanisms	167
Figure 6.13	Effect of effectiveness factor on SMR performance	167
Figure 6.14	Conversion of CO in the HTSR/LTSR/PrOx reactor as a function of the inlet temperature of the reformat gas	169
Figure 6.15	Probabilistic distributions of the total life cycle cost and the CO concentration of the FPS found by MCS	172
Figure 6.16	The probabilistic distributions of the total life cycle cost and CO concentration of the surrogate model of the FPS found by the MCS with a sampling of 10,000	173
Figure 6.17	Probabilistic distribution for different mean values of the CO concentration for the FPS found by MCS.....	174
Figure 6.18	Approximate hydrogen demand profile for 48 hours	177
Figure 6.19	Single-objective results for the dynamic FPS synthesis/design and operation/control optimization	178
Figure 6.20	Result for the dynamic multi-objective FPS synthesis/design and operation/control optimization	180
Figure 6.21	Zoom-in of the multi-objective optimization results in Figure 6.20	180
Figure 6.22	Uncertainty factors and their contributions to the uncertainty of the total life cycle cost of the FPS	181
Figure 6.23	All the FPS result from the single-/multi-objective dynamic optimizations in Figures 6.19 and 6.20.....	183

Figure 6.24	Uncertainty effects on the FPS synthesis/design and operation/control optimization	184
Figure 6.25	Effects of the magnitude of uncertainty on the FPS synthesis/design and operation/control optimization	185
Figure 6.26	Optimum operating steam-to-carbon ratio and fuel ratio on the Pareto set	186
Figure 6.27	Optimum dynamic air and hydrogen profiles required by the FPS and WRAS SLUB optimizations during a given DILGO iteration	188
Figure 6.28	Changing total life cycle cost of the PFMEC during the DILGO procedure with a 95% confidence interval and the variance in the cost indicated by error bars.....	190
Figure 6.29	Changing capital costs of the SS, FPS, and WRAS and operating cost during the DILGO procedure with a 95% confidence interval and the variance in cost indicated by error bars	190
Figure 6.30	Changing the coupling functions during DILGO iteration.....	191
Figure 6.31	Relationships between the single cell active area and cell current density and hydrogen consumption rate in the full load condition of 5 kWe.....	194
Figure 6.32	Optimum configuration of the PEMFC system.....	195
Figure 6.33	PEMFC system and its subsystems' purchase cost breakdown based on 500,000 units per year	197
Figure 6.34	Relationship between the number of production units and the capital cost and operating costs as a percentage of total life cycle cost	199
Figure 6.35	Relationship between the number of production units and the system purchase cost per kWe	199
Figure 6.36	Non-dimensionalized sensitivity (magnitude and direction) of the optimum total life cycle cost for each decision variable.....	201

Figure 6.37	Non-dimensionalized sensitivity (magnitude and direction) of the CO concentration of the outlet gas of the PrOx reactor for each decision variable in the FPS	203
Figure 6.38	3D depiction of the transient reformat gas temperature profile in each reactor	205
Figure 6.39	3D depiction of CH ₄ conversion in the SMR and CO conversion in the HTSR, LTSR, and PrOx reactor	206
Figure 6.40	CO generation and conversion through reactors for different operating points.....	207
Figure 6.41	Dynamic responses of the cell current density and cell voltage of the optimum and initial syntheses/designs over the 48 hours of operation	208
Figure 6.42	Dynamic responses of the compressor, expander, and motor work rate for the optimum and initial designs over the 48 hours of operation.....	209
Figure 6.43	Dynamic responses of the compressor, expander, and motor operating efficiency for the optimum and initial designs over the 48 hours operation.....	209
Figure 6.44	Comparison of the optimum and initial work recovery ratio by the expander	210
Figure 6.45	Optimal performance map of the compressor for the 5 kWe PEMFC system	211
Figure 6.46	Optimal performance map of the expander for the 5 kWe PEMFC system	212
Figure 6.47	Optimal performance map of the motor for the 5 kWe PEMFC system...	212
Figure 6.48	Optimum dynamic responses of the motor torque.....	213
Figure 6.49	Comparison of the optimum and un-optimized initial FPS efficiencies ...	214
Figure 6.50	Comparison of the optimum and un-optimized initial PEMFC system efficiencies with/without the expander unit.....	214

List of Tables

Table 1.1	Summary of differences among fuel cell types	5
Table 1.2	Summary of major advantages and disadvantages of fuel cell types.....	6
Table 1.3	Market share of the total fuel cell market by fuel cell type in 2006	7
Table 1.4	Comparison of fossil fuels and predicted PEMFC system emission levels (von Spakovsky et al., 2006)	9
Table 2.1	Summary of the related research in the literature	37
Table 3.1	Critical pressures and temperatures and molecular weights	50
Table 3.2	A typical chemical composition of natural gas	57
Table 3.3	List of the pre-exponential factors and activation energies/reaction enthalpies	62
Table 3.4	The diffusion volumes and molecular weights of the species involved	64
Table 3.5	Parameter values in the kinetic equation (3.69a)	69
Table 3.6	Kinetic models for the LTSR along with their activation energies and pre- exponential factors	69
Table 3.7	Heat transfer model and design equations for the steam generator	74
Table 3.8	Expander dynamic governing equations	84
Table 3.9	Brushless DC motor specifications	87
Table 3.10	Baseline purchase cost of the FPS	91
Table 3.11	Economic assumptions for the capital cost analysis	92
Table 3.12	Capital cost estimation of the FPS	93
Table 3.13	Baseline purchase cost of the WRAS	94
Table 3.14	Capital cost estimation of the WRAS	94
Table 3.15	Baseline purchase cost of the SS	95

Table 3.16	Capital cost estimation of the SS	95
Table 4.1	Set of random variables and the results of the response surface analysis	114
Table 4.2	Uncertainty analysis of the CO concentration in the SMR using the MCS .	116
Table 4.3	Uncertainty analysis of the CO concentration in the SMR using the AFOSM and RSA methods	116
Table 5.1	Comparison of the single-/multi-objective approaches for the FPS synthesis/ design and operation/control optimization problem under uncertainty	137
Table 5.2	Synthesis/design decision variables of the FPS and their ranges	142
Table 5.3	Operation decision variables of the FPS and their ranges	142
Table 5.4	Uncertainty factors and their assumptions considered in the FPS SLUB optimization	143
Table 5.5	Control gains for the FPS (Wang, 2008)	143
Table 5.6	Synthesis/design and operation decision variables of the SS and their ranges	145
Table 5.7	Uncertainty factor and assumption considered in the SS SLUB optimization	145
Table 5.8	Control gains for the SS (Wang, 2008)	146
Table 5.9	Synthesis/design decision variables of the WRAS and their ranges.....	147
Table 5.10	Uncertainty factors and their assumptions considered in the WRAS SLUB optimization	148
Table 5.11	Control gains for the WRAS (Wang, 2008).....	148
Table 6.1	Comparison of predicted outlet flow with those of Chen et al. (2006): Pressure=1 atm, T=675 K	162
Table 6.2	Operating conditions and reactor specifications for the SMR, HTSR, LTS, and PrOx reactors.....	165

Table 6.3	Assumed decision variable values for the validation of the WRAS model developed here	170
Table 6.4	Comparison of predicted performance of the WRAS with those of Osscarson (2003)	170
Table 6.5	Comparison of the uncertainty analysis results between by the MCS and the RSA method.....	173
Table 6.6	Multi-objective function optimization of the FPS	179
Table 6.7	Optimum synthesis/design and operation decision variable values of the FPS.....	182
Table 6.8	Optimum costs of the PEMFC system and its subsystems for each iteration of the DILGO procedure	189
Table 6.9	Optimum synthesis/design and operation decision variable values of the PEMFC system	193
Table 6.10	Optimum capital cost for the proposed PEMFC system based on 500,000 units per year.....	196
Table 6.11	Optimum purchase cost of each subsystem based on 500,000 units per year	197
Table 6.12	Effect of the number of production units per year on the optimum total life cycle cost and the system purchase cost per kWe for the proposed PEMFC system	199
Table 6.13	Operating characteristic of the optimum WRAS	211
Table 6.14	Comparison the optimum total life cycle cost of the 5 kWe PMEFC system obtained by Wang (2008) and this work.....	216
Table 6.15	Comparison optimum values of some major decision variables obtained by Wang (2008) and this work	216

Acronyms Index

AFOSM	Advanced First-order Second-moment	MCFC	Molten Carbonate Fuel Cell
AFC	Alkaline Fuel Cell	MCS	Monte Carlo Simulation
AI	Artificial Intelligence	MPP	Most Probable Point
APU	Auxiliary Power Unit	MIMO	Multi-input, Multi-output
BLDC	Brushless DC	NN	Neural Network
CDF	Cumulative Distribution Function	PFSA	Perfluorosulfonic Acid
DOE	Design of Experiment	PAFC	Phosphoric Acid Fuel Cell
DMFC	Direct Methanol Fuel Cell	PES	Power Electronics Subsystem
DILGO	Dynamic Iterative Local-global Optimization	PrOx	Preferential Oxidation
DMINLP	Dynamic Mixed Integer Non-linear Programming	PDF	Probability Distribution Function
FPI	Fast Probability Integration	PEMFC	Proton Exchange Membrane Fuel Cell
FDM	Finite Difference Method	RSA	Response Sensitivity Analysis
FOSM	First-order Second-moment	RSM	Response Surface Methodology
FCS	Fuel Cell System	SEQOPT	Sequential Approximate Optimization
FPS	Fuel Processing Subsystem	SQP	Sequential Quadratic Programming
GDL	Gas-Diffusion-Layer	SA	Simulated Annealing
GA	Genetic Algorithm	SOFC	Solid Oxide Fuel Cell
HX	Heat Exchanger	SS	Stack Subsystem
HTSR	High-temperature Water-gas shift Reactor	SG	Steam Generator
ILGO	Iterative Local-global Optimization	SMR	Steam-methane Reformer
LGO	Local-global Optimization	SMBO	Surrogate-model-based Optimization
LHV	Lower Heating Value	SLUB	System-level Unit-based
LTSR	Low-temperature Water-gas shift Reactor	TSE	Taylor Series Expansion
M&S Index	Marshall & Swift Equipment Cost Index	VAPCCI	Vatavuk Air Control Cost Index
MDF	Method of Feasible Directions	WRAS	Work-recovery Air-supply Subsystem

Nomenclature

A	Plate surface area in HX (m^2)	C_{FPS}	Capital cost of FPS (\$)
A_c	Bundle cross-flow area in SG (m^2)	C_{fuel}^{FPS}	Operating cost of FPS (\$)
A_{cell}	Activation are of a single cell	c_{H^+}	Dimensionless proton concentration
A_r	Effective Pt surface area per unit geometric surface area	C_i^{FPS}	Purchase cost of component i FPS (\$)
A_{ro}	Total Pt surface area per unit geometric surface area	$C_{indirect}^{FPS}$	Indirect cost of FPS (\$)
A_{SG}	Steam generator heat transfer area of SMR (m^2)	$C_{indirect}^{WRAS}$	Indirect cost of WRAS (\$)
b	Tafel slope (V)	$C_{install}^{FPS}$	Installation cost of FPS (\$)
B	Baffle space in SG (m)	$C_{install}^{WRAS}$	Installation cost of WRAS (\$)
P_j	Partial pressure of species j in SMR (bar)	C_j	Concentration of species j in SMR ($kmol/cm^3$)
B_M	Damping coefficient of motor	CL	Tube layout constant in SG
Bo	Boiling number for evaporator in SG	C_{main}^{FPS}	Maintenance cost for life time of FPS (\$)
C_1^{WRAS}	Compressor purchase cost of WRAS (\$)	C_{main}^{WRAS}	Maintenance cost per year
C_2^{WRAS}	Expander purchase cost of WRAS (\$)	$C_{N_{base}}$	Baseline purchase cost (\$)
C_3^{WRAS}	DC motor purchase cost of WRAS (\$)	C_{NG}	Natural gas price (\$)
C_4^{WRAS}	Baseline purchase cost of WRAS (\$)	Co	Convection number for evaporator in SG
C_6^{FPS}	Major part purchase cost of FPS (\$)	C_{oper}	Operating cost of PEMFC system (\$)
C_7^{FPS}	Auxiliary parts cost (\$)	$C_{original}$	Original price of a component (\$)
C_8^{FPS}	Baseline purchase cost of FPS (\$)	c_{pg}	Specific heat of reacting mixture in SMR ($kJ/(kmol K)$)
C_{amor}^{FPS}	Amortization cost for life time of FPS (\$)	$C_{present}$	Present price of a component (\$)
C_{amor}^{WRAS}	Amortization cost per year	c_{ps}	Specific heat of shell side gas in SMR ($kJ/(kmol K)$)
C_A^{ref}	Reference cost of a component (\$)	$c_{pt,ec}$	Specific heat of water in economizer, evaporator, and super-heater in SG ($kJ/(kg K)$)
		$c_{pt,ev}$	
		$c_{pt,s}$	
C_{dl}	Double-layer capacitance in cathode (F/cm^2)	CPT	Tube count calculation constant in SG

$C_{purchase}^{FPS}$	Purchase cost of FPS (\$)	D_s	Shell diameter in SG (m)
$C_{purchase}^{WRAS}$	Purchase cost of WRAS (\$)	E	Activation energy in HTSR (J/mol)
C_{SS}	Capital cost of SS (\$)	E_{ref}	Reference voltage (V)
C_{total}^{PEMFC}	Total life cycle cost of PEMFC system (\$)	E_j	Activation energy of reaction i in SMR (kJ/mol)
$C_{total,SD}$	Standard deviation of total life cycle cost of PEMFC system (\$)	E_o	Open-circuit voltage (V)
C_{UNC}^{PEMFC}	Uncertainty of total life cycle cost of PEMFC system (\$)	E_{oC}	Cathode potential (V)
C_{unit}	Single unit purchase cost (\$)	\dot{E}_{WRAS}	Motor parasitic power (W)
c_w	Specific heat of tube wall in SMR, SG (kJ/(kg K))	F	Faraday's constant
C_{WRAS}	Capital cost of WRAS (\$)	f	Friction factor in SMR
$D_{e,i}$	effective diffusivity of reaction i in SMR (cm ² /s)	f_{main}	Maintenance factor per year
D_{eq}	Equivalent diameter in SG (m)	Fr	Froude number for evaporator in SG
d_i	Inner diameter of tube in SMR (m)	$f(Z_i)$	Probability distribution function according to input Z_i
D_{ik}	Diffusivity of the gas pare $i - k$ in cathode (cm ² /s)	G	Mass flux in SG (kg/(m ² s))
d_{IN}^{HTSR}	HTSR tube inner diameter (m)	\vec{G}	A set of inequality constraints
d_{IN}^{LTSR}	LTSR tube inner diameter (m)	G_{CO}	Mean value of CO concentration (ppm)
$d_{IN}^{Pr Ox}$	PrOx reactor tube inner diameter (m)	G_{CO}^{SD}	Standard deviation of CO concentration (ppm)
d_{IN}^{SG}	SG single tube inner diameter (m)	G_g	Mass flux of reformat gas in SMR (kg/(m ² s))
d_{IN}^{SMR}	SMR single tube inner diameter (m)	$g_{M_j}(\vec{Z})$	Functional relationship between system input and output
$D_{j,k}$	Molecular diffusivity of pare $j - k$ in SMR (cm ² /s)	h	Operating hours per year
$D_{K,i}$	Knudsen diffusivity in SMR (cm ² /s)	\vec{H}	A set of equality constraints
d_o	Outer diameter of tube in SMR (m)	H^+	Bulk flow proton concentration in cathode (mol/cm ³)
d_{out}	Tube outer diameter in SG (m)	h_h	Heat transfer coefficient of hot gas side in HX (W/(m ² K))
d_p	Catalyst diameter in SMR (m)	H_i	Enthalpy of mixture in SMR (kJ/kmol)

h_i^{HX}	Height of a channel of HX i (m)	K_{H_s}	Standard catalyst activity in HTSR (mol/(s atm ^{1/2} m ³))
ΔH_j	Enthalpy change of reaction or adsorption of species j in SMR (kJ/kmol)	K_j	Adsorption constant of species j in SMR (bar ⁻¹)
h_s	Shell side heat transfer coefficient in SMR and SG (W/(m ² K))	L	Tube length in SMR, SG (m)
$h_{t,ec}$, $h_{t,ev}$, $h_{t,s}$	Heat transfer coefficients in the economizer, the evaporator, and the super-heater in SG (W/(m ² K))	L_e	Common effective diffusion path length parameter in SMR
h_w	Inside tube wall convective heat transfer coefficient in SMR (W/m ² K)	L^{HTSR}	HTSR length (m)
h_{water}	Heat transfer coefficient of water for evaporator in SG (W/(m ² K))	L_i^{HX}	Hot/gas-side length of HX i (m)
I	Cell current (A)	L^{LTSR}	LTSR length (m)
I_a	Armature current of motor (A)	L_M	Terminal inductance of motor (H)
I_{amor}	Capitalization ratio per year	L^{PrOx}	PrOx reactor length (m)
$I_{original}$	Cost index at the time the original cost was obtained	L^{SG}	SG length (m)
$I_{present}$	Present cost index	L^{SMR}	SMR length (m)
j	Cell current density (A/cm ²)	L_x	Plate width on the hot gas side in HX (m)
J_M	Inertia of motor (kgm ²)	L_y	Plate width on the cold gas side in HX (m)
j_o	Exchange current density (A/cm ²)	m	Mass of plate in HX (kg)
j_r	Reaction current density (A/cm ²)	\vec{M}	A set of system output
k_1, k_3	Rate coefficient of reactions 1 and 3 in SMR (kmol bar ^{1/2} /kg h)	$\dot{m}_{C,air}$	Mass flow factor of compressor (kgK ^{0.5} /(s bar))
k_2	Rate coefficient of reaction 2 in SMR (kmol/(kg h bar))	$\dot{m}_C^{B.D}$	Base design point pressure of compressor (kgK ^{0.5} /(s bar))
K_b	Voltage constant of motor (V/rad/s)	\dot{m}_C^{design}	Design mass flow factor of compressor (kgK ^{0.5} /(s bar))
K_{eq}	Equilibrium constant in HTSR	$\dot{m}_E^{B.D}$	Base design point mass flow factor of expander (kgK ^{0.5} /(s bar))
K_{eqi}	Equilibrium constant of reaction i in SMR	\dot{m}_E^{design}	Design mass flow factor of expander (kgK ^{0.5} /(s bar))
k_g	Reformate gas thermal conductivity in SMR (W/(mK))	M_i	Molecular weights in cathode (g/mol)
M_j	Molecular weight of species j in SMR (g/mol)	N^{SG}	Number of tubes of SG

n	Number of electrons of elementary electrochemical reaction	\dot{n}_T	Total molar flow rate in SMR (mol/s)
\dot{n}	Hot gas molar flow rate in HX (mol/s)	N_{tube}	Number of tubes in SG
N_{air}	Inlet air mole flow rate of cathode (mol/s)	Nu_{bare}	Tube side reference Nusselt number for economizer in SG
\dot{n}_{Air}	Air flow rate from WRAS (mol/s)	N_{units}	Production volume
N_{baffle}	Number of baffle in SG	$Nu_{t,ec}$	Tube side Nusselt number for economizer in SG
N_{base}	Base production volume per year	N_{year}	Life time (years)
N_C	Rotational speed of compressor (rpm)	P^o	Atmosphere pressure in SMR (kPa)
N_{cell}	Number of cells	p_{10}	Zero current oxygen partial pressure within cathode (bar)
N_E	Rotational speed of expander (rpm)	p_{anode}	Anode side pressure (bar)
n_{gear}	Gear ratio of WRAS	$p_{cathode}$	Cathode side pressure (bar)
N_{H_2}	Hydrogen consumption in a cell (mol/(cm ² s))	$p_C^{B.D}$	Base design point pressure ratio of compressor
\dot{n}_{H_2}	Hydrogen flow rate from FPS (mol/s)	p_C^{design}	Design pressure ratio of compressor
N_i^{HX}	Number of channels of HX i	P_{cell}	Output power of a single cell (W)
N_k	Superficial flux of species k in cathode (mol/cm ² s)	p_C^{in}	Inlet pressure of compressor (bar)
n_{load}	Number of teeth on the gear of the load shaft	p_C^{out}	Outlet pressure of compressor (bar)
N_M	Rotational speed of motor (rpm)	$p_{C,ratio}$	Pressure ratio of compressor
$N_M^{B.D}$	Base design point of motor rotational speed (rpm)	$p_{cr,i}$	Critical pressure in cathode (bar)
N_M^{design}	Design rotational speed of motor (rpm)	$p_E^{B.D}$	Base design point pressure ratio of expander
n_{motor}	Number of teeth on the gear of the motor shaft	p_E^{design}	Design pressure ratio of expander
\dot{n}_{NG}	Consumption rate of natural gas (mol/s)	p_E^{in}	Inlet pressure of expander (bar)
\dot{n}_o	Total inlet molar flow rate in SMR (mol/s)	p_E^{out}	Outlet pressure of expander (bar)
N_{pass}	Number of passes in SG	P_{gross}	Output power of PEMFC system (W)
\dot{n}_s	Molar flow rate of shell side gas in SMR and SG (mol/s)	P_i	Partial pressure of constituent i in SMR, HTSR, LTSR, PrOx
p_k	Partial pressure of species k in cathode (bar)	T_C^{in}	Inlet temperature of compressor (K)

P_o	Inlet pressure in SMR (bar)	T_C^{out}	Outlet temperature of compressor (K)
P_{ratio}	Pitch ration in SG	$T_{cr,i}$	Critical temperatures in cathode (K)
P_{req}	Load demand of PEMFC system (W)	ΔT_E	Temperature difference of expander (K)
Pr_s	Shell side Prandtl number in SG	T_E^{in}	Inlet temperature of expander (K)
$Pr_{t,ec}$	Tube side Prandtl number for economizer in SG	T_E^{out}	Outlet temperature of expander (K)
$Pr_{t,s}$	Tube side Prandtl number for super-heater in SG	T_h	Hot gas bulk temperature in HX (K)
p_{sat}	Saturation pressure in cathode (bar)	T_{Hs}	Standard catalyst temperature in HTSR (706.15K)
P_{stack}	Output power of a stack (W)	T_{inlet}^{HTSR}	Inlet reformat mixture gas temperature of the HTSR (K)
P_T	Pitch in SG	T_o	Inlet temperature in SMR (K)
$\dot{Q}_{wall/wat}$	Heat transfer rate in SG (W)	Tq_C	Required torque of compressor (Nm)
R	Gas constant	Tq_E	Torque of expander (Nm)
r_1, r_2, r_3	Rate of reactions 1, 2, and 3 in SMR (kmol/(kg h))	Tq_L	Load torque of WRAS (Nm)
Re_p	Reynolds number of reformat gas in SMR	$Tq_M^{B,D}$	Base design point of motor torque (Nm)
Re_s	Shell side Reynolds number in SG	Tq_M^{design}	Design torque of motor (Nm)
$Re_{t,ec}$	Tube side Reynolds number for economizer in SG	T_{ref}	Reference temperature of cathode model (343.15 K)
$Re_{t,s}$	Tube side Reynolds number for super-heater in SG	T_s	Bulk temperature of shell side gas in SMR and SG (K)
r_j	Rate of formation of species j in SMR (kmol/kg h)	T_w	Tube wall temperature in SMR, HX, and SG (K)
R_M	Terminal resistance of motor (ohms)	t_w	Tube wall thickness in SG (mm)
R_{ohm}	Initial ohmic resistance	\bar{u}	A set of coupling functions
SF_C^m	Scale factor of mass flow factor for compressor	V	Hot gas flow velocity in HX (m/s)
SF_C^p	Scale factor of pressure ratio for compressor	$V_{C,i}$	Volume of the catalyst in reactor i (SMR/HTSR/LTSR) of FPS (m ³)
T_c	Cold gas lk temperature in HX (K)	V_i	Volume of a reactor i (SMR/HTSR/LTSR) of FPS (m ³)
ΔT_C	Temperature difference of compressor (K)	V_M	Input voltage of motor (V)
V_s	Shell side gas velocity in SMR and SG (m/s)	\bar{X}	A set of synthesis/design variables

\dot{W}_1^{WRAS}	Compressor work at design of WRAS (W)	y	Twisting ratio in SG
\dot{W}_2^{WRAS}	Expander work at design of WRAS (W)	\bar{Y}	A set of operation/control variables
\dot{W}_C	Compressor work rate (W)	y_i	Molar fraction of constituent i in SMR, HTSR, LTSR, PrOx
\dot{W}_E	Expander work rate (W)	\bar{Z}	A set of system input values
\dot{W}_M	Work rate of motor (W)	\bar{z}_i	A set of local decision variables of subsystem i
$\dot{W}_{M,input}$	Input work rate to motor (W)		

Greek

α	Scale factor of cost function	μ	Reformate gas viscosity in SMR (kg/(ms))
β	Inlet nitrogen-oxygen mole ratio in cathode	μ_{M_i}	Mean value of system output M_j
β_{M_j}	Reliability index for system output M_j	ν_{M_j}	Variance of system output M_j
δ	Twisted tape thickness in SG (mm)	ν_{ji}	Stoichiometric coefficient of species j in reaction i in SMR
δ_i	Small step size of uncertainty factor i (load profile, fuel cost, and purchase cost)	ω	Angular velocity of motor (rad/s)
ε_b	Bed void fraction in SMR	Φ	Cumulative distribution function of the normal random input variables
ε_g	Porosity in cathode model	ϕ_i	Thiele modulus
η	voltage overpotential	ρ_{cat}	Catalyst density in SMR (kg/cm ³)
η_C	Compressor efficiency	ρ_g	Density of mixture in SMR (kg/m ³)
η_E	Expander efficiency	ρ_w	Tube material density in SMR, SG (kg/m ³)
η_i	Effectiveness factor of reaction i in SMR	σ_{M_j}	Standard deviation of system output M_j
η_M	Motor efficiency	ξ	Dimensionless of cathode diffusion layer
κ	Specific heat ratio	ξ_{AIR}^i	Cooling air ratio of component i ($\dot{n}_{AIR}^i / \dot{n}_{AIR}^{TOTAL}$)
ξ_{CH_4}	Natural gas feed ratio ($\dot{n}_{CH_4}^{BR} / \dot{n}_{CH_4}^{SMR}$)	$\bar{\lambda}$	A set of shadow prices

$\xi_{S/C}$	Steam to carbon ratio $\left(\dot{n}_{H_2O}^{SMR} / \dot{n}_{CH_4}^{SMR} \right)$	τ_{H^+}	Time constant of proton concentration (s)
τ	Tortuosity in cathode model		

CHAPTER 1

Introduction

Fuel cells are promising candidates as alternative energy conversion devices for transportation, stationary power/cogeneration, and portable applications. Over the last several decades, there has been an ever increasing interest worldwide in the development and use of fuel cells because they provide an efficient, safe, and reliable power solution. The most distinguishable fuel cell technology benefits are their higher average energy efficiencies and lower environmental emissions compared to other conventional power generation systems such as internal combustion engines. Moreover, fuel cell technologies could help in reducing our national dependence on oil. However, although fuel cell systems (FCSs) exhibit these great benefits, still there exist a number of technical barriers which must be overcome such as material durability, reliable interfacing with conventional utility grids, commercial viability, etc. Furthermore, to realize such system and the potential benefits, there is a need for optimal system synthesis/design and operation/control. Here, *synthesis* represents changes in system or component configuration and component/technology selection processes while *design* refers exclusively to the nominal design point capacity (size), performance, and geometry of a given component or technology, etc.

The optimal synthesis/design and operation/control of FCSs requires advanced techniques for being able to determine the syntheses/designs and dynamic operating stages of such systems which make them technically and economically viable, because FCSs are highly non-linear systems that have a number of reliability issues (e.g., catalyst poisoning, structural degradation, and temperature and pressure limitations) which must be addressed in order to avoid system failures. FCSs with their own fuel processing

typically consist of several subsystems: a fuel processing subsystem, a fuel cell stack subsystem, a work recovery-air supply subsystem, and a power electronics subsystem. Since each subsystem has significantly different physical characteristics (i.e. thermodynamics, kinetics, geometry, response times, etc.), their integration into a single optimal system renders the problems of dynamic system synthesis/design and operation/control to be highly complex. Moreover, it is also very important to synthesize/design and control the systems intelligently in order not only to avoid as mentioned above episodes of system failure but as well to obtain optimal system operation across an entire load spectrum both in terms of maximizing energy savings and minimizing environmental effects.

To deal with these problems effectively, novel techniques of system synthesis/design, system integration, optimal control, and effective optimization strategies must be developed. In addition, the uncertainties in the computational models used and in the results obtained must be evaluated in order to have sufficient confidence that the solutions developed are indeed viable.

The purpose of this doctoral work is to thoroughly study these issues and develop and apply appropriate techniques to address them.

1.1 Overview of Fuel Cell Technologies

Fuel cells are electrochemical devices which produce electrical energy directly from chemical energy via separate electrochemical reactions of hydrogen and oxygen. As a result, fuel cells are not limited by the thermodynamic limitation (i.e. Carnot cycle limitation) of conventional heat engines such as the Carnot cycle efficiency. The fuel cell's basic physical principles were discovered by British physicist William Robert Grove in 1839, and Ludwig Mond and Charles Langer first used the term *fuel cell* in 1889. After that, a long time passed before the first successful fuel cell devices were obtained by Francis Bacon in 1932. Since NASA adopted fuel cell systems as the electric power generating units for their spacecrafts in the 1950s~1960s, fuel cells have sparked much interest and activity as alternative power generators. More recently, fuel cell technologies appear to be on a trajectory to break through the cost and technical barriers

in various applications ranging from small portable devices and vehicles to large-scale power generators which are capable of replacing conventional power plants.

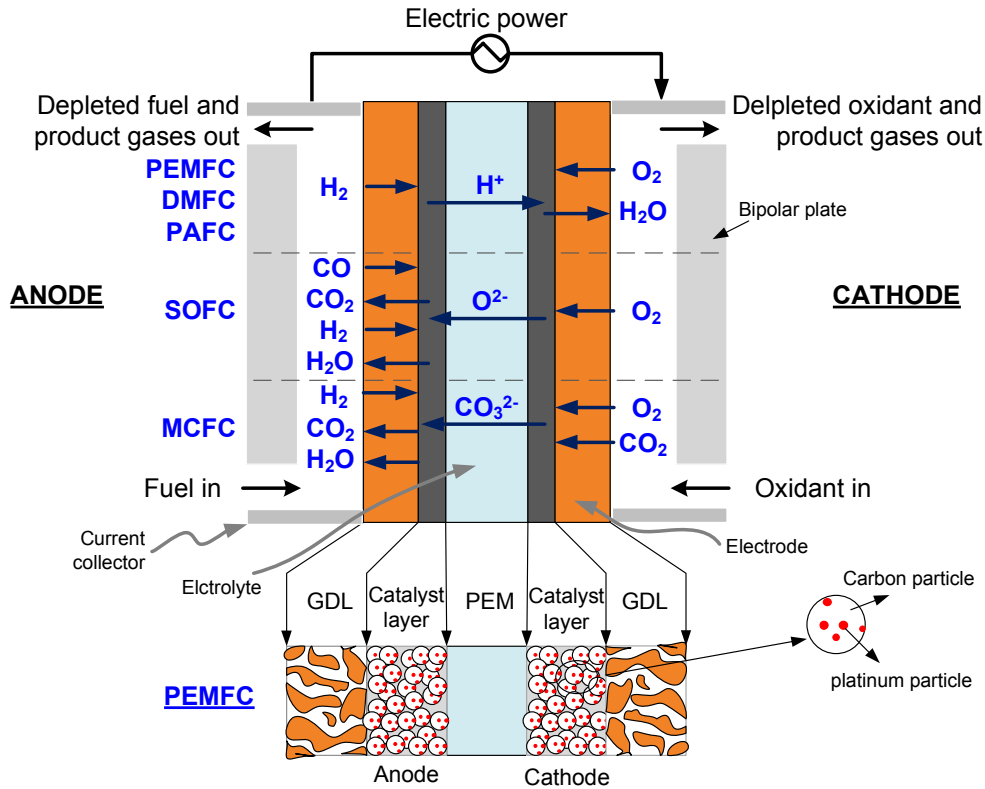


Figure 1.1 Diagram of a single cell.

A low temperature fuel cell such as a proton exchange membrane fuel cell (PEMFC) consists of five major parts, e.g., electrodes, membrane, gas-diffusion-layers, bipolar plates, and current collectors. A schematic diagram of a single cell is shown in Figure 1.1. As depicted in the figure, a cathode (positive electrode) and an anode (negative electrode) are separated by an electrolyte (e.g., a polymer membrane), and the entire assembly is connected to an external circuit via a current collector. The bipolar plate (interconnector) is used for separating the cells in a stack, connecting them electrically in series, and providing flow channels. In addition, some of the flow channels on the plate may act as cooling channel for the purpose of thermally managing in the stack. The fuel and oxidant are continuously fed into the cell, and the electrochemical reactions take place at the three-phase boundaries within the electrodes formed by the presence of catalyst as well as electron and ion conductors. In general, hydrogen is the

preferred fuel, and oxygen in air (or pure oxygen) is the typical oxidant except, for example, in a molten carbonate fuel cell (MCFC) in which CO_2 can also be an oxidant. The migration ion (e.g., H^+ , O^{2-} , CO_3^{2-}) depends on the fuel cell type. Figure 1.1 depicts the charge transfer ions and basic electrochemical reactions of each type of fuel cell.

Now, consider the particular case of a PEMFC. On the cathode side, oxygen diffuses through the gas-diffusion-layer (GDL) towards the electrolyte and is reduced, while hydrogen is oxidized on the anode side. The migration ion H^+ forms at the anode and carries the charge through the proton exchange membrane towards the cathode side. On the anode side, the electrons pass through the current collectors into an external circuit towards the cathode, and water is produced at the 3-phase boundaries on the cathode side. An electrical circuit is created by the ion transfer through the electrolyte and the electron transfer through the external circuit. The fuel cell generates electrical power as long as fuel is fed into the anode side of the cell.

1.1.1 Fuel Cell Types and Applications

Fuel cells are classified into five types based on the type of electrolyte: proton exchange membrane fuel cell (PEMFC), phosphoric acid fuel cell (PAFC), molten carbonate fuel cell (MCFC), solid oxide fuel cell (SOFC), and alkaline fuel cell (AFC). If a liquid fuel solution of a water-methanol instead of hydrogen is used as a fuel for a PEMFC, the fuel cell is called a direct methanol fuel cell (DMFC). A DMFC directly oxidizes methanol to provide electricity. The high temperature fuel cells (i.e. MCFCs and SOFCs) are considered the leading candidates for stationary power generation, while the low temperature fuel cells (in particular, the DMFCs and PEMFCs) are the leading candidates for portable, distributed, and/or transportation applications. An important attraction of high temperature fuel cells is that they are able to run on hydrocarbon fuels or CO via an internal reforming process or direct electro-oxidation, while low temperature fuel cell require hydrogen or a dilute water-methanol solutions as fuel. PEMFCs, in particular, which operate at around 80 °C and exhibit higher energy densities and efficiencies compared to DMFCs, are promising candidates for distributed power generation and transportation systems. If the PEMFC system runs on reformat (a mixture of hydrogen and other gases) generated via its own fuel processing subsystem,

cogeneration is also possible even though this can better be affected for such a system via hybridization with a heat pump and extensive energy integration. Among all the fuel cells listed above, the SOFCs and PEMFCs are expected to best meet a range of potential applications. However, none of the fuel cells are sufficiently viable economically and technically yet for significant market penetration.

Table 1.1 Summary of differences among fuel cell types.

	DMFC	PEMFC	PAFC	MCFC	SOFC
Electrolyte	Polymer	Polymer	H ₃ PO ₄	KLiCO ₃	ZrO ₂ with Y ₂ O ₃
Electrodes	Carbon	Carbon	Carbon	Ni and Ni ₂ O ₃	CaTiO ₃
Temperature (K)	300-360	<360	<470	870-920	1120-1320
Charge carrier	H ⁺	H ⁺	H ⁺	CO ₃ ²⁻	O ²⁻
External reforming	Yes	Yes	Yes	No, for some fuels	No, for some fuels and design
Sensitivity of CO/S	Yes/Yes	Yes/Yes	Yes/Yes	No/ <10ppm H ₂ S (anode) <1ppm SO ₂ (cathode)	No/ < 1ppm
Fuel	H ₂	H ₂	H ₂	H ₂ and CO	H ₂ and CO
Size range, kW	0.001~0.01	1~250	100~1000	100~2000	5~2000
Efficiency, %	20~25	~40	~45	45~50	45~50
Utilization type of energy	- Electricity	- Electricity - Heat	- Electricity - Heat	- Electricity - Heat & steam	- Electricity - Heat & steam
Projected system cost, \$/kW	-	1000~2000	5000 (current)	2000~3000	2000~3000

In Table 1.1, the major differences among fuel cell types are summarized, while some major advantages and disadvantages of each fuel cell are summarized in Table 1.2 (Fuel Cell Handbook, 2004; O'Hayre et al., 2006). Among the main applications for fuel cells are stationary power plants providing either primary or back-up power (i.e. auxiliary power), drive trains for vehicles, and portable applications (e.g., power units for laptops, cell phones, micro-air vehicles, etc). For example, small size (several hundred kW to 1~2 MW) high efficiency stationary power plants are achievable, because the efficiency of the fuel cells is not greatly affected by their size. Stationary fuel cell power plants have been developed using PAFC, PEMFC, MCFC, and SOFC technologies. Among these, large utility applications are envisioned for MCFCs and SOFCs, while PAFCs and PEMFCs favor small size power plants (<1000 kW). For larger plants (>1MW), MCFC and SOFC systems are the potentially less expensive solution. Moreover, their high operating

temperatures allow them to be coupled with other systems (e.g., a gas turbine-steam turbine combined cycle) which can maximize overall system efficiencies. Presently, PAFC systems are the most developed and mature fuel cell systems for stationary application but are not economically viable for most stationary applications due to their high cost (see Table 1.1).

Table 1.2 Summary of major advantages and disadvantages of fuel cell types.

Type	Advantages	Disadvantages
PEMFC	<ul style="list-style-type: none"> ♦ Quick system start-up and shut-down ♦ Proper portable applications ♦ Electrolyte has outstanding resistance to gas crossover. ♦ Highest power density of all the fuel cells 	<ul style="list-style-type: none"> ♦ Expansive catalyst (platinum) ♦ Difficulties in thermal/water management ♦ Poor CO, sulfur species, and NH₃ tolerance ♦ Complex system configuration (external fuel processing system with CO removal unit)
DMFC	<ul style="list-style-type: none"> ♦ Simple structure ♦ Good for low power/long operating hours 	<ul style="list-style-type: none"> ♦ Poor cell efficiency ♦ Poor for high power/short term operating
PAFC	<ul style="list-style-type: none"> ♦ Mature technology ♦ Cogeneration is available ♦ Excellent reliability and long-term running ♦ Relatively inexpensive electrolyte 	<ul style="list-style-type: none"> ♦ Slow reduction in the cathode side (requires platinum catalyst) ♦ Electrolyte is a corrosive liquid ♦ Relatively complex system configuration same as PEMFC systems
MCFC	<ul style="list-style-type: none"> ♦ Fuel flexibility ♦ Non-precious metal catalyst ♦ High quality waste heat for cogeneration ♦ Higher system efficiency than PAFC/PEMFC 	<ul style="list-style-type: none"> ♦ Corrosive and mobile electrolyte ♦ High temperature promotes material problems (degradation/lifetime issues) ♦ High contact resistance and cathode resistance limit power density (100-200 mW/cm²)
SOFC	<ul style="list-style-type: none"> ♦ Fuel flexibility ♦ Non-precious metal catalyst ♦ Solid electrolytes allow various shapes of cell ♦ No electrolyte moving and flooding in the electrodes ♦ High quality waste heat for cogeneration 	<ul style="list-style-type: none"> ♦ High temperature causes material problems such as thermal expansion ♦ Sealing issues ♦ Limited range of material selection ♦ Relatively expensive components and fabrication

PEMFC systems have had a very rapid development for small size stationary power plants and transportation applications in the last several years. As indicated in Table 1.1, the life cycle costs of PEMFC systems are potentially more favorable than any of the other types of fuel cell systems. Over the last decade, there has been a strong push to develop PEMFCs as drive trains because of the increasing price of gasoline. Off-board (i.e. without fuel reformer) fuel cell vehicles which run on pure hydrogen would be zero emission vehicles, and even with on-board reforming, such vehicle would yield significantly lower emissions than existing IC engine vehicle.

The major activity in fuel cell developments for transportation applications has focused on PEMFC technology because of its great advantages (i.e. low operating

temperature, high power density, and lower cost compared to other types of fuel cells) as described in Table 1.2. At present, most of the major automobile manufactures are investing a great deal of money to design and produce economically viable PEMFC based vehicles which can compete with or replace conventional internal combustion vehicles. Table 1.3 presents the market share of the total fuel cell market by type in 2006 (FuelCellToday, 2006). As seen in the table, the PEMFC is the dominant technology in small scale stationary plants and transportation applications, and even shares a fairly equal percentage of the market with DMFCs in the area of portable applications.

Table 1.3 Market share of the total fuel cell market by fuel cell type in 2006.

Type	Portable (%)	Transportation (bus, car, aircraft, motorcycle, etc) (%)	Large scale stationary plants (>50 kW) (%)	Small scale stationary plants (<50 kW) (%)
PMEFC	44	80	12	96
DMFC	46	20	-	-
SOFC	5		16	4
MCFC	5		45	-
PAFC			27	-

1.1.2 PEMFC System Characteristics

When compared with comparable conventional systems for energy conversion, PEMFCs exhibit a number of advantages. For example, fuel cell systems show, in general, higher average electrical efficiencies (from 40 to 60 %) than conventional energy systems (e.g., internal combustion engines, micro-turbines, etc.). Figure 1.2 shows that the full and partial load efficiency of the PEMFC system is at least 5 % higher than that of a number of other energy systems: PAFC, lean burn diesel engines, micro-turbines, and reciprocating internal combustion diesel engines (von Spakovsky et al., 2006). The partial load efficiency of PEMFC systems, in fact, remains fairly constant down to about 30 % of full-load, whereas that of the reciprocating internal combustion diesel engine begins to drop rapidly after 60 % of full-load. Thus, in general a PEMFC system not only exhibits higher full-load efficiency than any of the conventional power generation systems but is more efficient over a wider operating range than these other technologies.

As to emissions, the higher average efficiencies of PEMFC systems when compared with those of conventional power generation systems means that CO₂ emission are less than those of these other systems. This is also true for other types of emissions.

Table 1.4 shows a comparison of the emission levels associated with the combustion of fossil fuels in conventional power generation systems without additional cleanup with those that result from a PEMFC system using pure methane as fuel. As seen in the table, the PEMFC system can be thought as a $\text{NO}_x/\text{SO}_x/\text{CO}$ free system. The PEMFC system produces little SO_x and significantly less NO_x and CO produced at the burner than that of the combustion based systems. Even though the CO_2 production is significant, it is still less than for the conventional systems. Even in the case as seen in the table where there appears to be little difference with a comparable conventional system using natural gas, the difference widens when part load conditions and efficiencies are taken into account.

Another advantage that the PEMFC system has over comparable conventional systems is fuel flexibility. Hydrogen is the primary fuel for fuel cells and can be obtained from any hydrocarbon fuel. In addition, size flexibility is another advantage since fuel cell systems can be applied to a wide range of system outputs. This is true because the so-called “economy of scale” which is an important characteristic of heat engines (e.g., gas and steam turbine cycle systems, internal combustion engines, etc.) is not a limiting factor for fuel cells. Thus, fuel cells are equally applicable to large-, medium-, and small-scale applications (i.e. stationary power and co-/poly-generation, transportation, and portable power).

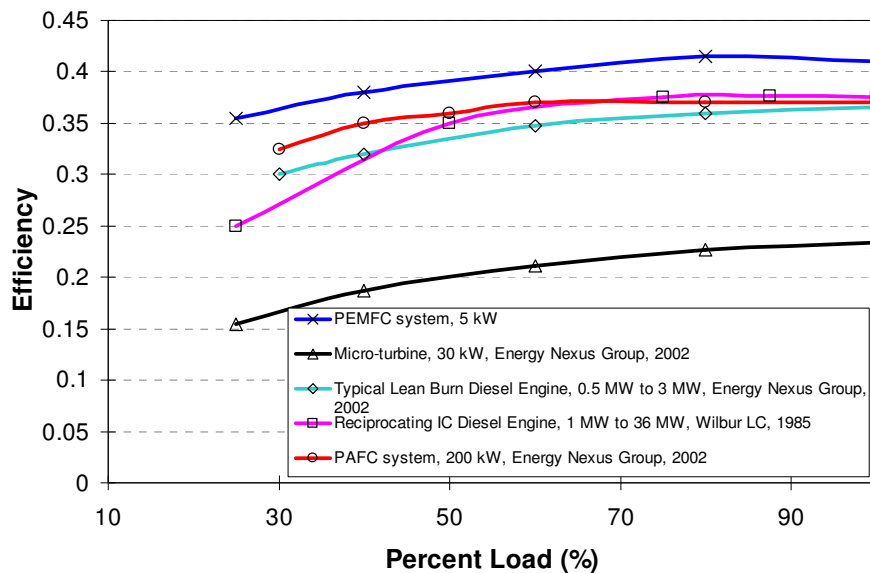


Figure 1.2 Comparison of full and partial load efficiencies of power generation systems (von Spakovsky et al., 2006).

Table 1.4 Comparison of fossil fuels and predicted PEMFC system emission levels (von Spakovsky et al., 2006).

Pollutant	Natural gas combustion (g/10 ⁶ kJ.fuel)	Oil combustion (g/10 ⁶ kJ.fuel)	Coal combustion (g/10 ⁶ kJ.fuel)	PEM FC system (g/10 ⁶ kJ.fuel)
CO ₂	50303.61	70511.05	89428.64	49549.55
CO	17.19782	14.1882	89.42864	~0
NO _x	39.55498	192.6155	196.485	~0
SO _x	0.429945	482.3987	1113.989	Under 0.2 ppm
Particulates	3.009618	36.11541	1179.77	~0
Mercury	~0	0.00301	0.006879	~0

1.1.3 Challenges in Fuel Cell Technologies

Nonetheless, with all of the advantages mentioned above, fuel cell systems still face a number of serious challenges before they will be practically viable, namely,

- *Economics*: Component costs are still too high for most stationary and transportation applications to be commercially competitive. Currently, fuel cells are only cost-effective for a few applications such as onboard the Space shuttle orbiter, or in small portable applications where they could compete head to head with existing battery technology.
- *Durability*: Relatively long life spans are required (e.g., 40,000 hours and 5,000 hours for stationary power/cogeneration and personal vehicles, respectively), which is still problematic, for example, for the fuel cell catalysts and electrolytes.
- *Reliability*: For example, effective interfacing with conventional utility grids for stationary applications as well as the effective handling of significant and persistent transient conditions for certain types of applications (e.g., transportation, residential power/cogeneration, etc.) are issues which still need to be worked out.

In addition, *energy density* is another crucial issue for fuel cell applications. Energy density (per mass) represents how much and how long for a given volume fuel cell can deliver electrical energy. Hydrogen is the major fuel for fuel cells and its gravimetric energy density is much higher than other conventional fuels such as diesel, gasoline, natural gas, etc. as shown in Figure 1.3 which is based on the lower heating value (LHV) of the fuel. However, as can be seen in Figure 1.4, the volumetric energy density of hydrogen is much lower than these other fuels because hydrogen is the lightest

molecule. Thus, due to its extremely low volumetric energy density, dramatic improvements in hydrogen fuel storage capacity for fuel cell systems is still required especially with respect to portable and transportation applications.

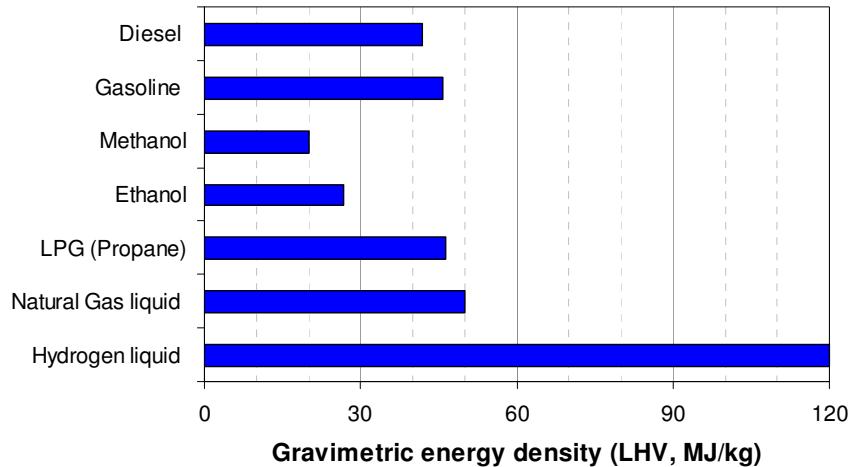


Figure 1.3 Gravimetric energy density of fuels based on the lower heating value (LHV).

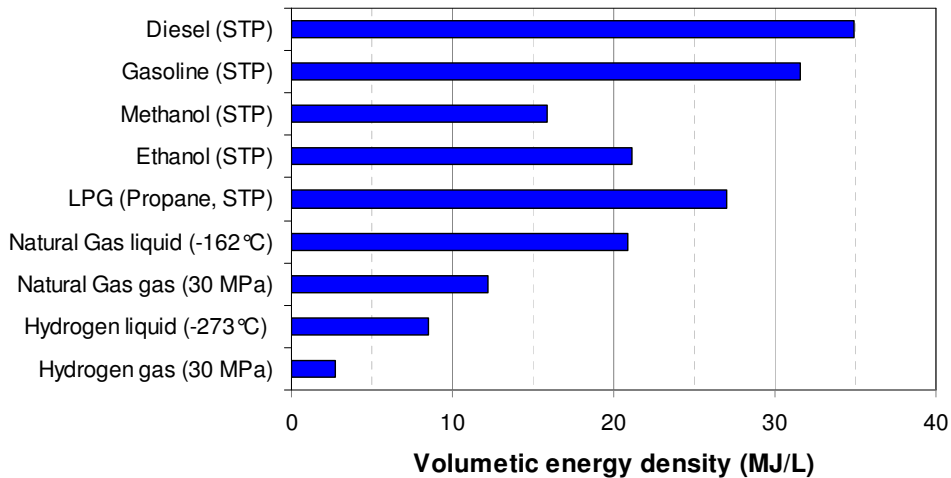


Figure 1.4 Volumetric energy density of fuels.

One of the main issues which system designers encounter is that supplying fuel to fuel cells is a difficult task. Most fuel cells use either pure hydrogen or a hydrogen rich gas mixture (i.e. reformat) as the fuel. Although direct hydrogen supply to fuel cells has several advantages (e.g., better performance, simple system structure, no contaminant problems, etc.), effective high-density storage systems which are sufficiently competitive with other energy carriers are not available yet. As a result, for many applications,

designers are only left with the option of using fuel processing equipment as the most effective means of delivering hydrogen to the fuel cell.

In certain applications, of course, hydrogen storage is recognized as an essential technology for the successful commercialization and market acceptance of hydrogen fueled vehicles. Sufficient hydrogen storage for a wide range of vehicle platforms is, however, a huge technical challenge in meeting all of the system design requirements: cost, safety, complexity, storage efficiency, energy efficiency, and storage capacity (i.e. driving range).

Three major technologies (i.e. compressed hydrogen, liquefied hydrogen, metal hydride and chemical hydride) are the most common and leading technologies of hydrogen storage. Compressed hydrogen is a straightforward manner of storing hydrogen, and it has modest storage efficiency. A current fiber-reinforced composite tank permits storage pressures as high as 70 MPa (Quantum Fuel Systems Worldwide, 2005). However, this method requires large amounts of energy to pressurize the hydrogen; and storage efficiencies, which are in terms of hydrogen mass and storage volume, are lower than with the other two methods. Additionally, high-pressure storage may introduce safety problems.

Liquefied hydrogen, which is obtained by cooling hydrogen gas below 22 K, allows hydrogen storage at low pressure. In principle, more liquid hydrogen can be stored in a given size tank because the volumetric capacity of liquid hydrogen is about 0.071 g/cm^3 , while that for compressed hydrogen is about 0.039 g/cm^3 at 70 MPa. However, about 30 % of the energy content of the hydrogen itself is consumed for hydrogen liquefaction, so that the overall energy efficiency is very low compared to other technologies.

Some metal hydrides (e.g., iron, titanium, manganese, nickel, and chromium alloys) have the potential for reversible hydrogen storage and release at the relatively lower temperatures and pressures required for fuel cell vehicles. These metal hydride materials absorb a great amount of hydrogen within the metal, and the hydrides release their stored hydrogen with minimal heating. Metal hydrides can contain incredibly large amounts of hydrogen, and it may be the most attractive hydrogen storage technique for certain portable applications. Nonetheless, the hydride metals are very heavy and

expensive. Furthermore, refueling times (e.g., 2010 target of 3 minutes for 5 kg of hydrogen, Satyapal et al., 2007) and thermal management during refueling are still in need of considerable improvement. Chemical hydrides are also one of the candidates of hydrogen storing methods. The oxidation reactions of chemical hydrides with water produce hydrogen, and sodium borohydride and ammonia-borane have been most studied. Chemical hydrides are absolutely potential candidate as hydrogen storage and supply material. However, development of catalysts accelerating the oxidation reaction of chemical hydrides is required to overcome slow reaction kinetics.

1.2 Energy System Synthesis/Design and Operation/Control

Large-scale and complex energy systems (e.g., power plants and FCSs), which consist of several subsystems and experience many interactions between subsystems, require multi-disciplinary approaches during the system synthesis/design and operation/control process to achieve the quality, cost, and performance goals for the systems. The typical approach to energy system synthesis/design and operation/control, in general, is to use simple trade-off analysis, rule-of-thumb, and both design and off-design simulations. Such an approach may not correctly predict the best interactions between subsystems, the impact of transient system/subsystem/component behavior during dynamic operation (e.g., start-up and shut-down stages, or rapid load changes), the optimum system configuration and design, the optimum operating strategies, etc. Moreover, although controller design should be conducted at the system integration stage as a part of the system synthesis/design process, it is typically left as a secondary task to be completed after the system synthesis/design task has been completed.

As energy systems become larger and more complex, the greater number of possible system configurations and technologies that could possibly meet the designer's objectives optimally increases greatly. In addition, the system may need to be developed taking into account both the transient and environmental effects on system performance. Thus, the difficulty of developing the entire system via the formulation of a single optimization problem in which the optimal synthesis/design and operation /control of the system are achieved simultaneously is great and rather problematic due to the

complexities involved. These complexities are further heightened with the introduction of uncertainty analysis into the problem, transforming the problem from a purely deterministic one into a probabilistic one. Uncertainties, system complexity and non-linearity, and large numbers of decision variables quickly render the single optimization problem unsolvable by conventional single-level optimization strategies¹. In fact, such a problem describes a dynamic mixed integer, non-linear programming (DMINLP) problem for which no general algorithms have been found.

Energy system synthesis/design and operation/control optimization is very much a multi-disciplinary process. It requires various technical expertises in dealing with, for example, the system modeling (thermodynamic, kinetic, geometric, economic, control, etc.), integration, control, optimization, uncertainties, etc. involved in the problem. In addition, novel techniques in the integration of development tools (e.g., different optimizers, analyzers, simulators, programming languages, etc.) are also necessary in order to obtain effective/robust computational frameworks which help make the process of system optimization viable. In many cases, even though model integration and analysis tools are available, engineers very often experience computational failures because of model complexities and non-linearities.

Over the last couple of decades, more and more powerful computer systems and software have become available for large-scale energy system development problems. However, even these high performance computer systems and software are not sufficient to make up for the ever increasing complexity of these problems, which are further complicated by the need in many applications to account for off-design behavior, whether on a transient basis as already mentioned above or on a quasi-stationary one. Conventional approaches are based on a single, full load condition at steady-state. This can significantly simplify the system optimization problem involved. However, because the optimization reflects only a single condition (e.g., full-load or some other specific load requirement), it may provide over-/underestimated solutions of synthesis/design and also lead to non-optimal solutions for operation/control. Therefore, with the exception of

¹A “single-level optimization” as apposed to “multi-level optimization” is one in which an optimizer is applied to a single optimization problem without decomposing the problem into a set of smaller problems. More details are given in Chapter 5.

systems which always operate at single load point, it is necessary to take into account part as well as full load conditions during the development phase of a system in order to ensure that the energy system synthesis/design and operation/control determined is indeed optimal for the set of load scenarios considered.

It is the focus of this doctoral work to address a number of the difficulties just outlined and to do so as they relate to the development of a 5 kWe PEMFC system for stationary applications. However, before outlining the specific objectives of this work, some discussion of uncertainties is in order.

1.3 Reliability and Uncertainty in Simulation

Simulation is the process of replicating the real world based on a set of assumptions and conceived models of reality. It may be performed theoretically or experimentally. For engineering purposes, simulation is applied to predict or study the performance and/or response of a system. With a prescribed set of values for a given set of decision variables, the simulation process yields a specific system response. Through repeated simulations, the sensitivity of a system's performance to variations in the system parameters may be examined or assessed. By this procedure, simulation may be used to appraise alternative syntheses/designs or to determine optimal operation/control strategies. One of the biggest deficiencies of simulations is that they cannot provide exact solutions, and may even oftentimes yield results which are far from reality due to the uncertainties present in the simulation process.

Uncertainties in the results of system synthesis/design and operation/control optimization can be affected by several uncertainty sources, and they can be categorized into direct like computational errors and indirect sources such as load profile and fuel cost (See Chapter 4). This doctoral research has focused on evaluating the uncertainties in system responses due to indirect sources of uncertainties because the system synthesis/design and operation/control optimization is significantly influenced by the load profile and cost information. Quantifying these uncertainties then becomes an important task in the development of the system.

Conventionally, in energy system development, system/subsystem/component models are treated deterministically, using a specific set of non-probabilistic input values

that produce a specific set of non-probabilistic output values. Even though these input values, which include the specific load profile (i.e. electrical, thermal, and/or aerodynamic) for which the system or subsystem is developed, can have significant uncertainties that inevitably propagate through the system to the outputs, such deterministic approaches are unable to directly quantify these uncertainties and their effect on the final synthesis/design and operation/control. This deficiency can, of course, be overcome by treating the inputs and outputs probabilistically. The difficulty with doing this, particularly when large-scale dynamic optimization with a large number of degrees of freedom is being used to determine the optimal synthesis/design and operation/control of the system, is that the traditional probabilistic approaches (e.g., the Monte Carlo simulation (Subramanyan and Diwekar 2005; Diwekar, Rubin, and Frey, 1997)) are so computationally intensive that, combined with large-scale optimization, they quickly render the problem computationally intractable.

To overcome this difficulty, response sensitivity analysis (RSA) methods (Hiskens, Pai, and Nguyen, 2000) and fast probability integration (FPI) methods (Gorla, 2004), which have been used in disciplines outside the domain of energy systems, are examined here to determine their applicability to energy system development. In particular, they are used in the probabilistic (non-deterministic) modeling, analysis, and optimization of the 5 kWe PEMFC system mentioned above in order to evaluate how much uncertainties influence the system synthesis/design optimization results.

1.4 Proposed Comprehensive Paradigm for Energy System Synthesis /Design and Operation/Control Optimization under Uncertainty

The challenges and problems of synthesis/design and operation/control optimization of dynamic energy systems such as the fuel cell system considered here can be summarized as follows:

- Complexity and non-linearity of the system/subsystems/components

- A large number of synthesis/design and operation/control decision variables for which optimal values must be determined by the optimization; may be too complex to solve via a conventional single-level optimization approach
- Extreme computational burden involved in simultaneously optimizing system synthesis/design and operation/control under uncertainty

The conventional paradigm for addressing these challenges and problems, typically consists of the following approach:

- As simplified steady-state model is used in single point simulation (e.g., at full load).
- Controller design is done separately from and typically after the system synthesis/design and operation; PID control architectures are usually developed and employed.
- If system-level optimization is used at all, it is as single-level optimization approach, in which the system model may need to be greatly simplified via a reduction in non-linearities and the number and type of decision variables involved.
- Uncertainty effects on system performance and development are ignored or only considered after the fact in some type of sensitivity analysis.
- System synthesis, design, control, operation, and uncertainty are treated as individual optimization or analysis problems or in some limited combination.

To handle the dynamic system synthesis/design and operation/control optimization problem under uncertainty as a single problem, a comprehensive paradigm for energy systems is proposed in this doctoral work as depicted in Figure 1.5. The paradigm consists of a stage for deterministic model development and one for optimization. In addition, a control architecture design process is carried out as part of the deterministic model development stage, and a stochastic simulation for uncertainty analysis is placed in between the system model development stage and the optimizer.

Once there is a request for system development, a conceptual system configuration and set of technologies for individual components are determined at the start of the deterministic modeling stage. During this stage, fully described thermodynamic, kinetic, geometric, and electrochemical models for the energy system

are developed and integrated into system-/subsystem-level units. The control architecture is also designed as part of the system/subsystem integration process. Note that conventional PID controllers may not be suitable for complex energy systems because multiple individual controllers are required to control multiple system variables. This difficulty can be overcome by using multi-input, multi-output (MIMO) state-space based control strategies provided that the linearity limitations for state-space control in a highly non-linear system can be surmounted (Wang, 2008).

The deterministic system model can then be optimized using various gradient-/non-gradient-based optimization algorithms. A hybrid optimization approach (i.e. a gradient-based optimization algorithm combined with a non-gradient-based algorithm to improve solution quality and calculation time) may be more applicable for this optimization process. To apply the optimization algorithm to the system optimization problem, multi-level decomposition strategies are used for handling the complex optimization problem more effectively.

For an uncertainty analysis of the system, a stochastic simulation process is required and is inserted between the deterministic system model and the optimizer. A set of given decision variables are generated by the optimizer, and then all or some of these variables, i.e. which contain uncertainties, are regenerated by the stochastic simulator which generates probabilistic (or uncertainty) information such as the mean and the variance of each variable. These newly generated decision variables are used as input variables for the deterministic system model simulation, so that the system generates outputs with probabilistic information (i.e. means, variances, and/or probability distribution functions). These system responses are then sent to the optimizer, and the whole process is repeated until the optimization result converges below a predefined limit.

The result of this comprehensive paradigm of system development is an optimal configuration, an optimal control architecture and set of operating strategies, and probabilistic information about the solution. The latter includes information on the confidence level of the solution or the degree to which one can be certain of its viability. It also may include the degree to which one can have confidence that certain critical inequality constraints (e.g., the concentration of CO never exceeding 10 ppm in the PEMFC) are always met.

Comprehensive Paradigm for Energy System Synthesis/Design and Operation/Control Optimization under Uncertainty

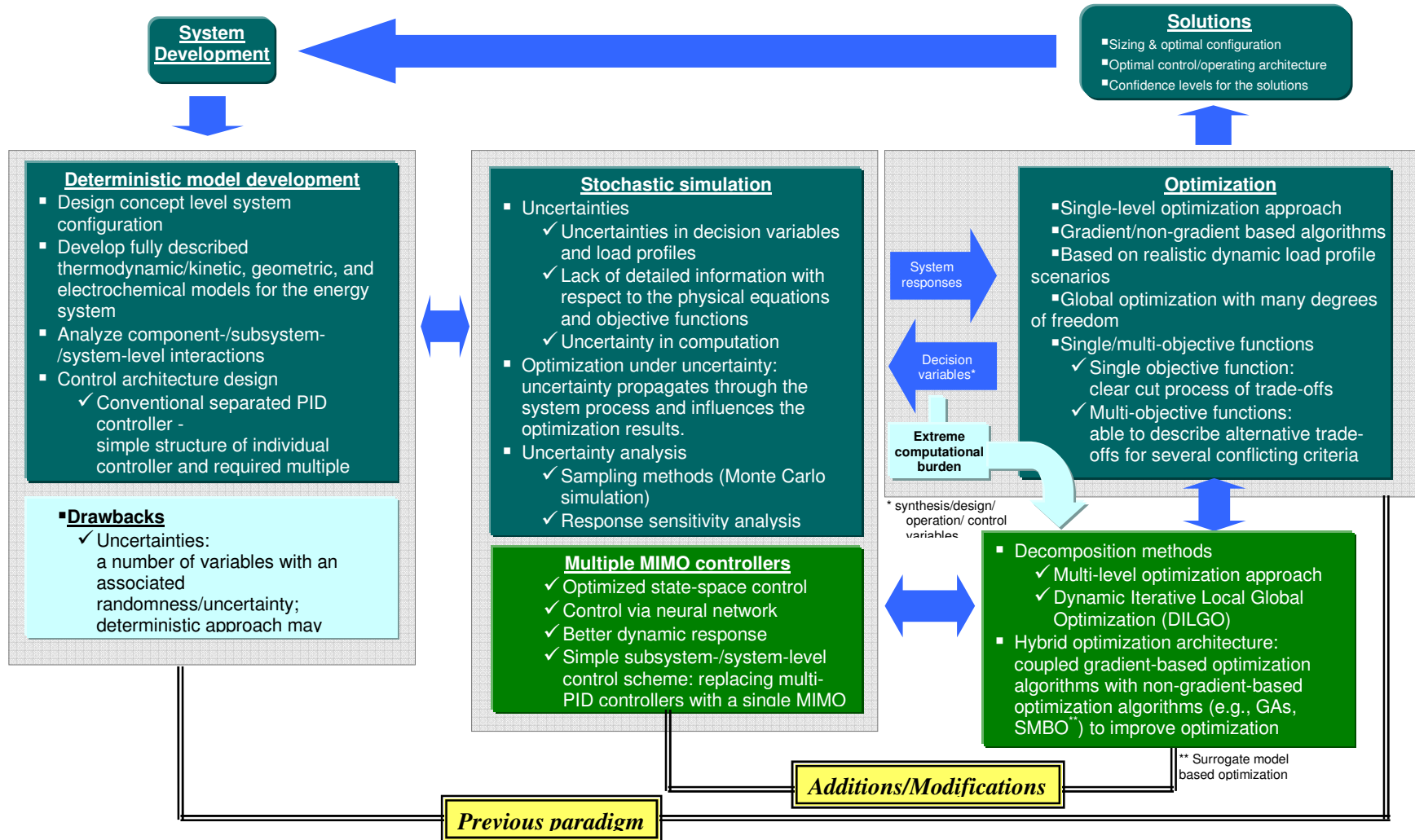


Figure 1.5 Proposed paradigm for the energy system synthesis/design and operation/control optimization under uncertainty.

1.5 Thesis Objectives, Original Contributions, and Practical Impacts

To address some of the challenges and issues raised in the previous sections, the overall goal of this doctoral work is to investigate the effects of uncertainties on energy system development at all levels (i.e. synthesis, design, operation, and control²) and to develop an approach for dealing with them. This approach will be demonstrated by dynamically and simultaneously determining the optimal synthesis/design and operation/control of a 5 kWe PEMFC system for highly transient loads. In order to accomplish this goal, the following major tasks are envisioned:

- Develop, implement, and validate a comprehensive set of detailed transient system/subsystem/component thermodynamic, kinetic, geometric, and cost models for a system composed of three subsystems: a stack subsystem (SS), a fuel processing subsystem (FPS), and a work recovery and air supply subsystem (WRAS); this will be done in collaboration with Wang (2008);
- Perform a parametric sensitivity analysis of the proposed system configuration to determine if it is adequate or in what ways it needs to be modified;
- Understand and then develop an integrated approach for applying stochastic modeling techniques and uncertainty analysis methodologies to the complex, highly non-linear system/subsystem/component models developed here; the excessive computational burdens inherent to traditional stochastic approaches (e.g., Monte Carlo simulation) must be resolved before such an integration is practically feasible;
- Integrate the stochastically based uncertainty approach developed into the dynamic synthesis/design and operation/control optimization of the overall PEMFC configuration in order to optimally synthesize, design and control the system and its subsystems; such a probabilistic approach must be able to quantify the degree of

² *Control issues* for large-scale energy systems (e.g., power plants or fuel cell systems) are well explained by Wang (2008) in his doctoral dissertation. The control architectures developed there are the ones used here in this doctoral work.

uncertainty which results in a number of the key decision variables and inequality constraints as well as quantify the variability of the load profile scenarios used to optimally develop the final system configuration, component designs, and control architecture;

- Develop an approach for conducting the planned optimizations within a multi- as opposed to single-objective framework;
- Determine the feasibility of applying the dynamic decomposition strategy for multi-level optimization called Dynamic Iterative Local-Global Optimization (DILGO) developed in Rancruel (2005) and Rancruel and von Spakovsky (2005) to the synthesis/design and operation/control optimization of the PEMFC system using a hybrid heuristic/gradient-based optimization algorithm and compare the results with those obtained using the gradient-based optimization algorithm by Wang (2008);

The originality of what is proposed here lies both in the development, implementation, and validation of a comprehensive set of detailed transient models for PEMFC system simulations as well as in the development of a probabilistic dynamic integrated synthesis/design and operation/control approach which utilizes single-/multi-objective optimizations as an integral part of the process. Additional points of originality are

- the application of approximate stochastic uncertainty approaches to the development of energy systems;
- a verification of the validity of using a dynamic decomposition as opposed to single-level strategy for large-scale optimization;
- a comparison of probabilistic/multi-objective results with those found using a deterministic single-objective approach.

The practical impact of this doctoral research on large-scale dynamic energy systems developments is as follows:

- advance the state-of-the-art beyond the deterministic system development approach by providing analytical solutions with known uncertainties with respect to the inequality constraints and system responses.

- provide comprehensive and high fidelity dynamic models for all components of a PEMFC system. The models are also applicable other types of fuel cell/energy systems.
- provide an effective way for dealing with complex energy systems over a set of dynamic operating conditions.
- provide a number of ideas for the optimal synthesis/design and operation of dynamic PEMFC systems.
- provide an overall practical approach for dynamic energy system synthesis/design and operation/control optimization under uncertainty.
- proposed a novel overall stationary PEMFC system configuration that guaranties system dependability and satisfies a variety of highly transient operating conditions.

These research objectives and practical impacts addressed above will be discussed as results of this work in Chapters 5 and 6.

CHAPTER 2

Literature Review

2.1 Energy System Synthesis/Design and Operation/Control

Although worldwide interest and research on fuel cell technologies have been conducted widely and a great number of research results on these subjects have been reported, most of the concerns and research have been focused on material and component-level development in order to obtain cost effective components and to overcome the technical barriers addressed in the previous chapter. Unfortunately, the system integration and optimal operation and control with respect to the many technological advances made have not yet reached a sufficiently practical level. In 2003, the Department of Energy (DOE) suggested a time-line for obtaining commercialized fuel cell systems in its *Fuel Cell Report to Congress*. This time-line is composed of four major phases:

- Phase 1 (2000-2005): develop stack designs and manufacturing methods.
- Phase 2 (2005-2008): improve the efficiency and durability of materials and reduce the cost of materials.
- Phase 3 (2008-2010): develop techniques for thermally integrating these systems and implement synthesis/design optimizations.
- Phase 4 (2010-2015): invest to establish a full manufacturing capacity and fuel infrastructure to successfully compete in the market place.

As suggested in the report, now is the beginning stage of research on system integration and synthesis/design in order to obtain cost effective and robust practical systems. Thus, few results on this aspect of fuel cell systems have been reported in the literatures.

2.1.1 Synthesis/Design and Operation/Control Optimization of Energy Systems

A typical approach for energy system synthesis/design is one based on a single, steady state load point (e.g., full load for a heat engine based cycle or part load for a direct energy conversion device such as a fuel cell). For example, Calise et al. (2006), Kamarudin et al. (2006a,b), Hubert, Achard, and Metkemeijer (2006), and Perna (2007) have applied this typical approach to the design of fuel cell systems. Such an approach, of course, fails to account for transient effects which reflect changing power demand, shut-down, and start-up. Even when transient effects are not that important, part load operations might be and a failure to account for these during system development can result in poor syntheses/designs. Gamou, Yokoyama, and Ito (2002) use a quasi-stationary approach to account for such part load effects in a non-transient manner. Note that this study and all the others cited in this chapter are summarized in Table 2.1 at the end of the chapter.

Gamou, Yokoyama, and Ito (2002) developed a model for a 1 MWe phosphoric acid fuel cell (PAFC) cogeneration system which supplies electricity and hot/cold water simultaneously. System capacities and maximum utility demands are optimized by considering operation strategies of the system which reflect all possible variations in energy demands. These possible variations are described by a probability distribution function which is discussed in section 2.2.2 later in this chapter. For the single-level synthesis/design optimization, a hierarchical optimization method is applied in which the optimization problem is conceptually broken down into synthesis/design decision variables and operation decision variables related hierarchically to each other. The optimum system electrical efficiency yields 38% and the cogeneration efficiency is 46% based on lower heating value.

In Calise et al. (2006), a steady-state 1.5 MWe hybrid solid oxide fuel cell-gas turbine (SOFC-GT) system model using an internal reforming tubular SOFC is developed as seen in Figure 2.1, and a conventional single-level optimization strategy is applied for the system synthesis/design optimization at full load condition. A genetic algorithm (GA) is adopted as the optimization tool to minimize the life cycle cost which only includes purchase cost of the system and operating cost as well as the total exergy destruction. A total of 48 decision variables are used to find the optimum system configuration and component designs.

Solutions from the system optimization show that the pre-reforming ratio, heat exchanger size, and SOFC active area play an important role in system performance. Moreover, the optimization results show that the optimum solution for the life cycle cost objective is very linearly independent on fuel cost because operating costs dominate the life cycle costs. Their model describes only steady-state behavior and the operation/control issues are not addressed in their optimization.

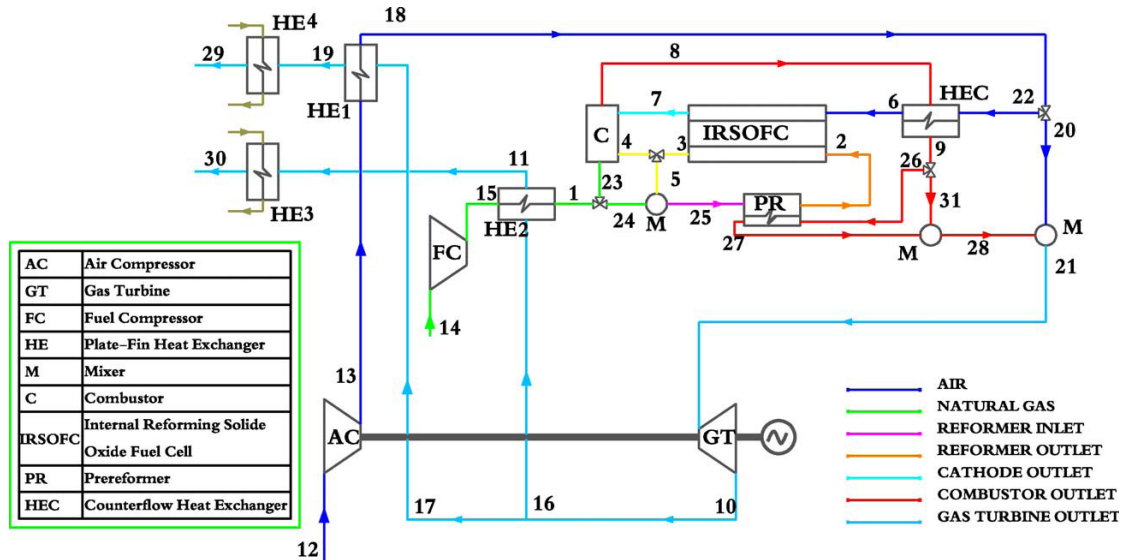


Figure 2.1 Schematic of the 1.5 MW hybrid SOFC-GT system (Reprinted from “Single-level optimization of a hybrid SOFC-GT power plant”, Vol. 159, pp 1169-1185, Calise et al., Journal of Power Sources, 2006, with permission from Elsevier).

Kamarudin et al. (2006a,b) develop a steady-state 5 kWe PEMFC system model which uses an autothermal reforming process and conduct a system synthesis/design optimization at a full load condition using a sequential quadratic programming (SQP) optimization algorithm. Figure 2.2 depicts the 5 kWe PEMFC system configuration. These authors do not consider the system design and operation/ control optimization but only focus on finding optimum system synthesis. They use a cost objective function which includes only the system purchase cost and installation cost for the optimization, and find the optimal cost, \$ 2500-3000/kW, of the PEMFC system based on 500,000 production unit per one year. These authors address the optimal system efficiency 47.5% with assuming the fuel processor efficiency is 96%. However, maximum efficiency of the typical fuel processors are around 85% (e.g., the optimum efficiency, 86%, of the fuel processor is found in this study) so their conclusion of the system electrical efficiency is overestimated.

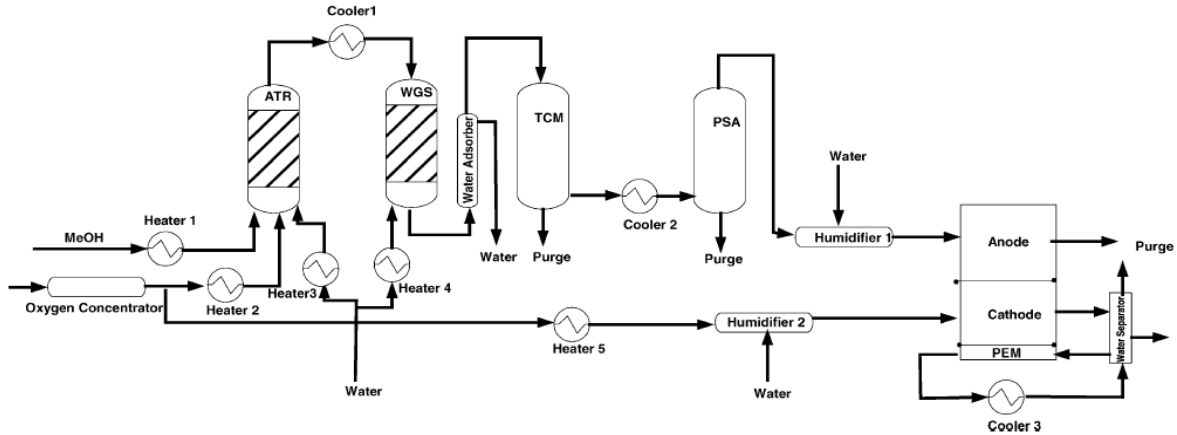


Figure 2.2 Schematic of the 5 kW PEMFC system (Reprinted from “Technical design and economic evaluation of a PEM fuel cell system”, Kamarudin et al., Journal of Power Sources, Vol. 157, pp 641-649, 2006a, with permission from Elsevier).

In Hubert, Achard, and Metkemeijer (2006), parametric studies on a 5 kWe PEMFC system (see Figure 2.3) for individual residential applications are reported. The authors develop an analytical model and then build five real systems. Their first prototypes show a maximum system electrical efficiency of 27.5% at 75% full load. The parametric study using their steady-state model reveals that the maximum system electrical efficiency is obtained at 75% full load because the stack efficiency decreases as fuel processor efficiency increases. They also show that the fuel processor efficiency dominates the system electrical efficiency. Their initial prototypes show 37.5 ~ 56.2% fuel processor efficiencies, and the fuel processor efficiency is enhanced in their new design to reach around 76.6%. Based on this, a new system is designed with a 36.4 % system electrical efficiency at full load and 38.2% at 70 % full load.

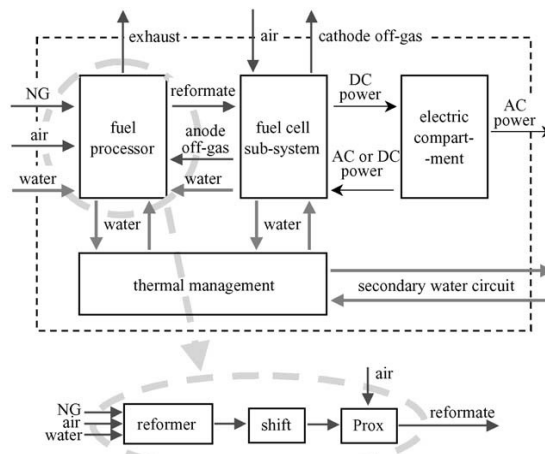


Figure 2.3 Schematic of the 5 kW cogeneration PEMFC system (Reprinted from “Study of a small heat and power PEMFC system generator”, Hubert, Achard, and Metkemeijer, Journal of power sources, Vol.156, pp 64-70, 2006, with permission from Elsevier).

Perna (2007) also reported parametric studies on a PEMFC system coupled with a steam reformer using ethanol as the fuel. A thermodynamic analysis of the steam reforming process is carried out to improve hydrogen production, and the system performance characteristics are investigated for various operating conditions (i.e. different temperatures and water-ethanol ratios) at steady state. System electrical efficiency based on the high heating value is assessed as a function of fuel utilization factor, and un-optimized maximum system electrical efficiency is 43% at a fuel utilization factor of 0.85 and a steam reforming temperature of 973 K.

As systems become more complex and when transient effects are important, more advanced approaches for system synthesis/design and operation optimization are required in order to develop a system able to operate as efficiently and cost effectively as possible at all load points. Furthermore, the developments of multi-input/multi-output control architectures which are both robust and optimal from a system synthesis/design standpoint are needed. However, the complexity of including these additional considerations and the computational burdens involved are great. For this reason, this type of dynamic system synthesis/design and operation/control optimization has not been studied widely for complex system.

Researchers who have addressed these issues include Rancruel (2005), Stiller (2006), and Sommer et al. (2004). Rancruel, in particular, develops a dynamic decomposition strategy (i.e. dynamic iterative local-global optimization; DILGO) for the large-scale synthesis/design and operation/control optimization of complex energy systems which he applies to the development of a 5 kWe SOFC power system with external fuel reforming for residential application. In this approach, the optimal control architecture is considered as part of the overall optimization problem to solve. This decomposition strategy is able to handle the optimization synthesis/design and operation/control decision variables 128 with the result that the optimal system developed using a set of complex highly nonlinear models results in a minimum life cycle cost for the system of \$ 24,843 based on 10 year operation and 200,000 production volume per year and system average system electrical efficiency of 57%. The optimal control architecture determined is able to effectively meet a variety of demanding load profile. Figure 2.4 depicts the optimum 5 kWe SOFC system which is obtained from the dynamic synthesis/design and operation/control optimization, and his dynamic optimization is carried out based on the approximate dynamic load profile seen in Figure 2.5.

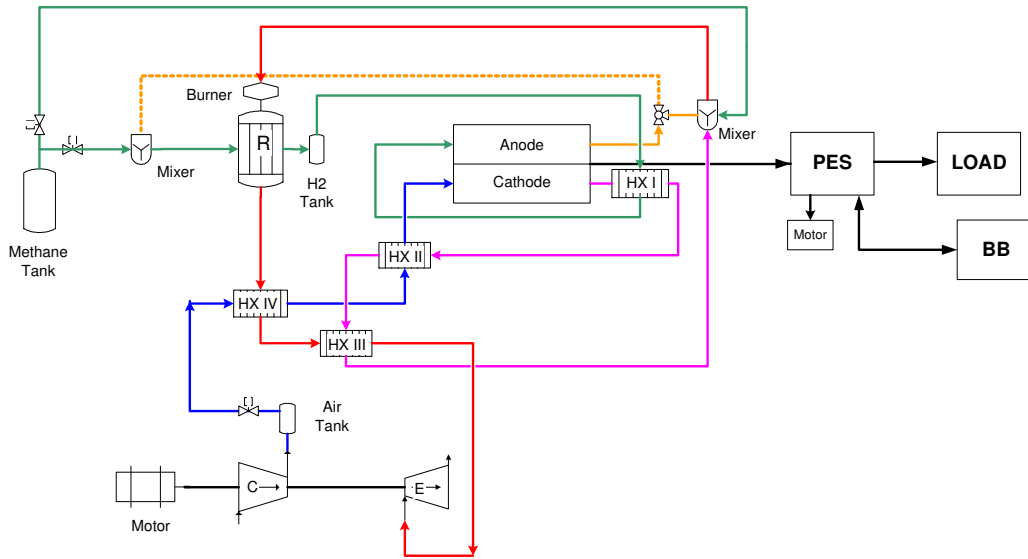


Figure 2.4 Schematic of the optimum 5 kW SOFC system resulting from synthesis/design and operation/control optimization (Rancruel, 2005).

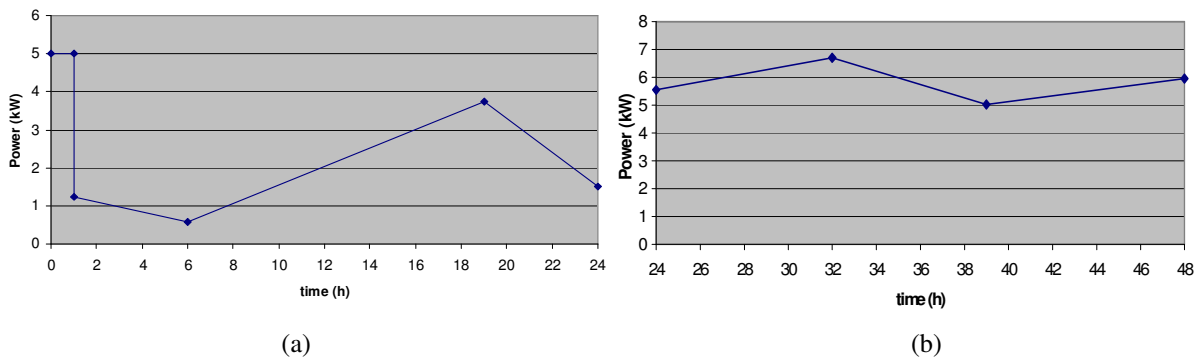


Figure 2.5 Electric load profiles of a peak cooling day (a) and a peak heating day (b) in Atlanta. (Rancruel, 2005).

In contrast to Rancruel, Stiller develops a hybrid 220 kW SOFC system coupled with gas turbine subsystem. The transient effects on system performance and operation (e.g., startup and shutdown stages) and control issues are evaluated in detail via a parametric study. Stiller investigates various transient responses of the system based on varying the input variable values and using different control architectures/strategies. The author shows the various characteristics of system behavior due to ambient conditions as well as degradation of the SOFC stack. Most of all, the author provides maps for steady state operation of the system in which a possible safe operating region is described as a function of fuel and air flow rates. Steady state part load performance (i.e. system efficiency and current density) is illustrated on the map using various system operating parameters (i.e. stack temperature, steam to carbon ratio, pressure ratio in the compressor, shaft speed, etc.).

In Sommer et al. (2004), the authors investigate in a parametric study the transient characteristics of a 13 kW PEMFC system which is coupled with an autothermal gasoline reformer and a CO removal unit consisting of a low-temperature water-gas shift reactor and a CO preferential oxidation reactor as seen in Figure 2.6. Dynamic responses (i.e. temperature

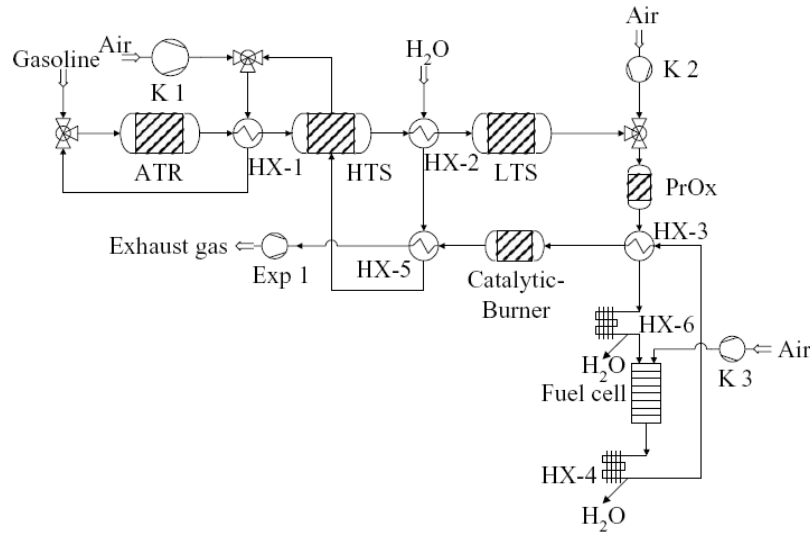


Figure 2.6 Schematic of the 13 kW PEMFC system with gasoline reformer (Reprinted from “Modeling and dynamic simulation of a fuel cell system with an autothermal gasoline reformer”, Sommer et al., Journal of Power Sources, Vol. 127, pp 313-318, 2004, with permission from Elsevier).

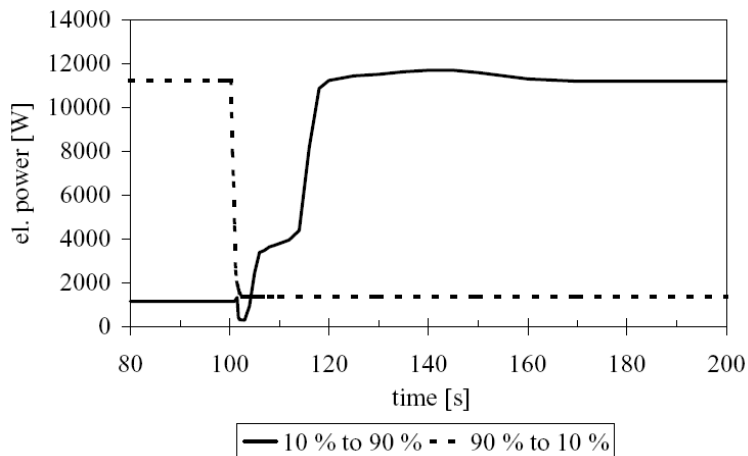


Figure 2.7 Transient behavior of the system for different load changes (Reprinted from “Modeling and dynamic simulation of a fuel cell system with an autothermal gasoline reformer”, Sommer et al., Journal of Power Sources, Vol. 127, pp 313-318, 2004, with permission from Elsevier).

and reformate composition variations in each reactor and heat exchanger) of the system are evaluated with respect to demand load changes. The conclusion drawn is that the dynamic behavior of the system is highly dominated by the response time of cooling water flow

through the heat exchanger network while the chemical reactors do not critically affect system response time. In addition, the proposed fuel cell system shows that the system can reach steady-state within 20 seconds for a case in which the demand load decreases from 90% of full load to 10% of full load and within 3 seconds for a load increase from 10% to 90% of full load. However, it takes around 100 seconds to reach steady-state for CO concentration at the outlet of the water-gas shift reactor. Figure 2.7 describes these transient behaviors of the PEMFC system.

Even though Stiller (2006) and Sommer et al. (2004) develop fully transient system models, they are not concerned with synthesis/design and optimization but focused instead on operation/control issues only. Thus, the only study found in the literature which does address all of these features is that by Rancruel (2005).

2.1.2 Multi-objective Optimization

An important consideration in the defining the synthesis/design and operation/control optimization problem is the choice of system objective e.g., whether or not to minimize system life cycle cost, exergy destruction, and/or pollutant emissions, and/or to maximize system efficiency. In general, traditional energy system synthesis/design optimization is focused on a single objective, for example, minimizing object of life cycle cost. However, the optimal synthesis/design with respect to the life cycle cost of the system may not be sufficient criterion for discarding other solutions because solutions with a higher system efficiency (and/or lower environmental effect) may, in spite of small increases in system life cycle cost, result in much more interesting syntheses/designs due to other considerations (e.g., energy and environmental policies or regulations which must be met). To deal with this, a multi-objective optimization can be used since it is able to provide a range of possible synthesis/design solutions which can be traded off against one another. Such a multi-objective approach is an effective way of providing significant information with respect to different objectives. Even though multi-objective optimizations may be very useful to decision makers (or system designers), they have not been applied widely to energy system synthesis/design probably because multi-objective optimizations are typically more computationally expensive.

Palazzi et al. (2007) employ a multi-objective optimization strategy in their fuel cell system analysis. They develop a 50 kWe SOFC system which is based on a planar SOFC stack, and Figure 2.8 depicts their system schematic. The computational model is a simplified steady-state model in which most of components for the balance of plant are not considered in detail i.e. they are treated as black boxes. Optimization of the system is conducted with regard to two independent objectives (i.e. maximizing the system efficiency and minimizing the system purchase cost) with system efficiencies ranging from 34% to 44%. In the optimization, five operating conditions (i.e. the reforming temperature, fuel utilization, oxygen to carbon ration, steam to carbon ratio, and air excess ratio) are chosen as the set of decision variables, and system configuration and the size of components are fixed. Although these were only five decision variables in the optimization, it took 4 days computing time (5~15 sec for a single simulation and 30,000 iteration number) to arrive at the solutions using a typical single core 2 GHz PC. In their paper, there might be some miscommunications related to the definitions of the decision variables and objective functions. In the text, they only mentioned the five operation decision variables but the system purchase cost can be optimized without synthesis/design decision variable.

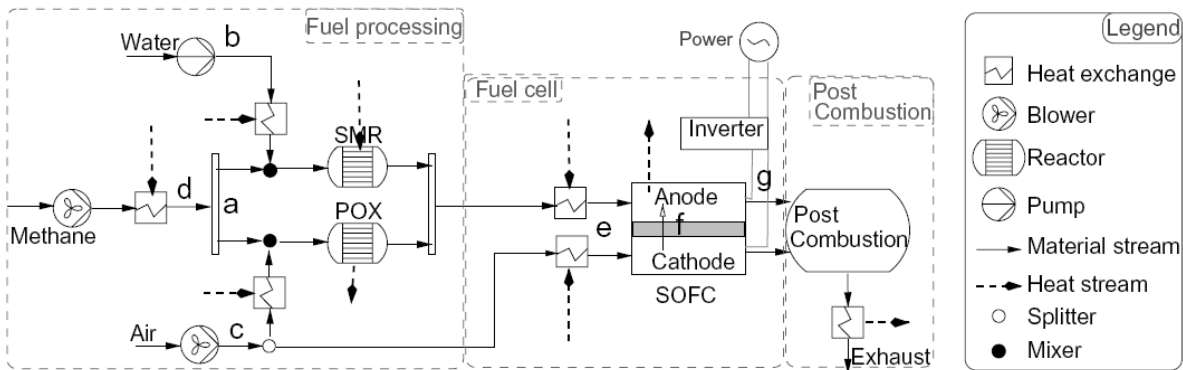


Figure 2.8 Schematic of the 50 kWe SOFC system (Reprinted from “A methodology for thermo-economic modeling and optimization of solid oxide fuel cell systems”, Palazzi et al., Applied Thermal Engineering, Vol. 27, pp 2703-2712, 2007, with permission from Elsevier).

Subramanyan, Diwekar, and Goyal (2004), and Subramnyan and Diwekar (2007) also apply a multi-objective optimization strategy to their energy system development. The authors utilize a hybrid fuel cell system model which combines two different types of fuel cells (a SOFC and a PEMFC) with a heat recovery steam generator in which water is vaporized into steam using the waste heat from the fuel cells. The hybrid SOFC-PEMFC system is described in Figure 2.9. The authors optimize the system based on six independent objectives;

minimizing capital cost/CO emissions/the cost of electricity, and maximizing current densities of the SOFC and PEMFC/overall system efficiency. The multi-objective optimization provides solutions in the form of a Pareto set which contains alternative potential solutions among the various objectives. The 1472 kWe hybrid fuel cell system shows maximum system efficiency of 73%, while a SOFC but without a PEMFC only obtains a maximum system efficiency of 52.4%. Only five decision variables (i.e. fuel utilization, equivalence ratio, operating pressure of the PEMFC, and air and fuel flow rate) are used to carry out the multi-objective optimization of the hybrid system.

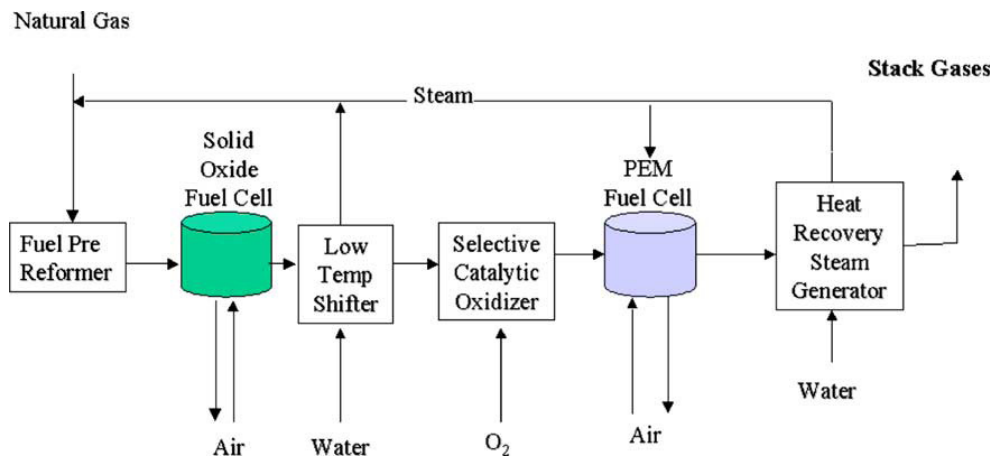


Figure 2.9 Schematic of the hybrid SOFC-PEMFC system (Reprinted from “Multi-objective optimization for hybrid fuel cells power system under uncertainty”, Subramanyan, Diwekar, and Goyal, *Journal of Power Sources*, Vol. 132, pp 99-112, 2004, with permission from Elsevier).

2.2 Probabilistic Approach: Uncertainty and Optimization

An issue not addressed in any of these parametric or optimization studies with the exception of two (i.e. Gamou, Yokoyam, and Ito, 2002; Subramanyan, Diwekar, and Goyal, 2004) is that of the uncertainties in the variables and the load profile scenarios used to develop the system. All models of real systems exhibit such uncertainties to one extent or another. Therefore, to obtain more realistic models and results that more closely reflect the real world, uncertainty should be considered more formally (as opposite to through sensitivity analysis) in the synthesis/design and operation/control optimization of energy systems.

Optimization under uncertainty has been widely used for decision-making procedures in work done on product management and scheduling. However, it is difficult to apply to

large-scale system optimizations because traditional probabilistic approaches are very computationally expensive. Even though such probabilistic approaches for uncertainty analysis can significantly improve the quality of the analysis results, only a few cases have been reported in the literature applied to energy system synthesis/design.

Traditional probabilistic approaches include Monte Carlo simulation (MCS) which is a typical sampling method which requires a large volume of samples in order to obtain the probabilistic information (i.e. the mean, variation, skewness, and probability distribution function). For example, it took around 90 minutes when only a single steam methane reformer (SMR) model developed during this doctoral work was run with a mere 1000 sampling numbers. This also required a large amount of computer memory (e.g., at least 2 Gb RAM only for the SMR simulation). Such a large volume of samples (for ten times this number is one or two orders magnitude higher) makes it prohibitive to apply sampling methods with large-scale optimization. To get around this problem, a number of approximate probabilistic modeling approaches have been proposed in the literature which can be grouped into two types of approaches: fast probability integration (FPI) and response sensitivity analysis (RSA) methods. These methods provide approximate solutions that can closely approximate the MCS result which is able to provide probably the exact solution. The advantage of FPI and RSA is that they guarantee highly effective computational time for which large-scale energy system optimization is crucial. These approaches are explained in detail in Chapter 5 and briefly discussed below in section 2.2.2 and 2.2.3.

Only a limited number of applications of any of these methods have been applied in the literature to the synthesis/design and operation of energy systems. For example, Subramanyan and Diwekar (2005, 2007) and Diwekar, Rubin, and Frey (1997) have applied the MCS approach to some aspect of uncertainty related to the design and/or operation of energy systems, while Gorla (2004) has done the same but using FPI. This latter method actually has its origination in the development of approximate but accurate uncertainty methods for structural design problems (e.g., Wang, 1985; Marvis and DeLaurentis, 2000; Youn, Choi, and Du, 2005). RSA methods have also been applied to energy system design (e.g., Gamou, Yokoyama, and Ito 2002; Hiskens, Pai, and Nguyen, 2000; and Hiskens and Alseddiqui, 2006) as well as to process operations (e.g., Bansal et al., 2000). A brief description of each of these citation is given in the following sections.

2.2.1 Monte Carlo Simulation (MCS) Approach

If one now briefly looks at the details of what each of these set of authors have done, one can begin with those who have applied the MCS approach because of its high accuracy and ease of application. For example, Subramanyan and Diwekar (2005) characterize and quantify two types of uncertainties in modeling a 560 MWe SOFC hybrid steam-/gas-turbine system, i.e. the model uncertainty resulting from the various experimentally reported polarization curves used to model the SOFC stack and material uncertainty resulting from variations in the electrolyte material performance properties. The authors generated two probability distribution functions (PDFs) and evaluated the uncertainties on the optimization of the hybrid system design and operation at steady state. The optimization results are expressed in cumulative distribution function as seen in Figure 2.10. As seen in the figure, the authors express the optimization result from the deterministic approach as the minimum value of the stochastic approach. Because of these uncertainties addressed above, the capital cost (purchase cost) is varied up to \$3547/kW with 90% confidence interval.

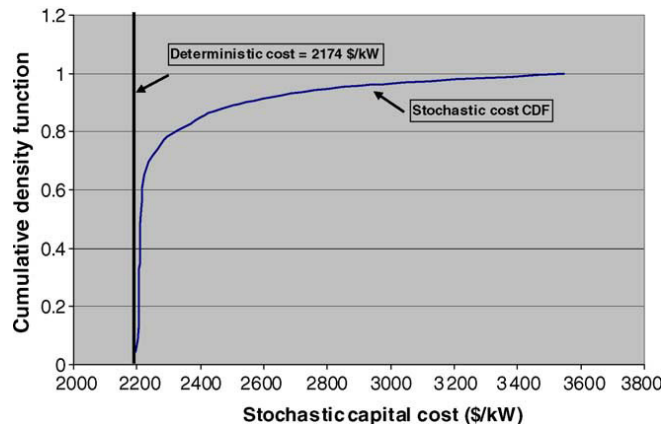


Figure 2.10 Comparison of deterministic stochastic capital cost values (Reprinted from “Characterization and quantification of uncertainty in solid oxide fuel cell hybrid power plants”, Subramanyan and Diwekar, *Journal of Power Sources*, Vol. 142, pp 103-116, 2005, with permission from Elsevier).

Diweker, Rubin, and Frey (1997) also apply uncertainty analysis to the design and operation at steady state of an integrated of 650 MWe gasification combined cycle (IGCC). This is done in the context of a system synthesis/design and operation optimization in which 21 design/operation variables are treated probabilistically by assigning mean values and

standard deviations to each and utilizing a MCS for the sampling required. As part of the synthesis optimization, a mixed integer nonlinear programming method is used. The authors perform the optimization using two different objective functions (i.e. minimizing the purchase cost and minimizing environmental effects by minimizing NO_x and SO_x emissions), and evaluate the effects of uncertainties in the input variables on optimization results. The final optimal cost and NO_x and SO_x emissions are expressed as cumulative probability density functions.

2.2.2 Response Sensitivity Analysis (RSA) Approach

All of the previous applications are necessarily limited to steady state operation only since sampling methods such as MCS are not appropriate for application to large-scale dynamic or quasi-stationary systems due to their high computational burden. As mentioned earlier, to circumvent these limitations, approximate probabilistic modeling methods such as RSA and FPI have been proposed. RSA has been used in uncertainty assessments in electronic power system analysis (Hiskens, Pai, and Nguyen, 2000; Hiskens and Alseddiqui, 2006) and for various industry decision-making problems.

Hiskens, Pai, and Nguyen (2000) and Hiskens and Alseddiqui (2006) used RSA for uncertainty estimation in the dynamic simulation of an IEEE 39 electronic bus system. Trajectory (i.e. system response or output) sensitivities are calculated by using first-order Taylor series expansions. They evaluate trajectory sensitivities of the system resulting from perturbations in the underlying parameters and/or initial conditions (inputs), and furthermore show that the results corresponded well to that from a MCS approach (e.g., the standard deviation of the system response shows less than 12% difference between RSA and MCS).

Gamou, Yokoyama, and Ito (2002) couple uncertainty considerations to the design and operation optimization of a hybrid 1 MW PAFC cogeneration system described briefly in section 2.1.1 by developing a single PDF of a load profile consisting of a series of different summer/winter power demand scenarios which vary according to time and day. In addition, uncertainties of $\pm 20\%$ of the average energy demand are assigned to all input variables. The authors used the RSA method to express energy demand functions (i.e. electricity demand and

heating/cooling water demands) in the objective function which is the annualized capital cost (including the purchase cost and annualized maintenance/amortized cost) and operating cost. They find that the optimal capacity of the fuel cell system decreases if the optimization process is performed taking into account the uncertainties. However, they only provide the possible maximum and minimum costs without providing any probabilistic information of the results in terms of uncertainties. Moreover, they do not consider system synthesis and control issues in their optimization.

2.2.3 Fast Probability Integration (FPI) Approach

FPI methods have been developed and used in structural engineering for sometime in order to characterize the limit state in design for quantifying safety margins on any critical factors which can lead to system failure. Wang (1985), Marvis and DeLaurentis (2000), and Youn, Choi, and Du (2005) have developed various FPI methods among which are the first-order, second-moment method and the advanced hybrid mean value methods for structural design. These methods are powerful tools for evaluating probabilistic information of systems and structures. However, their use for anything other than steady-state system analysis (or single point analysis) may be constrained because they require an optimization procedure to calculate the probabilistic information i.e. the means and variations of the system output. This is discussed in some detail in Chapter 5. Thus, a nested optimization which involves the system optimization in an outer loop and the probability optimization in an inner loop is required which for any large-scale dynamic system optimization problem requires huge computational resources and time.

2.2.4 Uncertainty and Optimization

Only a limited number of published researches in the literature are available on energy system optimizations with uncertainty. All of these are based on steady-state system models as indicated above (i.e. Subramanyan and Diwekar, 2004, 2007; Diwekar, Rubin, and Frey,

1997), and there is no published research with uncertainty analysis applied to dynamic energy system optimization.

Feehery, Tolsma, and Barton (1997) and Galambos and Holmes (1996) are something similar but on how to apply RSA method to optimization in general. They validate the efficiency of RSA method for optimization under uncertainty from a purely mathematical standpoint. Both use a second-order Taylor series expansion for determining mean value and variance via forward differencing schemes which are used to generate system response sensitivities. They are useful for parameter estimation, optimization, process sensitivity studies, model simplifications, and experimental design.

Although Sahinidis (2004) uses neither MCS, FPI, or RSA as his preferred stochastic approach but instead fuzzy logic, his work is included here because he provides an excellent review of how to integrate stochastic programming with optimization.

2.3 Some Comments

Finally, Table 2.1 summarizes the discussions in the previous paragraphs of the work found in the literature which specifically addresses issues of large-scale synthesis/design and operation/control optimization as well as uncertainty considerations. What is evident is that none of these works fully address the complete problem. Thus, the objective of the present work and that of the accompanying work by Wang (2008) is to fully address the dynamic synthesis/design, operation/control, and uncertainty aspects of complex energy system development using a 5 kWe PEM fuel cell system with catalytic fuel processing to demonstrate the feasibility of the techniques developed here.

Table 2.1 Summary of the related research in the literature.

Reference	Application and study	Parametric Analysis/Optimization	Stochastic modeling
Rancruel (2005)	<ul style="list-style-type: none"> Developed dynamic 5 kWe SOFC system model for stationary applications Developed optimal control strategies 	<ul style="list-style-type: none"> Developed a noble optimization strategy (DILGO) for dynamic energy system synthesis/ design and operation/control optimization 	-
Stiller (2006)	<ul style="list-style-type: none"> Developed dynamic SOFC/GT stationary system Evaluated several control strategies in transient 	<ul style="list-style-type: none"> Developed a safe operation region map for steady state part load operation 	-
Subramanyan, Diwekar (2005)	<ul style="list-style-type: none"> Developed a 560 MWe SOFC-GT system for stationary applications Characterized and quantified two types of uncertainty in the system modeling 	<ul style="list-style-type: none"> Evaluated the effect of the uncertainty on the optimization result Optimization was implemented at steady-state condition 	<ul style="list-style-type: none"> Monte Carlo method Two uncertainty sources <ul style="list-style-type: none"> model uncertainty material uncertainty Generated the PDFs using literatures
Diwekar, Rubin, and Frey (1997)	<ul style="list-style-type: none"> Developed to an 650 MWe integrated gasification combined cycle analysis (IGCC) 	<ul style="list-style-type: none"> Synthesis/design optimization under uncertainty at steady-state (cost, NOx emissions) Mixed integer nonlinear programming 	<ul style="list-style-type: none"> Monte Carlo method Using PDFs of input variables and cost functions
Perna (2007)	<ul style="list-style-type: none"> Developed a PEMFC system integrated with ethanol steam reformer Simplified steady state model 	<ul style="list-style-type: none"> Conducted only parameter study according to fuel utilization, steam/carbon ration, and operating temperature 	-
Hubert, Achard, and Metkemeijer (2006)	<ul style="list-style-type: none"> Developed an 5 kWe PEMFC system for residential application Built 5 units and tested in different conditions to find how to enhance the system efficiency 	<ul style="list-style-type: none"> Conducted only parameter study Found optimum design and operating strategies from empirical study 	-
Kamarudin et al. (2006)	<ul style="list-style-type: none"> Developed a 5 kWe PEMFC system models equipped with autothermal reformer 	<ul style="list-style-type: none"> Non-linear programming (NLP) and successive quadratic (SQP) Synthesis/design and operation optimization at steady state condition 	-
Calise et al. (2005)	<ul style="list-style-type: none"> Developed 1.5 MWe SOFC-GT Steady-state model 	<ul style="list-style-type: none"> Used GA for the system synthesis/ design optimization Single-level optimization 	
Gamou, Yokoyama, and Ito (2002)	<ul style="list-style-type: none"> Developed an 1 MWe phosphoric fuel cell cogeneration system 	<ul style="list-style-type: none"> Hierarchical optimization algorithm is applied for the system design and operation optimization Quasi-stationary system 	<ul style="list-style-type: none"> Sensitivity analysis method Clarified the influence of uncertainties in system optimization Developed a PDF of load profile scenario using real seasonal data

Table 2.1 Summary of the related research in the literature (continue).

Reference	Application and study	Parametric Analysis/Optimization	Stochastic modeling
Sommer et al. (2004)	<ul style="list-style-type: none"> Developed 13 kWe PEMFC system coupled with a controller Studied on transient behaviors of the system for steep changing of power demands 	-	-
Palazzi et al. (2007)	<ul style="list-style-type: none"> Developed 50 kWe SOFC system Simplified stead-state model 	<ul style="list-style-type: none"> Conducted two-objective function optimization with 5 decision variables 	-
Subramanyan, Diwekar, and Goyal (2004) Subramanyan and Diwekar (2007)	<ul style="list-style-type: none"> Developed 1472 kWe hybrid fuel cell system (SOFC with PEMFC) Simplified steady-state model 	<ul style="list-style-type: none"> Conducted six-objective function optimization with 5 decision variables Provided various information (with six objective functions) for design decision 	<ul style="list-style-type: none">
Hiskens, Pai, and Nguyen (2000) Hiskens and Alseddiqui (2006)	<ul style="list-style-type: none"> Electronic power system dynamic simulation (IEEE 39 bus system) 	-	<ul style="list-style-type: none"> Response sensitivity analysis Provided confidence level of system output Compared the results with that from Monte Carlo simulation
Galambos and Holmes (1996) Feehery, Tolsma, and Barton (1997)	-	-	<ul style="list-style-type: none"> Response sensitivity analysis Validated a efficiency of RSA for optimization under uncertainty
Sahinidis (2004)	-	-	<ul style="list-style-type: none"> Fuzzy logic Reviewed stochastic programming method in optimization process
Gorla (2004)	<ul style="list-style-type: none"> Developed a analytical SOFC/GT system without bottoming cycle Steady state operating condition 	<ul style="list-style-type: none"> Sensitivity of the system output according to the input random variables 	<ul style="list-style-type: none"> FPI method to evaluate system output for random input variables

CHAPTER 3

PEMFC SYSTEM DESCRIPTION AND MODELING

3.1 PEMFC System

The purpose of the application on which one is focused strongly influences fuel cell system design and configuration. Compact design and, thus, minimizing system size are the critical points in portable fuel cell systems, while reliability and system efficiency are critical in stationary fuel cell system designs. Furthermore, a fuel cell stack is not a stand-alone system because it requires several supporting components (e.g., fuel processing, cooling, power electronics, air supply, pumps, humidifiers, etc.) to be able to run.

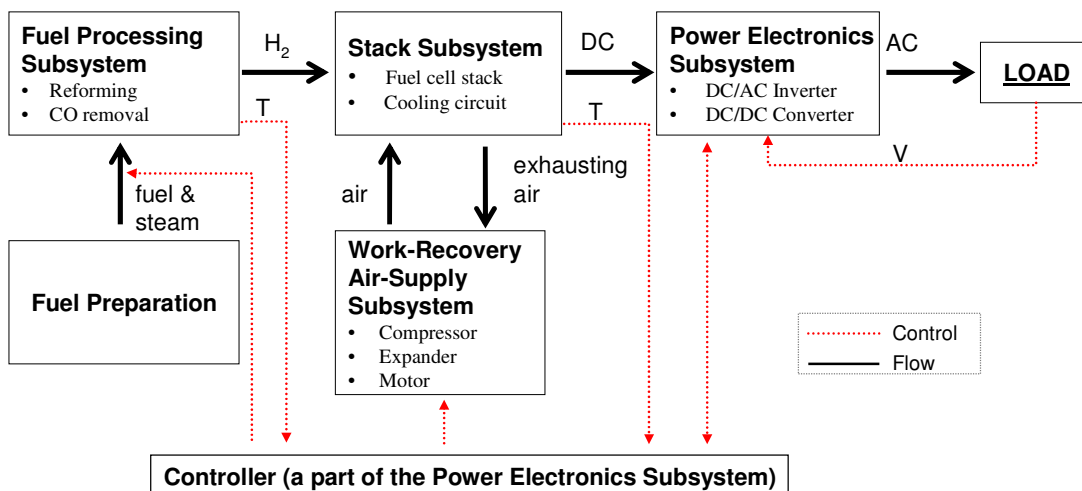


Figure 3.1 Schematic of a general PEMFC system for stationary applications.

In general, PEMFC systems with their own fuel conversion typically consist of several subsystems: a fuel processing subsystem (FPS), a fuel cell stack subsystem (SS), a work- recovery air-supply subsystem (WRAS), and a power electronics subsystem (PES) as shown in Figure 3.1. The fuel processing subsystem, whose purpose is to generate hydrogen rich gas (reformate) for fueling fuel cell, essentially consists of a reforming process and a CO removal unit. The hydrogen rich gas generated in the fuel processing subsystem is fed into the anode of the fuel cell and compressed air from the work-recovery air-supply subsystem is supplied to the cathode side. Because the electrochemical reactions in the stack are exothermic, the stack must be coupled with an effective cooling system in order to transfer energy in a heat interaction from the fuel cell stack and maintain an optimum operating temperature for the stack.

Hydrogen fuel for PEMFC systems is generated from other hydrocarbon fuels such as gasoline, diesel, methane, ethane, etc. The most practical oxidants for the fuel processor are air and steam. If steam is used as an oxidant, the reformer is referred to as a steam reformer; if air is used, a partial oxidation reformer, and if both air and steam are used together, an autothermal reformer. The selection of reformer type relies on a number of factors related to characteristics of each technology which are as follow:

- Steam reformer: It is the most developed technology and has higher system efficiencies compared to the other types. The reforming process is based on an endothermic catalytic reaction which needs thermal energy and makes the system be more complex. It requires high temperature and heat transfer surface.
- Partial oxidation reformer: It has the lowest efficiency but the simplest system configuration and is cheaper and faster than the other types of reformers. In addition, a wide range of fuels (i.e. gasoline, diesel, methane, etc) can be used as fuels. However, thermal integration with the fuel cell and control are difficult because of the higher operating temperatures (1200~1500 °C).
- Autothermal reformer: It is a combination of the steam and partial oxidation reformers. Thermal energy for steam reforming is provided by the partial combustion of the fuel, so no complex heat management is required resulting in a simpler design. However, the efficiency though better than the partial oxidation reformer is less than that of the steam reformer.

The WRAS supplies compressed air to the SS and recovers the waste energy of the exhausting air from the SS. This air still contains high quality thermal energy (i.e. high temperature and pressure). The waste thermal energy can be recovered through an expander unit and the recovered energy can be transferred to the compressor unit via a single shaft which connects the compressor and expander. By coupling both the expander and compressor, the fuel cell system is able to minimize parasitic power consumption and to achieve higher system efficiency.

The fourth subsystem of a fuel cell system is the PES which consists of DC/DC converter, DC/AC inverter, and a power supply management system as well as controller. A power regulation unit, the DC/DC converter, provides power at the correct voltage and maintains the voltages as constant over the entire operating regime. The DC/AC inverter provides AC power from the DC power supplied by the fuel cell stack so that the electric power is available to common AC power based electronic devices. This power regulation unit is necessary for most a large number of fuel cell applications, and stationary fuel cell systems, in particular, must provide electricity to the surrounding AC electricity grid line.

Another important function of the PES is power management and control by which the output of a fuel cell system meets the load demanded. A fuel cell system's output power has to be conditioned and controlled to deliver power even under large load variations. As seen in the Figure 3.1, a controller controls the entire system to satisfy the load demanded by controlling flow rates (i.e. fuel, steam, and air) and temperatures.

In addition to the subsystems mentioned above, a fuel cell system may incorporate energy buffer units (i.e. battery banks and transient reformate tank) which reduce system response time. Since energy buffer units increase system cost, whether or not to adopt the unit is left to the decision of the designer; and, of course, it may, in fact, be suggested by the system synthesis/design optimization procedure.

In this doctoral work, only three major subsystems (i.e. the SS, FPS, and WRAS) are considered to simplify the design problem without considering the PES which may be outside of mechanical engineer's expertise. However, recently, many interests on fuel cell and hybrid vehicles have increased and a number of researches related to PES have been carried out in detail by mechanical engineers (Arsie and Domenico, 2005; Kolavennu, Telotte, and Palanki, 2004; Jee and Bae, 2005).

3.1.1 PEMFC System Definition

In this doctoral research, the interest is in the development of a fuel cell system for a residential application which can supply electric power for a typical single 4-person family home. For this purpose, PEMFC technology is chosen for the system because it shows the best performance and reliability for small-scale stationary power generation units as indicated in Chapter 1. It is developed to meet a maximum system power output of 5 kWe. Figure 3.2 shows the system definition and development procedure for the fuel cell system.

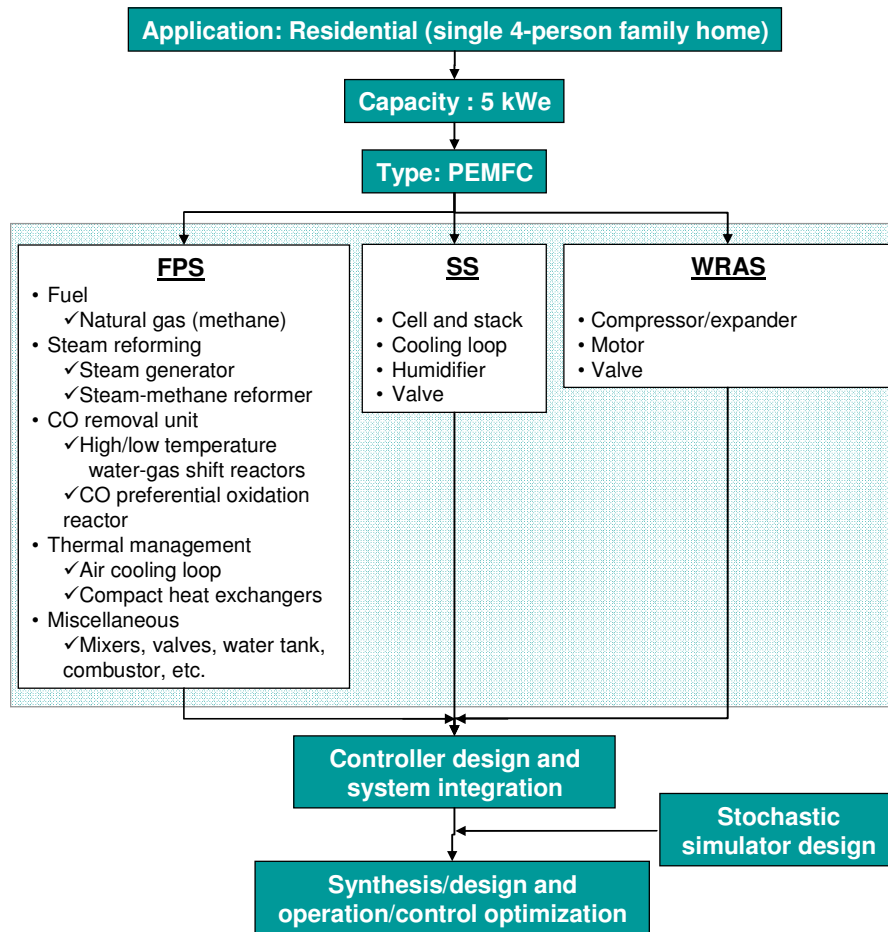


Figure 3.2 Diagram of system definition and synthesis/design procedure.

Once the fuel cell type and system requirements are determined, it is necessary to select the technologies for the components designs of each subsystem. A certain technology determines aspects of the system configuration such as a steam-methane reformer requires a steam generator. After completing development of the component models, these models are integrated into a subsystem/system level unit coupled with

controllers. Controller design is also a part of the system integration process because the control architecture and control gains are obtained from initially integrated subsystem/system models which provide system responses for a given input condition without feedback interaction between system inputs and outputs.

Once completed, the computational model represents a deterministic one, however, one that is unable to address uncertainty effects on system performance. In order to describe these, a stochastic simulator that generates probabilistic information on the load profile and cost functions is coupled with the deterministic system model. Finally, the deterministic PEMFC model with the stochastic simulator is used for the dynamic system synthesis/design and operation/control optimization based on minimizing the life cycle cost of the system taking the uncertainty effects on system performance into account. This describes a single objective optimization which could just as easily be replaced by a multi-objective optimization under uncertainty which, for example, maximizes system electrical efficiency and minimizes annualized system capital costs.

3.1.2 Conceptual Design of the PEMFC System

Through the system definition procedure, a conceptual design of the 5 kWe PEMFC system configuration is developed using an iterative process of analysis to arrive at the configuration proposed as shown in Figure 3.3. This conceptual configuration was developed taking into account all the equipment and recovery loops necessary for maximizing the total system electrical efficiency.

The main objective of the FPS is to provide the hydrogen rich gas required for the operation of the PEMFC stack. In particular, the FPS consists of three main steps; a desulphurization step as a fuel (e.g., natural gas) preparation process, a reforming step to reform the hydrocarbon fuel to hydrogen rich gas, and a CO removal unit to reduce the CO concentration level to less than 10 ppm. Organic sulphur contained in natural gas must be removed by the desulphurizer to prevent the detrimental effects on the catalysts in a typical PEMFC posed by the presence of sulfur. Even 1~2 ppm of H₂S can deactivate the electrochemical catalyst used in a PEMFC and drastically reduce the electrochemical reaction performance of the PFMFC. Paul and Frank (2005) show that the hydrocarbon

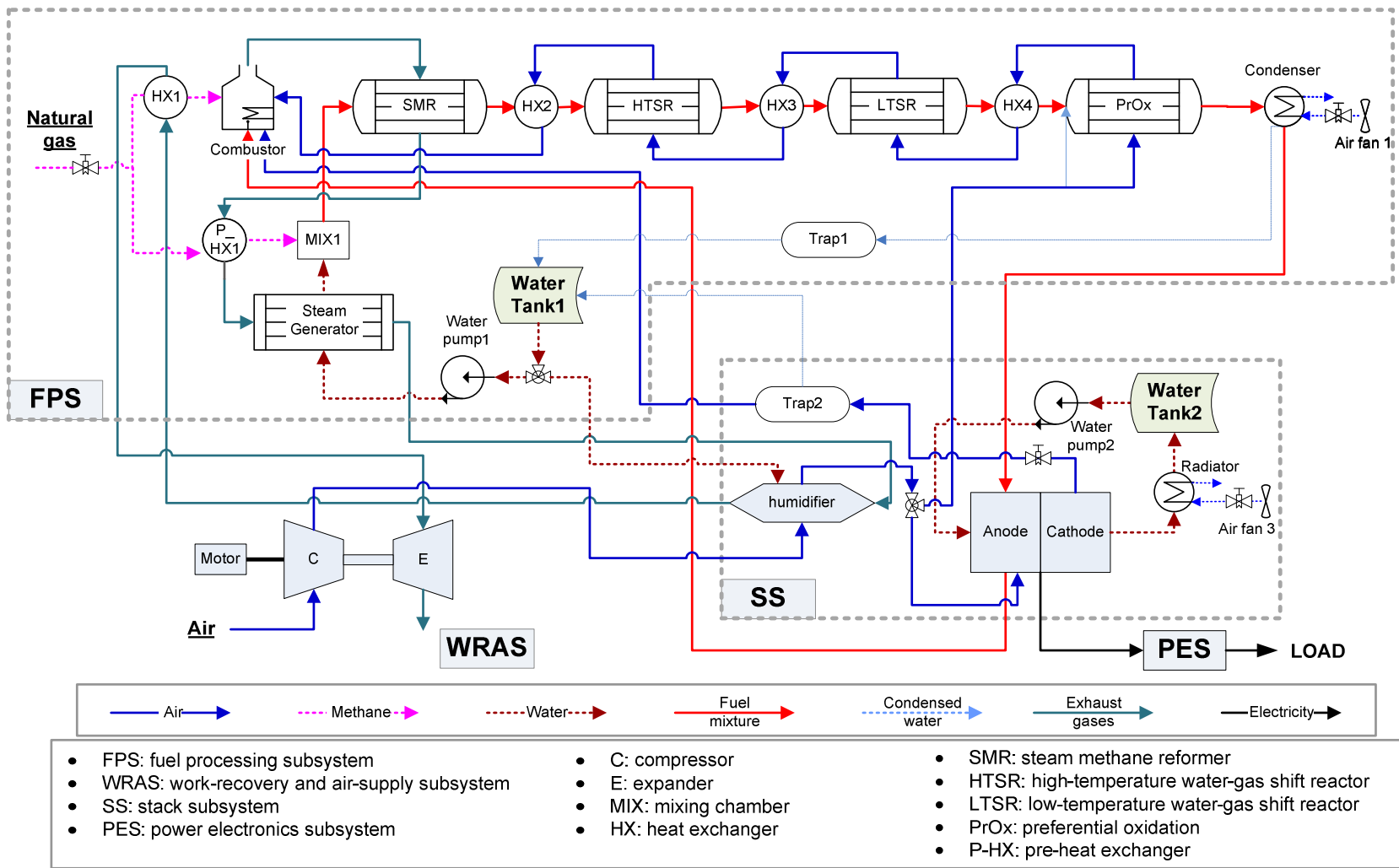


Figure 3.3 Proposed non-optimized 5 kW PEMFC system configuration at the beginning stage of system development.

fuel should be desulphurized to less than 200 ppb of H₂S prior to reforming. Because any kinetic models for the desulphurization process are not available from published documents, a desulphurization step is not considered in the computational model developed here.

For the reformer model, steam reforming technology is selected, and a steam generator and a combustor are introduced to support the steam-methane reforming process. Reformate gases from the steam methane reformer usually contain around 8~10% of CO concentration. It is, however, necessary to reduce the CO concentration level below 10 ppm for safe operation of the PEMFC system. To satisfy with this requirement, a three-step CO removal unit is designed for this fuel processing system which includes high- /low-temperature water-gas shift reactors and a CO-preferential oxidation reactor.

These four chemical reactors (i.e. the steam-methane reformer (SMR), high-/low-temperature water-gas shift reactors (HTSR and LTSR), and CO-preferential oxidation reactor (PrOx)) have different thermodynamic and kinetic characteristics. Steam-methane reforming is a highly endothermic process which requires external thermal energy source, while the water-gas shift reaction in the shift reactors is a slightly exothermic process. Preferential oxidation is a highly exothermic reaction. Furthermore, the temperatures of a number of FPS components (i.e. the reactors, steam generator, and combustor) have to be controlled carefully, and the flow and utilization of energy from several sources within the fuel cell system configuration via heat interactions have to be managed effectively to achieve high overall efficiency.

In particular, the operating temperature of the SS significantly affects overall system performance. The higher the operating temperature of the stack, the more electricity can be generated. However, current PEMFC technology is based on perfluorosulfonic acid (PFSA) polymer membranes (e.g., Du Pont's Nafion™ series) as the electrolyte, and the conductivity of the membrane relies on the presence of water to solvate the protons from the sulfonic acid groups. Thus, the operating temperature is constrained to be below the boiling temperature of the water at 1 atm (100 °C), and generally it is controlled to less than or equal to 80 °C at atmospheric pressure. Recently, there has been a lot of research interest in high-temperature (> 120 °C) polymer electrolyte membrane developments because of several advantages: higher tolerance to

CO (1 % of CO at 150 °C with only small power losses), no cathode flooding, enhancement of the cathode kinetic reaction rate, more effective heat management, no humidification, simpler system configurations, better heat utilization, etc. (Choi et al., 2007 and Lobato et al., 2007). However, the PEMFC system developed in this doctoral work is based on Du Pont's Nafion™ which requires dealing with the Nafion™ issues of humidification and temperature the catalyst issue of CO poisoning. Therefore, thermal management plays a significant role in the operation of the SS as well. The PEMFC stack is integrated with a water cooling cycle that controls the operating temperature of the stack to meet the requirements of thermal management.

The WRAS plays a significant role in the energy integration of the whole system. It consists of a compressor, an expander, and a motor. The compressor provides compressed air to the fuel cell stack and other balance of plant (BOP) components and is driven by an expander and motor. An electric motor is used to supply additional power to the compressor in case the power extracted from the expander is not enough to run the compressor.

Having briefly described the design of the 5 kWe PEMFC configuration arrived at during the conceptual stage, it is time to describe in detail the component models developed for this configuration.

3.2 Stack Subsystem (SS)

3.2.1 Description of the SS

The SS consists of a PEMFC stack and a cooling loop as seen in Figure 3.4. Several mathematical models of PEMFC stacks appear in the literature. The majority of them, however, are only able to simulate a stack's steady state behavior. For this work, a semi-empirical, one-dimensional approach based on Ceraolo, Miulli, and Pozio (2002) has been chosen to model both the steady state and transient behavior of a single PEMFC and the stack. Unless otherwise indicated the model equations which follow are taken directly from this reference. In this model, some empirical equations (e.g., proton conductivity and internal resistance of the polymer membrane, Nafion™ 115) have been

used with the chemical-physical model of the phenomena taking place inside of the cell to simplify the fuel cell model and to improve calculation efficiency.

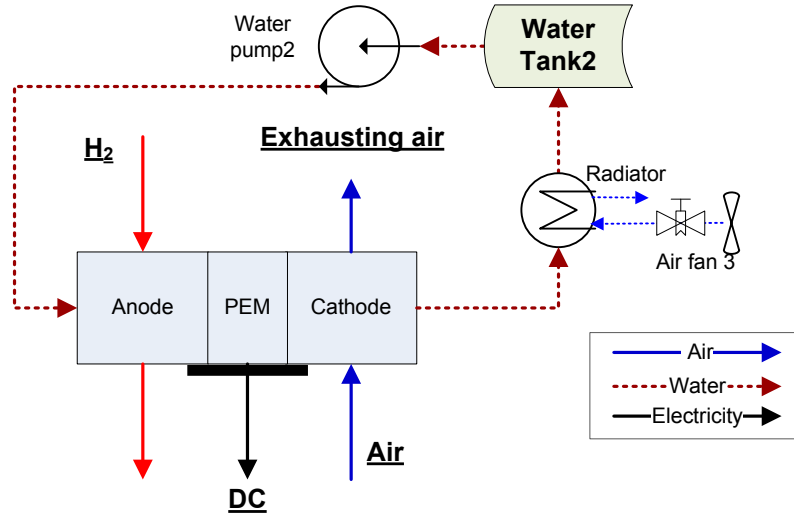


Figure 3.4 Schematic of the Stack Subsystem (SS).

This model considers a single cell which utilizes an H_2 rich mixture gas as the fuel and air as the oxidant, both humidified. The temperature of the fuel cell stack is assumed to be uniform (a good assumption as the temperature variation across the stack is relatively small) and is used to determine the flow rate of the stack cooling water used to maintain this stack temperature. The water vapor contained in the reactant mixtures in the pores of the cathode-side gas diffusion and electrode-catalysts layers is assumed to be in equilibrium with the surrounding liquid phase so that, consequently, the partial water pressure is uniform throughout these layers. Furthermore, the membrane electrolyte is assumed to be saturated completely with water so that its conductivity is only a function of temperature. The SS model was developed by Wang (2008) and the SS model has been used as a part of the PEMFC system model for system synthesis/design and operation/control optimization in this doctoral research.

3.2.2 Mathematical Model of a Single PEMFC and the Stack

This fuel cell model does not consider the anode overpotential, and the voltage across the anode is assumed as a constant value (Springer et al., 1996). Thus, the

mathematical model for the PEMFC only describes the chemical-physical behaviors on the cathode side. The basic assumptions of this model are as follow:

- One-dimensional model: all quantities are described in the direction orthogonal to the anode and cathode.
- Gas diffusion layer and catalyst layer have a constant porosity and tortuosity.
- Temperature is uniform over the entire cell surface.
- Air total pressure is uniform, while the partial pressures of its components vary, that is, the deriving force is the concentration difference in oxygen and not the pressure gradients.
- Partial water pressure is uniform.
- Membrane is considered as being completely saturated with water so that its proton conductivity is only a function of temperature.

3.2.2.1 Cathode Gas Diffusion and Catalyst Layer

The cathode catalyst layer is where the oxygen, protons, and electrons react to produce water, so gas diffusion through this layer is needed to describe the electrochemical activity occurring in the PEMFC. Figure 3.5 depicts the diffusion of oxygen from the flow channels through the gas diffusion layer (GDL) to and through the catalyst layer and the diffusion of protons from the membrane through the catalyst layer.

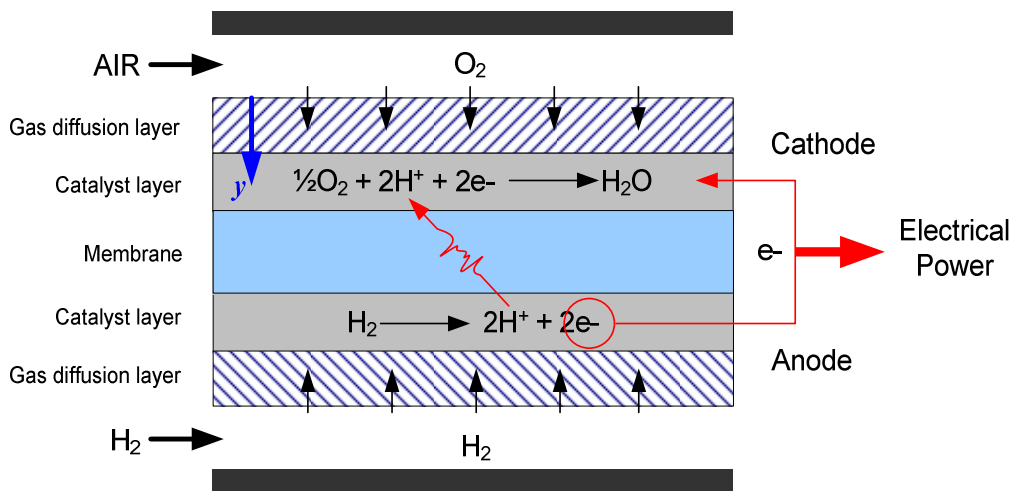


Figure 3.5 Description of species diffusion through the electrode and membrane and the electrochemical reactions of a single PEMFC.

Air mixed with water vapour diffuses through the GDL (y-direction), and its behaviours can be described by species equations and the Stefan-Maxwell equation of diffusions, i.e.

Species equations:

$$\frac{\varepsilon_g}{RT} \frac{\partial p_i}{\partial t} + \frac{\partial N_i}{\partial y} = 0 \quad (3.1)$$

Stephan-Maxwell equations of diffusion:

$$\frac{\varepsilon_g}{\tau^2} \frac{\partial p_i}{\partial y} = \sum_{k=1}^3 \frac{RT}{p_c d_{ik}} (p_i N_k - p_k N_i) \quad (3.2)$$

$$p_{cathode} = p_1 + p_2 + p_3 \quad (3.3)$$

where $i(k) \in (1,3)$ indicates constituents (1– O₂, 2 – H₂O, and 3 – N₂)

p_i : partial pressure of each constituent (bar)

$p_{cathode}$: pressure at the cathode (bar)

$p_{cathode} d_{ik}$: pressure-diffusivity products (bar-cm²/s)

N_k : superficial flux of species k (mol/cm²s)

ε_g : porosity which is the ratio between pore volume and total layer volume

τ : tortuosity which is the ratio between the actual pore length and macroscopic diffusion layer thickness

The pressure-diffusivity products can be estimated from their critical temperatures ($T_{cr,i}$, K) (Bird, Stewart, and Lightfoot, 1960) and pressures ($p_{cr,i}$, bar) and the molecular weights (M_i) as given in Table 3.1. Thus, as a function of temperature only, they can be written as

$$\begin{aligned} p_{cathode} d_{12} &= D_{12}(T) \\ &= 3.55 \cdot 10^{-4} \sqrt{\left(\frac{1}{M_1} + \frac{1}{M_2}\right)} \frac{(p_{cr1} p_{cr2})^{1/3}}{(T_{cr1} T_{cr2})^{0.750}} T^{2.334} = 4.281 \cdot 10^{-7} T^{2.334} \end{aligned} \quad (3.4)$$

$$\begin{aligned} p_{cathode} d_{13} &= D_{13}(T) = 1.882 \cdot 10^{-3} \sqrt{\left(\frac{1}{M_1} + \frac{1}{M_2}\right)} / (\sigma_{13}^2 \Omega_{13}) T^{3/2} \\ &= 5.338 \cdot 10^{-5} T^{1.5} / \exp\left(\frac{83.63}{T}\right) \end{aligned} \quad (3.5)$$

$$\begin{aligned}
p_{cathode} d_{23} &= D_{23}(T) \\
&= 3.687 \cdot 10^{-4} \sqrt{\left(\frac{1}{M_2} + \frac{1}{M_3}\right)} \frac{(p_{c2} p_{c3})^{1/3}}{(T_{c2} T_{c3})^{0.750}} T^{2.334} = 4.477 \cdot 10^{-7} T^{2.334}
\end{aligned} \tag{3.6}$$

Table 3.1 Critical pressures and temperatures and molecular weights.

Subscript	Species	M [g/mol]	T _{cr} (K)	p _{cr} (bar)
1	O ₂	31.999	154.35	50.4
2	H ₂ O	18.015	647.3	221.2
3	N ₂	28.013	126.05	33.93

The partial pressure of the H₂O in the vapor phase of the reactants of the cathode macropores corresponds to the saturation pressure which can be expressed as

$$p_{sat}(T) = 7.714 \cdot 10^5 \exp\left(\frac{-5052.9}{T}\right) \tag{3.7}$$

By assuming a uniform temperature and total pressure within the cell and using equations (3.4) and (3.6), equations (3.1) and (3.2) for constituent 2 (the water vapor) become

$$\frac{\partial N_2}{\partial y} = 0 \tag{3.8}$$

$$N_2 = N_2(t) = \frac{p_2}{p_c - p_2} [N_1(y, t) + N_3(x, t)]_{y=a} \tag{3.9}$$

where a is any value in the y -direction within the cathode layer. For convenience, a is chosen to be at the cathode membrane interface. At this interface, the instantaneous oxygen flux is directly proportional to the current flux per unit volume, j_r , of the Butler-Volmer equation for the electro-chemistry in the cell, and the nitrogen flux at the interface between cathode and membrane can be assumed to be zero. Thus,

$$N_1(L_d, t) = N_{1dc} = \frac{j_r(L_d, t)}{4F} \tag{3.10}$$

$$N_3(L_d, t) = 0 \tag{3.11}$$

where L_d is the thickness of the cathode layer. Equation (3.1), then, becomes, using equations (3.10) and (3.11),

$$N_2 = N_2(t) = \frac{p_2}{p_c - p_2} \frac{j_r(L_d, t)}{4F} \tag{3.12}$$

Finally, by combining equations (3.1), (3.2), and (3.4), a single partial differential equation is obtained as follows:

$$\frac{\partial p_1}{\partial t} = \omega \frac{\partial^2 p_1}{\partial \xi^2} - \psi \frac{j_r}{4F} \frac{\partial p_1}{\partial \xi} \quad (3.13)$$

in which ξ is the dimensionless distance y/L_d and

$$\omega = \frac{1}{\tau^2 L_d^2 (p_2/D_{12} + (p_{cathode} - p_2)/D_{13})} = \frac{1}{\tau^2 L_d^2 (p_{sat}/D_{12} + (p_{cathode} - p_{sat})/D_{13})} \quad (3.14)$$

$$\psi = \frac{RT}{\epsilon_g L_d (p_{cathode} - p_2)} = \frac{RT}{\epsilon_g L_d (p_{cathode} - p_{sat})} \quad (3.15)$$

To solve this partial differential equation, two boundary conditions have to be defined. At the interface between the flow channels and the diffusion layer, the partial pressure of oxygen can be expressed as

$$p_1(0, t) = p_{10} = \frac{p_{cathode} - p_{sat}}{1 + \beta} \quad (3.16)$$

where β is the mole ratio between the nitrogen and oxygen of the inlet air.

In addition, the Stephan-Maxwell diffusion equation at $\xi = 1$ can be used as the second boundary condition, namely,

$$\frac{\partial p_1}{\partial \xi}(1, t) = \frac{\psi}{\omega} \frac{j_r(1, t)}{4F} [p_1(1, t) + p_{sat} - p_{cathode}] \quad (3.17)$$

3.2.2.2 Proton Concentration

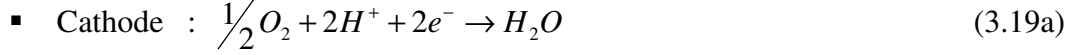
The dimensionless proton concentration c_{H^+} varies in time with the current density. As the cell current rises, the water production and hydration of the polymeric material in the cathode/catalyst layer rises as well. A general expression for the overall time behaviour of the proton concentration is expressed by the following empirical differential equation

$$u \left(-\frac{\partial c_{H^+}}{\partial t} \right) \frac{\partial c_{H^+}}{\partial t} + \frac{c_{H^+}}{\tau_{H^+}} = \frac{1 + \alpha_{H^+} j^3}{\tau_{H^+}} \quad (3.18)$$

where u is the Heaviside step function, τ_{H^+} the time constant related to the c_{H^+} dynamics, and α_{H^+} a parameter linking c_{H^+} to the cell current.

3.2.2.3 Electrochemical Reaction

The reactions taking place in the catalyst layers of the electrodes as shown in Figure 3.5 are as follows:



The current that is created by these electrochemical reactions depends directly on the potential difference between the carbon support for the catalyst and the polymer material surrounding the carbon supported catalyst as well as on the reactant concentrations. The reaction current density j_r can be expressed by the Butler-Volmer equation as

$$j_r = j_0 A_r \left[\frac{p_1}{p_1^0} \frac{[H^+]}{[H^+]_0} \exp\left(\frac{\alpha n F}{RT} \eta\right) - \exp\left(-\frac{(1-\alpha)nF}{RT} \eta\right) \right] \quad (3.20)$$

where $[H^+]$ is the bulk flow proton concentration, $[H^+]_0$ the reference proton concentration, η the voltage overpotential due to activation and concentration losses, α the transfer coefficient, n the number of electrons of the elementary electrochemical reaction, A_r the effective catalyst area per unit geometric area, and j_0 the exchange current density.

In a PEM fuel cell, there is a positive overpotential for the cathodic polarisation and a negative one for the anode. In general, when the overpotential is cathodic, the second term in the Butler-Volmer equation becomes negligible, and j_r can be more simply expressed by the following equation:

$$j_r = j_0 A_r \left[\frac{p_1}{p_1^0} \frac{[H^+]}{[H^+]_0} \exp\left(\frac{\alpha n F}{RT} \eta\right) \right] \quad (3.21)$$

However, at low current density, the second term cannot be neglected, since the overpotential of the cell tends to zero when the current of the fuel cell tends to zero. In this case, the Butler-Volmer equation can be expressed as

$$j_r = j_0 A_r \left[\frac{p_1}{p_1^0} \frac{[H^+]}{[H^+]_0} \exp\left(\frac{\alpha n F}{RT} \eta\right) - 1 \right] \quad (3.22)$$

Note that in this equation, when j_r equals zero, then η must equal zero to satisfy this equation. The cell current density, j , is the sum of the reaction current density, j_r , and the charge storage which represents stored charge in the electrical double layer at the interface between the catalyst layer and the diffusion layer and is expressed as

$$j = j_r + C_{dl} \frac{\partial \eta}{\partial t} \quad (3.23)$$

where C_{dl} is the double layer capacitance and is assumed constant.

Solving equations (3.21) and (3.23) is a complex problem because of the number of partial differential equations. To make this problem simpler, Ceraolo, Miulli, and Pozio (2002) introduced a parameter A_r , which is a ratio between the total catalytic surface and cell surface, to be a function of the cell current density such that

$$A_r = A_{r,0} \exp(-a_1 j - a_2 j^5) \quad (3.24)$$

where

$$a_1 = a_{1,ref} p_{O_2}^{\alpha_1} N_{air}^{\alpha_2} \exp\left(\frac{k_1}{T} - \frac{k_1}{T_{ref}}\right) \quad (3.25a)$$

$$a_2 = a_{2,ref} \frac{p_{sat}}{p_c} N_{air}^{\alpha_3} \exp\left(\frac{k_2}{T} - \frac{k_2}{T_{ref}}\right) \quad (3.25b)$$

and the expressions for a_1 and a_2 have been correlated very precisely with experimental results obtained at different temperatures and pressures of the reactant gases. Constant values for α_1 , α_2 , α_3 , k_1 , k_2 , T_{ref} , $a_{1,ref}$, and $a_{2,ref}$ in equation (3.25) can be found in Ceraolo, Miulli, and Pozio (2002).

Now by introducing the Tafel slope b , equation (3.22) can be rearranged as

$$j_r = j_0 A_r \left[\frac{p_{O_2}}{p_{O_2}^0} \frac{[H^+]}{[H^+]_0} \exp\left(\frac{\eta}{b}\right) - 1 \right] \quad (3.26)$$

where $b \equiv \frac{RT}{\alpha n F}$ (3.27)

Equation (3.26) describes the current of reaction for the entire range of current density. However, the Tafel slope b , although given by equation (3.27) is for the case of $j_r < j_o$, and must be reevaluated for the case of $j_r > j_o$. In this case, which corresponds to high current density, experimental data has shown that the Tafel slope does not depend on temperature anymore. Hence, equation (3.28) below is used and α and n are no longer constant. For high current density, as oxygen reduction proceeds on the free-oxide Platinum, the high current Tafel slope can be considered as constant between 30 °C and

80 °C, which corresponds to the desired interval of temperature. The Tafel slope for high current density then is

$$b_h = \frac{RT}{n\alpha F} = 0.0504 \quad (3.28)$$

Experimentally, the point at which the Tafel slope switches from equation (3.27) to equation (3.28) takes place at an overpotential given by

$$\eta_b = E_0 - 0.8 \quad (3.29)$$

To ensure continuity at this switching point, the difference between the low and high exchange current densities can be obtained imposing continuity at $\eta = \eta_b$. This result in

$$\Delta j = j_{0l} A_{r0} \left[\exp\left(\frac{\eta_b}{b_l} - \frac{\eta_b}{b_h}\right) - 1 \right] \quad (3.30)$$

where Δj is the difference in high and low exchange current densities. Equation (3.30) and equation (3.27) and (3.28) can now be used along with a step function to determine an exchange current density and Tafel slope which applies not only at the switching point but across the entire range of current densities, i.e.

$$j_0 = j_{0l} + \Delta j \cdot u(\eta - \eta_b) \quad (3.31)$$

$$b = b_l + (b_h - b_l) \cdot u(\eta - \eta_b) \quad (3.32)$$

Finally, by combining equation (3.24) and equations (3.30) and (3.31), the product of j_o and A_r , which appears in equation (3.26) can be written as

$$j_0 A_r = j_{0l} A_{r0} \left\{ 1 + \left[\exp\left(\frac{\eta_b}{b_l} - \frac{\eta_b}{b_h}\right) - 1 \right] \cdot u(\eta - \eta_b) \right\} \cdot \exp(-a_1 j - a_2 j^5) \quad (3.33)$$

where

$$j_{0l} A_{r0} = j_{ref} \exp\left(-\frac{k_0}{T} + \frac{k_0}{T_{ref}}\right) p_{O_2}^{\alpha_0} \quad (3.34)$$

and where of values for all of the constants are available in Ceraolo, Miulli, and Pozio (2002). With these last two equations and equation (3.23), the cell current density, j , can be calculated as a function of time.

3.2.2.4 Cell Voltage

The Nernst equation describes the open-circuit voltage of a cell and it is given by

$$E_0 = E_{ref} + \frac{dE_0}{dt}(T - T_{ref}) + \frac{RT}{2F} \ln(p_{H_2} p_{O_2}^{1/2}) \quad (3.35)$$

It can be modified to improve agreement with experimental data as follow:

$$E_0 = E_{ref} + \frac{dE_0}{dt}(T - T_{ref}) + k \frac{RT}{2F} \ln(p_{H_2} p_{O_2}^{1/2}) \quad (3.36)$$

where the parameter k is slightly less than 1. Ceraolo, Miulli, and Pozio (2002) suggest 0.755 for Nafion™ 115 from their study.

The cell voltage drops in three ways: activation loses, ohmic loses, and concentration loses. Activation losses are caused by the slowness of the reactions taking place on the surface of the electrodes. A proportion of the voltage generated is lost in driving the chemical reaction that transfers the electron to or from the electrode. Ohmic losses are the straightforward resistance to the flow of electrons through the material of the electrodes and the various interconnections, as well as the resistance to the flow of protons through the electrolyte. Concentration losses result from the change in concentration of the reactants at the surface of the electrodes. The reduction in concentration is the result of a failure to transport sufficient reactant to the electrodes surface, or alternatively reaching a point when the transfer of any more reactant to the surface does no good since the reaction is already consuming as much as it can.

Through the cathode kinetics described in Section 3.2.2.3, activation and concentration loses are described in terms of the voltage overpotential η due to loses from both of them. The cell voltage which includes all overpotential factors can be expressed as

$$V = E_0 - \eta - R_{ohm} j \quad (3.37)$$

The third term on the right-hand side of equation (3.37) represents ohmic loses and is proportional to cell current density and the internal ohmic resistance R_{ohm} . The passage of the current through the cell causes ohmic voltage drops due to the transfer of electrons in the electrodes and conductive graphite plates and due to the transfer of protons through the membrane. The conductivity of the graphite is much larger than that of the membrane. Consequently, the voltage drops due to electron transfer can be assumed to be

negligible. Ceraolo, Miulli, and Pozio (2002) report an internal ohmic resistance model for a Nafion™ 115 as a function of temperature given by

$$R_{ohm} = R_{ref} + \alpha_T (T - T_{ref}) \quad (3.38)$$

where T_{ref} is the reference temperature 343.15 K and α_T is a correction coefficient term given in the reference.

3.2.2.5 Gross Stack Output

The voltage of a single cell is limited to about 1 v, and usually is only about 0.6~0.7 v at operational current level (O'Hayre et al., 2006). However, fuel cell systems are required to supply much higher voltage than the single cell voltage. To obtain the required output voltage level, fuel cells are interconnected in series in order to construct stack. Overall output power of a fuel cell stack can be expressed as follows:

- For a single cell: $P_{cell} = VI = V(jA_{cell}) \quad (3.39a)$

- For a stack: $P_{stack} = (VI)N_{cell} = [V(jA_{cell})]N_{cell} \quad (3.39b)$

in which I is the cell current (A), A_{cell} the activation area of a single cell, and N_{cell} the number of cells.

3.3 Fuel Processing Subsystem (FPS)

3.3.1 Description of the FPS

Several reforming technologies have been developed to produce hydrogen which is produced from hydrocarbon fuels with oxidants such as steam and/or oxygen, i.e. steam reforming, partial oxidation reforming, and autothermal reforming. For the present application, a typical steam reformer is selected for the FPS proposed here which uses natural gas as its fuel. Steam reformers have been extensively used for many years to produce hydrogen for chemical plants and oil refinery plants.

In most fuel cell systems for stationary applications, the majority of hydrocarbon fuels can be used as fuels for residential applications of fuel cells. Among these hydrocarbon fuels, natural gas is leading candidate for a number of reasons among which are that it is widely available, clean, and fairly easy to reform. Natural gas exists as a

mixture of gases and usually consists mainly of methane. Table 3.2 presents a typical composition of natural gas obtained from Union Gas Limited (2006). Based on this data, it is assumed here that natural gas can be represented by a pure methane gas.

Table 3.2 A typical chemical composition of natural gas.

Component	Typical Value (mol %)
Methane	94.69
Ethane	2.58
Propane	0.20
Nitrogen	1.60
Carbon dioxide	0.81
Etc	0.12

Once hydrogen is obtained from natural gas through the reforming process, it enters on the anode side of the fuel cell stack where it reacts electrochemically while oxygen, which enters the stack with the air, reacts electrochemically on the cathode side. For the residential application, the PEMFC system configuration described in Figure 3.2 does not need a methane compressor nor a fuel tank to supply methane to the reformer since the system can be supplied continuously through a natural gas line with enough pressure to run a PEMFC system.

A FPS for a PEMFC system must not only generate hydrogen fuel efficiently but must also remove contaminants (i.e. sulphur and carbon monoxide). Therefore, the FPS model developed here consists of a SMR, high/low temperature water-gas shift reactors (HTSR/LTSR), a preferential oxidation (PrOx) reactor, a steam generator, a combustor, and heat exchangers. Natural gas is fed into the combustor and the SMR. Before natural gas reaches the combustor to produce thermal energy to support the steam reforming process, it gets thermal energy from the combustor exhausting gases via the heat exchanger 1 (HX1). Natural gas to the SMR which is mixed with steam from the steam generator also thermal energy from the combustion gases which exhaust from the SMR. Fuel and steam are fed into the SMR, and the SMR produces hydrogen rich gases.

The reformat gas from the SMR goes to the HTSR followed by the LTSR, and then to the PrOx reactor to remove CO. The HTSR, LTSR, and PrOx involve exothermic processes and their operating temperature are around 600 ~ 700 K for the HTSR, 450~550 K for the LTSR, and 400~550 K for the PrOx. Thermal management for the

reactors plays an important role because a very low CO concentration (around 10 ppm) must be achieved for the PEMFC and this essentially depends on the operating temperatures for each reactor. To maintain the appropriate inlet temperature of the reformat gas at each reactor, compact heat exchangers are placed between the reactors to drop the reformat gas temperature via a heat interaction with the cooling air. The temperature of the cooling air which occurs after the HX between the SMR and the HTSR is around 800~ 900 K and the cooling air is used for combusting natural gas. Initially, the cooling air path through each reactor (HTSR, LTSR, and PrOx) and the HXs (HX2 to HX4) is designed as single path as seen in Figure 3.6. The intention is to achieve a simple FPS configuration which maximizes system efficiency by waste heat recovery using the heat exchanger network. As is seen in later in Chapter 5, this cooling path is of necessity somewhat more complicated. However, discussion of this is left for later.

The outlet temperature of the PrOx may be around 400~550 K which is too high for the stack. Thus, the gas temperature must be controlled carefully for safe operation of the PEMFC stack. For this reason, a condenser is used to cool down the temperature of the hydrogen rich gases, and the condensed water is trapped and fed back to water the tank. After passing through the condenser, the reformat gas is 100 % humidified. Therefore, an additional humidifier for the reformat gas is not necessary for this system. Finally, reformat gas from the FPS is supplied to the SS. The following sections provide a description of the various FPS components and the transient kinetic, thermodynamic, and heat transfer models used to simulate these components and this subsystem.

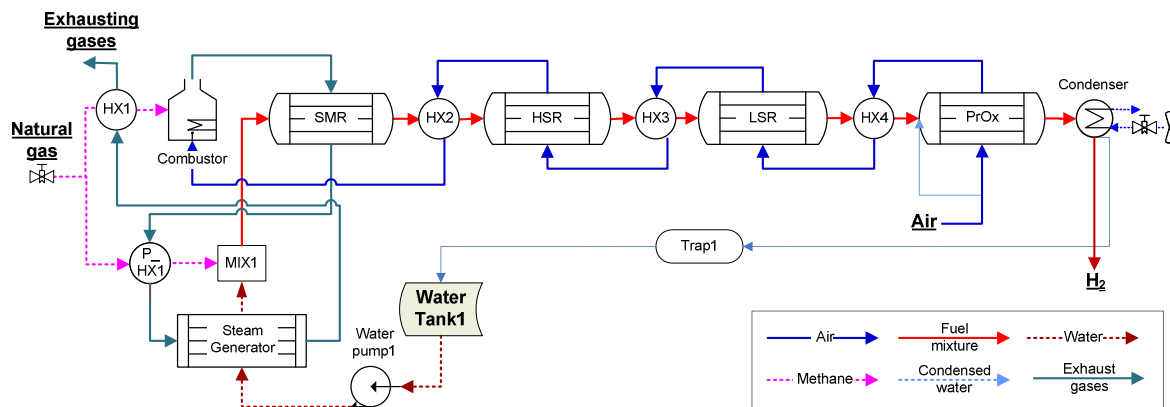


Figure 3.6 Configuration of the initially proposed fuel processing subsystem.

3.3.2 Steam Methane Reformer (SMR)

A plug-flow steam methane reformer is the typical technology for hydrogen production in industry. A detailed kinetic model for the SMR is that developed and validated by Xu and Froment (1989) using the generalized Langmuir-Hinshelwood kinetic model which is based on a rate determining step and uniform surface assumption. Xu and Froment's model has been widely accepted as the basis for the design of SMRs as well as other types of reactors, and this model also is adopted for the design of the SMR in this doctoral work. However, to obtain a more accurate model for a practical reformer in which large catalyst pellets are used, the reformer's intrinsic reaction kinetics are combined with transport limitation terms.

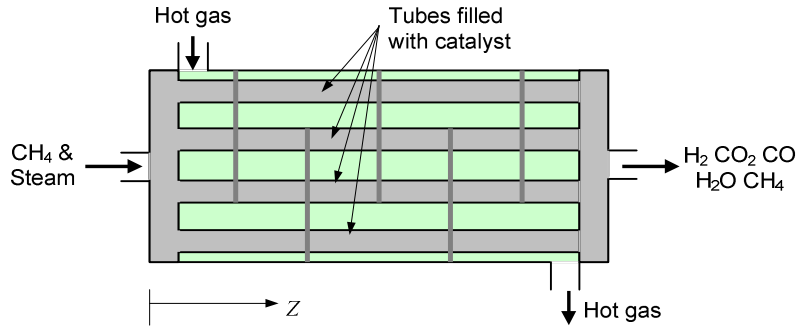


Figure 3.7 Schematic of the proposed SMR.

A number of assumptions are introduced to facilitate the modeling of the SMR, and the most significant are as follow:

- The reactor type is assumed to be a plug flow reactor.
- Only three chemical kinetic reaction mechanisms are assumed active.
- The model is one dimensional along the reactor.
- Ideal gas behavior is assumed for the thermodynamic property calculations.
- Fick's law is used for the diffusional limitation modeling.
- A shell-tube heat exchanger structure is assumed for the basic reactor structure, and the pipe shapes as straight hollow cylinders as shown in Figure 3.7.
- Pellet shape is assumed for the catalyst geometry.
- No carbon deposition is allowed in the SRM.
- The walls of the reactor are adiabatic.

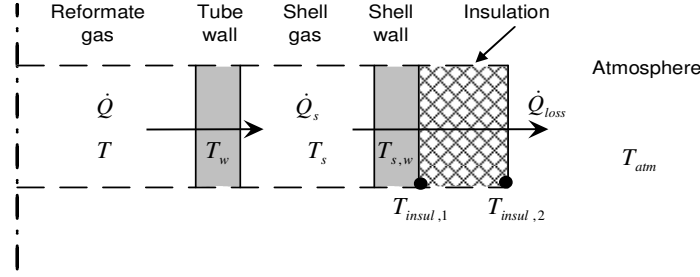


Figure 3.8 Fundamental description of the heat transfer mechanism in a reactor model.

As seen in Figure 3.8, in particular, adiabatic assumption of the outer shell side wall can be explained as

$$\dot{Q} = \dot{Q}_s + \dot{Q}_{loss} \quad (3.40)$$

where \dot{Q} is the heat transfer rate from reformat gas to shell side gas, \dot{Q}_s is the heat transfer rate by shell side gas, and \dot{Q}_{loss} is the heat loss rate to atmosphere. If the outer shell is completely insulated, \dot{Q}_{loss} can be ignored.

For example, at the middle of the SMR for full load operation, the reformat gas temperature T , tube wall temperature T_w , and shell side gas temperature T_s are 1068.5 K, 1102.5 K, and 1136 K, respectively. In addition, the reformat gas side heat transfer coefficient, h_w , and shell side gas heat transfer coefficient, h_s , are 89.8 W/m²K and 92.7 W/m²K, respectively. \dot{Q}_{loss} can be estimated by calculating the inner and outer temperature of the insulator. If $T_{insul,1}$ is assumed to be same temperature as T_s , the outer temperature $T_{insul,2}$ can be calculated as

$$\dot{Q}/A = h_w(T - T_w) = -5926.8 \text{ W/m}^2 \approx k/L_{thick} (T_{insul,2} - T_{insul,1}) \quad (3.41)$$

where k is the thermal conductivity of the insulator (assumed 0.04 W/mK) and L_{thick} is the thickness of the insulator (assumed 0.01 m). Then, $T_{insul,2}$ is about 374 K, and heat loss can be also roughly calculated as

$$-\dot{Q}_{loss}/A = -h_{natural}(T_{insul,2} - T_{atm}) = -370 \text{ W/m}^2 \quad (3.42)$$

where $h_{natural}$ is the natural convective heat transfer coefficient (assumed 5 W/m²K) and the atmosphere temperature T_{atm} is assumed to be 300 K. These sample calculations (equations (3.41) and (3.42)) show that heat loss is less than 6.2% if the outer wall of the shell is insulated. The latest insulation materials show thermal conductivities of around 0.01 W/mK, so less than a 1.6% level of heat loss can be achievable. For the lowest operating condition (40% of full load) during dynamic simulation in this work, the heat loss is around 5.1%. Therefore, the

adiabatic assumption for the shell wall side is reasonable for the entire dynamic operation regime if the shell is well insulated.

3.3.2.1 Reaction Kinetics

Even though there are 11 possible reaction mechanisms in the SMR, three are dominant:



The endothermic demethanation reaction mechanism is the first one listed above while the second reaction mechanism is the exothermic water-gas shift reaction. However, both reactions must be accompanied by the overall reaction $R3$ in order to describe the reaction kinetics correctly. Each rate of reaction r_i contains information for both the forward and backward reactions of each reaction mechanism and is expressed as follows:

$$r_1 = \frac{k_1}{P_{H_2}^{2.5}} \left[P_{CH_4} P_{H_2O} - \frac{P_{H_2}^3 P_{CO}}{K_{eq1}} \right] / DEN^2 \quad (3.46a)$$

$$r_2 = \frac{k_2}{P_{H_2}} \left[P_{CO} P_{H_2O} - \frac{P_{H_2} P_{CO_2}}{K_{eq2}} \right] / DEN^2 \quad (3.46b)$$

$$r_3 = \frac{k_3}{P_{H_2}^{3.5}} \left[P_{CH_4} P_{H_2O}^2 - \frac{P_{H_2}^4 P_{CO_2}}{K_{eq3}} \right] / DEN^2 \quad (3.46c)$$

$$DEN = 1 + K_{CO} P_{CO} + K_{H_2} P_{H_2} + K_{CH_4} P_{CH_4} + K_{H_2O} \frac{P_{H_2O}}{P_{H_2}} \quad (3.47)$$

where the k_i represent the rate coefficients of each reaction i , the P_j the partial pressures of each species j , the K_{eqi} the equilibrium constants of each reaction i , and the K_j the adsorption constants of each species j .

Equilibrium constants K_{eqi} are determined via the following expressions:

$$K_{eq1} = \exp\left(-\frac{26830}{T} + 30.114\right) \quad (3.48a)$$

$$K_{eq2} = \exp\left(\frac{4400}{T} - 4.036\right) \quad (3.48b)$$

$$K_{eq3} = K_{eq1} \cdot K_{eq2} \quad (3.48c)$$

The adsorption constants and rate constants are determined by the van't Hoff and Arrhenius relations, respectively, with the pre-exponential factors, the activation energies, and reaction enthalpies gives as listed in Table 3.3. Thus,

$$K_j = A(K_j) \exp\left(\frac{\Delta H_j}{RT}\right), \quad j = CH_4, H_2O, CO, CO_2, H_2 \quad (3.50)$$

$$k_i = A(k_i) \exp\left(\frac{E_i}{RT}\right), \quad i = 1, 2, 3 \quad (3.51)$$

The rate of reaction of species j is then calculated using

$$r_{CH_4} = -(r_1 + r_3) \quad (3.52a)$$

$$r_{H_2O} = -(r_1 + r_2 + 2r_3) \quad (3.52b)$$

$$r_{H_2} = 3r_1 + r_2 + 4r_3 \quad (3.52c)$$

$$r_{CO} = r_1 - r_2 \quad (3.52d)$$

$$r_{CC_2} = r_2 + r_3 \quad (3.52e)$$

Table 3.3 List of the pre-exponential factors and activation energies/reaction enthalpies.

Pre-exponential factors		Activation energy/ Reaction enthalpy [kJ/mol]	
$A(k_1)$	4.255×10^{15} [kmol.bar ^{0.5} /(kg _{cat} .h)]	E_1	240.1
$A(k_2)$	1.955×10^6 [kmol/(kg _{cat} .h.bar)]	E_2	67.13
$A(k_3)$	1.020×10^{15} [kmol.bar ^{0.5} /(kg _{cat} .h)]	E_3	243.9
$A(K_{CO})$	8.23×10^{-5} [bar ⁻¹]	ΔH_{CO}	-70.65
$A(K_{H_2})$	6.12×10^{-9} [bar ⁻¹]	ΔH_{H_2}	-82.90
$A(K_{CH_4})$	6.65×10^{-4} [bar ⁻¹]	ΔH_{CH_4}	-38.28
$A(K_{H_2O})$	1.77×10^5	ΔH_{H_2O}	88.68

3.3.2.2 Diffusional Limitation

In order to apply the intrinsic kinetics to the sizing of a real reactor, the diffusional limitations must be taken into account for reasonable kinetics in the reactor. Diffusion is the migration of a species in space, as a result of a variation in its chemical

potential, in the direction of decreasing potential. The variation in chemical potential may arise as a result of variations in the driving forces due to concentration, pressure, and temperature gradients. Three diffusion modes are generally considered in assessing the diffusional limitation: molecular diffusion which is the result of molecular collisions in the pores of the particle, Knudsen diffusion which is the result of molecular collisions with the walls of the pores, and surface diffusion due to a gradient in surface concentration. Since it is hard to get enough information about pore structure and other factors needed for evaluating diffusion, Fick's law is used to take into account these phenomena as a function of pressure and temperature.

In this work, the effective diffusivity is estimated in terms of molecular diffusivity for diffusion in a binary system and Knudsen diffusivity characterized by the porosity ε and tortuosity τ of the diffusion medium. For a gas mixture, equation (3.53) shows the relationship between the overall diffusivity $D_{e,i}^*$, which only accounts for chemical potential variations, and the effective diffusivity $D_{e,i}$ which accounts for the structural characteristics of each catalyst pellet via the porosity and tortuosity (Missen, 1998). Thus,

$$D_{e,i} = \frac{\varepsilon}{\tau} D_{e,i}^* \quad (3.53)$$

where
$$\frac{1}{D_{e,i}^*} = \frac{1}{D_{K,i}} + \frac{1}{D_{i,m}} \quad (3.54)$$

and
$$D_{i,m} = \frac{1 + y_i}{\sum_{\substack{j=1 \\ k \neq j}}^m \frac{y_j + y_k}{D_{j,k}}} \quad (3.52)$$

Here y_i is the mole fraction of species i in the mixture, $D_{j,k}$ is the molecular diffusivity, and $D_{K,i}$ is the Knudsen diffusivity. The former of these last two diffusivities is estimated using the Fuller-Schettler-Giddings diffusivity, namely,

$$D_{j,k} = \frac{10^{-3} T^{1.75} \sqrt{\frac{1}{M_j} + \frac{1}{M_k}}}{P^o \sqrt{V_j^{1/3} + V_k^{1/3}}} \quad (3.56)$$

where M_j and M_k are the molecular weights of species j and k , V_j and V_k are the diffusion volumes of species j and k , and P^o is the atmospheric pressure. $D_{j,k}$ has units of cm^2s^{-1} and P^o is kPa . Table 3.4 shows the diffusion volumes and the molecular weights for the species involved.

Among the many Knudsen diffusivity models, Satterfield's formula is adopted here and r_e is the average pore radius in cm . Thus,

$$D_{k,i} = 9700r_e \left(\frac{T}{M} \right)^{1/2} \quad (3.57)$$

Table 3.4 The diffusion volumes and molecular weights of the species involved.

Species	Diffusion volume	Molar weight	Species	Diffusion volume	Molar weight
CO	18.9	28.01	O ₂	16.6	32.0
CO ₂	26.9	44.01	H ₂	7.07	2.016
H ₂ O	12.7	18.01	CH ₄	24.4	32.04

For the SMR model developed here, the shape of pellet is assumed to be spherical so that the effectiveness factor η_i for the catalyst is given by (Missen, 1998)

$$\eta_i = \frac{3}{\phi_i} \left(\frac{1}{\tanh \phi_i} - \frac{1}{\phi_i} \right) \quad (3.58)$$

where ϕ_i is the Thiele modulus and is defined as

$$\phi_i = L_e \left(\frac{k_i}{D_{e,i}} \right)^{1/2} \quad (3.59)$$

Here, L_e is a common effective diffusion path length parameter, k_i the rate coefficient of reaction i , and $D_{e,i}$ the effective diffusivity of reaction i . Combining the diffusion effectiveness factors with the intrinsic kinetic model makes the SMR model developed able to describe the chemical reactions of the SMR more correctly. The following section explains how the reactor model is established using the effectiveness factor.

3.3.2.3 Governing Equations for the SMR Modeling

A dynamic model is developed to describe the SMR's behavior using transient mass and energy balances as well as a pressure loss correlation for non-isothermal, and non-adiabatic operating conditions. These are as follow:

▪ **Mass balance**

The transient tube-side differential mass balance for the plug-flow reactor describes the chemical kinetics in the reactor and can be expressed in terms of the concentration C_j as

$$\varepsilon_b \frac{\partial C_j}{\partial t} = -\frac{\partial(uC_j)}{\partial z} + (1 - \varepsilon_b) \rho_{cat} \sum_{i=1}^3 v_{ji} \eta_i r_i \quad (3.60)$$

where j is the species, i the reaction number, v_{ji} the stoichiometric coefficient of species j in reaction i , ε_b the bed void fraction, u the superficial velocity, η_i the effectiveness factor of the reaction i , and ρ_{cat} the density of the catalyst.

▪ **Energy balance**

Three separate energy balances for the SMR to describe the transient energy interactions of the reactor are: used the tube-side energy balance, the shell-side energy balance, and the tube wall energy balance. They are as follow:

Tube- side energy balance

$$(\varepsilon_b \rho_g c_{pg}) \frac{\partial T}{\partial t} = -\frac{\partial(u \rho_g c_{pg} T)}{\partial z} - (1 - \varepsilon_b) \rho_{cat} \sum_{i=1}^3 \eta_i r_i H_i + h_w \frac{4}{D_i} (T_w - T) \quad (3.61)$$

where T is the bulk temperature of the mixture, c_{pg} the specific capacity of the reacting mixture, ρ_g the density of the mixture, and H_i the enthalpy of the mixture. In the last term on the right hand side, h_w is the inside tube wall convective heat transfer coefficient and T_w is the wall temperature.

In the last equation, the left hand side represents energy storage in the gas, the first term on the right hand side describes convective energy flow along the axis of the reactor, the next term is the energy generation/consumption due to the chemical reaction mechanisms, and the last term is the heat interaction between the wall and the gas. The heat transfer coefficient h_w for a packed-bed tubular reactor is obtained from the following empirical correlations (Li and Finlayson, 1977):

$$h_w = 2.03 \cdot \text{Re}_p^{0.8} \cdot \frac{D_i}{k_g} \cdot \exp\left[-\frac{6d_p}{D_i}\right] \quad \text{for spherical packing} \quad (3.62)$$

$$(20 \leq Re_p \leq 7600, 0.05 \leq d_p/D_i \leq 0.3)$$

$$h_w = 1.26 \cdot Re_p^{0.95} \cdot \frac{D_i}{k_g} \cdot \exp\left[-\frac{6d_p}{D_i}\right] \quad \text{for cylindrical packing} \quad (3.63)$$

$$(20 \leq Re_p \leq 800, 0.03 \leq d_p/D_i \leq 0.2)$$

$$Re_p = \frac{G_g d_p}{\mu} \quad (3.64)$$

where Re_p is Reynolds number, k_g the gas thermal conductivity, d_p the catalyst diameter, G_g the mass flux, and μ the gas viscosity.

Shell-side energy balance

$$\left(\frac{\dot{n}_s}{V_s} c_{ps}\right) \frac{\partial T_s}{\partial t} = -\dot{n}_s c_{ps} \frac{\partial T_s}{\partial z} - h_s \pi d_o (T_s - T_w) \quad (3.65)$$

where T_s is the bulk temperature of the gas, \dot{n}_s the molar flow rate of gas, c_{ps} the specific heat at constant pressure of the gas, V_s the flow velocity of the gas, d_o the outer diameter of the tube, and h_s the heat transfer coefficient on the shell-side. The heat transfer coefficient h_s is determined via the heat exchanger model which is briefly outlined in Section 3.3.5 below.

Tube wall energy balance

$$\rho_w (d_o^2 - d_i^2) c_w \frac{\partial T_w}{\partial t} = 4h_s d_o (T_s - T_w) - 4h_w d_i (T_w - T) \quad (3.66)$$

where ρ_w is the tube material density, c_w is the specific heat of the tube material, and d_i is the inner diameter of the tube.

▪ Pressure distribution

The axial pressure distribution can be described by the Ergun equation (Bird, Stewart, and Lightfoot, 1960) as

$$f = \frac{1 - \varepsilon_b}{\varepsilon_b^3} \left(1.75 + 150 \frac{(1 - \varepsilon_b) \mu}{d_p \rho_g u} \right) \quad (3.67)$$

$$\frac{dP}{dz} = -f \cdot \frac{\rho_g u^2}{d_p} 10^{-5} \quad (3.68)$$

where f is the friction factor of the flow due to the catalyst particles, d_p the catalyst particle diameter, and P the pressure of the mixture gas. Of course, overall pressure drop along the reactor is also calculated by

$$\Delta P = L \left(-f \cdot \frac{\rho_g u^2}{d_p} 10^{-5} \right) \quad (3.69)$$

here ΔP is the total pressure drop in the reactor and L is the reactor length.

Concentration, flow rate, and temperature of the reformat gas is related to this pressure term. If there is a significant pressure gradient in the reactor, the axial pressure distribution is, using the ideal gas equation of state, as follows (Fogler, 1999):

$$\frac{dP}{dz} = \left(-f \cdot \frac{\rho_g u^2}{d_p} 10^{-5} \right) \left(\frac{P_o}{P} \right) \left(\frac{T}{T_o} \right) \left(\frac{\dot{n}_T}{\dot{n}_o} \right) \quad (3.70)$$

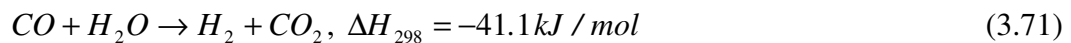
where P_o , T_o , and \dot{n}_o are the inlet pressure, temperature, and molar flow rate of the reformat gas, respectively, and \dot{n}_T is the total molar flow rate in the reactor.

3.3.3 CO Removal Unit

Although the amount of CO exiting the SMR is not significant (on the order of 6 ~ 10% on a molar basis) compared to the other species, a PEMFC does not tolerate even this amount of CO since it poisons the fuel cell electrode catalysts. To eliminate the remaining CO, both HTSR and LTSR are used for converting CO to CO₂. However, via water-gas shift reactions only, it is hard to reduce the CO content to less than 10 ppm. Thus, another CO cleanup unit (e.g., a CO PrOx reactor) is combined with the HTSR and LTSR to reduce the CO level in the PEMFC to a safe level.

3.3.3.1 High-/Low-Temperature Water-Gas Shift Reactors (HTSR/LTSR)

The basic water-gas shift reaction is



This reaction is an exothermic reaction for which many catalysts have been developed. These are classified into two types and have been used extensively in industry: iron-based catalysts and copper-based catalysts (Amadeo and Laborde, 1995). Iron-based catalysts are used in so-

called high-temperature, water-gas shift reactions (600 ~ 700 K), and copper-based catalysts are used in so-called low-temperature, water-gas shift reactions (450 ~ 550 K).

The forward water-gas shift reaction is thermodynamically favored at low temperature due to its higher equilibrium limitation, and, of course, lower pressure increases hydrogen production and decreases the operating cost of the FPS. However, even though copper-based catalysts have good activity at lower temperature, these kinds of catalysts have a low resistance to poisoning and thermal stress at lower temperature, and the life span of the copper-based catalysts is shorter than when the catalyst is operated at higher temperature (Ettouney, Shaban, and Nayfeh, 1995). In addition, reaction rates at higher temperature for these catalysts are higher so that the size of the LTSR increases the lower the temperature is. Therefore, in order to control the CO level effectively while maintaining high system reliability, two water-gas shift reactors are used, one at low temperature using the copper-based catalyst and the other at high temperature using the iron-based catalyst. However, note that since 1995, the reactor/catalyst technology has evolved to the point where only a single water-gas shift reactor is used. Nonetheless, our reactor models are not based on this newer technology since data for this technology is still proprietary and, thus, not available in the literature.

▪ **High-Temperature Water-Gas Shift Reactor (HTSR)**

Ettouney, Shaban, and Nayfeh (1995) establish an analytical model of a HTSR/LTSR based on Saraf and Singh (1977), Borgars and Campbell (1974), and Slack and James (1974). Their model shows good agreement with data collected from industry. Borgars's and Campbell's rate equation (equation (3.72a)) and Saraf's and Singh's equation (equation (3.72b)) are developed for the iron-based catalyst kinetics in the HTSR. Both models are adopted in this work, using Fe₂O₃-Cr₂O₃ as the catalyst. The rate equations are

$$r_{CO} = K_{H_s} \exp\left[\frac{E}{R}\left(\frac{1}{T_{H_s}} - \frac{1}{T}\right)\right] \sqrt{P}(y_{CO}) \left(1 - \frac{K}{K_{eq}}\right) \quad (3.72a)$$

$$r_{CO} = \exp\left(-\frac{2500}{RT} + 8.02\right) \sqrt{P}(y_{CO}) \left(1 - \frac{K}{K_{eq}}\right) \quad (3.72b)$$

where K_{H_s} and T_{H_s} are the standard catalyst activity and temperature given in Table 3.5, E is the activation energy given in the same table, R is the ideal gas constant, and K_{eq}

which is the equilibrium constant has the same form as equation (3.48b). The mole fraction ratio K is defined as

$$K = \frac{y_{H_2} y_{CO_2}}{y_{CO} y_{H_2O}} \quad (3.73)$$

Table 3.5 Parameter values in the kinetic equation (3.69a).

Parameter	Value
K_{H_s}	42.669[mol _{CO₂} (s · atm ^{0.5} · m ³) ⁻¹] for $P < 10 \text{ atm}$
	37.870[mol _{CO₂} (s · atm ^{0.5} · m ³) ⁻¹] for $P > 10 \text{ atm}$
T_{H_s}	70615 K
E	48150 J / mol

Table 3.6 Kinetic models for the LTSR along with their activation energies and pre-exponential factors.

Slack and James (1974)	$r_{CO} = \frac{513.15}{T} \frac{K_L y_{CO} y_{H_2O}^{0.5} \left(1 - \frac{K}{K_{eq}}\right)}{\left(\frac{1}{P} + K_A y_{CO} + K_B y_{CO_2}\right)}$				
Moe (1962), Choi and Stenger (2003), Lin et al. (2006)	$r_{CO} = k P_{CO} P_{H_2O} \left(1 - \frac{K}{K_{eq}}\right)$				
Amadeo and Laborde (1995)	$r_{CO} = \frac{0.92 e^{-454.2/T} P_{CO} P_{H_2O} \left(1 - \frac{K}{K_{eq}}\right)}{\left(1 + 2.2 e^{101.5/T} P_{CO} + 0.4 e^{158.3/T} P_{H_2O} + 0.0047 e^{2737.9/T} P_{CO_2} + 0.05 e^{1956/T} P_{H_2}\right)^2}$				
Slack and James (1974)	$K_L = k_L \exp\left(\frac{E_L}{R} \left(\frac{1}{T_s} - \frac{1}{T}\right)\right)$	$\frac{E_L}{R}$	-3620 K	k_L	68.4 mol _{CO} (m ³ · s · atm) ⁻¹
	$K_A = k_A \exp\left(\frac{E_A}{R} \left(\frac{1}{T_s} - \frac{1}{T}\right)\right)$	$\frac{E_A}{R}$	-4580 K	k_A	4.31 (atm) ⁻¹
	$K_B = k_B \exp\left(\frac{E_B}{R} \left(\frac{1}{T_s} - \frac{1}{T}\right)\right)$	$\frac{E_B}{R}$	-1500 K	k_B	1.35 (atm) ⁻¹
		T_s	513.15 K		
	Pre-exponential factor (mol/kg s)		Activation energy		
Moe (1962)	-5.97 × 10 ⁻⁴		12.88-1885.5/T		
Choi and Stenger (2003)	-8.22 × 10 ⁴		-47400, J/mol		
Lin et al. (2006)	-2.137 × 10 ⁴		-47400, J/mol		

▪ **Low-Temperature Water-Gas Shift Reactor (LTSR)**

A number of studies on the use of copper-based water-gas shift catalysts appear in the literature (Amadeo and Laborde, 1995; Giunata, Amadeo, and Laborde, 2006; Choi and Stenger, 2003; Lin et al. 2006; Moe, 1962; Slack and James, 1974) along with a number of kinetic models for CO conversion in the LTSR. These kinetic models are all based on the Langmuir-Hinshelwood formulation and are summarized in the Table 3.6. Amadeo's and Laborde's and Choi's and Stenger's models represent intrinsic kinetics, while the others include external and internal transfer limitations.

▪ **Governing Equations for the HTSR/LTSR Modeling**

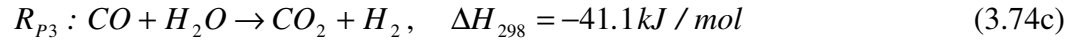
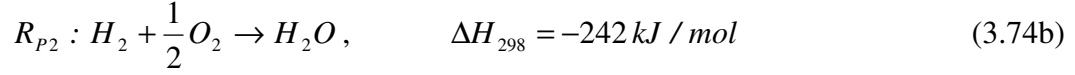
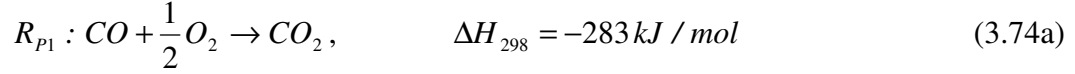
The governing equations of mass and energy along with the associated pressure distribution correlations are the same as those for the SMR (see Section 3.3.2.3).

3.3.3.2 Preferential Oxidation (PrOx) Reactor

Removing CO to acceptable levels before the hydrogen-rich gases enter the fuel cell is of critical importance. A PEMFC system requires an extremely low concentration of CO (less than 10 ppm) even under transient conditions (Jimenez et al., 2005). Various types of CO cleanup methods have been developed: preferential oxidation, methanation, membrane separation, pressure-swing adsorption, and so forth. Among these, CO PrOx technology is used here as the last step of the FPS.

Several different kinetic models for CO preferential oxidation have been introduced by Goerke, Pfeifer, and Schubert (2004), Choi (2004), Lin et al. (2006), etc. A number of these kinetic studies only concentrate on CO oxidation without taking into account other possible reactions in the process such as the water-gas shift reaction. However, in the CO oxidation process, the water-gas shift reaction dominates the overall process over a specific temperature at which the reverse water-gas shift reaction starts to generate CO from CO₂. Kim and Lim (2002), Choi and Stenger (2004), Goerke, Pfeifer, and Schubert (2004), and Chin, Alexeev, and Amirdis (2005) experimentally show the effect of the water-gas shift reaction on the CO oxidation process, and, Choi and Stenger (2004) suggest a kinetic model for CO oxidation which accounts for the effects of this additional reaction mechanism. In this study, Choi and Stenger's kinetic PrOx model using a platinum-iron catalyst is adopted.

There are three possible reaction mechanisms (i.e. CO oxidation-equation (3.74a), H₂ oxidation-equation (3.74b), and water-gas shift reaction-equation (3.74c)) in the PrOx process as follows, and all of them are considered in this study:



The rate of reactions associated with each are expressed as

$$r_{p1} = 3.528 \times 10^2 \exp\left(-\frac{33092}{RT}\right) P_{O_2}^{0.5} P_{CO}^{-0.1} \quad (3.75a)$$

$$r_{p2} = 2.053 \times 10^1 \exp\left(-\frac{18742}{RT}\right) P_{O_2}^{0.5} \quad (3.75b)$$

$$r_{p3} = 4.402 \times 10^3 \exp\left(-\frac{34104}{RT}\right) \left(P_{CO} P_{H_2O} - \frac{P_{CO_2} P_{H_2}}{K_p} \right) \quad (3.75c)$$

where the equilibrium constant K_p is same as in equation (3.48b).

▪ **Governing Equations for the PrOx Reactor Modeling**

The governing equations for mass and energy along with the associated pressure distribution correlations are same as those for the SMR (see Section 3.3.2.3). The only difference is that the diffusion effectiveness factors for the PrOx reactor are obtained from Lin's experimental study (Lin et al., 2006).

3.3.4 Steam Generator (SG)

A steam generator (SG) model for a 5 kWe SOFC system is developed by Rancruel (2005). For a SOFC system, a SG is required to supply steam to the SMR only during the start-up stage. During normal operation, the system simply recirculates steam from the hot exhaust gases exiting the SOFC stack. However, in case of the PEMFC system, steam must be supplied to the SMR by the SG continuously during the system's entire operating regime since the exhaust gas temperature from the PEMFC system is only around 80 °C. Thus, the SG plays an

important role in PEMFC system operation. Figure 3.9 shows the basic structure of the proposed horizontal type of SG.

The shell-tube type heat exchanger structure employed here is a single-pass shell and single-pass tube, and the model for this arrangement is simplified further by assuming a straight cylinder with twisted-tape to facilitate the calculation process. The SG consists of an economizer, an evaporator, and a superheater with a cross-flow arrangement. Since the SG can be broken into in three different regions, their heat transfer mechanisms are integrated based on the identical shell-tube heat exchanger design process.

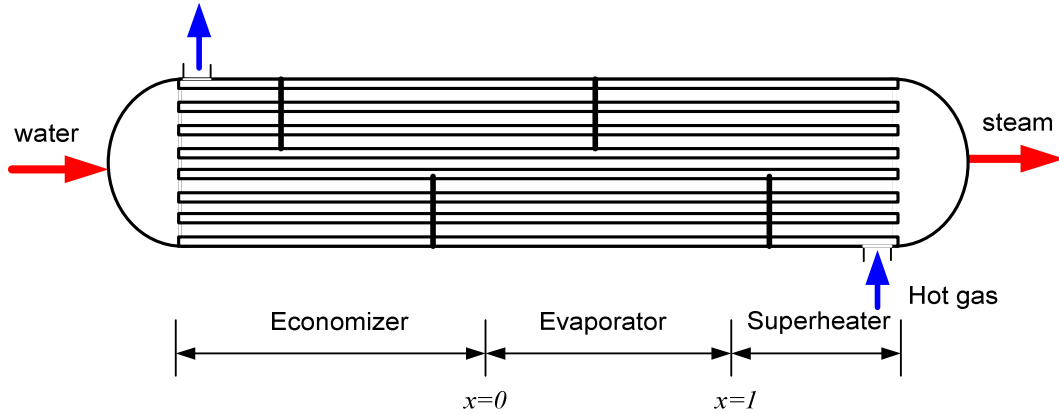


Figure 3.9 Schematic of the horizontal type of steam generator.

The dynamic models for the economizer, evaporator, and superheater are established by the energy balances, equations (3.76) to (3.78) below. The heat transfer rate between the tube wall and water depends on the region and is described in equation (3.78). The first of the balance equations is established for the shell-side as follows:

Shell-side energy balance

Energy balance between the shell side and tube wall can be expressed as

$$\left(\frac{\dot{n}_s}{V_s} c_{ps} \right) \frac{\partial T_s}{\partial t} = -\dot{n}_s c_{ps} \frac{\partial T_s}{\partial z} + h_s \pi d_o (T_s - T_w) \quad (3.76)$$

where \dot{n}_s is the molar flow rate on the shell side, V_s the hot gas flow velocity, T_s the hot gases bulk temperature, T_w the wall temperature, d_o the outer diameter of the tube, and h_s the convective heat transfer coefficient on the shell side.

Tube-wall energy balance

For the tube wall, thermal energy from shell side flows to water inside of the tubes, and its balance equation is

$$\rho_w (d_o^2 - d_i^2) c_w \frac{\partial T_w}{\partial t} = 4h_s d_o (T_s - T_w) - \dot{Q}_{wall / water} \quad (3.77)$$

where ρ_w is the wall density, d_i the inner diameter of the tube, c_w the specific heat of the wall, and $\dot{Q}_{wall / water}$ is the heat transfer rate between the wall and the water.

Wall-water energy balance

In equation (3.77), the heat transfer rate from the tube-wall to the water is in each region as

$$\dot{Q}_{wall / water} = (c_{pt,ec} \dot{n}_t) \frac{\partial T}{\partial z} = h_{t,ec} \pi d_i (T_w - T) \quad \text{for the economizer} \quad (3.78a)$$

$$\dot{Q}_{wall / water} = \dot{n}_t \frac{\partial h}{\partial z} = h_{t,ev} \pi d_i (T_w - T) \quad \text{for the evaporator} \quad (3.78b)$$

$$\dot{Q}_{wall / water} = c_{pt,s} \dot{n}_t \frac{\partial h}{\partial z} = h_{t,s} \pi d_i (T_w - T) \quad \text{for the superheater} \quad (3.78c)$$

where $c_{pt,ec}$, $c_{pt,ev}$, and $c_{pt,s}$ are the specific heats at constant pressure of the water on the tube side for each region, \dot{n}_t is the water molar flow rate, T is the water temperature, and $h_{t,ec}$, $h_{t,ev}$, and $h_{t,s}$ are the convective heat transfer coefficients in the economizer, the evaporator, and the superheater, respectively.

Since the water molar flow rate on the tube side is very low (i.e. the liquid phase velocity is less than 0.002 m/s), two types of flow regimes (laminar or turbulent) are considered. To enhance the heat transfer performance, a twisted tape insert tube model (Webb, 1994) is selected from among various heat transfer enhancement techniques since this model is consistent with the flow characteristics in this system. The greatest difficulty encountered in modeling the SG modeling is that of not being able to find the boundaries of evaporator region. In order to deal with this issue, the flow rates of hot gases and water are set in a constant ratio to each other so that the evaporator region can be established. The appropriate governing equations (see the development below) as well as design equations (see Table 3.7) are obtained from Kakac and Liu (1998) and Thome (2004) for the shell-tube heat exchanger design.

Table 3.7 Heat transfer model and design equations for the steam generator.

Parameters		Value	Parameters		Value
t_w	Tube wall thickness (mm)	0.5	y	Twisting ratio	2.5
N_{pass}	Number of passes	1	δ	Twisted tape thickness (mm)	0.4
CTP	Tube count calculation constant	0.93	P_{ratio}	Pitch ratio	1.25
CL	Tube layout constant	1	N_{baffle}	Number of baffle	2
Assigned Variables			Assigned Variables		
d_{in}	Tube inner diameter		L	Tube length	
N_{tube}	Number of tubes				
Heat Transfer Model Design for the Steam Generator					
<ul style="list-style-type: none"> Shell-Side Heat transfer Model (Kakac and Liu, 1998) 					
Parameters		Expressions			
d_{out}	Tube outer diameter	$d_{out} = d_{in} + 2t_w$			
P_T	Pitch	$P_T = P_{ratio} d_{out}^{SG}$			
D_s	Shell diameter	$D_s = 0.637 \sqrt{\frac{CL}{CTP} \pi N_{tube} (P_T)^2}$			
B	Baffle spacing	$B = 0.6 D_s^{SG}$			
D_{eq}	Equivalent diameter	$D_{eq} = \frac{4(P_T^2 - \pi d_{out}^2 / 4)}{\pi d_{out}}$			
C_{clear}	Clearance	$C_{clear} = P_T - d_{out}$			
A_c	Bundle cross-flow area	$A_c = \frac{D_s C_{clear} B}{P_T}$			
Re_s	Reynolds number	$Re_s = \frac{G_{sh} D_{eq}}{\mu_{gas}}$			
Pr_s	Prandtl number	$Pr_s = \frac{\mu_{gas} c_{p, gas}}{k_{gas}}$			
h_s	Heat transfer coefficient	$h_s = \frac{k_{gas}}{D_{eq}} (0.683 Re_s^{0.466} Pr_s^{1/3}) \quad \text{for } Re_s > 40$ $h_s = \frac{k_{gas}}{D_{eq}} (0.911 Re_s^{0.385} Pr_s^{1/3}) \quad \text{for } Re_s < 40$			
<ul style="list-style-type: none"> Tube-Side Heat Transfer Model for the Economizer (for a single tube) 					
$Re_{t,ec}$	Reynolds number	$Re_{t,ec} = \frac{4\dot{n}_{water}}{\pi d_{in} \mu_{H_2O}}$			
$Pr_{t,ec}$	Prandtl number	$Pr_{t,ec} = \frac{\mu_{H_2O} c_{p, water}}{k_{water}}$			
$h_{t,ec}$	Heat transfer coefficient	$h_{t,ec} = Nu_{t,ec} \frac{k_{water}}{d_{in}}$			

Table 3.7 Heat transfer model and design equations for the steam generator (continue).

<ul style="list-style-type: none"> Tube-Side Heat Transfer Model for the Economizer (for a single tube) (Thomer, 2004) 		
Parameters		Expressions
$Nu_{t,ec}$	Nusselt number	$Nu_{t,ec} = Nu_{bare} \left(1 + \frac{0.769}{y} \right) \quad \text{for } Re_{t,ec} > 2000$ $Nu_{t,ec} = 4.36 \left(\frac{k_{H_2O}}{d_{in}} \right) \quad \text{for } Re_{t,ec} < 2000$
Nu_{bare}	Nusselt number on smooth tube	$Nu_{bare} = 0.023 Re_e^{0.8} Pr_e^{0.4} \left(\frac{\pi}{\pi - 4(\delta/d_{in})} \right)^{0.8} \left(\frac{\pi + 2 - 2(\delta/d_{in})}{\pi - 4(\delta/d_{in})} \right)^{0.2}$
<ul style="list-style-type: none"> Tube-Side Heat Transfer Model for the Evaporator (for a single tube) (Kakac and Liu, 1998) 		
Co	Convection number	$Co = \left(\frac{1}{x} - 1 \right)^{0.8} \left(\frac{\rho_{steam}}{\rho_{water}} \right)^{0.5}$
Bo	Boiling number	$Bo = \frac{\dot{q}_{ev}}{G h_{fg}}$
Fr	Froude number	$Fr = \frac{G^2}{\rho_{water} g d_{in}}$
G	Mass flux	$G = \frac{\dot{n}_{water}}{A_{tube}}$
\dot{q}_{ev}	Surface heat flux	$\dot{q}_{ev} = \frac{(\dot{n}_{gas} c_{p,gas} (T_{gas,in} - T_{gas,out}))_{ev}}{N_{tube} A_{ev}}$
$h_{t,ev}$	Heat transfer coefficient	$h_{t,ev} = h_{water} \left(0.6683 Co^{-0.2} (25 Fr)^{0.3} + 1058 Bo^{0.7} \right)$
h_{water}	Heat transfer coefficient for water	$h_{water} = \frac{k_{water}}{d_{in}} \left(0.023 \frac{G(1-x)d_{in}}{\mu_{water}} \right)^{0.8} Pr^{0.4}$
<ul style="list-style-type: none"> Tube-Side Heat Transfer Model for the Superheater (for single tube) (Thomer, 2004) 		
$Re_{t,s}$	Reynolds number	$Re_{t,s} = \frac{4\dot{n}_{steam}}{\pi d_{in} \mu_{steam}}$
$Pr_{t,s}$	Prandtl number	$Pr_{t,s} = \frac{\mu_{steam} c_{p,steam}}{k_{steam}}$
Nu_{bare}	Nusselt number on smooth tube	$Nu_{bare} = 0.023 Re_{t,s}^{0.8} Pr_{t,s}^{0.4} \left(\frac{\pi}{\pi - 4(\delta/d_{in})} \right)^{0.8} \left(\frac{\pi + 2 - 2(\delta/d_{in})}{\pi - 4(\delta/d_{in})} \right)^{0.2}$
$Nu_{t,s}$	Nusselt number	$Nu_{t,s} = Nu_{bare} \left(1 + \frac{0.769}{y} \right) \quad \text{for } Re_{t,s} > 2000$ $Nu_{t,s} = 4.36 \left(\frac{k_{H_2O}}{d_{in}} \right) \quad \text{for } Re_{t,s} < 2000$
$h_{t,s}$	Heat transfer coefficient	$h_{t,s} = Nu_{t,s} \frac{k_{steam}}{d_{in}}$

3.3.5 Heat Exchangers (HXs)

Both shell-tube type heat exchangers and corrugated-type compact heat exchangers (Kim, 2002) are used to model the heat exchangers in the FPS model. As described in the section on the SG and the SMR, the shell-tube type heat exchanger is applied to the SG and THE SMR/HTSR/LTSR/PrOx reactors. A compact heat exchanger model is applied to the natural gas preheater and the heat exchangers between the reactors for thermal management (see Figure 3.6).

The shell-tube heat exchanger model is already described in Section 3.3.4. In order to describe the transient responses for a compact heat exchanger, Rancruel (2005) develops a fin-type compact heat exchanger for his 5 kWe SOFC system using a spatially discrete computational method and shows results with high accuracy. That transient thermal response of a compact heat exchanger cannot be solved analytically because there are no general solutions of the partial differential equations which described the governing equations of heat exchanger plates and fluid temperature.

Most of heat transfer models in literatures are applicable for higher Reynolds number i.e. at least higher than 2000. However, the compact heat exchangers in the PEMFC system developed are run at low Reynolds numbers of around 100~1000. Kim (2002) develops several types of compact heat exchangers (e.g., dimpled-type, corrugated-type, etc.) for gas-to-gas operating applications at low Reynolds number from 200 to 5000 which can satisfy the operating condition of the heat exchangers in the PEMFC system. Therefore, in this doctoral work, the discrete modeling method is adopted but a corrugate-type compact heat exchanger (Kim, 2002) is selected instead since it shows better heat transfer performance and is consistent with the operating conditions (flow rate and temperature ranges) of the 5 kWe PEMFC system modeled here.

Figure 3.10 depicts the spatial discretization of the compact heat exchanger. As seen in the figure, this model considers only two flow directions (i.e. the x -direction for hot gas path and the y -direction for cold-gas path), and i and k are the indices of the discrete segments. The governing equations (equations (3.79) to (3.83)) describing the behavior of the compact heat exchanger are considered independently at each segment, and the outlet temperatures of each segment are calculated using two inlet temperatures. The two outlet temperatures of a given segment become the inlet temperatures of the

neighboring segments. In this way, the outlet temperatures along the cold-gas and hot-gas sides can be calculated.

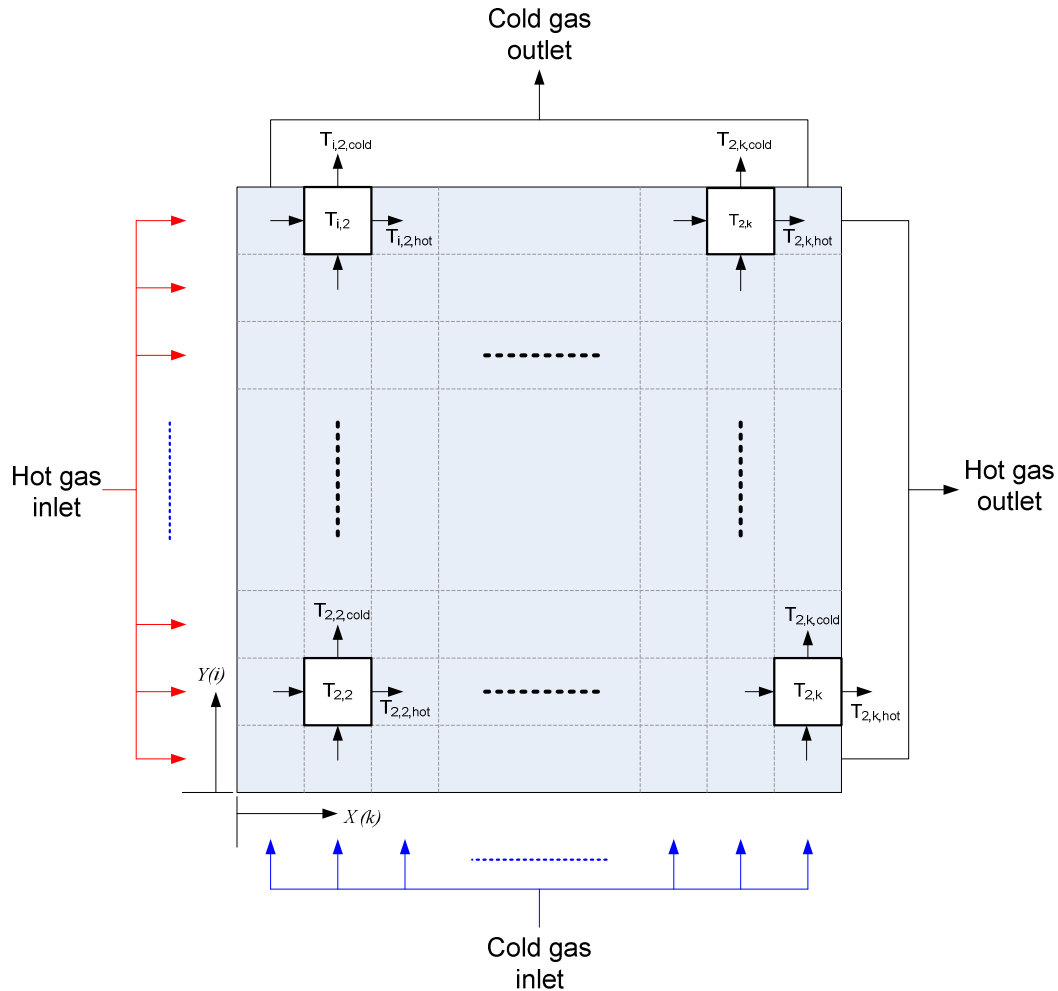


Figure 3.10 Compact heat exchanger spatial discretization.

The following energy balance equations are applied to the cold-gas side, hot-gas side, and heat exchanger plates for the compact heat exchangers, assuming cross-flow:

Hot-gas side energy balance

For the hot-gas side, the balance is

$$\left(\frac{\dot{n}c_p}{V} \right)_h \frac{\partial T_h}{\partial t} = (\dot{n}c_p)_h \frac{\partial T_h}{\partial x} + (hL_y)_h (T_h - T_w) \tag{3.79}$$

where \dot{n} is the molar flow rate, V the hot-gas flow velocity, T_h the hot-gas bulk temperature, T_w the wall temperature, L_y the plate width on the cold-gas side, and h_h the convective heat transfer coefficient (see equation (3.83) below).

Cold-gas side energy balance

On the cold-gas side, the energy balance can be expressed similar to that of hot-gas side energy balance as

$$\left(\frac{\dot{n}c_p}{V}\right)_c \frac{\partial T_c}{\partial t} + (\dot{n}c_p)_c \frac{\partial T_c}{\partial y} + (hL_x)_c (T_c - T_w) \quad (3.80)$$

where T_c is the wall temperature, L_x the plate width on the hot-gas side, and h_c the convective heat transfer coefficient (see equation (3.83) below).

Plate energy balance

The last balance is on the plate and is

$$(mc_p)_w \frac{\partial T_w}{\partial t} = (hA)_c (T_c - T_w) + (hA)_h (T_h - T_w) \quad (3.81)$$

where m is the mass of the plate and A is the plate surface area.

Finally, the modeling of the pressure losses in the corrugate-type compact heat exchanger uses the following friction factor f correlation (Kim, 2002):

$$f = 3.867 \text{Re}^{-0.196} \quad (3.82)$$

while the heat transfer coefficients are determined from (Kim, 2002).

$$Nu = 0.122 \text{Re}^{0.724} \text{Pr}^{1/3} \quad (3.83)$$

3.4 Work-Recovery and Air-Supply Subsystem (WRAS)

3.4.1 Description of the WRAS

The WRAS plays an important role in fuel cell system operation, and Figure 3.11 describes the configuration of the WRAS unit. It consists of a compressor (C) which supplies compressed air to cathode side of the fuel cell stack, an expander (E) that recovers waste thermal energy from exhausting air of the fuel cell stack, and a DC motor (Motor). In principle, the compressor is driven by extracted power from the expander.

However, the power from the expander is not enough to run the compressor, so the DC motor is used to supply additional power to the compressor.

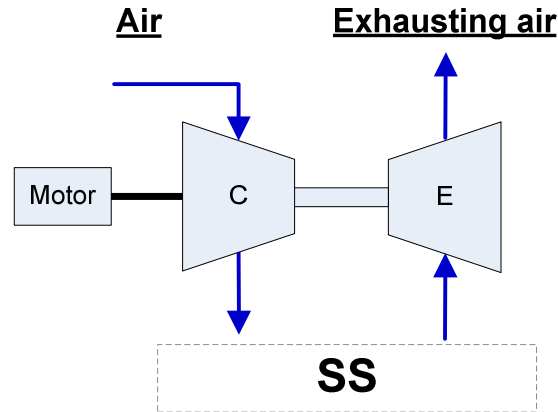


Figure 3.11 Schematic of the WRAS.

It has been shown that a fuel cell system performance and overall system efficiency is highly dependant on an air management subsystem. A fuel cell system favors high (relatively speaking) pressure and an air management subsystem (i.e., especially the air compressor) takes charge of this function. However, to run the air compressor, 5 ~ 30% of the output power of a fuel cell system is consumed. This parasitic power is a major problem when operating a fuel cell system at pressure. Thus, appropriate compressor choice and design is one of the most important issues in a fuel system design.

By combining an expander unit with the compressor, a higher overall system efficiency can be achieved. Even though it is an important part of fuel system design, have been reported only a few studies have been reported. Rancruel (2005) developed a WRAS for a 5 kWe SOFC system and determined size of each component of the WRAS as a part of the system optimization based on life cycle cost. Oscarsson (2003) introduced Opcon Autorotor AB technology, an integrated twin screw expander-compressor unit, for a fuel cell system, and the author showed experimentally that power consumption of the compressor could be reduced up to 35% by using the twin-screw type expander. It corresponded to 10% of the power output of the stack. Ahluwalia, Wang, and Kumar (2003) adopted an integrated compressor-expander unit for their hybrid vehicle system (100 kWe and 160 kWe). The 100 kWe fuel cell system without an expander unit needs a 27 kWe motor for the air management subsystem. However, they show that it could be

reduced to a 9.5 kWe motor by combining it with an expander unit. In addition, overall system efficiency is also increased from 47 % (without expander) to 54 % (with expander).

In this work, the air management subsystem is named the Work-Recovery Air-Supply subsystem (WRAS). To design an appropriate WRAS, compressor, expander, and motor performance maps which describe component behaviors as a function of pressure ratio, flow rate, and shaft rotation speed are necessary. A screw compressor/expander performance map is obtained from Larminie and Dicks (2003) and a motor performance map from Ishida, Shiga, and Sadahiro (2003). Each component model based on these maps is described in the following sections in detail. This subsystem model is developed with Wang (2008) and shared in both doctoral researches.

3.4.2 Compressor and Expander

3.4.2.1 Compressor

A screw type compressor and expander are selected. Because a screw compressor can get a high discharge pressure at low mass flow rates and at low speeds, it provides better performance compared to other conventional compressors like the centrifugal compressor over the entire fuel cell operating range. The other advantage of the screw compressor is that it provides the oil-free output required by fuel cell systems. Therefore, even though screw compressors are more expensive than other typical compressors, they are a better choice for small scale fuel cell systems.

Now, the compressor work rate (or power) is given by

$$\dot{W}_C = \dot{m}_{C,air} c_p \Delta T_C \quad (3.84)$$

where $\dot{m}_{C,air}$ is the mass flow rate of air, c_p the specific heat of the air, and ΔT_C the temperature difference between inlet and outlet air. The temperature difference can be calculated for steady-state using

$$\Delta T_C = T_C^{out} - T_C^{in} = \frac{T_C^{in}}{\eta_C} \left[\left(\frac{p_C^{out}}{p_C^{in}} \right)^{\frac{\kappa-1}{\kappa}} - 1 \right] \quad (3.85)$$

where T_C^{in} and T_C^{out} are the inlet and outlet temperatures, p_C^{in} and p_C^{out} the inlet and outlet pressures, η_C the compressor efficiency at a given flow rate and pressure ratio, and κ the

specific heat ratio. Any mechanical efficiency or leakage is ignored in this model.

Once the compressor outlet pressure, flow rate, and compressor efficiency for a given pressure and flow rate are known, the outlet compressor temperature and compressor work can be calculated. However, the compressor efficiency varies according to the flow rate and the pressure ratio which is a ratio between the outlet pressure and inlet pressure. Thus, a compressor performance map, which addresses the relationship between the flow rate, the rotational speed, the pressure ratio, and the compressor efficiency is needed. When it is available, dynamic operation of a compressor can be correctly described.

For this reason, a gPROMS™ coded version of a screw compressor performance map is developed by Wang (2008) based on Larminie and Dicks (2003) and used for the WRAS design here. Figure 3.12 depicts the developed compressor performance map. The latest version of a screw compressor for small fuel cell systems exhibits up to a maximum 70% efficiency (Osscarson, 2003), so the maximum efficiency of the compressor is set to 70% on this map, and the map scaled accordingly.

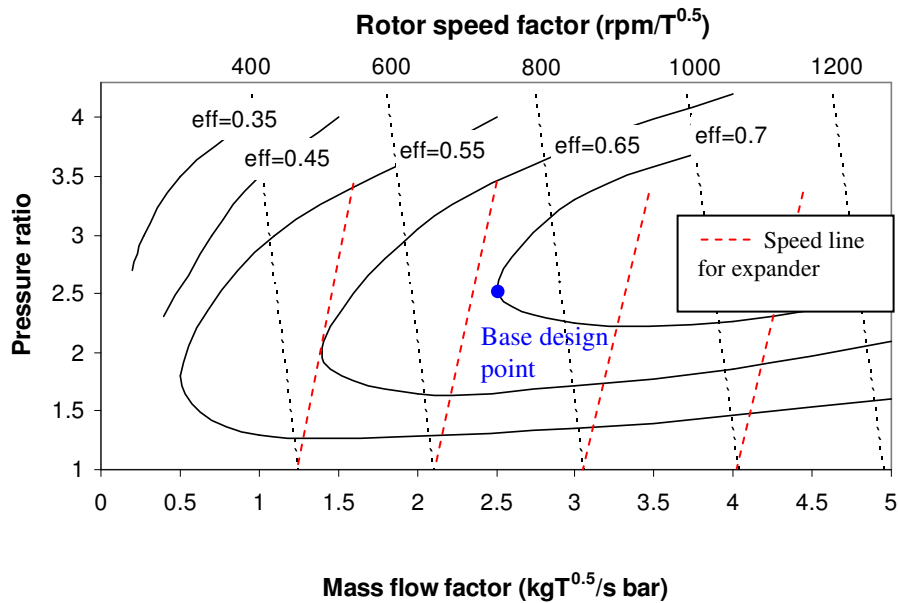


Figure 3.12 Developed compressor performance map for simulation (Wang, 2008).

Dynamic operation of the compressor can be expressed as a function of the mass flow factor equal to $\dot{m}_{C,air} \sqrt{T_C^{in}} / p_C^{in}$, pressure ratio equal to p_C^{out} / p_C^{in} , and the rotor

speed factor equal to N_C^{rpm}/T_C^{in} . The compressor performance map can be described using two correlative equations for rotational speed and efficiency based on a certain pressure ratio and mass flow rate, namely,

$$N_C = f(p_{C,ratio}, \dot{m}_{C,air}) \quad (3.86)$$

and $\eta_C = f(p_{C,ratio}, \dot{m}_{C,air}) \quad (3.87)$

Thus, once the pressure ratio and mass flow rate are known, rotational speed and efficiency are calculated using equations (3.86) and (3.87).

The map in Figure 3.12 cannot be used directly for the fuel cell system because this map is for a 250 kWe system. In order to describe an appropriate operation of the compressor for the 5 kWe PEMFC system developed in this doctoral work, the map needs to be scaled down by using scaling factors for the mass flow rate and pressure ratio. Thus, equation (3.86) and (3.87) can be modified as follow:

$$N_C = f(p_C SF_C^p, \dot{m}_C SF_C^m) \quad (3.88)$$

and $\eta_C = f(p_C SF_C^p, \dot{m}_C SF_C^m) \quad (3.91)$

where SF_C^p is the scaling factor for the pressure ratio and SF_C^m that for the mass flow rate.

Typically, a compressor or expander design for an energy system is primarily about selecting the proper component which can satisfy the maximum capacity required. This simple selection process may provide engineers proper and reasonably priced devices. However, during dynamic operation, the compressor operates in a lower mass flow rate region (i.e. also lower efficiency region) of the performance map, and may, thus, need more parasitic power. Figure 3.13 describes two different compressors. Compressor 1 is smaller than the compressor 2, and each has a different mass flow rate scale for the same pressure ratio P_o . If both compressors are based on the same technology, compressor 1 may be less expensive than compressor 2. Conventional off-design may choose compressor 1 because its price is lower and it can cover all possible operating points. However, if life cycle costs are considered, compressor 2 may be the better choice because it operates in the higher efficiency region and may consume less parasitic power. Therefore, selecting the proper compressor or expander should be left as a part of the system synthesis/design and operation optimization.

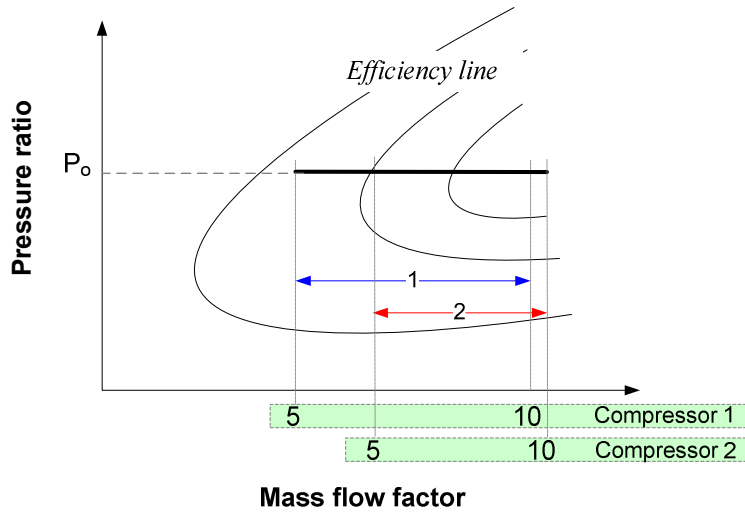


Figure 3.13 Selecting a compressor.

To modify the performance map in Figure 3.12 for 5 kWe PEMFC system, scale factors in equations (3.88) and (3.89) are defined as

$$SF_C^p = \frac{p_C^{B.D}}{p_C^{design}} \quad (3.90)$$

and $SF_C^m = \frac{\dot{m}_C^{B.D}}{\dot{m}_C^{design}} \quad (3.91)$

where $p_C^{B.D}$ and $\dot{m}_C^{B.D}$ are the base design point pressure ratio and mass flow rate factor, respectively. p_C^{design} and \dot{m}_C^{design} are the design pressure ratio factor and mass flow rate factor determined by the optimization. As seen in Figure 3.12, the base design point is set to (2.5, 2.5) on the map. If the operating pressure ratio p_C and mass flow rate factor \dot{m}_C are equal to p_C^{design} and \dot{m}_C^{design} , the performance map represents the originally scaled map.

Finally, a moment balance between each component should be addressed with an energy balance equation (equation (3.84)) to describe the integrated WRAS, and it can be done by

$$\begin{aligned} \dot{W}_C &= \dot{m}_{C,air} c_p \Delta T_C \\ &= Tq_C \left(\frac{2\pi N_C}{60} \right) \end{aligned} \quad (3.92)$$

where Tq_C is the required torque of the compressor. Compressor rotational speed N_C and the

compressor torque Tq_C are determined by the DC motor and expander, as is explained in Section 3.4.4.

3.4.2.2 Expander

Because there are no available screw expander performance maps in the literatures, a modified compressor map has been used for the expander design. For the expander, the slope of the rotational speed lines in the compressor performance map is changed from a negative slope for the compressor to a positive one for the expander. As seen in Figure 3.12, red lines represent the rotational speed of the expander, but the efficiency line is assumed to be same for the both of them. In addition, mass flow rate and pressure ratio are also properly scaled using the same scaling factors as for the compressor. Thus, for the expander,

$$N_E = f\left(p_E \frac{p_E^{B,D}}{p_E^{design}}, \dot{m}_E \frac{\dot{m}_E^{B,D}}{\dot{m}_E^{design}}\right) \quad (3.93)$$

$$\text{and } \eta_E = f\left(p_E \frac{p_E^{B,D}}{p_E^{design}}, \dot{m}_E \frac{\dot{m}_E^{B,D}}{\dot{m}_E^{design}}\right) \quad (3.94)$$

where $p_E^{B,D}$ and $\dot{m}_E^{B,D}$ are the base design point of pressure ratio and mass flow rate factor, respectively. p_E^{design} and \dot{m}_E^{design} are the design pressure ratio factor and mass flow rate factor which are determined by the optimization. The base design point is also set to (2.5, 2.5) on the map the same as for the compressor design. The energy and momentum balance equations for the expander are summarized in Table 3.8.

Table 3.8 Expander dynamic governing equations.

Variable Description		Equation
\dot{W}_E	Expander work rate	$\dot{W}_E = \dot{m}_{E,air} c_p \Delta T_E = Tq_E \left(\frac{2\pi N_E}{60} \right)$ $\Delta T_E = T_E^{out} - T_E^{in} = \eta_E T_E^{in} \left[1 - \left(\frac{p_E^{out}}{p_E^{in}} \right)^{\frac{\kappa-1}{\kappa}} \right]$
T_E^{in}	Inlet temperature	
T_E^{out}	Outlet temperature	
ΔT_E	Temperature difference between the inlet and outlet	
p_E^{in}	Inlet pressure	
p_E^{out}	Outlet pressure	
η_E	Expander efficiency	
N_E	Expander rotational speed (rpm)	
Tq_E	Torque for the expander	

3.4.3 Electrical Motor

The compressor needs a back-up DC motor because the extracted work from the expander is not enough for running the compressor. There are several different DC motor types such as induction motor, DC Brush motor, and Brushless DC motor. Among these, a brushless DC (BLDC) motor is selected here because of its several advantages for a small system such as

- Compact size and light weight
- High efficiency
- Innovating structure to have high torque performance
- Excellent energy saving during heavy-load operation and high torque and low rpm
- Low noise, no brush maintenance
- Much higher power and torque density than conventional motors

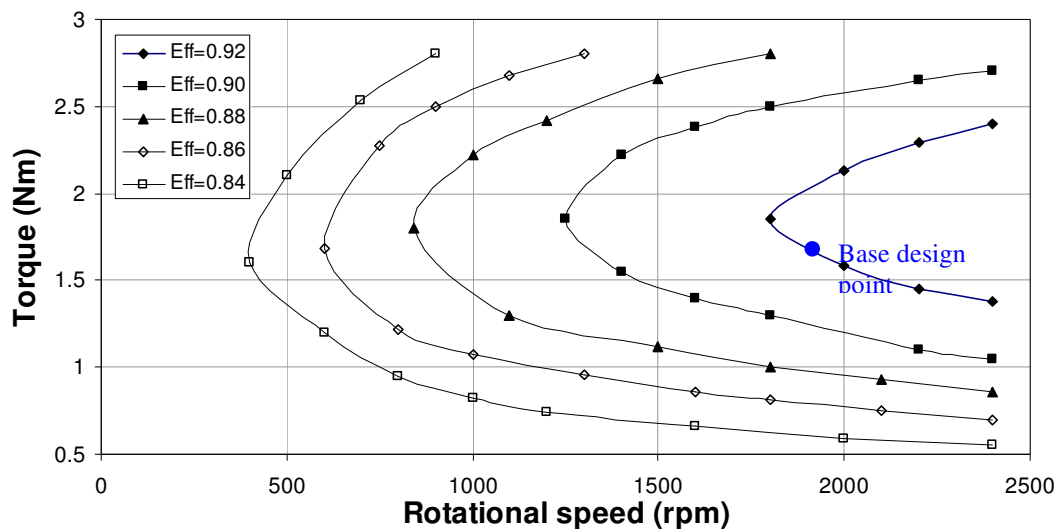


Figure 3.14 Computationally regenerated 50RM230 DC motor.

In the same manner as for the compressor and expander, a motor model for dynamic simulation requires a proper performance map of a BLDC motor. Ishida, Shiga, and Sadahiro (2003) report their developments of high performance BLDC motors, and their 50RM230 model has been used for this doctoral research. Figure 3.14 shows the computationally regenerated performance curve of the 50RM230.

The motor efficiency η_M of the 50RM230 model is correlated as a function of

motor torque Tq_M and rotation speed N_M , namely,

$$\eta_M = f\left(Tq_M \frac{Tq_M^{B.D}}{Tq_M^{design}}, N_M \frac{N_M^{B.D}}{N_M^{design}}\right) \quad (3.95)$$

in which $Tq_M^{B.D}$ and $N_M^{B.D}$ are the base design point of motor torque and rotational speed, respectively. Tq_M^{design} and N_M^{design} are the design motor and rotational speed which are determined by the optimization. The base design point is also set to 1.9 of motor torque and 1900 of rotational speed as shown in Figure 3.14.

Electrical balance

In order to describe dynamic characteristics of a DC motor, one electrical and mechanical balance equation must be considered. The former is given by

$$V_M = R_M I_a + L \frac{dI_a}{dt} + K_b \omega \quad (3.96)$$

where V_M is the input voltage of the motor, R_M the terminal resistance, I_a the armature current, L_M the terminal inductance, K_b the voltage constant, and ω the angular velocity of the motor. The second term on the right-hand side is usually ignored because it has very small value compared to other terms. It is ignored here as well. The mechanical balance is expressed as

Torque balance

$$J_M \frac{d\omega}{dt} = Tq_M - B_M \omega - Tq_L \quad (3.97)$$

in which J_M is the inertia of the rotor and the equivalent mechanical load, B_M the damping coefficient associated with the mechanical rotational system of the machine, and Tq_L the load torque which is related to the mechanical and electrical powered by

$$\dot{W}_M = Tq_M \omega \quad (3.98)$$

$$\text{and } \dot{W}_{M,input} = \dot{W}_M / \eta_M \quad (3.96)$$

Variation in the power required results in an immediate change in the required torque which results in the dynamic variation of the angular velocity. In addition, a variation in the angular velocity causes a variation in the current or the voltage (i.e. it depends on controller). The change in current or voltage results in the variation of efficiency which

can be obtained from the motor performance map. This dynamic variation continues until the power required is equal to the output power produced by the motor.

Table 3.9 Brushless DC motor specifications.

Specifications		Moog Inc.		Pacific Scientific	
		BN42-53AF-01	BN42-53AF-02	FGS2751	FGS2753
Terminal voltage (V)		24	50	90	180
Torque (Nm)	Peak torque	18.0774	18.0774	-	-
	Continuous stall torque	3.5025	3.6014	-	-
	Rated torque	3.1874	2.9164	4.0675	6.1012
Rated speed (rpm/rad/s)		1740 / 182	2820 / 295	1750	1750
Rated current (A)/Peak current (A)		29.2	29.2	9.5 / 81	7.8 / 62
Torque constant, Kt (torque sensitivity, Nm/A)		0.1229	0.1631	0.49713	0.8926
Back EMF, Kb(Ke) (voltage constant)	V/krpm	12.80	17.10	-	-
	V/rad/s	0.1229	0.1631	-	-
Terminal resistance (ohms)		0.065	0.106	0.5	1.2
Terminal inductance (H)		0.241E-03	0.428E-03	3.4E-03	13.5E-03
Motor constant (Nm/W ^{0.5})		0.48194	0.50102	-	-
Rotor inertia (kg-m ²)		4939.9E-07	4939.9E-07	-	-
Mech. time constant (ms)		2.1	2.0	-	-
Electrical time constant (ms)		3.71	4.04	-	-
Rated power (W)		580	861	750	1100

Table 3.9 provides the BLDC motor specifications for several commercial models which can be applied here, and specifications for model BN42-53AF-02 of Moog Inc. have been used for the motor in this doctoral work because the maximum required work of the motor is around 850 W (in case of without the expander) for the 5 kWe PEMFC system developed and all information of the motor is available for the motor modeling.

3.4.4 Coupling of the Compressor, Expander, and Motor

The compressor and expander are connected via a single shaft so that the extracted power by the expander transfers to the compressor, and the DC motor and compressor are also linked through a gear drive as shown in Figure 3.15. The required load on the motor is given by

$$\dot{W}_M = \dot{W}_C - \dot{W}_E \quad (3.100)$$

Moreover, the rotational speeds of the compressor or expander, N_C and N_E should be the same because they are linked via a single shaft as seen in Figure 3.15. However, the

rotational speed of the motor is determined by the rotation speed of the compressor and a gear ratio n_{gear} in the gear drive such that

$$N_E = N_C = N_M / n_{gear} \quad (3.101)$$

and
$$n_{gear} = \frac{n_{load}}{n_{motor}} \quad (3.102)$$

where the gear ratio is a ratio of the number of teeth on the gear of the motor shaft, n_{motor} , and the number of teeth on the gear of the load shaft, n_{load} .

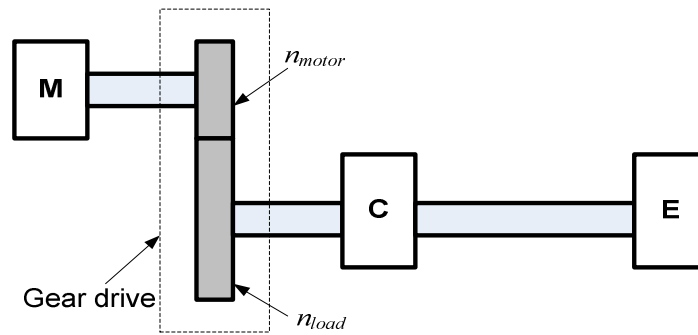


Figure 3.15 Schematic of linkages between components of the WRAS.

Via the above two constraints equations, the compressor, the expander, and the motor are coupled together. During dynamic operation of the PEMFC system, the flow rate and pressure of the air demanded are varied according to the desired conditions. This can be done by a controller which adjusts the input voltage or current of the motor.

3.5 Cost Models for the PEMFC System

The system synthesis/design and operation/control optimization of the PEMFC system carried out here is one of minimizing the life cycle cost of the system which is composed of capital investment cost and operating cost. The operating cost represents the fuel cost required during operation of the PEMFC system, and the capital investment cost consists of the purchase cost, maintenance cost, service cost, taxes, etc. Peter, Timmerhaus, and West (2003) categorize the capital investment cost into direct and indirect costs as follow:

- Direct cost
 - Equipment purchase cost
 - Installation cost
 - Maintenance cost
 - Amortization cost
- Indirect cost
 - Costs for inspection, supervision, taxes, contingencies, etc.

In order to describe life cycle cost of the PEMFC system, all the types of costs listed above have been considered in detail in the thermoeconomic analysis of the PEMFC system.

A very important task is to establish the proper cost models for the economic analysis of an energy system. There are many cost models for energy system components, and the cost functions are, in general, expressed in terms of an original price and cost indexes. A cost index is a value for a given time showing the cost at that time relative to a certain base time (i.e. at the time the original cost was obtained). The current cost of a certain unit is given by

$$C_{present} = C_{original} \left(\frac{I_{present}}{I_{original}} \right) \quad (3.103)$$

where $C_{present}$ is the present price of the component, $C_{original}$ the original price, $I_{present}$ the present cost index, and $I_{original}$ the cost index at the time the original cost was obtained. $C_{original}$ for a certain type of equipment is, in general, expressed as a function of geometric variables with some correction factors related to operating pressure, temperature, efficiency, material, etc.

The cost indexes and original prices of some components (i.e. heat exchangers, chemical reactors, compressor, etc.) are provided by several organizations. In particular, *Chemical Engineering* provides a monthly Chemical Engineering Plant Cost Index, Vatavuk Air Control Cost Index (VAPCCI), and the Marshall & Swift Equipment Cost Index (M&S Index). These are used widely for economic analysis of energy systems.

Although there are many available cost indexed based cost models, it is difficult find appropriate cost models for small scale energy systems like the 5 kWe PEMFC

system because most of them are for large scale energy systems like power plants and oil refineries. Moreover, some available cost functions for small scale systems are even not expressed generally as given by equation (3.103). One of the biggest problems of the cost models applicable for small scale systems is that there may be big differences between the real market prices and the predicted prices. That is because the original prices are obtained from large scale units. Extrapolating to the price of a small scale unit on the basis of the cost function of a large scale unit, in general, overestimates the unit purchase price. For example, a cost function for a compact heat exchanger in Peters, Timmerhaus, and West (2003) predicts around \$1,000 for 1 m² of heat transfer area, even though the real market price is around \$100 for the same size of compact heat exchangers. This discrepancy is clarified using equation (3.104) which is explained in the following section. If the cost function of heat exchangers is based on the large scale heat exchangers, the reference cost in the equation (3.104) is too large to describe small scale heat exchangers. That discrepancy comes from the reference cost. Using unrealistic cost models prejudice the system synthesis/design and operation/control optimization. Therefore, it is necessary to establish and use appropriate cost functions for the optimization process.

In addition, cost functions for fuel cell technologies have not been provided by those organizations which have given cost index based cost models. Thus, in this doctoral research, cost functions for the 5 kWe PEMFC system are obtained from several different literature sources, and are modified by comparing them to real market prices.

3.5.1 Cost Models of the FPS

The cost model of equipment is usually expressed by using the power relationship in terms of a reference cost C_A^{ref} of the equipment and geometric variables X such as volume, heat transfer area, or mass so that

$$C_A = C_A^{ref} (X)^b \quad (3.104)$$

where b is the cost capacity factor which is obtained from a correlation of real prices. All the cost models of equipment purchase cost used in this research are expressed by the equation.

The cost functions for the FPS purchase cost are given in Table 3.10. The cost

function of the SMR, HTSR, and LTSR are obtained from Georgopoulos (2002), and they have been modified to reflect current market prices provided by Johnson Matthey Catalysts, Inc.: KATALCO 23-4 for the SMR, KATALCO 71-5M for the HTSR, and KATALCO 83-3 for the LTSR. The purchase cost of the PrOx is obtained from Kamarudin et al. (2006b). The steam generator cost model of Rancruel (2005) has been modified based on the current cost information provided by Baratto, Diwekar, and Manca (2005a).

Table 3.10 Baseline purchase cost of the FPS.

Variable Description		Model Equation
C_1^{FPS}	Bare reactor purchase cost for the SMR, HTSR, and LTSR	$C_1^{FPS} = 4990(V_{SMR} + V_{HTSR} + V_{LTSR})^{0.4}$
V_i	Volume of a reactor i	
C_2^{FPS}	Catalyst purchase cost for the SMR, HTSR, and LTSR	$C_2^{FPS} = 33548.9V_{C,SMR} + 15467.8V_{C,HTSR} + 24296.5V_{C,LTSR}$
$V_{C,i}$	Volume of the catalyst in a reactor i	
C_3^{FPS}	PrOx reactor purchase cost	$C_3^{FPS} = 1.6 \times 10^5 V_{PrOx}$
C_4^{FPS}	Total heat exchangers purchase costs	$C_4^{FPS} = \sum_{j=1}^n (125.5 A_{HX,j}^{0.4887})$
$A_{HX,j}$	Plate surface area of a heat exchanger j	
n	The number of heat exchangers	
C_5^{FPS}	Steam generator purchase cost	$C_5^{FPS} = 96.2 A_{SG}^{0.7}$
A_{SG}	Steam generator heat transfer area	
C_6^{FPS}	Purchase cost of the major parts	$C_6^{FPS} = \sum_{k=1}^5 C_k^{FPS}$
C_7^{FPS}	Auxiliary parts cost (pipes, controller, pumps, valves, mixing chambers, etc.)	$C_7^{FPS} = 0.2 C_6^{FPS}$
C_8^{FPS}	Baseline purchase cost of the FPS	$C_8^{FPS} = C_6^{FPS} + C_7^{FPS}$

One of the most important types of components of the FPS is the heat exchanger since the FPS requires a complex heat exchanger network. There are a number of cost models (Peter, Timmerhaus, and West, 2003; Couper et al., 2005; Rancurel, 2005; Kamarudin et al., 2006; Haslego and Polley, 2002, etc.) for the compact heat exchangers, but the cost functions predict too much of a difference in prices for the same size heat exchanger. Among them, Haslego's and Polley's (2002) cost model for a compact heat exchanger is close to the requirements (i.e. operating temperature and pressure, type of working fluid, material, and size) of the PEMFC system modeled here, and it is this heat exchanger cost which is used here corrected by the market price offered by Des Champs Technologies.

There are several auxiliary components in the FPS such as pipes line, controller, valves, mixing chambers, combustor, water pumps, etc. The cost of each of these is much lower than those of the other major components, and, thus, they affect little the system synthesis/design and operation/control optimization because they primarily just support the other major components. Their costs are usually considered as 20% of the purchase cost of the major components (Baratto, Diwekar, and Manca, 2005a). It should be noted that the cost information given below is based on a 500,000 unit/year production (Arthur D. Little, Inc, 2001; Carlson et al., 2005; Baratto, Diwekar, and Manca, 2005), and these purchase costs are considered as the baseline costs of the components.

Table 3.11 Economic assumptions for the capital cost analysis.

Parameter Description		Value
N_{units}	Production volume	500000
h	Operating hours per year	7920
N_{year}	Life time (years)	10
f_{main}	Maintenance factor per year	0.1 (10%)
I_{amor}	Interest rate per year	0.05 (5%)

For the assessment of the capital cost of the FPS, several economic assumptions are made and are summarized in Table 3.11. Of course, these assumptions are also applied to the economic analysis of the SS and WRAS. Then, based on the baseline purchase cost of the FPS, a single unit purchase cost of the FPS is calculated. The life cycle cost of this FPS has been addressed in terms of the single unit purchase cost as shown in Table 3.12.

The maintenance factor and capitalization factor were assumed based on Peter, Timmerhaus, and West. (2003). The capital cost analysis implemented is based on a 500,000 unit/year production volume. The effect of a change in the production volume on the single unit cost is taken into account by applying an appropriate scaling factor to the FPS purchase cost. For the purpose of describing this effect, the single unit cost is given by

$$C_{unit} = C_{N_{base}} \left(\frac{N_{unit}}{N_{base}} \right)^{\alpha} \quad (3.105)$$

in which C_{unit} is the single unit purchase cost based on the production volume N_{unit} ,

$C_{N_{base}}$ the baseline manufacturing cost based on the production volume N_{base} , and α the scale factor. The latter expresses the reduction rate of manufacturing cost for the production volume N_{unit} . Perry's Chemical Engineers' Handbook (1997) suggests -0.2196 for the scaling factor based on a production volume of 100,000 units and Oyarzabal (2001) uses -0.362 on the basis of a 500,000 unit production volume. The later number is used for the scaling factor in this analysis.

Table 3.12 Capital cost estimation of the FPS.

Variable Description		Model Equation
f_{cap}	Capitalization factor	$f_{cap} = \frac{I_{amor}(1 + I_{amor})^{N_{year}}}{(1 + I_{amor})^{N_{year}} - 1}$
$C_{purchase}^{FPS}$	Purchase cost of the FPS	$C_{purchase}^{FPS} = C_8^{FPS} \left(\frac{N_{units}}{500000} \right)^{-0.362}$
$C_{install}^{FPS}$	Installation cost of the FPS	$C_{install}^{FPS} = 0.2C_{purchase}^{FPS}$
$C_{indirect}^{FPS}$	Indirect cost of the FPS	$C_{indirect}^{FPS} = 0.101C_{purchase}^{FPS}$
C_{main}^{FPS}	Maintenance cost for life time	$C_{main}^{FPS} = (C_{indirect}^{FPS} + C_{purchase}^{FPS})f_{main}N_{year}$
C_{amor}^{FPS}	Amortization cost for life time	$C_{amor}^{FPS} = (C_{indirect}^{FPS} + C_{install}^{FPS} + C_{purchase}^{FPS})f_{cap}N_{year}$
$C_{capital}^{FPS}$	Capital cost of the FPS	$C_{capital}^{FPS} = C_{main}^{FPS} + C_{amor}^{FPS}$

The installation cost of the FPS is assumed to be equal to 20% of the FPS purchase cost, and 10.1% of the FPS purchase cost is considered as the indirect cost, which is slightly above the 8.6% found in Baratto, Diwekar, and Manca (2005a). Finally, the life cycle cost of the FPS can be expressed as a sum of the purchase cost, installation cost, maintenance cost, amortization cost, and indirect cost as seen in Table 3.12.

The FPS operating cost, of course, is associated with fuel consumption during fuel cell system operation and is given by

$$C_{fuel}^{FPS} = C_{NG} \int_{t=0}^{Lifetime} \dot{n}_{NG} dt \quad (3.106)$$

where C_{NG} is the natural gas price and \dot{n}_{NG} is the consumption rate of natural gas during operation. Then, natural gas price is obtained from the Energy Information Administration (2006), and average residential price of 13.75 \$/kft³ has been used here.

3.5.2 Cost Models of the WRAS

In the same manner as the cost model development for the FPS, the baseline purchase cost models for the WRAS are established first and then the life cycle cost of the WRAS is evaluated. The compressor and expander purchase cost models are adopted from Baratto, Diwekar, and Manca (2005), and the DC motor purchase cost is assumed to be 20% of the compressor purchase cost based on Carlson et al. (2005). Tables 3.13 and 3.14 show the baseline purchase costs and capital cost estimations of the WRAS, respectively.

Table 3.13 Baseline purchase cost of the WRAS.

Variable Description		Model Equation
C_1^{WRAS}	Compressor purchase cost	$C_1^{WRAS} = 256\dot{W}_1^{WRAS}$
\dot{W}_1^{WRAS}	Compressor work at design	
C_2^{WRAS}	Expander purchase cost	$C_2^{WRAS} = 256\dot{W}_2^{WRAS}$
\dot{W}_2^{WRAS}	Expander work at design	
C_3^{WRAS}	DC motor purchase cost	$C_{motor}^{WRAS} = 0.2C_{comp}^{WRAS}$
C_4^{WRAS}	Baseline purchase cost of the WRAS	$C_4^{WRAS} = \sum_{i=1}^3 C_i^{WRAS}$

Table 3.14 Capital cost estimation of the WRAS.

Variable Description		Model Equation
$C_{purchase}^{WRAS}$	Purchase cost of the WRAS	$C_{purchase}^{WRAS} = C_4^{WRAS} \left(\frac{N_{units}}{500000} \right)^{-0.362}$
$C_{install}^{WRAS}$	Installation cost of the WRAS	$C_{install}^{WRAS} = 0.2C_{purchase}^{WRAS}$
$C_{indirect}^{WRAS}$	Indirect cost of the WRAS	$C_{indirect}^{WRAS} = 0.101C_{purchase}^{WRAS}$
C_{main}^{WRAS}	Maintenance cost per year	$C_{main}^{WRAS} = (C_{indirect}^{WRAS} + C_{purchase}^{WRAS})f_{main}N_{year}$
C_{amor}^{WRAS}	Amortization cost per year	$C_{amor}^{WRAS} = (C_{indirect}^{WRAS} + C_{install}^{WRAS} + C_{purchase}^{WRAS})f_{cap}N_{year}$
$C_{capital}^{WRAS}$	Capital cost of the WRAS	$C_{capital}^{WRAS} = C_{main}^{WRAS} + C_{amor}^{WRAS}$

3.5.3 Cost Models of the SS

Most of fuel cell stack cost models are, in general, simply expressed in terms of the gross output power of the stack. However, in that case, the cost model can not describe the size (i.e. number of cell, N_{cell} , and the cell activation area, A_{cell}) and technology (i.e. type

of membrane, catalyst loading, type of bipolar plate, etc.) effects on the stack optimization. Therefore, the stack purchase cost is broken down into stack components purchase cost of the stack (i.e. purchases of the membrane, bipolar plates, and electrodes) and the assembly cost based on Oei et al. (1997) and Oyarzabal (2001). Their cost models have been modified to reflect current prices by comparing to Carlson et al. (2005).

Table 3.15 Baseline purchase cost of the SS.

Variable Description		Model Equation
C_1^{SS}	Membrane cost	$C_1^{SS} = (0.00229256A_{cell} + 0.0182)N_{cell}$
C_2^{SS}	Bipolar plate cost	$C_2^{SS} = (0.00111671A_{cell} + 0.2485)N_{cell}$
C_3^{SS}	Electrode cost	$C_3^{SS} = 0.029742A_{cell}N_{cell}$
C_4^{SS}	Assembly cost	$C_4^{SS} = 24.98 + 0.28105N_{cell}$
C_5^{SS}	Stack purchase cost	$C_5^{SS} = \sum_{i=1}^4 C_i^{SS}$
C_6^{SS}	Auxiliary parts cost (cooling cycle, humidifier, valve, controller, etc)	$C_6^{SS} = 13/6 C_5^{SS}$
C_7^{SS}	Baseline purchase cost of the SS	$C_7^{SS} = C_5^{SS} + C_6^{SS}$

As seen in Table 3.15, the price of the SS is composed of the stack purchase cost and the purchase costs for auxiliary parts including a cooling loop, a humidifier, valves, and controllers. The capital cost of the SS is summarized in Table 3.16.

Table 3.16 Capital cost estimation of the SS.

Variable Description		Model Equation
$C_{purchase}^{SS}$	Purchase cost of the SS	$C_{purchase}^{SS} = C_7^{SS} \left(\frac{N_{units}}{500000} \right)^{-0.362}$
$C_{install}^{SS}$	Installation cost of the SS	$C_{install}^{SS} = 0.2C_{purchase}^{SS}$
$C_{indirect}^{SS}$	Indirect cost of the SS	$C_{indirect}^{SS} = 0.101C_{purchase}^{SS}$
C_{main}^{SS}	Maintenance cost per year	$C_{main}^{SS} = (C_{indirect}^{SS} + C_{purchase}^{SS})f_{main}N_{year}$
C_{amor}^{SS}	Amortization cost per year	$C_{amor}^{SS} = (C_{indirect}^{SS} + C_{install}^{SS} + C_{purchase}^{SS})f_{cap}N_{year}$
$C_{capital}^{SS}$	Capital cost of the SS	$C_{capital}^{SS} = C_{main}^{SS} + C_{amor}^{SS}$

CHAPTER 4

UNCERTAINTY ANALYSIS METHODS FOR DYNAMIC SYSTEM ANALYSIS

All of the models presented in the previous chapter and which will eventually be presented for the whole system in this dissertation contain variables and parameters which have uncertainties associated with them. Uncertainties in the results of system synthesis/design and operation/control optimization can be affected by several uncertainty resources, and they can be categorized into direct and indirect sources as follow:

- Direct uncertainty sources
 - the input values used for variables and parameters of the system model
 - pressure, temperature, flow rate, etc.
 - physical expressions used in modeling
 - rate of reactions, heat transfer models, gas diffusion models, etc.
 - chemical/physical properties
 - uncertainties in the correlation equations for the properties
 - ideal gas model compare to the perfect gas model
 - etc.
 - computational errors
 - truncation errors in finite difference methods (FDMs)
 - different schemes of FDM (i.e. backward, forward, or central)
- Indirect uncertainty sources
 - load profiles
 - a single operating scenario used to develop the system cannot address all possible operating circumstances of the system

- cost functions
 - simplified cost functions may not be sufficient for describing specific technologies which are adopted in the system design
 - possible big gaps between the real market price and predicted price of the cost functions

Since not incorporating these uncertainties into the modeling process may produce misleading results, it is important to consider uncertainty effects on system simulation and synthesis/design and operation/control. This doctoral research has focused on evaluating the uncertainties in system responses due to indirect source of uncertainty (i.e. uncertainties in the load profile and from the cost functions) because the system synthesis/design and operation/control optimization is significantly influenced by the load profile and cost information. In this chapter, several uncertainty assessment techniques are described with the goal of choosing the most appropriate and promising and integrating it into the modeling process in this work.

A deterministic model (i.e. one without uncertainty considerations) or nondeterministic/probabilistic model (i.e. one with uncertainty considerations) can be described in general terms by

$$\vec{M} = f(\vec{X}, \vec{Y}) \quad (4.1)$$

where the vector \vec{M} represents a set of system output values, and vectors \vec{X} and \vec{Y} correspond to a set of synthesis/design and operation/control variables, respectively. If the model is a nondeterministic or probabilistic one and the uncertainties on \vec{X} and \vec{Y} are known, their effects on system development and performance can be evaluated via several possible probabilistic design methods, i.e.

- Sampling methods
 - Monte Carlo simulation (MCS)
 - Adaptive important sampling method
 - Latin hypercube simulation
 - etc.
- Approximate methods

- Response sensitivity analysis (RSA) method
- Fast probability integration (FPI) methods
 - Advance mean-value method
 - First-/second-order reliability methods
 - Hybrid mean-value method
 - etc.

Among the sampling methods, Monte Carlo simulation (MCS) is the most common traditional probabilistic simulation technique for performing a probabilistic analysis on a model via a very large number of repeated simulations. However, when large-scale dynamic optimization with a large number of degrees of freedom is being used to determine the optimal synthesis/design and operation/control of the system, the MCS is so computationally intensive that combined with large-scale optimization it renders the problem computationally intractable. Because of this weakness, other modified sampling methods have been proposed; but these are still inadequately modified for being able to apply them to large-scale system simulation and optimization.

This computational difficulty can be overcome by the use of RSA or FPI methods. These are approximate methods which can only approach the results gleaned from sampling methods such as MCS which provides exact solutions as the number of samples approaches infinity. Of course, how close the approach is and how robust the convergence to a solution determines the viability of the approximate methods. Among these methods, the RSA method and first-order second-moment (FOSM) reliability method (an example of an FPI approach) have been adopted and developed for use with the dynamic energy system synthesis/design and operation/control optimization of the present research.

4.1 Monte Carlo Simulation (MCS)

Once the probabilistic information of a variable such as the mean value, the variance, and/or the probability distribution is known, the randomness of the variable can be simulated close to its true or real randomness using a random number generator. Such

a generator is based on a computational algorithm and is, thus, only a pseudo-random number generator. This type of generator is useful for simulating the real randomness of the variables in computational studies.

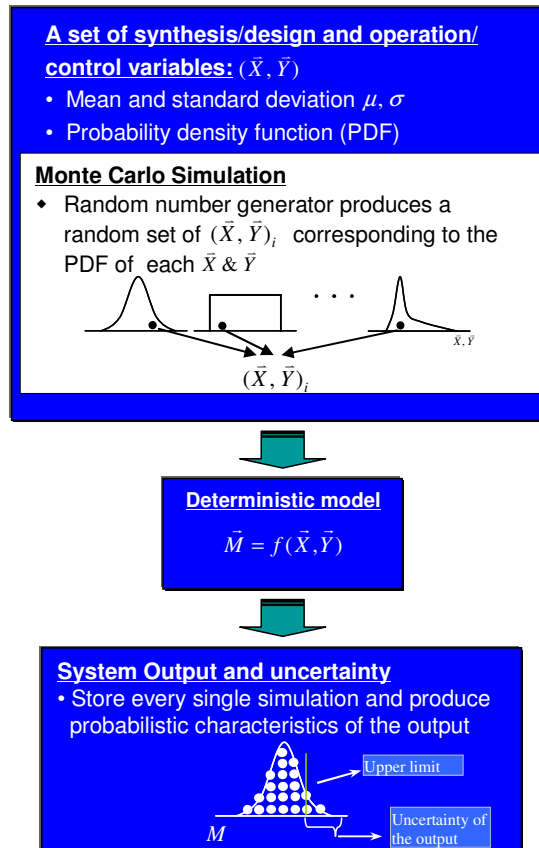


Figure 4.1 Basic concept of MCS coupled with system modeling.

In a real world system, synthesis/design and operation/control variables show characteristics of randomness with a certain degree of uncertainty. This uncertainty can be described by random numbers corresponding to particular probabilistic distributions. MCS can then be used (and has widely been used) to determine the propagation of this uncertainty in the computational analysis of various physical and mathematical problems. MCS is particularly distinguished as a probabilistic simulation technique since it can solve extremely complex and discontinuous problems precisely provided the model is simulated with a high enough sampling number. Figure 4.1 illustrates how MCS is applied in system modeling. In this figure, the set (\bar{X}, \bar{Y}) represents the input

synthesis/design and operation/control decision variables of the system, while $(\bar{X}, \bar{Y})_i$ is the random variable set generated in a single process (i.e. sample). Of course, probabilistic information (i.e. uncertainties) of load profiles and cost functions can be described in the same manner as is done for synthesis/design and operation/control decision variables.

By repeating the same process based on a set of randomly generated input variable values and storing the system output values, a set of probabilistic values and probability distribution functions (PDFs) of the output variables is obtained. This type of approach explicitly results in exact uncertainty (relatively speaking) propagation from the input variables to the system response provided, of course, that the sampling number is high enough. Moreover, the probabilistic information of the system output quantifies the range in the confidence level with which the synthesis/design and operation/control of the system can be viewed relative to the objective limits set on the system. However, even though MCS produces exact solutions and is a powerful probabilistic design method for complex nonlinear energy systems, it is not very practical because of the very large computational effort or burden required.

4.2 Response Sensitivity Analysis (RSA) Based on Taylor Series Expansion (TSE)

One of the practical uncertainty analysis methods commonly used is the sensitivity-based approximation approach, response sensitivity analysis (RSA) method, in which system outputs can be found by a Taylor series expansion. Simulation of a deterministic model provides a set of outputs which may give an incomplete and frequently misleading representation of the system. To complete this information, the sensitivity (variability) and uncertainties in the results are needed. Deterministic point simulation gives no value of the range of sensitivity (variability) which may be expected in the system, and it also does not provide uncertainties in the results. The sensitivity-base uncertainty analysis method, RSA method, can estimate system uncertainties based on response sensitivity analysis by using Taylor series expansion.

The first order moment (mean value) and the second order moment (standard deviation) of the outputs can be estimated easily through the Taylor series expansion. Once the system has highly nonlinear behaviors and the input values have non-normal distribution characteristics, the RSA method may have some errors in its results. However, it can be applicable to dynamic system simulation because it is a computationally inexpensive method compared to MCS.

Using the RSA method, there are only two cases in which probability information (i.e. the PDF, mean, and variance) for the system outputs (\vec{M}) can be determined precisely, i.e. in which the propagation of uncertainty from the inputs ($\vec{Z} = \{\bar{X}, \bar{Y}\}$) to the outputs (\vec{M}) can be found precisely. They are as follow:

- i) If an explicit functional relationship ($g_{M_j}(\vec{Z})$) between each system output (M_j) and the inputs (\vec{Z}) is known and the normal or non-normal PDF ($f(Z_i)$) corresponding to each system input (Z_i) is given and is statistically independent from each of the others, probability information for each system output can be determined analytically/numerically precisely such that the PDF of M_j is given by

$$f_{M_j} = f(M_j) = f(\vec{Z}) = f(Z_1)f(Z_2)\dots f(Z_n), \quad (4.2)$$

the mean is found via

$$\mu_{M_j} = \mu(M_j) = \int_{-\infty}^{+\infty} g_{M_j} f(\vec{Z}) d\vec{Z} \quad (4.3)$$

and the variance by

$$v_{M_j} = v(M_j) = \int_{-\infty}^{+\infty} (g_{M_j} - \mu(M_j))^2 f(\vec{Z}) d\vec{Z} \quad (4.4)$$

- ii) If an implicit linear functional relationship ($g_{M_j}(\vec{Z})$) exists between each system output (M_j) and the inputs (\vec{Z}) and each PDF ($f(Z_i)$) corresponding to each system input (Z_i) is a normal distribution which is statistically independent from each of the others, the system outputs are also normal distributions and precise probability information for each output can be obtained numerically.

However, it is almost impossible for the case of real energy systems to find an explicit functional relationship ($g_{M_j}(\vec{Z})$) between each system output (M_j) and the inputs (\vec{Z}) and solving the integral equations (4.3) and (4.4) can be rather difficult. Furthermore, resorting to an implicit linear relationship affects the quality of the model used to represent the real system, resulting in a loss of information which may not be desirable. Thus, two other possible cases are considered here in which, using the RSA method coupled with first-order Taylor series expansion, one can obtain approximate probabilistic information for each of the system outputs. The two possible cases are as follow:

- i) If only the mean and variance of each system input (Z_i) are known (the exact PDFs are not known) and an implicit nonlinear functional relationship ($g_{M_j}(\vec{Z})$) between each system output (M_j) and the inputs (\vec{Z}) is available, the approximate mean and variance of each system output (M_j) can be estimated by using a Taylor series expansion about the mean values μ_{Z_i} of the inputs, i.e.

$$M_j \cong g_{M_j}(\mu_{\vec{Z}}) + \sum_{i=1}^n (Z_i - \mu_{Z_i}) \left. \frac{\partial g_{M_j}(\vec{Z})}{\partial Z_i} \right|_{\mu_{Z_i}} + \frac{1}{2} \sum_{i=1}^n \sum_{k=1}^n (Z_i - \mu_{Z_i})(Z_k - \mu_{Z_k}) \left. \frac{\partial^2 g_{M_j}(\vec{Z})}{\partial Z_i \partial Z_k} \right|_{\mu_{Z_i \text{ or } k}} + \dots \quad (4.5)$$

However, determining the PDF ($f(M_j)$) corresponding to each system output (M_j) is not practical.

- ii) If an implicit or explicit linear functional relationship ($g_{M_j}(\vec{Z})$) exists between each system output (M_j) and the inputs (\vec{Z}) and each PDF ($f(Z_i)$) corresponding to each system input (Z_i) is a non-normal distribution which is statistically independent from each of the others, the approximate mean and variance of each system output (M_j) can be estimated by using a Taylor series

expansion about the mean values of the inputs (see equation (4.5) above). Again, determining the PDF ($f(M_j)$) corresponding to each system output (M_j) is not practical.

For both of these last two cases, the first-order approximate mean and variance of each output, M_j , are as follow:

$$\mu_{M_j} = \mu(M_j) \approx g_{M_j}(\mu_{Z_1}, \mu_{Z_2}, \dots, \mu_{Z_n}) \quad (4.6)$$

$$v_{M_j} = v(M_j) \approx \sum_{i=1}^n \left(\frac{\partial g_{M_j}}{\partial Z_i} \right)^2 v(Z_i) + \sum_{i=1}^n \sum_{k=1}^n \frac{\partial g_{M_j}}{\partial x_i} \frac{\partial g_{M_j}}{\partial x_k} \chi(Z_i, Z_k) \quad (4.7)$$

where $\chi(Z_i, Z_k)$ is the covariance of Z_i and Z_k . Furthermore, if the $f(Z_i)$ is uncorrelated, i.e. statistically independent, then the variance of M_j reduces to

$$v_{M_j} = v(M_j) \approx \sum_{i=1}^n \left(\frac{\partial g_{M_j}}{\partial Z_i} \right)^2 v(Z_i) \quad (4.8)$$

Square root of the variance of M_j represents the standard deviation of the M_j , σ_{M_j} . For greater accuracy, a second-order mean can be determined using the following expression:

$$\mu_{M_j} = \mu(M_j) \approx g_{M_j}(\mu_{Z_1}, \mu_{Z_2}, \dots, \mu_{Z_n}) + \frac{1}{2} \sum_{i=1}^n \left(\frac{\partial^2 g_{M_j}}{\partial Z_i^2} \right) v(Z_i) \quad (4.9)$$

The above first-order approximations may be successively improved by including higher-order terms in the Taylor series. In order to find the 2nd-order variance, the third and fourth moments of all the \bar{Z} must be known, which is seldom the case. Thus, for practical purposes, the first-order variance (equations (4.7) or (4.8)) and the second-order mean (equation (4.9)) are generally used. In equations (4.5) to (4.9), the derivative term $\partial g_{M_j} / \partial Z_i$ is called the *system response sensitivity* for M_j associated with Z_i .

These approximate expressions for the M_j and the corresponding means and variances are also utilized by the FPI methods discussed in the following section. However, there is an essential difference between RSA and FPI, namely, that FPI is “limit state” driven. For example, if one wants to design a system probabilistically to

always meet or better a given design limit, $g_{l_{M_1}}$, for output M_j , i.e. to meet or better the constraint

$$h_1(\vec{Z}) = g_1(\vec{Z}) - g_{l_{M_1}} = 0 \quad (4.10)$$

use of an FPI approach automatically satisfies this constraint and provides the corresponding minimum ratio between the mean and the variance which corresponds to the highest probability or certainty that this constraint will be met, i.e. it provides the minimum uncertainty. In contrast, the RSA method is not “limit state” driven and, thus, the mean and the variance it provides which nonetheless corresponds to some “limit state”

$$h_1(\vec{Z}) = g_1(\vec{Z}) - g_{l_{M_1}} = C \quad (4.11)$$

does so only after the process of design is complete and not because the design process is driven by this constraint limit. C in equation (4.11) is, of course, a constant which may turn out to be zero so that the result of the RSA method is identical to that of FPI. However, it, in fact, may not be. If not (see Figure 4.2), the RSA method either satisfies equation (4.10) but with a lower probability or greater uncertainty (i.e. $C < 0$) or is unable to satisfy equation (4.10) at all (i.e. $C > 0$). In this figure, β is the reliability index, which is the ratio between the mean and standard deviation of h_1 (see equation (4.24)).

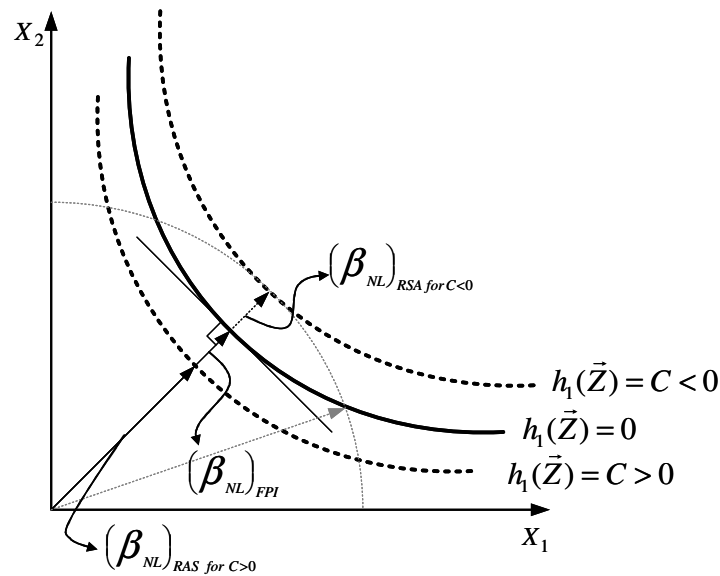


Figure 4.2 Basic ideas of RSA for a non-linear system.

Now, if there are no explicit functional relationship ($g_{M_j}(\vec{Z})$) between the system responses and inputs, the partial derivatives of these functions with respect to the input variables cannot be determined analytically. However, they can be determined numerically using finite difference schemes. For example, for the i^{th} input variable, using the mean plus or minus one step size δ , the j^{th} output M_j can be written as

$$M_{ji}^+ = g(\mu_{Z_1}, \mu_{Z_2}, \dots, (\mu_{Z_i} + \delta), \dots) \quad (4.12)$$

$$M_{ji}^- = g(\mu_{Z_1}, \mu_{Z_2}, \dots, (\mu_{Z_i} - \delta), \dots) \quad (4.13)$$

Employing the second-order central difference scheme, the system response sensitivity for M_j is expressed as

$$\frac{\partial g_{M_j}}{\partial Z_i} = \frac{M_{ji}^+ - M_{ji}^-}{2\delta} + O(\delta^2) \quad (4.14)$$

where the term $O(\delta^2)$ is called as the second-order truncation error. If the truncation error is not that significant, equation (4.14) can be approximated as

$$\frac{\partial g_{M_j}}{\partial Z_i} \approx \frac{M_{ji}^+ - M_{ji}^-}{2\delta} \quad (4.15)$$

Then, the first-order variance of M_j is

$$v_{M_j} \approx \sum_{i=1}^n \left[\frac{M_{ji}^+ - M_{ji}^-}{2\delta} \right]^2 v_{Z_i} \quad (4.16)$$

where the variance v_{Z_i} is the variance of the input Z_i .

Note that the perturbation step size δ should be small enough to minimize the truncation error, but also large enough to avoid sensitivity to simulation error. If the truncation error is large and/or step size is too small, it is helpful to use a 4th-order central difference scheme which has a truncation error term of the order $O(\delta^4)$ and it is given by

$$\frac{\partial g_{M_j}}{\partial Z_i} \approx \frac{M_{ji}^{--} - 8M_{ji}^- + 8M_{ji}^+ - M_{ji}^{++}}{12\delta} \quad (4.17)$$

$$\text{Where } M_{ji}^{++} \approx g(\mu_{Z_1}, \mu_{Z_2}, \dots, (\mu_{Z_i} + 2\delta), \dots) \quad (4.18)$$

$$\text{and } M_{ji}^{--} \approx g(\mu_{Z_1}, \mu_{Z_2}, \dots, (\mu_{Z_i} - 2\delta), \dots) \quad (4.19)$$

Finally, a summary of the characteristics for RSA are as follow:

- RSA is based on calculations involving the statistical moments (mean, variance, skewness, etc.) of the inputs and does not require their PDFs (i.e. normal, gamma, Poisson, etc.).
- Approximate statistical moments of the system responses (i.e. outputs) are obtained from Taylor series expansions directly.
- Whether or not the input variables are statistically correlated (dependent) or uncorrelated (independent) makes a difference as to which approximate relations are used (e.g., equation (4.7) versus (4.8)).
- Lower order estimations (e.g., the use of equation (4.6)) may cause some errors for highly nonlinear responses.
- Higher order estimations (e.g., the use of equation (4.9)) address adequately highly skewed distributions.
- The RSA method is applicable directly to large-scale system analysis for which the system has piecewise smooth response behavior whether or not the explicit response function is available.

The biggest advantage of the RSA method is that the uncertainty of the system output is found in a few numbers of calculations in parallel, while MCS requires extremely large number of sampling simulations. The number of calculation of the RSA is determined by the number of variable which need to find finite differences. In addition, unlike as will be seen with the FPI methods, the RSA does not need any kind of nested optimization in its calculation procedure (see Section 4.3.2), and it is the most practical methodology for large-scale dynamic energy system synthesis/design and operation/control optimization. Therefore, the RSA method has been applied to uncertainty evaluation of the PFEMFC system responses in this doctoral research.

4.3 Fast Probability Integration (FPI) Methods

The other practical uncertainty analysis methodologies for energy system development are fast probability integration methods. For system limitation/critical

factors which cause system failure such as too high a concentration of CO in a PEMFC system, the effect of uncertainty in the input variables must be addressed in system development. Conventionally, safety-factor based designs, which only roughly take into account uncertainties with a certain confidence level or range, have been widely used by engineers to provide a margin of safety necessary for ensuring the quality of a design. However, the safety-factor based design approach usually makes conservative design decisions since safety factors are commonly obtained from limited experimental samples or rules of thumb. Moreover, this method does not account correctly for the possible probabilistic information associated with the input variables. In order to overcome these deficiencies, fast probability integration (FPI) methods which are approximate reliability methods were developed by structural engineers for the risk/reliability analysis. However, applications of these methods have been limited primarily to structural design or small-scale systems.

FPI methods give approximate solutions but are efficient probabilistic analysis tools. The most distinguishable characteristics of these methods are that they do not need the probability density functions of the input variables. Approximate probabilistic information of the system outputs is obtained using only the means and standard deviations of the input variables via numerical analysis. Therefore, it is also practical to couple FPI with multidisciplinary energy system development and optimization. However, FPI methods are more practical for a steady-state, single point optimization of the system because it requires a nested optimization procedure (i.e. a probability optimization nested within an overall system optimization) to find the probabilistic information of the system responses. It is explained in Section 4.3.2.

4.3.1 Fundamental Concept of Reliability Analysis

The basic concept of reliability analysis is illustrated by the following process:

- Choose specific performance criteria and the system input variable set \vec{Z} under uncertainty.
- Define the system performance function M_j and limit state $g_{l_{M_j}}$ such that

$$\vec{M}_j = g_{M_j}(\vec{Z}) \quad (4.20)$$

which is a constraint to be met in the limit to

$$g_{M_j}(\vec{Z}) - g_{l_{M_j}} = h_{M_j} = 0 \quad (4.21)$$

- Determine the overall PDF, $f(\vec{Z})$, of the input variable set \vec{Z}_i for the case when the \vec{Z}_i are statistically independent (uncorrelated)

$$f(\vec{Z}) = f(Z_1)f(Z_2)\dots f(Z_n) \quad (4.22)$$

- Calculate the probability of failure, p_f , directly by integrating the PDF

$$p_f = \int \dots \int_{h_{M_j} < 0} f(Z_1, Z_2, \dots, Z_n) dZ_1 dZ_2 \dots dZ_n \quad (4.23)$$

Note that p_f is what is referred to as the cumulative distribution function (CDF).

If the random variables are statistically dependent, the overall PDF, $f(\vec{Z})$, is practically impossible to obtain. Even if it is possible as in the case when the Z_i are statistically uncorrelated, solving equation (4.23) can be rather difficult. Thus, analytical approximation approaches called fast probability integration (FPI) methods are required to compute the integral. Both first- and second-order FPI methods have been developed (e.g., Haldar and Mahadevan, 2001; Ang and Tang, 1984). The former are described first in the following section.

4.3.2 First-Order FPI Method

The basic first-order FPI method is referred to as first-order, second-moment (FOSM) method in the literature and, as discussed in Section 4.2 on RSA, uses first-order Taylor series expansions (TSEs) linearized about the mean values of the input variables (\vec{Z}) and the first- and second-moment statistics (means and variances). There is another first-order FPI method the so-called advanced first-order, second-moment (AFOSM) method. In the FOSM method, information on the PDFs of the input variables is ignored. However, in the advanced first-order, second-moment (AFOSM) methods, this information is appropriately used.

4.3.2.1. Advanced First-Order Second-Moment (AFOSM) Method

AFOSM methods assume that the input variables are statistically independent (uncorrelated) and normally distributed, and that the outputs \bar{M} are also normally distributed. With the AFOSM method, a reliability index β_{M_j} , is introduced such that

$$\beta_{M_j} = \frac{\mu_{M_j}}{\sigma_{M_j}} \quad (4.24)$$

where μ_{M_j} and σ_{M_j} are the mean and the standard deviation of output M_j which is given by the performance function $g_{M_j}(\bar{Z})$, i.e.

$$M_j = g_{M_j}(\bar{Z}) \quad (4.25)$$

The probability of failure in terms of the reliability index can be obtained by

$$p_f = \Phi(-\beta_{M_j}) = 1 - \Phi(\beta_{M_j}) \quad (4.26)$$

$$\beta_{M_j} = \Phi^{-1}(1 - p_f) \quad (4.27)$$

where Φ is the CDF of the standard normal random input variables.

- For normal random variables

Hasofer and Lind (1974) developed a type of AFOSM method for normal random input variables. The standard or reduced random input variables Z'_i with zero means and unit standard deviations are determined BY

$$Z'_i = \frac{Z_i - \mu_{Z_i}}{\sigma_{Z_i}} \quad \text{for } i = 1, 2, \dots, n \quad (4.28)$$

Using this equation, the “limit state” constraint limit is transformed such that

$$h_{M_j}(\bar{Z}') = 0 \quad (4.29)$$

The reliability index β_{M_j} is then calculated as

$$\beta_{M_g} = \sqrt{(\bar{Z}'^*)^T (\bar{Z}'^*)} \quad (4.30)$$

where the superscript T refers to the transpose and the superscript $*$ to the design or optimal point. Physically, the reliability index is the minimum distance from the origin of the axis in the reduced coordinate system to the limit state surface (e.g., see Figure 4.2 in

Section 4.2), and the point, \vec{Z}'^* , represents the worst combination of the stochastic input variables and is appropriately named the design point (see Figure 4.3).

The reliability index in the AFOSM method is obtained based on geometry, and Figure 4.3 depicts the basic idea of the AFOSM method for a linear and nonlinear system. It is obvious that the nearer \vec{Z}'^* is to the origin, the larger is the failure probability. Thus, the minimum distance point on the limit state surface, $h_{M_j}(\vec{Z}')$, is also the most probable point (MPP) of failure in the system. An optimization is required to find this point. This is explained in detail next.

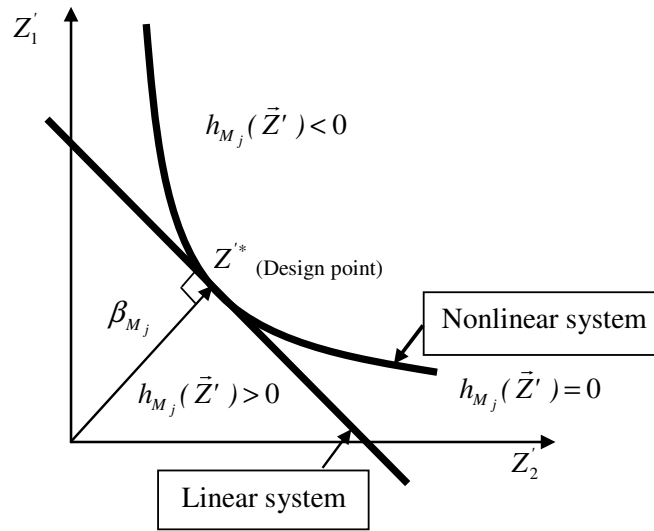


Figure 4.3 AFOSM for a linear/nonlinear system depicted in the reduced coordinate frame.

- Optimization to find the MPP

Two optimization algorithms are commonly used to obtain the MPP and the corresponding reliability. The first method by Rackwitz and Fiessler (1976) is used when the performance function (g_{M_j}) is known. In this method, the limit state equation (equation (4.29)) is used in a constrained optimization of the reliability index (equation (4.30)) for finding the minimum design point using Lagrange's method of undetermined multipliers. However, in many practical problems, this performance function may not be explicitly available. Therefore, alternative methods such as a Newton-Raphson type recursive algorithm have been widely used for the reliability analysis of implicit

performance function problem. However, in the gPROMS™ dynamic development environment used for the modeling and simulation in this doctoral work, a recursive or iterative type of approach is not supported. Thus, the first method is more appropriate here provided an explicit performance functions, g_{M_j} , can be found. To this end a response surface methodology (RSM) is adopted for the moment to determine the practicality of finding such explicit performance functions for a system. This is discussed in the next section.

For a linear system, the reliability index can be calculated directly using equations (4.21) and (4.24). However, for the nonlinear case, the computation of the minimum distance β_{M_j} becomes an optimization problem as follows:

$$\text{Minimize } \beta_{M_j} = \sqrt{(\bar{Z}')^T (\bar{Z}')} \quad (4.31)$$

$$\text{subject to } h_{M_j}(\bar{Z}') = 0 \quad (4.32)$$

This constrained optimization is transformed into an unconstrained one using Lagrange's method of undetermined multipliers. This is done by defining the Lagrangian L using the Lagrange multiplier λ such that

$$\begin{aligned} L &= \sqrt{(\bar{Z}')^T (\bar{Z}')} + \lambda h_{M_j}(\bar{Z}') \\ &= \sqrt{Z_1'^2 + Z_2'^2 + \dots + Z_n'^2} + \lambda h_{M_j}(Z_1' + Z_2' + \dots + Z_n') \end{aligned} \quad (4.33)$$

Minimization of L with respect to the Z_i' results in the optimal set of values for the Z_i' which lead to the minimum distance β_{M_j} , i.e. a system of $n+1$ equations in $n+1$ unknowns Z_i' given by

$$\frac{\partial L}{\partial Z_i'} = \frac{Z_i'}{\sqrt{Z_1'^2 + Z_2'^2 + \dots + Z_n'^2}} + \lambda \frac{\partial h_{M_j}}{\partial Z_i'} \quad (4.34)$$

$$\text{And } \frac{\partial L}{\partial \lambda} = g(\bar{Z}') = 0 \quad (4.35)$$

is solved for the optimal $Z_i'^*$, yielding the most probable failure point \bar{Z}^* . The reliability index can, thus, be expressed as

$$\beta_{M_j} = -\frac{\bar{H}_{M_j}^{*T} \bar{Z}^*}{\sqrt{\bar{H}_{M_j}^{*T} \bar{H}_{M_j}^*}} = -\frac{\sum_{i=1}^n Z_i^* \left(\frac{\partial h_{M_j}^{*T}}{\partial Z_i} \right)^*}{\sqrt{\sum_{i=1}^n \left(\frac{\partial h_{M_j}^{*T}}{\partial Z_i} \right)^{2*}}} = -\sum_{i=1}^n \alpha_i^* Z_i^* \quad (4.36)$$

where $\bar{H}_{M_j} = \left(\frac{\partial h_{M_j}}{\partial Z_1}, \frac{\partial h_{M_j}}{\partial Z_2}, \dots, \frac{\partial h_{M_j}}{\partial Z_n} \right)$ (4.37)

where the α_i^* are the direction cosines along the axes Z_i^* . Figure 4.4 depicts the proposed optimization procedure for the AFOSM method to find the most probable point and the reliability index.

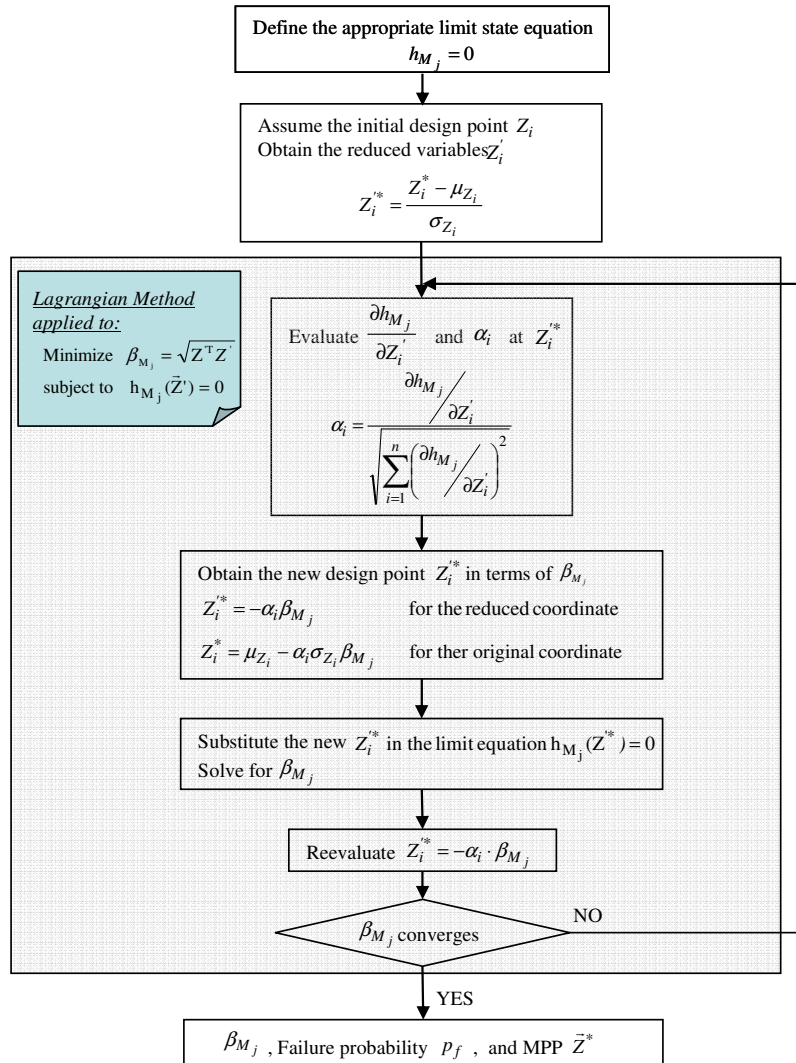


Figure 4.4 Optimization procedure for the AFOSM method.

4.3.2.2 Response Surface Methodology (RSM)

As mentioned earlier, in order to be able to use the AFOSM method as described above, an explicit performance function must be found for the nonlinear system. However, for complex systems, these performance functions $g_{\vec{M}}(\vec{Z})$ are not typically available in closed form. An approximate explicit closed form performance function can, nonetheless, be generated using a response surface methodology (RSM) which is often times used as a surrogate for computationally intensive, high-fidelity mathematical models or simulations. RSM provides a correlation function through regression analysis which relates a set of system input variables to a set of system outputs. The polynomials used here to approximate the $h_{M_j}(\vec{Z})$ via sample simulations are up to third order. For better fits in certain cases, the response variables, \vec{M} , can be fitted using fractions, powers, logarithm, exponentials, etc.

4.4 Validation of Uncertainty Analysis Methodologies

MCS, the FPI method (i.e. AFOSM), and the RSA method are compared using the approximate SMR model obtained by RSM. In this comparison, single point operation (not dynamic operation) is assumed and direct uncertainty sources (i.e. the steam-to-carbon ratio, pressure, and temperature) are assumed as uncertainty factors. Note that these assumptions are just for facilitating the simulation and comparison. In the actual synthesis/design and operation/control optimization in this doctoral research, the system is in a dynamic operating regime and indirect uncertainty sources (i.e. uncertainties in the cost functions and load profiles) are considered.

4.4.1 Determining the System Performance Function

As explained in Section 4.3.2, an explicit form of the system performance function can be used for determining the most probable point and its uncertainty using the AFOSM method. The response surface methodology (RSM) is first used to determine the system performance function of the SMR as a polynomial function of input variables.

However, in the gPROMS™ dynamic development environment used here, RSM is not supported. Thus, for this procedure, the SMR model in gPROMS™ is integrated with ModelCenter™ which supports integration and analysis tools for individual models programmed in different software languages (e.g., C++, Matlab™, FORTRAN, etc).

Table 4.1 presents the set of input variables (steam-to-methane ratio, inlet pressure and temperature) and the results for the performance function predicting the response of the mole fraction of CO, y_{CO} . This function is a fully quadratic polynomial equation obtained by using 27 sets of these input variables over given an operating range. Prediction with this function corresponds closely to the real modeling results, and Figure 4.5 shows a comparison between the results for the actual model (y_{CO}) and the approximate model (y'_{CO}).

Table 4.1 Set of random variables and the results of the response surface analysis.

Random variables		Predictor	Coefficient
S/C	3.0 ~ 3.5	Constant	0.5199035E-01
P	1.5 ~ 2.0 bar	S/C	-0.3743978E-01
T	873 ~ 973 K	Temperature	0.1504400E-03
y_{CO}	Response variable	Pressure	-0.6181595E-02
		S/C*S/C	0.4443208E-02
Data for response variable		Temperature*Temperature	-0.5635753E-08
SD	= 0.4134E-00005	Pressure*Pressure	0.2903988E-03
$y_{CO_{avg}}$	= 0.6348E-00001	S/C*Temperature	-0.1411380E-04
COV	= 0.01%	S/C*Pressure	0.1295245E-02
R-Sq	= 100.00%	Temperature*Pressure	-0.1819265E-05

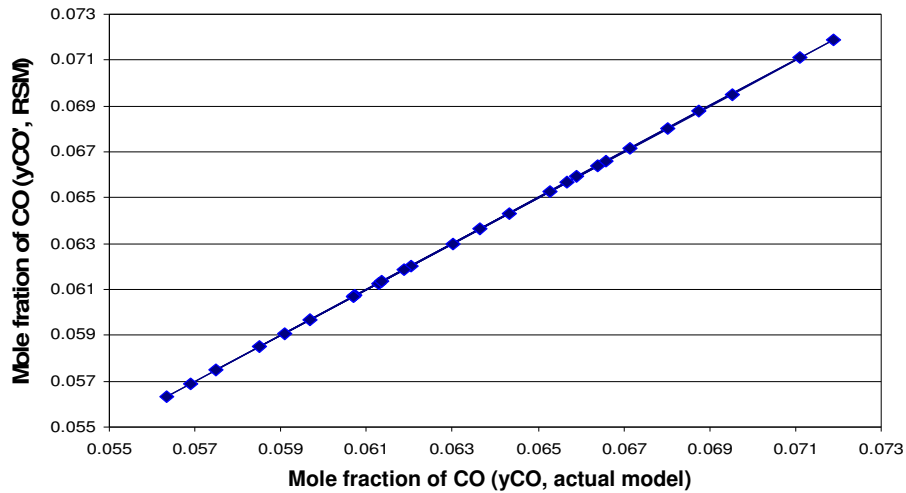


Figure 4.5 Comparison of the output response from the actual model and the approximate model.

4.4.2 Comparing the MCS, FPI, and RSA Methods

The uncertainty analysis methodologies (i.e. MCS, FPI, and RSA) are compared using the approximate SMR model obtained by RSM. This approximate model is in effect the performance function $g_{M_j}(\vec{Z})$ for output M_j which in the example given in the previous section is $y_{CO} = y'_{CO}$. To illustrate this here, the CO concentration of the SMR is investigated in this comparison of stochastic methods, and Table 4.2 shows the probabilistic information for the input variables: the steam-to-carbon ratio (S/C), temperature, and pressure. For the purpose of this comparison, all input and output values are assumed as normal distributions.

The limit state equation $h_{y_{CO}}(\vec{Z})$ of the system performance function y'_{CO} and limit y_{CO_l} is given by equation (4.38). Output values which lie outside of the limit indicate a system failure to operate properly, i.e. $h_{y_{CO}} > 0$, while $h_{y_{CO}} < 0$ indicates a system operating as desired where

$$h_{y_{CO}} = h_{y_{CO}}(\vec{Z}) = y'_{CO} - y_{CO_l} \quad (4.38)$$

and $y'_{CO} = y'_{CO}(S/C, T, P)$ (4.39)

Tables 4.2 and 4.3 show the simulation results applying the MCS, AFOSM, and RSA methods. A CO concentration of 0.0615 is assumed as the limit state value. The MCS predicts 97.6 percent reliability at $y_{CO_l} = 0.0615$ with a sampling of 100,000. As seen in Table 4.2, the output converges to a specific number as the sampling number increases. For the case at hand, the MCS result for a sampling size of 100,000 and 97.6 percent reliability is assumed to be the true value for purposes of comparison with the other stochastic methods (see equation (4.2)).

The simulation error in MCS with a 95 % confidence level³ is expressed as

$$\varepsilon \% = \sqrt{\frac{1 - P_f}{N P_f}} 200 \% \quad (4.40)$$

³ A 95% confidence level indicates the range determined by the mean $\pm 2\sigma$ of a normal distribution over one can have confidence that the value of the variable involved will be, for example, less than or equal to some limit value. The mean $\pm 1\sigma$ results in a confidence level of about 68.3% while $\pm 3\sigma$ results in 99.7%. Either of these latter two confidence levels result in a modified expression for ε %, i.e. the square root term multiplied by 100% and 300% respectively.

where p_f is the objective probability of simulation failure and N is the number of simulations. As can be seen in Table 4.3, with MCS (p_f) of 1%, and a sampling size of 10, the simulation error is 629% compared to 6.3% with 100, a probability of failure 100,000 samples.

Table 4.2 Uncertainty analysis of the CO concentration in the SMR using the MCS.

Input variables		Mean				Standard deviation				
S/C ratio		3.5				0.05				
Temperature		923 K				5 K				
Pressure		1.5 bar				0.05 bar				
# of sampling	S/C		Po		To		yCO		Reliability (0.0615)	Simulation error (%)
	Mean	SD	Mean	SD	Mean	SD	Mean	SD		
10	3.505	0.047	1.483	0.0726	925.85	4.379	0.05971	0.00097	1	629
100	3.502	0.050	1.496	0.0574	922.92	5.027	0.05949	0.0009	1	199
500	3.502	0.047	1.499	0.0511	922.84	4.798	0.05947	0.0009	0.992	89
1000	3.499	0.052	1.501	0.0506	923.08	4.494	0.05952	1.01E-3	0.977	63
10000	3.501	0.050	1.499	0.0499	922.96	5.001	0.0595	9.9E-4	0.979	19.9
100000	3.5	0.005	1.499	0.0501	922.99	5.006	0.05951	0.00099	0.976	6.3

Table 4.3 Uncertainty analysis of the CO concentration in the SMR using the AFOSM and RSA methods.

Analysis method	yCO		Reliability (0.0615)
	Mean	SD	
AFOSM	0.05951461 (2 nd)	0.0009983	0.9767523
RSA	0.05950401	0.0009835	0.978871

The AFOSM method and RSA method are also evaluated using the same conditions as used for the MCS. Table 4.3 presents the results which show that each method predicts values close to the true value, i.e. within 0.3%. Since the approximate SMR performance function has good agreement with the actual performance function, both the RSA and AFOSM methods predict results close to those founding using the MCS.

Finally, Figure 4.6 compares the results of the MCS, AFOSM, and RSA methods using the cumulative probability across the entire possible output range. This probability shows great correspondence between the MCS result and those from the AFOSM/RSA methods. Furthermore, it took around 57 minutes using a dual-core, 3.2 GHz PC with 2G RAM to complete the 100,000 MCS samples even though it a simplified and approximate performance function was used. If MCS method had been applied directly to the actual

model, the computational time would have been significantly greater i.e. on the order of 8+ days. In contrast, the RSA and FPI methods are much more efficient. For example, to get the probability information for a single point on Figure 4.6, the AFOSM method converges in less than 12 iterations (4 for convergence and 3 for finding roots in the subroutine) for the given limit state equation. However, the AFOSM method requires a number of independent calculations for different limit states to get the PDF of the system output because the FPI methods are only applicable for finding the probabilistic information of a single point (i.e. a single limit state). Moreover, if the approximate system performance function is not available, a relatively large computational time for the optimization to find the probabilistic information is required. When nested within the system level synthesis/design and operation/control optimization for the computational time increases significantly so that the FPI method is still too computationally expensive (even though much less so than the MCS).

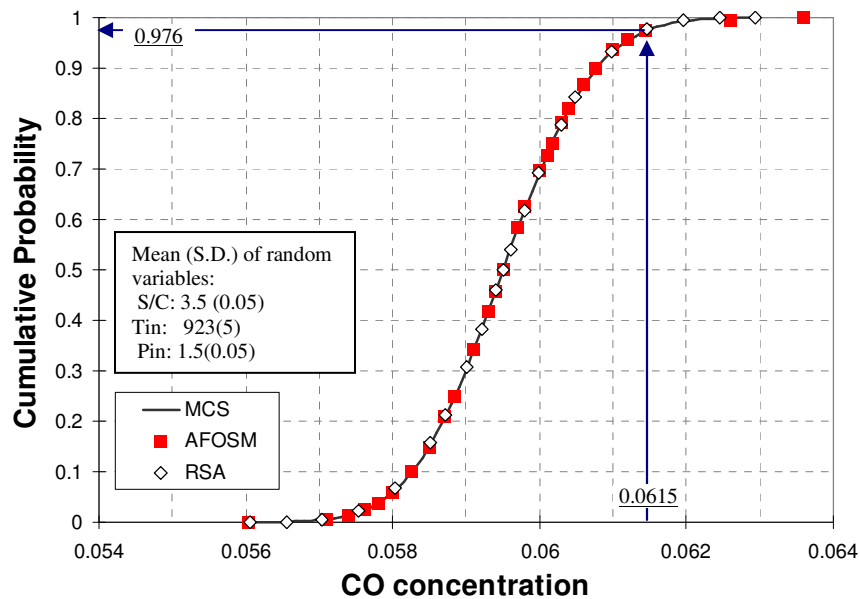


Figure 4.6 Comparison of the uncertainty analysis results for the MCS, AFOSM, and RSA methods.

In case of the RSA method, as few as two simulations are required, each of which includes $2n + 1n$ simultaneous calculations to find the mean and variance of the system outputs (equations (4.6) and (4.8)) where n is the number of input variables which have

uncertainties. From the mean and variance of a single system output, each point in Figure 4.7 is calculated assuming a normal distribution.

As shown in Table 4.2 and 4.3 and Figure 4.7, the AFOSM and RSA are efficient and accurate stochastic analysis methods for the SMR. In particular, the RSA method is the more practical for dynamic system optimization because it can find the probabilistic information of the outputs in as few as two simulations. Therefore, the RSA method is employed here as the uncertainty analysis method to calculating uncertainties and to determine their effects on the PEMFC system synthesis/design and operation/control optimization problem.

CHAPTER 5

OPTIMIZATION STRATEGY FOR DYNAMIC PEMFC SYSTEM SYNTHESIS/DESIGN AND OPERATION/CONTROL OPTIMIZATION UNDER UNCERTAINTY

At the beginning stage of a system synthesis/design and operation/control optimization process, three things must be decided relative to the optimization. The first one is to determine what kind of optimization algorithm (e.g., gradient-based, non-gradient-based, or hybrid) is to be employed for the optimization. The second is to choose either a single or multi-objective approach, while the third is to choose between a single-level or a multi-level optimization strategy. Each of these is discussed in turn in the following sections.

5.1 Optimization Algorithms

Synthesis/design and operation/control optimization problems of complex energy systems are, in general, dynamic mixed integer non-linear programming (DMINLP) problems. Although no general solution algorithm for such problems exists, a number of optimization algorithms have been developed which can be used to aid in finding a solution. These can be classified into gradient-based, non-gradient-based, and hybrid heuristic/gradient based optimization algorithms.

The gradient-based optimization algorithms (gradient descent or ascent) refer to search methods for real-value functions. These methods use the gradient of a given function as well as function values to find the direction of descent or ascent of the given

function. Several gradient-based optimization algorithms have been introduced for solving non-linear programming problems. If a gradient-based optimization method handles constraints implicitly (i.e. as an unconstrained problem), it is classified as an indirect method. Otherwise, the methods are known as direct methods. The Lagrange Multiplier method is the typical indirect method, while the Sequential Quadratic programming (SQP) method and the Method of Feasible Directions (MFD) are typical direct methods.

The biggest advantages of the gradient-based optimization algorithms are that they are straightforward in their application and are relatively fast. Gradient-based optimization is effective for relatively small solution spaces defined by a small number of degrees of freedom which are characterized by a set of continuous variables. However, most large-scale energy system optimization problems consist of a mix of continuous and discrete variables and non-convex synthesis/design and operation/control surfaces with discontinuous points and a great number of local minima. Thus, the optimization procedure based on gradient methods easily gets stuck at these local minima points. Multi-starting the optimizer from different regions of the solution space which is very problematic when a large number of degrees of freedom are involved can help to improve the quality of the solution and minimize the weaknesses of the gradient-based optimization methods. Nonetheless, gradient-based optimization algorithms show poor characteristics for finding solutions for a noisy solution space (i.e. for a highly non-linear system) and cannot be applied for discrete directly variables because the gradients with respect to integer numbers are not defined.

In order to overcome the weaknesses of the gradient-based optimization methods listed above, a number of non-gradient-based and optimization methods with specialized search schemes have been developed. These kinds of optimization algorithms specialize in performing global as apposed to local searches. Among them, the most developed and well-known methods for global search are Simulated Annealing (SA), Neural Network (NN), Connectivity Matrix method, Genetic Algorithm (GA), Artificial Intelligence (AI), etc. (Rancruel, 2005).

The GA, in particular, has been one of the most widely applied to complex system optimization problems because when properly developed and conditioned, it has strong

characteristics for finding local-global optimum points. Moreover, the GA is ideal for problems with discrete decision variables, since it does not require gradients (i.e. it is not affected by noisy search spaces). Also, the GA is less prone to get stuck at local optima. Thus, it can be one of the best options for large-scale, non-linear energy system synthesis/design and operation/control optimization. However, it requires a very large number of expensive function evaluations. If it is applied to a large-scale system optimization under uncertainty, it requires extremely powerful computational tools and resources (Jansson et al., 2007). For example, it takes around 7 ~ 15 minutes for a single simulation of the FPS developed in this work using a dual-core 3.2 GHz based PC environment. If a GA is applied to the optimization of this problem with 34 degrees of freedom and a mix of continuous and discrete decision variables, it takes more than one week to find an optimum. Therefore, the GA may not be the practical method for solving such problems. Nonetheless, a SQP method and a GA were applied to solve the dynamic PEMFC system synthesis/design and operation/control optimization problem under uncertainty posed here, before it was concluded that this kind of complex and computationally burdened problem needs a more efficient optimization method which is less computationally expensive yet has good global search characteristics. For this purpose, a surrogate-model-based optimization (SMBO) method which is kind of hybrid heuristic/gradient-based optimization methods is introduced in this doctoral research.

Recently, SMBO methods have received increased attention for the design of computationally burdened problems such as the design and analysis of aerospace systems, structures, propulsion systems, etc., because SMBO methods are inexpensive (i.e. much less computationally burdened compared to the gradient/non-gradient-based optimization methods) and effective for solving complex problems (Jansson, Wakeman, and Manson, 2007; Rikards et al., 2006; Papalambros, 2002; Audet et al., 2000). They are composed of four essential stages (Queipo et al. 2005):

1. Design of Experiments (DOE): set up sampling plan for a given design space;
2. Numerical simulation at selected locations: sample data from selected points;
3. Construction of surrogate model by using the sample set;

4. Model validation: check the quality of the surrogate model developed.

In particular, selecting one methodology for building surrogate models using the sample set determines the main characteristics of the SMBO approaches. There are many surrogate model constructors such as the polynomial regression method, neural networks, radial basis functions, the Kriging method, etc. Among these, the most widely used methodologies are the polynomial regression method (Rikards et al., 2006 and Jansson, Wakeman, and Manson, 2007) and the Kriging method (Audet et al., 2000 and Sacks et al., 1989a,b), and their fundamental mathematical backgrounds are well explained by Queipo et al. (2005).

One of the biggest weaknesses of SMBO methods is inaccuracies in their surrogate models. To improve the accuracy of the models requires continuous updating of the surrogated model generated. Audet et al. (2000) at Boeing has developed a SMBO algorithm named Sequential Approximate Optimization (SEQOPT) which is provided by a commercial system analysis tool called ModelCenter™ from Phoenix Integration, Inc. The SEQOPT uses orthogonal arrays for determining the sampling plan in the DOE stage and the Kriging method for generating the surrogate model. In order to improve the accuracy of the model, an updating algorithm for the surrogate model is developed using a pattern search procedure in which possible local-global optimum points are evaluated finely over the local and then updated continuously. For nonlinear constrained optimization of the surrogate model approach, multi-start SQP processes are combined with the DOE, surrogate model building, and model updating processes into a single optimization algorithm. Figure 5.1 depicts the optimization algorithm of the SEQOPT algorithm. Once DOE determines a sampling set for the given design space, SEQOPT simulates for the sampling set and builds a surrogate model based on the sampled data. The surrogate model generated is optimized using the SQP method, and the solutions from the optimization are validated using the actual computational model. The system response data from the previous validation process and from the local pattern search process are updated to improve the surrogate model. This procedure is iterated until there is no improvement. Audet et al. (2000) evaluated the SEQOPT algorithm using an airplane wing platform design problem which has 15 degrees of freedom with 11 constraints and found solution after 304 simulations of the design model. In the present

research, the SEQOPT algorithm has been primarily used as an optimization tool with a gradient-based optimization method (i.e. SQP).

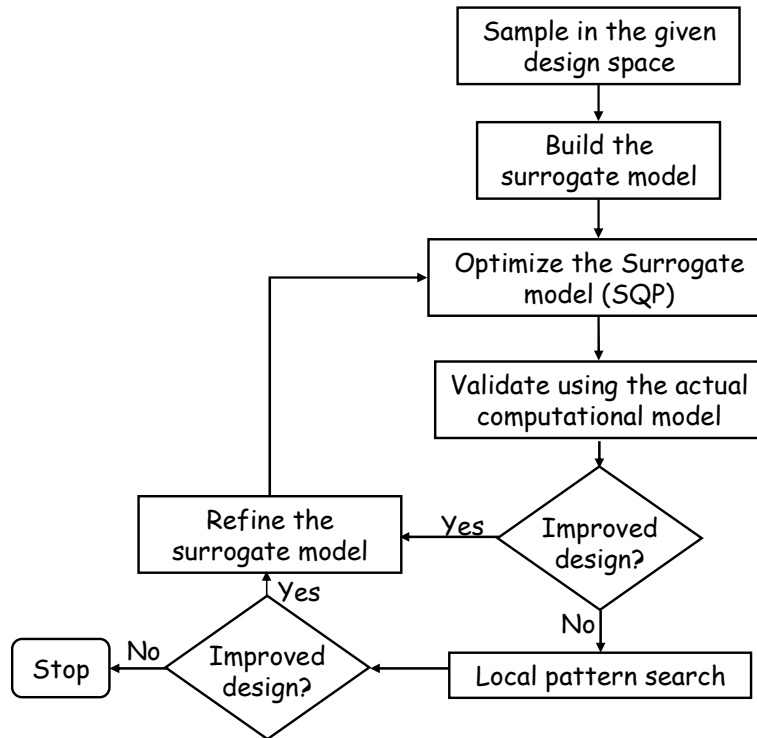


Figure 5.1 Optimization algorithm of the SEQOPT algorithm.

5.2 Single/Multi-Objective Optimization

Energy system synthesis/design and operation/control optimization problems consist of modifying the system configuration and component design, operation, and control parameters according to a single or to multiple objective(s). These objectives, in general, can be classified into three categories: thermodynamic ones such as maximizing system efficiency and minimizing exergy destruction, economic ones like minimizing life cycle cost, and environmental ones such as minimizing pollutant emissions (Toffolo and Lazzaretto, 2002). A general statement of the deterministic, constrained, multi-objective optimization problem having n objectives for energy system synthesis/design and operation/control is as follows:

$$\text{Mim/Max } f = f(f_1(\bar{X}, \bar{Y}), \dots, f_n(\bar{X}, \bar{Y})) \quad (5.1)$$

w.r.t. \vec{X}, \vec{Y}

$$\text{subject to } \vec{H}(\vec{X}, \vec{Y}) = 0 \quad (5.1a)$$

$$\vec{G}(\vec{X}, \vec{Y}) \leq 0 \quad (5.1b)$$

where f_i is a n independent objective of the optimization with respect with a set of synthesis/design decision variables \vec{X} and a set of operation/control decision variables \vec{Y} , the vector \vec{H} is the equality constraints characterizing the behavior of the system (i.e. the mass and energy balances of the system as well as the performance constraints that the system must follow), and \vec{G} the inequality constraints describing physical limits on system behavior.

Conventionally, energy system syntheses/designs, in general, are focused on the economic objective of the system. However, the optimal synthesis/design and operation/control with respect to the cost of the system may not be sufficient because solutions with a higher system efficiency (and/or lower environmental effect) may, in spite of small increases in total cost, result in much more interesting syntheses/designs due to these other considerations (e.g., energy and environmental policies or regulations which must be met).

These objectives usually conflict with each other (i.e. increasing system efficiency causes an increase in investment costs) so that it is impossible to find optimal solutions which can satisfy the multiple objectives simultaneously. To deal with this, multi-objective optimizations provide a space called the Pareto domain of possible synthesis/design and operation/control solutions which can be traded off against one another using information essential for doing this effectively.

The Pareto approach to multi-objective optimization is used to find the optimal set of decision variable values, since the concepts of Pareto dominance and optimality are straightforward tools for determining the best trade-off solutions among conflicting objectives. Figure 5.2 depicts the Pareto set and domain in a two-objective function space. The Pareto domain contains all possible outcomes which satisfy all the constraints of the system, and the Pareto set represents the trade-offs between competing objectives through the entire objective functions space.

Typical optimization methods like gradient-based optimization methods are not effective algorithms for the Pareto approach of multi-objective optimization problems because most are unable to find multiple solutions in a single optimization procedure. If they are applied to multi-objective optimization problems, multi-implementation of the optimization is required to generate the Pareto set. To overcome their insufficiency, GAs have been used widely for searching the Pareto optimal solutions of multi-objective optimization problems because these optimization techniques by their very nature generate a set of solutions (i.e. called a population) to carry out their tasks. Thus, the use of GAs for a multi-objective optimization problem can make the population converge to the overall set of optimal solutions in a single run of the optimization. However, even though multi-objective optimization is quite useful to decision makers, it has not been applied widely to energy system synthesis/design and operation/control because GAs are computationally expensive as has already been discussed in Section 5.1.

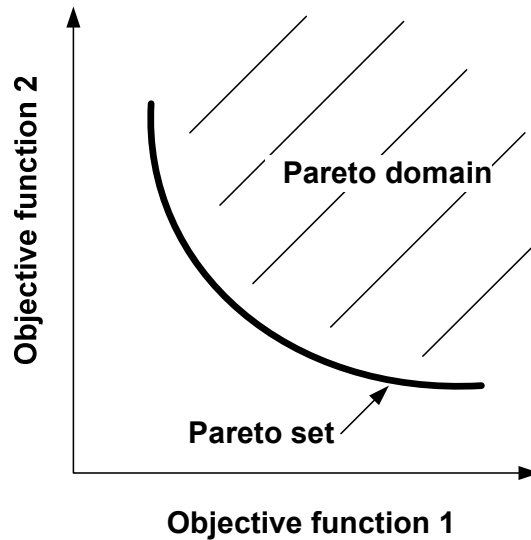


Figure 5.2 Pareto set and domain in a multi-objective function space.

Although the SEQOPT method used for the present research is not specialized in solving multi-objective problems, it is similar to GAs in that it generates a set of solutions in a single run. Nonetheless, the SEQOPT method does not provide the Pareto set in a single run but instead requires multiple runs to generate the Pareto set for a given set of

multi-objectives. However, since the SEQOPT method is a less expensive method than the GAs, it can be an efficient alternative to GAs.

In a multi-objective optimization using the SEQOPT method, the optimizer searches the solution space based on a single objective by treating the other objective function as a constraint, followed by the optimization of the objective function treated as a constraint in the previous step and the previous objective function now treated as a new constraint. This process of optimization is continued back-and-forth until there is no improvement. During the iterative optimization procedure, each single optimization run gives one optimum solution with a set of feasible solutions, and the sum of the set of feasible solutions of each run provides the Pareto set and domain as seen in Figure 5.2. This idea has been applied to the FPS synthesis/design and operation/control optimization, and the results are presented and discussed in Chapter 6.

Finally, even though multi-objective optimization offers design engineers more information with respect to all possible design objectives, it requires lots of computational time. Thus, a single economic objective function (i.e. total life cycle cost of the system) has been used for the overall PEMFC system synthesis/design and operation/control optimization. The total life cycle cost contains capital investment cost and life cycle operating cost which can be considered as an equivalent quantity of the system efficiency in terms of cost. Therefore, the total life cycle cost of the system effectively describes both objectives by a single objective function. A total life cycle cost optimization of the FPS is also compared to the results by the multi-objective optimization approach in Chapter 6.

5.3 Single/Multi-Level Optimization Approach for Energy System Synthesis/Design and Operation/Control

5.3.1 General Concepts of Decomposition Techniques

If a system synthesis/design and operation/control optimization problem is uncomplicated enough to be solved by using any of the typical optimization algorithms

addressed in the previous sections, a single-level optimization approach is directly applicable. However, many energy system synthesis/design operating/control problems are not that simple but can, nonetheless, be handled by sophisticated multi-level optimization strategies (i.e. decomposition strategies) which facilitate the optimization process. Example of such decomposition strategies applied to the large-scale optimization of energy system synthesis/design and operation/control can be found in Munoz (2000), Oyarzabal (2001), Georgopoulos (2002), and Rancruel (2005).

Decomposition breaks the large-scale optimization problem down into a set of approximately equivalent smaller optimization problems in order to facilitate the optimization procedure. Decomposition approaches are very effective for facilitating the optimization of dynamic systems which have highly nonlinear characteristics with a large number of degrees of freedom. Figure 5.3 shows a schematic of the general single- and multi-level optimization process. Conceptually, the decomposition process is placed in between the deterministic model and the optimizer as shown Figure 5.3.

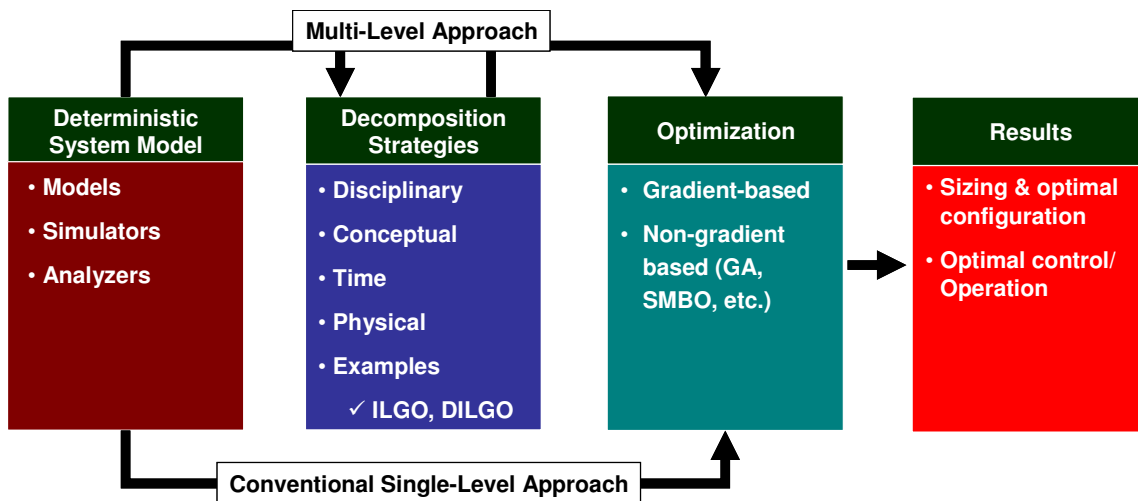


Figure 5.3 Schematic of the general deterministic single- and multi-level optimization process.

Decompositions in the multi-level approach can be achieved in four ways (Rancruel, 2005):

1. *Disciplinary decomposition* divides an optimization problem based on its different disciplines (e.g., a problem's thermodynamics and economics). Decision variables in a thermal system can be divided into purely thermo-

physical and transport variables which are related to the discipline of thermodynamics and other discipline variables like geometry which address the economics of the problem.

2. *Conceptual decomposition* divides a synthesis/design and operation/control problem into two separate problems: one of synthesis/design followed by one of operation/control. Each has its own subset of decision variables, i.e. a sub-set of synthesis variables affecting system configuration via the existence/non-existence of components and streams and of design affecting component geometries and ii) a sub-set of operation/control variables affecting system/subsystem/component operation and controller function and stability.
3. *Physical decomposition* breaks a system-level optimization problem down into a set of unit-level (i.e. component- or subsystem-level) problems.
4. *Time decomposition* transforms a dynamic optimization problem into a quasi-stationary one consisting of a series of stationary time segments.

In this doctoral research, only physical decomposition has been applied to the dynamic PEMFC system synthesis/design and operation optimization problem which is decomposed into three separate subsystem-level optimization problems.

5.3.2 Physical Decomposition Techniques for Large-Scale Energy System Optimization Problems

Various physical decomposition techniques have been introduced in the literature and, in general, can be classified as methods of either local-global optimization (LGO) or iterative local-global optimization (ILGO). A dynamic version of the latter also exists designated as DILGO. Both ILGO and DIGO have been developed and their efficiencies validated in energy system synthesis/design operation/control optimization applied to high performance problems aircrafts and SOFC/PEMFC system by Munoz and von Spakovsky (2000a,b,c), Oyarzabal (2001), Georgopoulos (2002), Oyarzabal, von Spakovsky, and Ellis (2004), Rancruel and von Spakovsky (2003), and Rancruel (2003,

2005). Readers are referred to these references for a deeper understanding of the concepts of these physical decomposition techniques (i.e. LGO, ILGO, and DILGO). However, a brief discussion of each is presented in the following sections.

5.3.2.1 Local-Global Optimization (LGO) Approach

In the LGO method, two levels (i.e. the subsystem- or unit-level and the system-level) of optimization are implemented instead of a single-level. At the local or unit level, an optimization for an each unit (subsystem) and each set of values of coupling functions between units (subsystems) is carried out. These optimization results are, then, used in a system-level (or global) optimization using the coupling functions as decision variables.

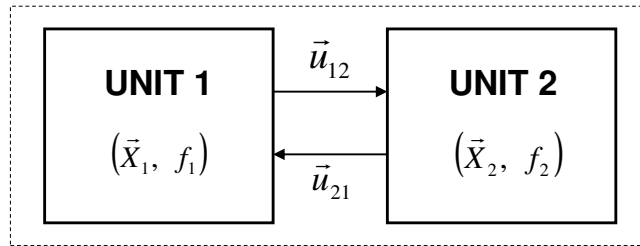


Figure 5.4 Physical decomposition of a two-subsystem or two-unit energy system.

As an illustrations, consider the optimization problem for the system depicted in Figure 5.4 decomposed into two subsystems or unit with local unit (subsystem) variable sets \bar{X}_1 and \bar{X}_2 . The system-level optimization problem is given by

$$\text{Minimize } f = f(\bar{z}, \bar{u}_{12}, \bar{u}_{21}) = f_1(\bar{z}_1, \bar{u}_{12}, \bar{u}_{21}) + f_2(\bar{z}_2, \bar{u}_{12}, \bar{u}_{21}) \quad (5.2)$$

$$\text{w.r.t } \bar{z}_1, \bar{z}_2, \bar{u}_1, \bar{u}_2$$

$$\text{subject to } \bar{H}_1(\bar{X}_1, \bar{u}_1) = 0, \bar{H}_2(\bar{X}_2, \bar{u}_2) = 0 \quad (5.2a)$$

$$\bar{G}_1(\bar{X}_1, \bar{u}_1) \leq 0, \bar{G}_2(\bar{X}_2, \bar{u}_2) \leq 0 \quad (5.2b)$$

$$\text{where } \bar{z} = \bar{z}_1 \cup \bar{z}_2, \bar{z}_1 = [\bar{X}_a \in \bar{X}_1], \bar{z}_2 = [\bar{X}_b \in \bar{X}_2] \quad (5.3)$$

and \bar{u}_{12} and \bar{u}_{21} are the coupling functions between subsystems while \bar{z}_1 and \bar{z}_2 are the local subsystem (unit) decision variable sets. With these definitions, the conventional LGO problem is defined as

System-level (or global) Problem

$$\text{Minimize } f = f_1^*(\bar{z}_1, \bar{u}_{12}, \bar{u}_{21}) + f_2^*(\bar{z}_2, \bar{u}_{12}, \bar{u}_{21}) \quad (5.4)$$

$$\text{w.r.t } \bar{u}_{12}, \bar{u}_{21}$$

$$\text{subject to } \bar{H}_1(\bar{X}_1) = 0, \bar{H}_2(\bar{X}_2) = 0 \quad (5.4a)$$

$$\bar{G}_1(\bar{X}_1) \leq 0, \bar{G}_2(\bar{X}_2) \leq 0 \quad (5.4b)$$

Unit-level (or local) Problem

i) Sub-problem 1

$$\text{Minimize } f_1 = f_1(\bar{z}_1, \bar{u}_{12}, \bar{u}_{21}) \quad (5.5)$$

$$\text{w.r.t } \bar{z}_1$$

$$\text{subject to } \bar{H}_1(\bar{X}_1) = 0 \quad (5.5a)$$

$$\bar{G}_1(\bar{X}_1) \leq 0 \quad (5.5b)$$

ii) Sub-problem 2

$$\text{Minimize } f_2 = f_2(\bar{z}_2, \bar{u}_{12}, \bar{u}_{21}) \quad (5.6)$$

$$\text{w.r.t } \bar{z}_2$$

$$\text{subject to } \bar{H}_2(\bar{X}_2) = 0 \quad (5.6a)$$

$$\bar{G}_2(\bar{X}_2) \leq 0 \quad (5.6b)$$

where the superscript * in the system-level objective function represents the fact that f_1 and f_2 are optimized with respect to their local subsystem optimizations.

As described above, the LGO technique has the advantage of breaking a large-scale optimization problem down into smaller unit-level problems. However, it is computationally expensive because each unit-level optimization must be carried out independently many times within the system-level (or global) optimization problem resulting in a set of nested optimizations.

5.3.2.2 Iterative Local-Global Optimization (ILGO) Approach

The nesting of optimizations in the LGO approach can be eliminated by recognizing that the system-level information of optimizing the system-level objective

with respect to the coupling functions can be embedded directly into the unit-level objectives. Munoz and von Spakovsky (2000a,b,c) recognized this in developing their iterative local-global optimization (ILGO) approach which embeds this information at the local level in the form of gradient (i.e. shadow price) information of subsystem responses to variations in the coupling functions, which represent subsystem-to-subsystem interactions associated with strictly system-level optimization degrees of freedom. The ILGO is defined as

System-level, Unit-based Optimization Problem

i) Sub-problem 1

$$f_1' = f_1(\bar{z}_1, \bar{u}_{12}, \bar{u}_{21}) + f_{2o}^*(\bar{z}_2, \bar{u}_{12}, \bar{u}_{21}) + \sum_k (\lambda_{12}^2 \Delta u_{12}^{(1)})_k + \sum_l (\lambda_{21}^2 \Delta u_{21}^{(1)})_l \quad (5.7)$$

w.r.t \bar{z}_1

$$\text{subject to } \bar{H}_1(\bar{X}_1) = 0 \quad (5.7a)$$

$$\bar{G}_1(\bar{X}_1) \leq 0 \quad (5.7b)$$

ii) Sub-problem 2

$$f_2' = f_2(\bar{z}_2, \bar{u}_{12}, \bar{u}_{21}) + f_{1o}^*(\bar{z}_1, u_{12}, u_{21}) + \sum_k (\lambda_{12}^1 \Delta u_{12}^{(2)})_k + \sum_l (\lambda_{21}^1 \Delta u_{21}^{(2)})_l \quad (5.8)$$

w.r.t \bar{z}_2

$$\text{subject to } \bar{H}_2(\bar{X}_2) = 0 \quad (5.8a)$$

$$\bar{G}_2(\bar{X}_2) \leq 0 \quad (5.8b)$$

where the f_{io}^* are the independent optimal solution values of the local objectives for units 1 and 2 and the $\bar{\lambda}_{ij}^i$ and $\bar{\lambda}_{ij}^j$ are the vectors of shadow prices associated with the coupling function changes, i.e. the marginal changes due to changes in the coupling functions for the optimal values of f_1 and f_2 . The subscript o represents an initial or reference values from the previous optimization of the other sub-problem. The shadow prices are defined as

$$\lambda_{ij}^i = \frac{\partial f_{io}^*}{\partial u_{ij}}, \quad \left(\text{e.g., } \lambda_{12}^1 = \frac{\partial f_{1o}^*}{\partial u_{12}} \right) \quad (5.9)$$

$$\text{and } \lambda_{ij}^j = \frac{\partial f_{jo}^*}{\partial u_{ij}}, \left(\text{e.g., } \lambda_{12}^2 = \frac{\partial f_{2o}^*}{\partial u_{12}} \right) \quad (5.10)$$

Furthermore, the changes in the coupling functions given in the objective functions above are defined as changes with respect to the decision variable sets associated with each unit such that

$$\Delta u_{ij}^i = \frac{\partial u_{ij}}{\partial \bar{z}_i} \Delta \bar{z}_i \quad (5.11)$$

$$\text{and } \Delta u_{ij}^j = \frac{\partial u_{ij}}{\partial \bar{z}_j} \Delta \bar{z}_j \quad (5.12)$$

As seen in equation (5.7) and (5.8), system-level, unit-based optimization provides system-level optimization results and not local or unit-level sub-problems because system-level information has been addressed directly in each local or unit-level objective function. This is the most distinguishable feature of ILGO over LGO and results in the nested optimizations from which LGO suffers being eliminated in the ILGO approach.

5.3.2.3 Dynamic Iterative Local-Global Optimization (DILGO) Approach

DILGO is a version of ILGO for the dynamic optimization of energy systems using physical decomposition. DILGO was developed by Rancruel (2005) and validated using a dynamic SOFC based auxiliary power unit (APU) synthesis/design and operation/control optimization problem. DILGO has also been employed in this doctoral research because this optimization strategy is the most suitable approach for the type of large-scale dynamic energy system synthesis/design and operation/control optimization problems tackled here.

For dynamic applications, the system-level, unit-based optimization problems defined in the ILGO approach are modified by the integral of coupling function change over time, and then, the equation (5.7) and (5.8) are given as

$$f_1' = f_1(\bar{z}_1, \bar{u}_{12}, \bar{u}_{21}) + f_{2o}^*(\bar{z}_2, \bar{u}_{12}, \bar{u}_{21}) + \sum_k \left(\int_{t=0}^T \dot{\lambda}_{12}^2 \Delta u_{12}^{(1)} dt \right)_k + \sum_l \left(\int_{t=0}^T \dot{\lambda}_{21}^1 \Delta u_{21}^{(1)} dt \right)_l \quad (5.13)$$

$$f_2' = f_2(\bar{z}_2, \bar{u}_{12}, \bar{u}_{21}) + f_{1o}^*(\bar{z}_1, \bar{u}_{12}, \bar{u}_{21}) + \sum_k \left(\int_{t=0}^T \dot{\lambda}_{12}^1 \Delta u_{12}^{(2)} dt \right)_k + \sum_l \left(\int_{t=0}^T \dot{\lambda}_{21}^2 \Delta u_{21}^{(2)} dt \right)_l \quad (5.14)$$

$$\text{where } \dot{\lambda}_{ij}^i(t) = \left(\frac{\partial \dot{f}_{io}^*(t)}{\partial u_{ij}(t)} \right) \quad (5.15)$$

$$\text{and } \dot{\lambda}_{ij}^j(t) = \frac{\partial \dot{f}_{jo}^*(t)}{\partial u_{ij}(t)} \quad (5.16)$$

Constraints are defined in the same manner as in ILGO (i.e. equations (5.7a,b) and (5.8a,b)). Note again that readers can find the detailed development procedure of DILGO in Rancruel (2005).

5.4 Applying DILGO to the Dynamic PEMFC System Synthesis /Design and Operation/Control Optimization under Uncertainties

Dynamic operation of an energy system should be taken into account during its synthesis/design optimization when the system experiences transient conditions for a large fraction of its life. In addition, the complexity of the PEMFC system makes the synthesis/design and operation/control optimization problem difficult to handle with a single-level optimization approach. Thus, DILGO is adopted for the PEMFC system synthesis/design and operation/control optimization in this doctoral research. In the following sections, a system-level, unit-based optimization problem is defined for each subsystem, and the detailed DILGO approach for the PEMFC system synthesis/design and operation/control optimization is described.

5.4.1 System-Level Dynamic Synthesis/Design and Operation/Control Optimization Problem

The PEMFC system is decomposed into three subsystems and its system-level, dynamic synthesis/design and operation/control problem is expressed as

$$\begin{aligned} \text{Minimize } C_{total}^{PEMFC} &= C_{SS} + C_{FPS} + C_{WRAS} + C_{oper} & (5.17) \\ \text{w.r.t } \{ \bar{X}_{SS}, \bar{Y}_{SS} \}, \{ \bar{X}_{FPS}, \bar{Y}_{FPS} \}, \{ \bar{X}_{WRAS}, \bar{Y}_{WRAS} \} & \end{aligned}$$

$$\text{subject to } \vec{H}_{SS} = 0, \vec{G}_{SS} \leq 0 \quad (5.17a)$$

$$\vec{H}_{FPS} = 0, \vec{G}_{FPS} \leq 0 \quad (5.17b)$$

$$\vec{H}_{WRAS} = 0, \vec{G}_{WRAS} \leq 0 \quad (5.17c)$$

where C_{SS} , C_{FPS} , and C_{WRAS} are the capital investment costs for each subsystem and C_{oper} is the system operating cost (i.e. fuel cost during operation). The operating cost given here is the same as equation (3.106) of Chapter 3.

5.4.2 Uncertainty Considerations in System-Level Dynamic Synthesis /Design and Operation/Control Optimization

In energy system synthesis/design and operation/control problems, uncertainties should be considered with respect to its objective function(s) and constraints since

- i. system design engineers need to know and to provide the level of certainty with which the development objectives from optimization (e.g., total life cycle cost or capital investment cost of the system) have been met; and
- ii. uncertainties in the constraints must be known in order to guarantee the safety margins for the system developed, and an uncertainty analysis incorporated into the system development process gives more reasonable solutions than the conventional approach in which system size and operating conditions are determined by safety factors resulting in an overly conservative system.

As discussed in Chapter 4, three uncertainty factors (i.e. with respect to the load profile, the cost functions, and certain inequality constraints (e.g., that on the CO concentration)) are considered in the system synthesis/design and operation/control optimization. For example, the total life cycle cost can be expressed in terms of expected total life cycle cost with a certain range, i.e. it can be expressed by deviation of the expected total life cycle cost in terms of the standard deviation.

The PEMFC system synthesis/design and operation/control problem under uncertainty can be defined as a multi-objective optimization problem of minimizing the

total life cycle cost of the system and minimizing the variation of the total life cycle cost (i.e. the variation caused by uncertainties in the load profile and cost functions). Thus, the problem is given by

$$\text{Minimize } C_{total}^{PEMFC} = C_{SS} + C_{FPS} + C_{WRAS} + C_{oper} \quad (5.18)$$

$$C_{UNC}^{PEMFC} = C_{total,SD} \quad (5.19)$$

$$\text{w.r.t } \{\bar{X}_{SS}, \bar{Y}_{SS}\}, \{\bar{X}_{FPS}, \bar{Y}_{FPS}\}, \{\bar{X}_{WRAS}, \bar{Y}_{WRAS}\}$$

$$\text{subject to } \bar{H}_{SS,UNC} = 0, \bar{G}_{SS,UNC} \leq 0 \quad (5.20a)$$

$$\bar{H}_{FPS,UNC} = 0, \bar{G}_{FPS,UNC} \leq 0 \quad (5.20b)$$

$$\bar{H}_{WRAS,UNC} = 0, \bar{G}_{WRAS,UNC} \leq 0 \quad (5.20c)$$

where $C_{total,SD}$ is the variation of the total life cycle cost in terms of the standard deviation, the subscript UNC indicates that these constraints include uncertainties. The standard deviation of the total life cycle cost can be obtained by using equations (4.16) of Chapter 4.

Both objective functions (5.18) and (5.19) are defined in terms of cost so that they may be expressed as in a single objective function. Assuming an equal weighting for both objective functions, the single objective function is written as

$$\text{Minimize } C_{total,UNC}^{PEMFC} = C_{total}^{PEMFC} + C_{UNC}^{PEMFC} \quad (5.21)$$

This assumption has been evaluated using the FPS synthesis/design and operation/control optimization problem, and the single-objective and the multi-objective approaches for the FPS are defined as follow:

i) Two-objective functions for the FPS synthesis/design

$$\text{Minimize } C_{total}^{FPS} = C_{FPS} + C_{oper} \quad (5.22)$$

$$C_{UNC}^{FPS} = C_{total,SD}^{FPS} \quad (5.23)$$

ii) Single-objective function for the FPS synthesis/design

$$\text{Minimize } C_{total,UNC}^{FPS} = C_{total}^{FPS} + C_{UNC}^{FPS} \quad (5.24)$$

Constraints for both problems are given by equation (5.20b). Uncertainty in the load profile, fuel cost, and purchase cost are considered in this comparison. Uncertainties are

expressed in terms of standard deviations, and the standard deviation of the total life cycle cost of the FPS can be expressed by the equation (4.16) as

$$C_{UNC}^{FPS} = \sqrt{\left(\frac{C_{total,load}^{FPS+} - C_{total,load}^{FPS-}}{2\delta_{load}^{FPS}} \right)^2 v_{load}^{FPS} + \left(\frac{C_{total,fuel}^{FPS+} - C_{total,fuel}^{FPS-}}{2\delta_{fuel}^{FPS}} \right)^2 v_{fuel}^{FPS} + \left(\frac{C_{total,COST}^{FPS+} - C_{total,COST}^{FPS-}}{2\delta_{COST}^{FPS}} \right)^2 v_{COST}^{FPS}} \quad (5.25)$$

where δ_{load} , δ_{fuel} , and δ_{COST} are the small step sizes, respectively, in the load profile, fuel cost, and purchase cost used for calculating system response sensitivities. The cost terms in the denominators are calculated relative to each step sizing equations (4.12) and (4.13). An v_{load} , v_{fuel} , and v_{COST} are the variances of the load profile, fuel cost, and purchase cost. 8% standard deviation (i.e. the variance is square root of standard deviation) of the load profile, a 8% standard deviation of fuel cost, and a 10% of standard deviation of purchase cost are assumed for this calculation.

Uncertainties on the constraints must also be addressed during the optimization process. In case of the PEMFC system, CO concentration is one of the critical factors which can lead to system failure. In this study, an inequality constraint on the CO concentration is expressed for both the single-/multi-objective optimizations as

$$G_{CO,95\%} = G_{CO} + 2G_{CO}^{SD} \leq 10 \text{ ppm} \quad (5.26)$$

$$\text{where } G_{CO}^{SD} = \sqrt{\left(\frac{G_{CO,load}^{FPS+} - G_{CO,load}^{FPS-}}{2\delta_{load}^{FPS}} \right)^2 v_{load}^{FPS}} \quad (5.27)$$

and G_{CO} is the mean value of the CO concentration of the reformat gas after the PrOx and G_{CO}^{SD} is the standard deviation of this CO concentration. By multiplying the standard deviation by 2, 95% confidence interval for the CO concentration can be described, i.e. the result of the optimization will guarantee that this constraint is met with a certainty of 95%.

Among the uncertainties in the load profile, fuel cost, and cost functions, only the uncertainty of the load profile affect variations in the CO concentration because the other uncertainties are not system responses but system cost. Therefore, standard deviation of the CO concentration of the FPS can be expressed as equation (5.27).

Table 5.1 compares the optimization results under uncertainty for the single-objective approach with those for the multi-objective approach using SEQOPT. Each optimization approach was carried out twice to check the consistency of the results. The single-objective approach found the optimum $C_{total,UNC}^{FPS}$ values, while the multi-objective approach provided the optimum total life cycle cost C_{total}^{FPS} and its standard deviation C_{UNC}^{FPS} . As seen in Table 5.1, the optimization results of the objective functions based on both approaches showed less than a 0.14% difference between single- and multi-objective approaches. From the comparison, it can be concluded that single-objective approach instead of the multi-objective approach can be used for the PEMFC system synthesis/design and operation/control problem under uncertainties. The actual optimization process is discussed in Chapter 6.

Note that the results in Table 5.1 are obtained from initially developed cost functions for the FPS system model and that some of these have since been further updated after that fact. Thus, the values in Table 5.1 are somewhat different from the final results in presented Chapter 6.

Table 5.1 Comparison of the single-/multi-objective approaches for the FPS synthesis/design and operation /control optimization problem under uncertainty.

Cost(\$)	Single-objective approach		Multi-objective approach	
	1	2	1	2
C_{total}^{FPS}	41666	41641	41706	41699
C_{UNC}^{FPS}	3065	3072	3068	3043
$C_{total,UNC}^{FPS}$	44731	44713	44774	44742

5.4.3 Decomposition and Coupling Function Definition for the Dynamic PEMFC System Synthesis/Design and Operation/Control Optimization under Uncertainty

In order to apply the DILGO approach to the dynamic PEMFC system synthesis/design and operation/control optimization under uncertainty, the PEMFC system must be decomposed into subsystems and coupling functions in such a way to

minimize the loss of system-level information at the subsystem-level. The PEMFC system is physically broken down into three subsystems (i.e. the SS, FPS, and WRAS), and these are used as the basis to replace the system-level optimization problem based on the total life cycle cost of the system with three system-level, unit-based (SLUB) optimization sub-problems.

The system configuration determines the coupling functions. Each subsystem boundary and the set of coupling functions used here which represent material/energy flows or required operating conditions between subsystems are depicted in Figures 5.5 and 5.6. The PES is not modeled here, and the SS and the PES are coupled by a controller to make the output power P_{gross} from the SS meet the power requirement P_{req} of the load demand.

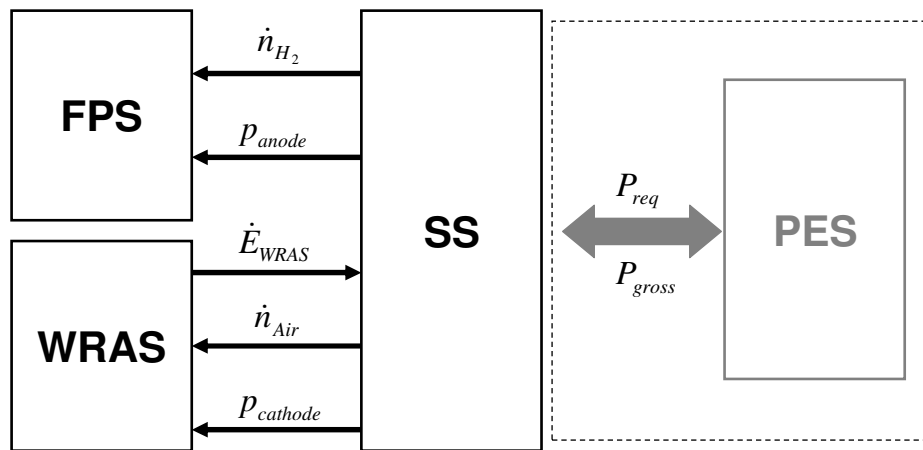


Figure 5.5 Subsystem boundaries and coupling functions.

Initially proposed system configuration seen in Figure 3.3 has interactions between the FPS and WRAS to recover waste thermal energy of the exhaust gases from the steam generator by the expander in the WRAS. However, that configuration requires more energy to supply compressed air to the FPS than is gained by the expander unit. Other changes to the initial PEMFC system configuration were also made during studies on system integration, control, and thermal management. Figure 5.6 describes the final version of the PEMFC system configuration to maximize system efficiency and to facilitate the thermal management of the system. This system configuration is used as the initial configuration during the synthesis/design and operation/control optimization. For

this configuration, five coupling functions are determined for the SLUB optimizations of the PEMFC system: the anode and cathode side pressures p_{anode} and $p_{cathode}$, the hydrogen flow rate \dot{n}_{H_2} from the FPS, the air flow rate \dot{n}_{Air} from the WRAS, and the motor parasitic power \dot{E}_{WRAS} . Figure 5.5 depicts subsystem boundaries and coupling functions.

The SS can be considered as the main subsystem of the PEMFC system because the FPS and the WRAS are run to satisfy the requirements (i.e. pressure, hydrogen and air flow rates) of the SS for a given load demand. To generate gross electric power for a specific load and required parasitic power \dot{E}_{WRAS} , the SS requires a certain amount of hydrogen and air (i.e. \dot{n}_{H_2} and \dot{n}_{Air}) as well as also operating pressure (inside pressure of the stack) to minimize the total life cycle cost. These required hydrogen and air flow rates and pressure become the base profiles for conducting the SLUB optimizations of the dynamic FPS and WRAS. Even though stack temperature is also an important operating parameter, inlet temperatures of the air and hydrogen are not considered as coupling functions because these temperatures are managed by controllers so they are not affected by the other subsystems.

The following sections provide a detailed formulation of the SLUB optimization sub-problem for each subsystem as well as a list of all the decision variables.

5.4.3.1 FPS System-Level, Unit-Based Optimization

The SLUB optimization sub-problem for the FPS can be formulated as

$$\text{Minimize } C'_{FPS} = C_{FPS} + C_{oper} + C_{total,UNC}^{FPS} + C_{SS}^* + C_{WRAS}^* \quad (5.28)$$

$$\text{w.r.t } \{ \bar{X}_{FPS}, \bar{Y}_{FPS} \}$$

$$\text{subject to } \bar{H}_{FPS} = 0 \quad (5.28a)$$

$$\bar{G}_{FPS} \leq 0 \quad (5.28b)$$

$$\begin{bmatrix} \dot{n}_{H_2} - \dot{n}_{H_2}^* \\ p_{andoe} - p_{anode}^* \end{bmatrix} = 0 \quad (5.28c)$$

$$\text{where } C_{total,UNC}^{FPS} = \sqrt{C_{UNC}^{FPS} + C_{UNC}^{SS*} + C_{UNC}^{WRAS*}} \quad (5.29)$$

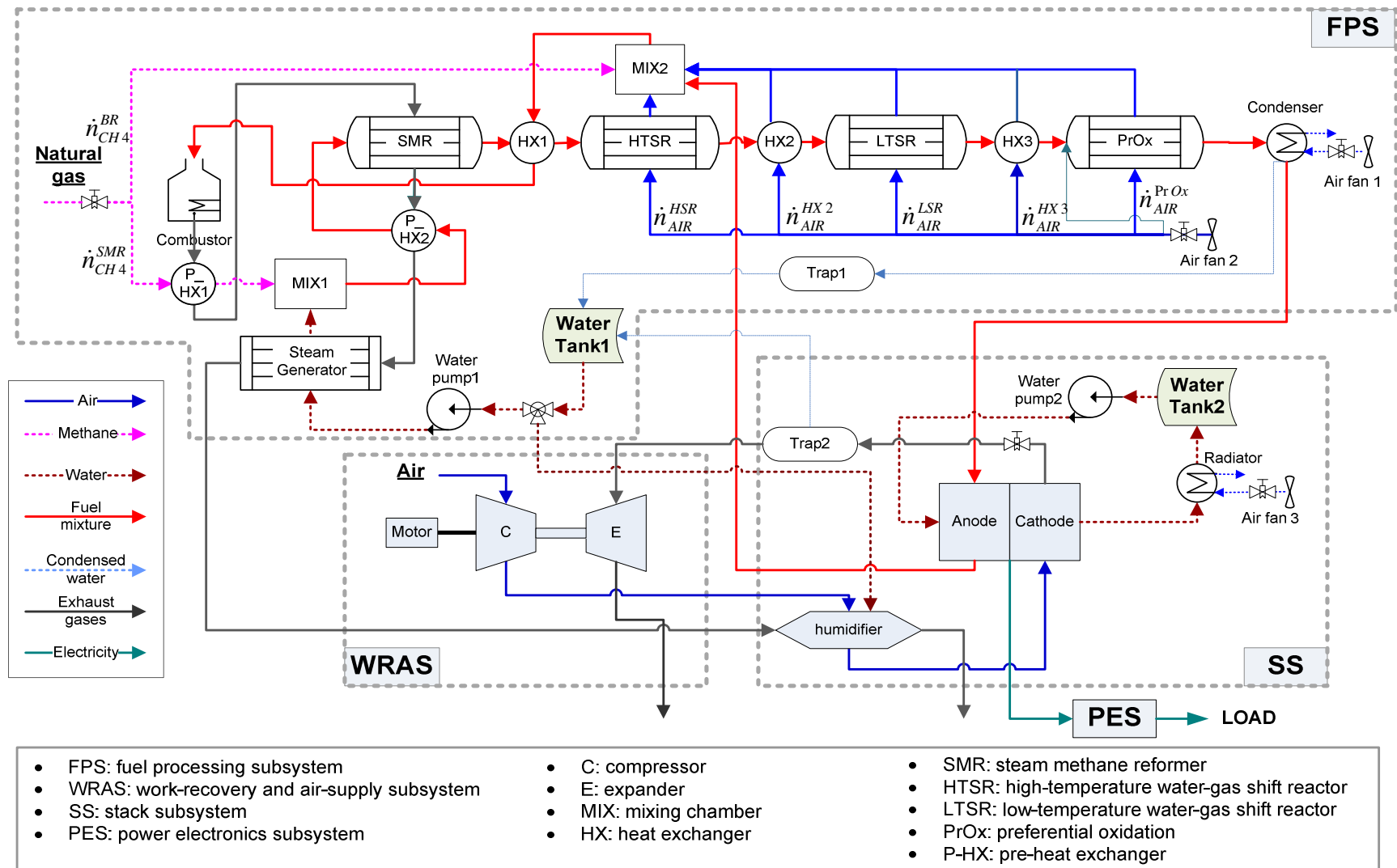


Figure 5.6 Proposed non-optimized PEMFC system configuration for the dynamic synthesis/design and operation optimization.

$$\begin{aligned}
C_{UNC}^{FPS} = & \left(\frac{C_{total,load}^{FPS+} - C_{total,load}^{FPS-}}{2\delta_{load}^{FPS}} \right)^2 \mathbf{v}_{load}^{FPS} + \left(\frac{C_{total,fuel}^{FPS+} - C_{total,fuel}^{FPS-}}{2\delta_{fuel}^{FPS}} \right)^2 \mathbf{v}_{fuel}^{FPS} \\
& + \left(\frac{C_{total,COST}^{FPS+} - C_{total,COST}^{FPS-}}{2\delta_{COST}^{FPS}} \right)^2 \mathbf{v}_{COST}^{FPS}
\end{aligned} \tag{5.30}$$

The vector of equality constraints \vec{H}_{FPS} represents the thermodynamic, kinetic, and geometric models of the FPS and the vector of inequality constraints \vec{G}_{FPS} indicates physical limitation of the FPS such as the limit on CO concentration (equations (5.26) and (5.27)). Equation (5.28c) indicates that the coupling functions \dot{n}_{H_2} and p_{anode} must take the values which are found by solving the previous SS SLUB optimization sub-problem. Thus, the FPS SLUB optimization sub-problem is solved by fixing the inputs and optimizing the output, i.e. in this case the natural gas required.

Equation (5.28) represents the system-level objective function for the SLUB optimization of the FPS. The SLUB objective function C_{FPS}^i consists of contributions from the FPS (i.e. capital cost C_{FPS} (or capital investment cost for the life cycle) of the FPS and the cost of fuel consumed C_{oper}), the optimum values for the capital costs of the SS C_{SS}^* and WRAS C_{WRAS}^* obtained from solving the sub-problems (5.31) and (5.36) (see below), and the variation of the total life cycle cost in terms of its standard deviation (i.e. $C_{total,UNC}^{FPS}$). This standard deviation is expressed by equations (5.29) and (5.30). C_{UNC}^{FPS} captures uncertainties in the unit-level optimization of the FPS based on uncertainties in the cost functions (i.e. purchase cost) of the FPS, load profile (i.e. variations in the hydrogen requirement), and fuel cost. C_{UNC}^{SS*} and C_{UNC}^{WRAS*} represent unit-level uncertainties obtained from the previous SLUB optimization of the SS and WRAS using equation (5.33) (see below) for C_{UNC}^{SS*} and equation (5.38) (see below) for C_{UNC}^{WRAS*} .

The synthesis/design and operation decision variables for the FPS and their ranges are given in Tables 5.2 and 5.3. In addition, the given values and assumptions for the probabilistic calculation of the uncertainties are presented in Table 5.4. Note that the optimal control architecture and its control gains can be determined as part of a energy system synthesis/design and operation/control optimization problem. Wang (2008) has

done this for the optimal control architecture design of this PEMFC system based on a state-space control for a set of multi-input multi-output (MIMO) controllers. For the FPS, the fuel feed flow rate should be controlled to meet the load requirement, and at least one of the temperatures must be controlled in order to operate the FPS optimally. The inlet reformat mixture gas temperature of the HTSR is chosen as a control variable. In this doctoral research, the controller and control gains for each subsystem are obtained from Wang (2008), and the gains which are obtained from a preliminary subsystem-level optimization by Wang are listed in Table 5.4. Readers are referred to Wang (2008) for more details about the control part of the PEMFC system developed.

Table 5.2 Synthesis/design decision variables of the FPS and their ranges.

Component	Description		Range
SMR	L^{SMR}	Reactor length (m)	$0.5 \leq L^{SMR} \leq 2$
	d_{IN}^{SMR}	Reactor single tube inner diameter (m)	$0.01 \leq d_{IN}^{SMR} \leq 0.03$
HTSR	L^{HTSR}	Reactor length (m)	$0.2 \leq L^{HTSR} \leq 0.8$
	d_{IN}^{HTSR}	Reactor tube inner diameter (m)	$0.04 \leq d_{IN}^{HTSR} \leq 0.1$
LTSR	L^{LTSR}	Reactor length (m)	$0.2 \leq L^{LTSR} \leq 0.8$
	d_{IN}^{LTSR}	Reactor tube inner diameter (m)	$0.05 \leq d_{IN}^{LTSR} \leq 0.1$
PrOx	L^{PrOx}	Reactor length (m)	$0.3 \leq L^{PrOx} \leq 0.8$
	d_{IN}^{PrOx}	Reactor tube inner diameter (m)	$0.05 \leq d_{IN}^{PrOx} \leq 0.1$
Heat exchangers	L_i^{HX}	Hot/gas-side length of HX i (m) $i = P_HX1, P_HX2, HX1, HX2, HX3$	$0.01 \leq L_i^{HX} \leq 0.7$
	N_i^{HX}	Number of channels of HX i	$2 \leq N_i^{HX} \leq 7$
	h_i^{HX}	Height of a channel of HX i (m)	$0.003 \leq h_i^{HX} \leq 0.005$
SG	L^{SG}	SG length (m)	$0.8 \leq L^{SG} \leq 2.0$
	d_{IN}^{SG}	SG single tube inner diameter (m)	$0.003 \leq d_{IN}^{SG} \leq 0.01$
	N^{SG}	Number of tubes	$7 \leq N^{SG} \leq 15$

Table 5.3 Operation decision variables of the FPS and their ranges.

	Description	Range
$\xi_{S/C}$	Steam to carbon ratio $\left(\dot{n}_{H_2O}^{SMR} / \dot{n}_{CH_4}^{SMR} \right)$	$2.5 \leq \xi_{S/C} \leq 6$
ξ_{CH_4}	Natural gas feed ratio $\left(\dot{n}_{CH_4}^{BR} / \dot{n}_{CH_4}^{SMR} \right)$	$0.25 \leq \xi_{CH_4} \leq 0.43$
ξ_{AIR}^i	Cooling air ratio of component i $\left(\dot{n}_{AIR}^i / \dot{n}_{AIR}^{TOTAL} \right)$ $i = HTSR, HX2, LTSR, HX3, PrOx$	$0.01 \leq \xi_{AIR}^i \leq 0.5$
T_{inlet}^{HTSR}	Inlet reformat mixture gas temperature of the HTSR (K)	$590 \leq T_{inlet}^{HTSR} \leq 700$

Table 5.4 Uncertainty factors and their assumptions considered in the FPS SLUB optimization.

Uncertainty (Standard deviation)			Probability distribution
$\sigma_{H_2}^{FPS} \left(= \sqrt{V_{H_2}^{FPS}} \right)$	Load profile	8% of the load	Normal distribution
$\sigma_{fuel}^{FPS} \left(= \sqrt{V_{fuel}^{FPS}} \right)$	Fuel cost	8% of the fuel cost	Normal distribution
$\sigma_{COST}^{FPS} \left(= \sqrt{V_{COST}^{FPS}} \right)$	Purchase cost	10% of each component purchase cost	Normal distribution

Table 5.5 Control gains for the FPS (Wang, 2008).

Gains for the temperature control		Gains for the fuel flow rate control	
$K^{FPS} (1)$	-0.015	$K^{FPS} (5)$	0.02
$K^{FPS} (2)$	1.0×10^{-7}	$K^{FPS} (6)$	1.0×10^{-12}
$K^{FPS} (3)$	1.0×10^{-5}	$K^{FPS} (7)$	1.0×10^{-4}
$K^{FPS} (4)$	1.0×10^{-7}	$K^{FPS} (8)$	1.0×10^{-12}

5.4.3.2 SS System-Level, Unit-Based Optimization

In the same manner as the FPS, the SLUB optimization sub-problem for the SS can be formulated as

Minimize

$$C_{SS}' = C_{SS} + C_{total,UNC}^{SS} + C_{FPS}^* + C_{WRAS}^* + C_{oper}^* + \int_{t=0}^T \dot{\lambda}_{H_2} \Delta \dot{n}_{H_2} dt \quad (5.31)$$

$$+ \int_{t=0}^T \dot{\lambda}_{p_{anode}} \Delta p_{anode} dt + \int_{t=0}^T \dot{\lambda}_{Air} \Delta \dot{n}_{Air} dt + \int_{t=0}^T \dot{\lambda}_{p_{cathode}} \Delta p_{cathode} dt$$

w.r.t $\{\bar{X}_{SS}, \bar{Y}_{SS}\}$

$$\text{subject to } \bar{H}_{SS} = 0 \quad (5.31a)$$

$$\bar{G}_{SS} \leq 0 \quad (5.31b)$$

$$[\dot{E}_{WRAS} - \dot{E}_{WRAS}^*] = 0 \quad (5.31c)$$

$$\text{where } C_{total,UNC}^{SS} = \sqrt{C_{UNC}^{SS} + C_{UNC}^{FPS*} + C_{UNC}^{WRAS*}} \quad (5.32)$$

$$C_{UNC}^{SS} = \left(\frac{C_{total,COST}^{SS+} - C_{total,COST}^{SS-}}{2\delta_{COST}^{SS}} \right)^2 v_{COST}^{SS} \quad (5.33)$$

The vector of equality constraints \vec{H}_{SS} represents the thermodynamic, kinetic, and geometric models of the SS and the vector of inequality constraints \vec{G}_{SS} indicates physical limitation of the SS. Equation (5.31c) indicates that the coupling function \dot{E}_{WRAS} must take the value which is found by solving the previous WRAS SLUB optimization sub-problem.

Equation (5.31) represents the system-level objective function for the SLUB optimization of the SS. The SLUB objective function, C'_{SS} , consists of the contributions of the SS (i.e. capital cost (or capital investment cost for the life cycle) of the SS C_{SS}), the optimum values of the life cycle cost and fuel costs of the FPS C_{FPS}^* and C_{oper}^* , respectively, and of the capital cost of the WRAS C_{WRAS}^* obtained from solving sub-problems (5.28) and (5.36) (see below), the variation of the total life cycle cost in terms of its standard deviation of it (i.e. $C_{total,UNC}^{SS}$), and additional terms that represent the impact which variations in the local SS decision variables have on the local objectives of the FPS and WRAS. These variations rates are taken into account by means of the shadow price and coupling function variations. Each shadow price rate provides direction and the marginal change in the optimum value of the FPS and WRAS SLUB optimizations due to marginal changes in the value of each SS coupling function output (i.e. \dot{n}_{H_2} , \dot{n}_{Air} , p_{anode} , and $p_{cathode}$). The shadow price rates are defined as

$$\dot{\lambda}_{H_2}(t) = \partial \dot{C}_{FPS}^* / \partial \dot{n}_{H_2} \quad (5.34a)$$

$$\dot{\lambda}_{p_{anode}}(t) = \partial \dot{C}_{FPS}^* / \partial p_{anode} \quad (5.34b)$$

$$\dot{\lambda}_{Air_2}(t) = \partial \dot{C}_{WRAS}^* / \partial \dot{n}_{Air} \quad (5.34c)$$

$$\dot{\lambda}_{p_{cathode}}(t) = \partial \dot{C}_{WRAS}^* / \partial p_{cathode} \quad (5.34d)$$

The marginal changes in the coupling functions are give by

$$\Delta \dot{n}_{H_2} = \dot{n}_{H_2} - (\dot{n}_{H_2}^*)_o \quad (5.35a)$$

$$\Delta p_{anode} = p_{anode} - (p_{anode}^*)_o \quad (5.35b)$$

$$\Delta \dot{n}_{Air} = \dot{n}_{Air} - (\dot{n}_{Air}^*)_o \quad (5.35c)$$

$$\Delta p_{cathode} = p_{cathode} - (p_{cathode}^*)_o \quad (5.35d)$$

where the subscript o refers to the optimum (indicated by the superscript $*$) coupling function value which is obtained from the previous DILGO iteration.

The standard deviation of the SS capital cost $C_{total,UNC}^{SS}$ is also expressed by equations (5.32) and (5.33). C_{UNC}^{SS} represents the uncertainty in the unit-level optimization of the SS. For the SS, the uncertainty of the cost function (or purchase cost of the SS) is only considered because uncertainties in the fuel cost and load profile are already considered in equation (5.30) as a part of the FPS SLUB optimization sub-problem. C_{UNC}^{FPS*} and C_{UNC}^{WRAS*} represent the unit-level uncertainties obtained from the previous SLUB optimization of each subsystem using equation (5.30) for C_{UNC}^{FPS*} and equation (5.38) (see below) for C_{UNC}^{WRAS*} .

The synthesis/design and operation decision variables for the SS and their ranges are given in Table 5.6. In addition, the given value and assumptions for the probabilistic calculation of the uncertainties are presented in Table 5.7. Furthermore, the SS must control the output current and fuel utilization to meet the load demand and optimally control the system. As indicated above already, the controls are explained in detail by Wang (2008); and Table 5.8 shows the list of the controller gains which have been used for the SS simulation.

Table 5.6 Synthesis/design and operation decision variables of the SS and their ranges.

Description		Range
L^{SS}	Each side of the cell length (m)	$0.15 \leq L^{SS} \leq 0.5$
N^{SS}	Number of cells	$20 \leq N^{SS} \leq 50$
$p^{SS} (= p_{anode}, p_{cathode})$	Stack operating pressure (bar)	$1.0 \leq p^{SS} \leq 5.0$

Table 5.7 Uncertainty factor and assumption considered in the SS SLUB optimization.

Uncertainty (Standard deviation)		Probability distribution
$\sigma_{COST}^{SS} \left(= \sqrt{V_{COST}^{SS}} \right)$	Purchase cost	10 % of the each component purchase cost Normal distribution

Table 5.8 Control gains for the SS (Wang, 2008).

Gains for the current control		Gains for the fuel utilization control	
$K^{SS} (1)$	2.364×10^{10}	$K^{SS} (7)$	1.794×10^9
$K^{SS} (2)$	-1.475×10^{14}	$K^{SS} (8)$	-1.119×10^{13}
$K^{SS} (3)$	5.372×10^4	$K^{SS} (9)$	4.071×10^3
$K^{SS} (4)$	359.189	$K^{SS} (10)$	27.749
$K^{SS} (5)$	-277.649	$K^{SS} (11)$	-21.749
$K^{SS} (6)$	392.421	$K^{SS} (12)$	29.664

5.4.3.3 WRAS System-Level, Unit-Based Optimization

The SLUB optimization sub-problem for the WRAS is also defined as

$$\text{Minimize } C'_{WRAS} = C_{WRAS} + C_{total,UNC}^{WRAS} + C_{SS}^* + C_{FPS}^* + C_{oper}^* + \int_{t=0}^T \dot{\lambda}_{\dot{E}_{WRAS}} \Delta \dot{E}_{WRAS} dt \quad (5.36)$$

$$\text{w.r.t } \{ \vec{X}_{WRAS}, \vec{Y}_{WRAS} \}$$

$$\text{subject to } \vec{H}_{WRAS} = 0 \quad (5.36a)$$

$$\vec{G}_{WRAS} \leq 0 \quad (5.36b)$$

$$\begin{bmatrix} \dot{n}_{Air} - \dot{n}_{Air}^* \\ p_{cathode} - p_{cathode}^* \end{bmatrix} = 0 \quad (5.36c)$$

$$\text{where } C_{total,UNC}^{WRAS} = \sqrt{C_{UNC}^{WRAS} + C_{UNC}^{SS*} + C_{UNC}^{FPS*}} \quad (5.37)$$

$$C_{UNC}^{WRAS} = \left(\frac{C_{total,Air}^{WRAS+} - C_{total,Air}^{WRAS-}}{2\delta_{Air}^{WRAS}} \right)^2 \nu_{Air}^{WRAS} + \left(\frac{C_{total,COST}^{WRAS+} - C_{total,COST}^{WRAS-}}{2\delta_{COST}^{WRAS}} \right)^2 \nu_{COST}^{WRAS} \quad (5.38)$$

The vector of equality constraints \vec{H}_{WRAS} represents the thermodynamic and geometric models of the WRAS and the vector of inequality constraints \vec{G}_{WRAS} indicates physical limitation of the WRAS. Equation (5.36c) indicates that the coupling functions \dot{n}_{Air} and $p_{cathode}$ must take the values which are found by solving the previous SS SLUB optimization sub-problem.

Equation (5.36) represents the system-level objective function for the SLUB optimization of the WRAS. The SLUB objective function, C'_{WRAS} , is comprised of the

contributions of the WRAS (i.e. capital cost (or capital investment cost for the life cycle) of the WRAS C_{WRAS}), the optimum values of the capital cost and fuel costs of the FPS C_{FPS}^* and C_{oper}^* , respectively, and of the capital cost of the SS C_{SS}^* obtained from solving sub-problems (5.28) and (5.31), the variation of the WRAS total life cycle cost in terms of its standard deviation (i.e. $C_{total,UNC}^{WRAS}$), and additional term that represents the impact which variations in the local WRAS decision variable have on the local objective of the SS. This variation “is taken into account” by means of the shadow price rate and coupling function variation. The shadow price rate provides direction and the marginal change in the optimum value of the SS SLUB optimization due to a marginal change in the value of the coupling function \dot{E}_{WRAS} . The shadow price rate is defined as

$$\dot{\lambda}_{\dot{E}_{WRAS}}(t) = \partial \dot{C}_{SS}^* / \partial \dot{E}_{WRAS} \quad (5.39)$$

The marginal change of the coupling function is give by

$$\Delta \dot{E}_{WRAS} = \dot{E}_{WRAS} - (\dot{E}_{WRAS}^*)_o \quad (5.40)$$

The standard deviation of the total life cycle cost $C_{total,UNC}^{WRAS}$ of the WRAS SLUB optimization sub-problem is also expressed by equations (5.37) and (5.38). C_{UNC}^{WRAS} represents the uncertainty in the unit-level optimization of the WRAS. For the WRAS, uncertainties in the cost function (or purchase cost of the SS) and air flow rate which has variations due to uncertainties in the load profile are considered. C_{UNC}^{FPS*} and C_{UNC}^{SS*} represent unit-level uncertainties obtained from the previous SLUB optimization of each subsystem using equation (5.30) for C_{UNC}^{FPS*} and equation (5.33) for C_{UNC}^{SS*} .

Table 5.9 Synthesis/design decision variables of the WRAS and their ranges.

Component	Description		Range
Motor	Tq_{design}^{Motor}	Motor design torque (Nm)	$0.5 \leq Tq_{design}^{Motor} \leq 2.0$
	rpm_{design}^{Motor}	Motor design rotational speed (rpm)	$500 \leq rpm_{design}^{Motor} \leq 5000$
Compressor	$p_{design}^{Compressor}$	Compressor design pressure ratio	$1.0 \leq p_{design}^{Compressor} \leq 5.0$
	$\dot{m}_{design}^{Compressor}$	Compressor design mass flow factor (kgT ^{0.5} /s.bar)	$0.05 \leq \dot{m}_{design}^{Compressor} \leq 0.2$
Expander	$p_{design}^{Expander}$	Expander design pressure ratio	$1.0 \leq p_{design}^{Expander} \leq 5.0$
	$\dot{m}_{design}^{Expander}$	Expander design mass flow factor (kgT ^{0.5} /s.bar)	$0.05 \leq \dot{m}_{design}^{Expander} \leq 0.2$

The synthesis/design decision variables for the WRAS and their ranges are given in Table 5.9. In addition, the given values and assumptions for the probabilistic calculation of the uncertainties are presented in Table 5.10. Furthermore, compressor outlet pressure and air flow rate must satisfy the SS's requirements and need to be controlled. Table 5.11 shows the list of the controller gains which have been used for this system simulation and are based on a preliminary optimization of this subsystem conducted by Wang (2008).

Table 5.10 Uncertainty factors and their assumptions considered in the WRAS SLUB optimization.

Uncertainty (Standard deviation)			Probability distribution
$\sigma_{COST}^{WRAS} \left(= \sqrt{V_{COST}^{WRAS}} \right)$	Purchase cost	10% of the each component purchase cost	Normal distribution
$\sigma_{Air}^{WRAS} \left(= \sqrt{V_{Air}^{WRAS}} \right)$	Load profile	8% of the load (i.e. implies that 8% more of air is needed)	Normal distribution

Table 5.11 Control gains for the WRAS (Wang, 2008).

Gains for the air flow rate control		Gains for the pressure control	
$K^{WRAS} (1)$	6.540×10^3	$K^{WRAS} (5)$	0.0116
$K^{WRAS} (2)$	-0.0532	$K^{WRAS} (6)$	1.331×10^{-6}
$K^{WRAS} (3)$	0.2484	$K^{WRAS} (7)$	-3.839×10^{-7}
$K^{WRAS} (4)$	-21.239	$K^{WRAS} (8)$	-6.500×10^{-3}

5.4.4 Solution Approach: Modeling and Applying DILGO

5.4.4.1 System Model and Computational Framework Development

Figure 5.3 in Section 5.3.1 shows a schematic of the general deterministic optimization using decomposition strategies and it provides general ideas on how to apply multi-level optimization for energy system synthesis/design and operation/control problems. In order to include the uncertainty analysis process into the optimization procedure, Figure 5.4 can be modified to look like Figure 5.7 in which system-level optimization under uncertainty is described. As seen in Figure 5.7, a stochastic simulator is placed in between the deterministic system model and the optimizer, and the optimization process is conducted as it would be for a deterministic optimization.

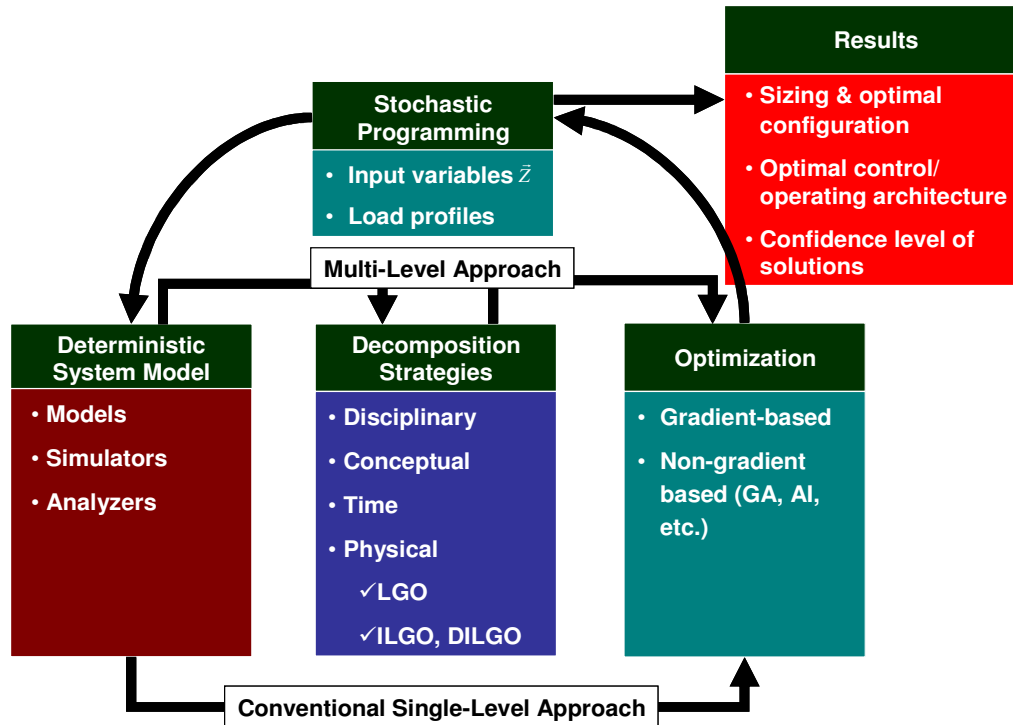


Figure 5.7 Schematic of general optimization under uncertainty.

In this doctoral research, a commercial dynamic development environment package called gPROMS™ has been used for developing the PEMFC system model. gPROMS™ provides only a gradient-based optimization algorithm (i.e. SQP) which is suitable for solving DMINLP problems. Because it does not support any non-gradient optimization algorithms (e.g., SEQOPT or GAs) which are part of the focus on this research, it is necessary to use external tools which provide these optimization algorithms by coupling with gPROMS™ with other software. Therefore, the PEMFC system model in gPROMS™ is integrated with ModelCenter™ which supports the SEQOPT and GA algorithms as well as some other analysis tools such as response surface methodologies and various stochastic modelers. Unfortunately, ModelCenter™ does not support a direct interface with gPROMS™ or vice versa. Thus, an interface framework is developed here using Visual Basic Applications in Excel. Figure 5.8 depicts the basic structure of the integrated procedure. It is used as the framework for the system synthesis/design and operation/control optimization in this work.

The simulation result of a gPROMS™ model can be exported through output channel as a text data, and Excel can open the text file using gPROMS™ library codes

called “Foreign_object” and “FPI”. ModelCenter™ which is an analyzer and optimizer in here can read data file in an Excel file, and, of course, the text data from the simulation is also read by the ModelCenter™. In this case, the simulation of the gPROMS™ model provides a set of data and it is translated into ModelCenter™, that is, ModelCenter™ is a dependent of gPROMS™. However, since ModelCenter™ is the optimizer, the gPROMS™ model must be controlled by ModelCenter™. In order to make this process, Visual Basic Applications in Excel is used with a gPROMS™ library named “gORUN” which supports the reverse process so that the optimizer of ModelCenter™ can handle the gPROMS™ model.

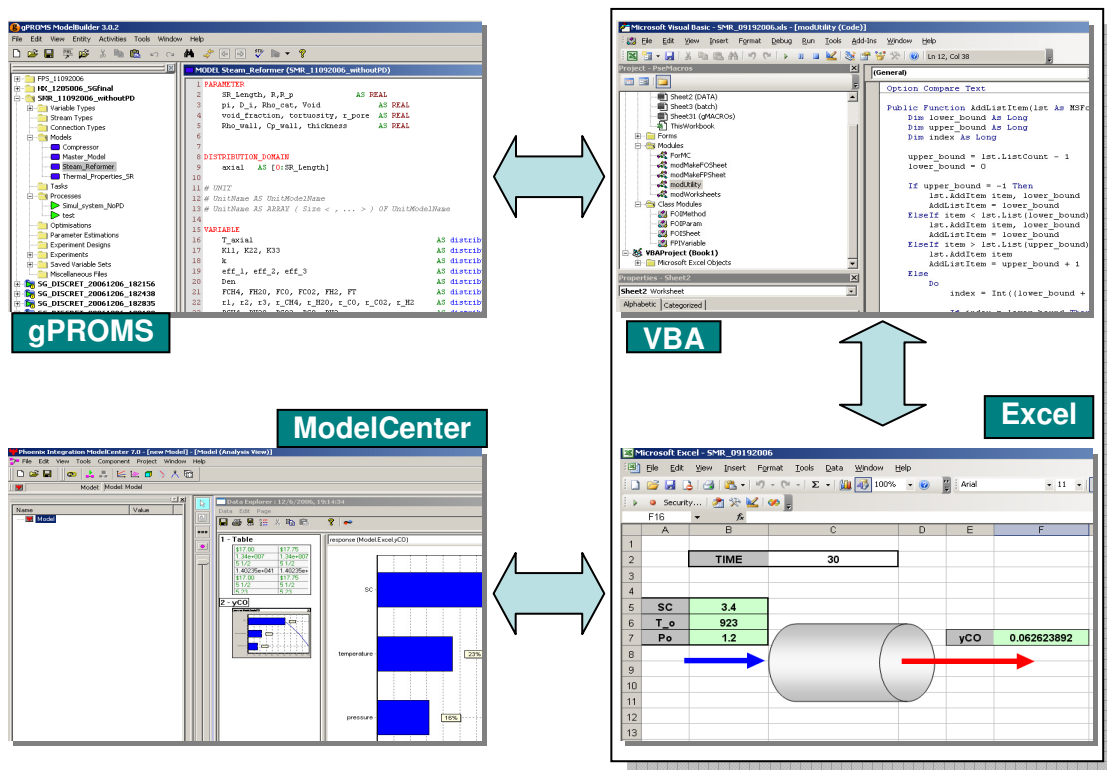


Figure 5.8 Configuration of the developed interface framework.

5.4.4.2 Applying DILGO to the PEMFC System Synthesis/Design and Operation/Control Optimization

Once the dynamic PEMFC system model and analysis tools are ready, it is necessary to set up an appropriate strategy for applying the DILGO to the system synthesis/design and operation/control optimization problem. Rancruel (2005) proposed a parallel computational scheme for the dynamic SOFC system synthesis/design and

operation/control optimization. Figure 5.9 depicts a parallel computational scheme for the DILGO strategy applied to the PFMEC system and shows the coupling function and shadow price rate flows between subsystems and each subsystem SLUB optimization scheme.

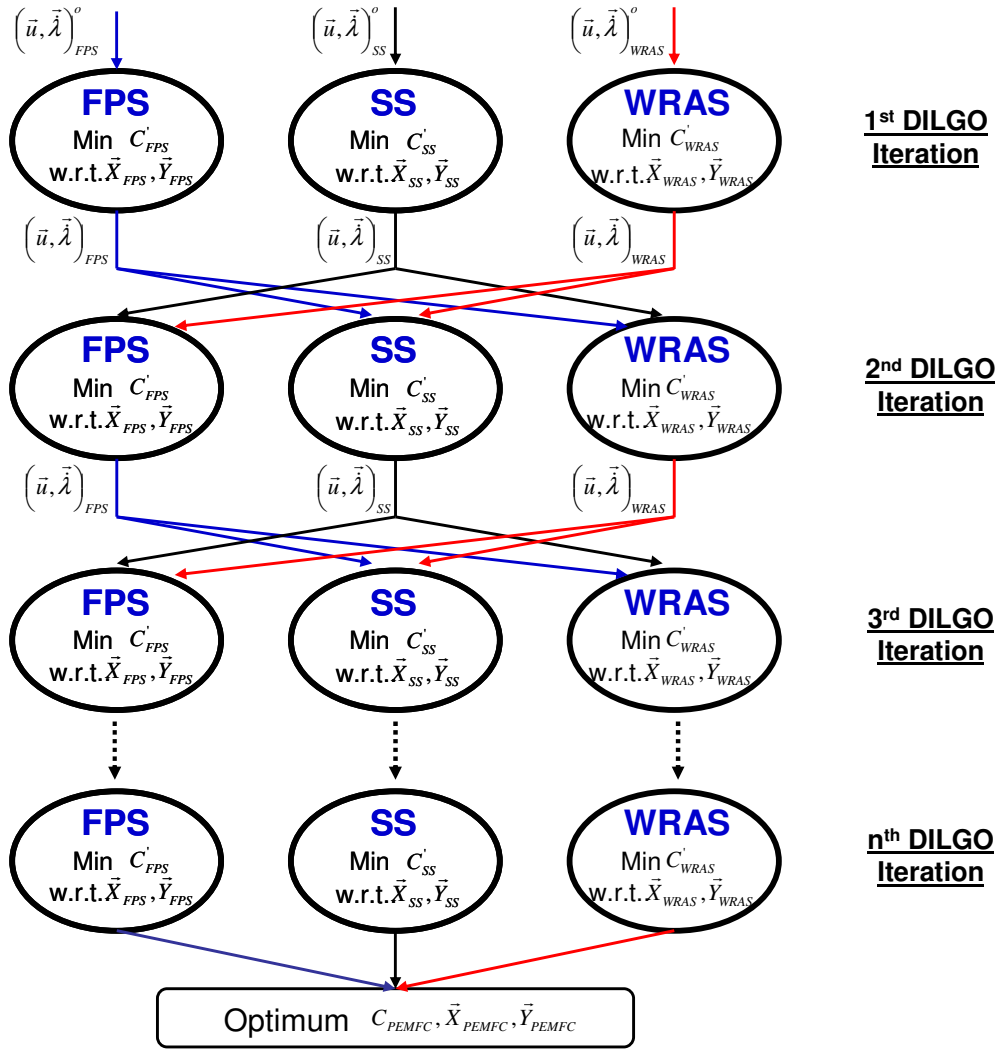


Figure 5.9 Parallel computational scheme for the DILGO (or ILGO) strategy applied to the PEMFC system.

For the first DILGO iteration, all shadow price rates are initially assumed to be zero because there is no information about them at the beginning of the DILGO procedure, while all coupling functions and uncertainties (i.e. C_{UNC}^{FPS*} and C_{UNC}^{SS*} for C_{UNC}^{WRAS} , C_{UNC}^{SS*} and C_{UNC}^{WRAS*} for C_{UNC}^{FPS} , and C_{UNC}^{FPS*} and C_{UNC}^{WRAS*} for C_{UNC}^{SS}) in each subsystem

are given reasonable values which are determined by prior simulations. Once the shadow prices, coupling functions, and uncertainties of the subsystems are found from the first DILGO iteration, they are used for the second DILGO iteration. Therefore, each subsystem SLUB optimization can be conducted in parallel from the second DILGO iteration forward. At the end of each DILGO iteration, each subsystem SLUB optimization produces updated shadow price rates, coupling functions, and a feasible optimum system-level total life cycle cost and uncertainties. These values are passed to the next DILGO iteration of each subsystem SLUB optimization, and the DILGO procedure continues until the improvement of the SLUB optimization result of each subsystem is below a predefined limit.

The parallel computational scheme shows good convergence speed because more information is updated on the next iteration than the sequential computational scheme. However, for conducting the DILGO based on parallel approach requires a high performance computer which can conduct multiple computations in parallel or multiple computer processes with each machine or processor carrying out a subsystem SLUB optimization simultaneously with these on all of the other machines. If none of these resources are available (i.e. only a limited computational resource such as a single machine can be used for the computations), parallel scheme is not possible. In that case, a sequential approach must be used as shown in Figure 5.10.

In case of the PEMFC system developed here, there are no interactions between the FPS and WRAS so that these subsystems only interact with the SS. The SS determines the required fuel and air flow rate profiles by which the FPS and WRAS SLUB optimizations are conducted. Therefore, the sequential scheme for the DILGO optimization approach for the PEMFC system synthesis/design and operation/control can be depicted as in Figure 5.10. Initially, the uncertainties (i.e. C_{UNC}^{FPS} and C_{UNC}^{WRAS}) for the FPS and WRAS and the four coupling functions (i.e. \dot{n}_{H_2} , \dot{n}_{Air} , p_{anode} , and $p_{cathode}$) which are taken into account in the SS SLUB optimization are obtained from the first DILGO iteration of the FPS and WRAS SLUB optimizations. For the first DILGO iteration the shadow price rates for the FPS and WRAS SLUB optimization sub-problems are assumed to be zero (as is done in the parallel scheme), and the coupling functions and uncertainties of other subsystems are given reasonable values. The coupling functions

and shadow price rates from the FPS and WRAS are then passed to the SS SLUB optimization. At the end of the latter, newly generated fuel and air profiles, coupling functions, shadow price rates, and the uncertainty of the SS (i.e. C_{UNC}^{SS*}) are used for the next DILGO iteration of the FPS and WRAS, and the DILGO procedure is repeated until a set of predefined limits on the SLUB optimization are reached.

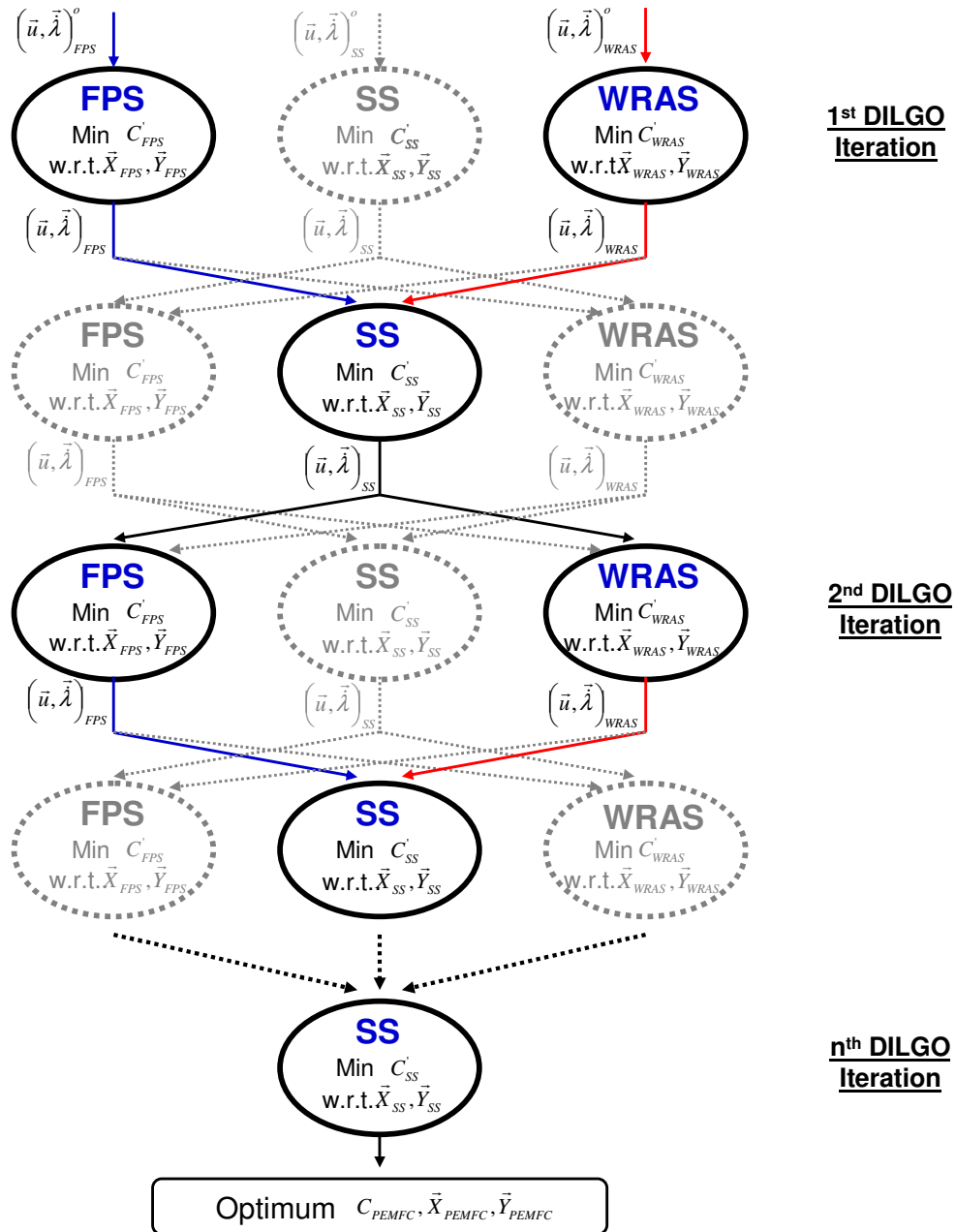


Figure 5.10 Sequential computational scheme for the DILGO (or ILGO) strategy applied to the PEMFC system.

5.5 Residential Load Profile Development

In order to conduct synthesis/design and operation/control optimization of the proposed dynamic PEMFC system, the electrical energy requirements for a single 5 kWe residential building should be established in the form of a dynamic load profile. For this purpose, daily electricity consumption profiles for a 4-person family, residential buildings in 2006 are obtained from Southern California Edison, and the mean and standard deviation of the load profiles are obtained. Daily electricity consumption profiles are depicted for 24 hours in Figures 5.11 and 5.12. The former represents winter season electrical load demands for a single residential house from December to February. The latter describes the electrical load demands from June to August.

The load profile for the system synthesis/design and operation/control optimization must reflect realistic operating scenarios for the system's entire operating span. In this research, it is assumed that the power demanded during the summer and winter seasons is the most critical for system operation because more power is required during these seasons compared to the spring and fall. Therefore, an approximate two-day load profile for the system optimization is developed from these profiles in which half of the load profile represents the summer season and the rest the winter season. During the summer season, the average peak load demand is around 1.5 kWe. Thus, all the load profiles are scaled up to meet the peak load at 5 kWe by multiplying by the scaling factor $5/1.5$.

Figure 5.13 describes the developed 48-hour load profile. In order to facilitate the calculation process, the peak point on the load profile is shifted to starting point. As seen in the figure, mean profile represents the real power consumed during the summer and winter, and the modified profile is a simplified load profile of the mean profile to be used for synthesis/design and operation/control process. In addition, as seen in Figure 5.11 and 5.12, the load profile for each day varies from day to day, and these variances should be taken into account during the optimization because the PEMFC system is expected to support all of these power demands. Thus, variations in the day-to-day load profiles are described as an uncertainty in the power demand for the mean load profile. The 48 hours modified load profile in Figure 5.13 is multiplied by 182 to express it for a whole year.

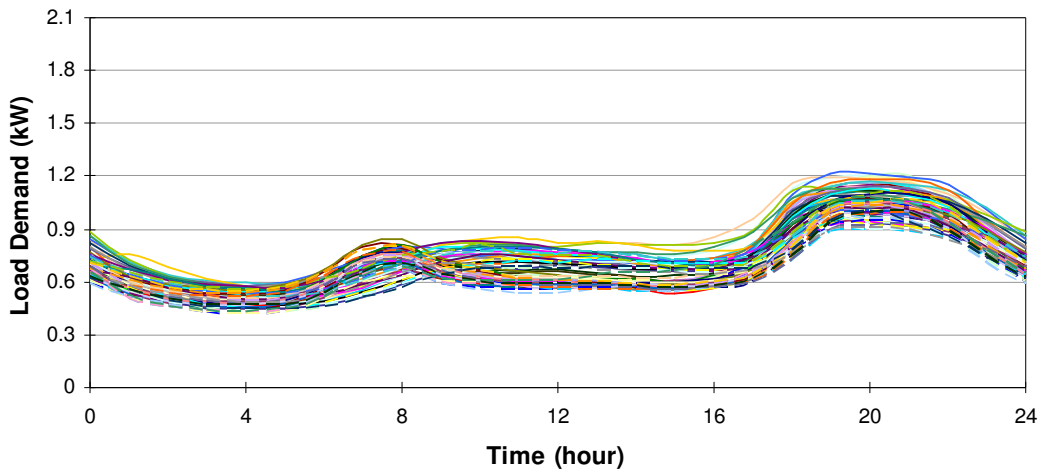


Figure 5.11 Electricity demand per day from December to February in Southern California in 2006.

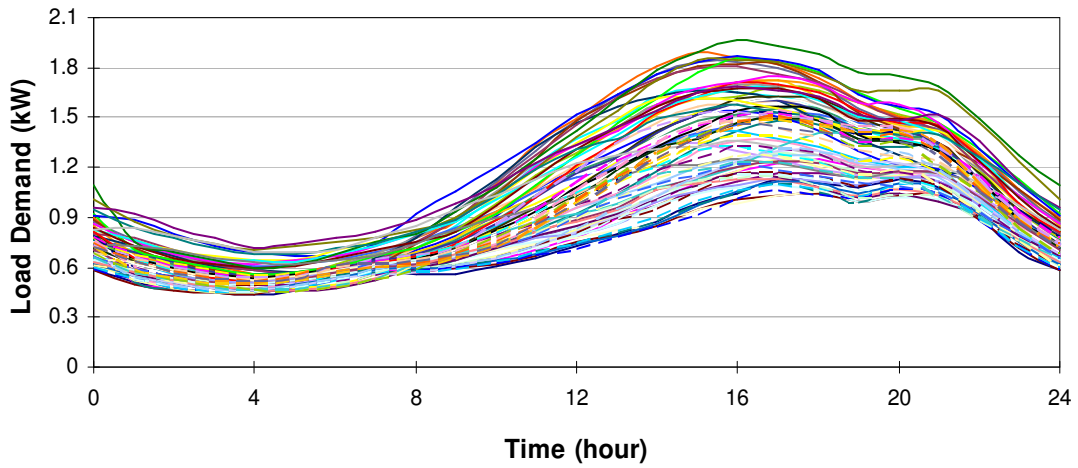


Figure 5.12 Electricity demand per day from June to August in Southern California in 2006.

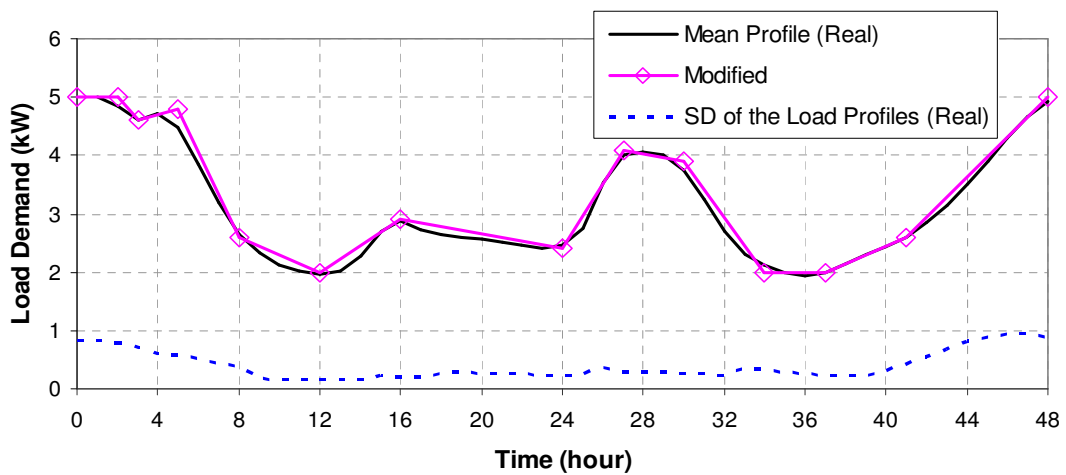


Figure 5.13 Approximated electricity demand profile and the variance of the demand profile over a 48 hours, winter-summer period in Southern California area in 2006.

CHAPTER 6

RESULTS AND DISCUSSIONS

The 5 kWe PEMFC system modeling and system descriptions are addressed in Chapter 3 and analysis methodologies (i.e. optimization strategies and uncertainty analysis) for the system have been explained in Chapter 4 and 5. In Chapter 6, results of the component-/subsystem-/system-level simulations in various dynamic and steady-state operating regimes, uncertainty effects on dynamic system performance and optimizations, and synthesis/design and operation/control optimization of the dynamic PEMFC system using the DILGO strategy are discussed. Moreover, the dynamic behavior of the PEMFC system at the optimum synthesis/design and operation/control values is presented, and system characteristics at these optimum values are discussed as well.

Note that this doctoral research has been carried out in collaboration with Wang (2008) using different approaches. Wang has focused on the control issues and architectures of the PEMFC system and the transient behavior of the system coupled with controllers employing gradient-based, single-level and multi-level optimizations for the synthesis/design and operation/control of the system optimization. In contrast, this doctoral research has focused on uncertainty effects on system synthesis/design and operation with controls, using hybrid heuristic/gradient-based optimization, i.e. SMBO, along with single- and multi-level as well as single- and multi-objective optimizations for system synthesis/design and operation under uncertainty. Results from Wang's work and this work are compared and discussed in the latter part of this chapter.

6.1 Validation and Characteristics of each Subsystem

The proposed 5 kWe PEMFC system consists of three subsystems and each subsystem is composed of several components as described in Chapter 3. The first step of

component modeling is to determine suitable technology for the component design. For example, there are several different reforming methods as introduced in Section 3.1 of Chapter 3, and of these, the steam methane reforming process is applied to this PEMFC system. Once a technology for a component is determined, it is necessary to find its appropriate fundamental physical/chemical models which are obtained empirically as introduced in Chapter 3. These kinds of models are usually expressed in a generalized or non-dimensionalized form such as the rate of reaction, which in its generalized form is a function of reactor volume (or catalyst weight) and reaction time. Similarly, the heat transfer model, which is usually expressed in terms of Nusselt number and Reynolds number, is a function of the heat transfer coefficients and flow/geometry characteristics. These physical/chemical models are, then, applied to specific geometries and operating conditions which are determined by system designers.

To make sure whether or not these physical/chemical models described correctly the component design and whether or not the computational model represents realistic system or component behavior, one must always validate the computational models by comparing with the original experimental data with which the models are developed or with some other experimental results. In this section, the validations for some of the major component models are presented by comparing with such data. In addition, the characteristics of individual components and subsystems are discussed as well.

6.1.1 SS Model

The transient PEMFC stack model is developed based on the single cell model of Ceralo, Miulli, and Pozio (2002). Figure 6.1 shows a comparison of the simulated and measured cell voltage for different pressures at given steady-state conditions (i.e. an operating temperature of 343 K and an inlet air flow rate of 1500 scc/min). For this comparison, the anode side pressure is fixed at 1 bar and 2 bar for 1 bar and 3 bar of the cathode side pressure, respectively. As seen in the figure, the predicted cell voltages of the model show good agreement with the experimental results which are from the reference. The dynamic response characteristic of the cell model is also compared with the reference as shown in Figure 6.2. For this comparison, the operating temperature is assumed at 343 K and the cathode and anode side pressures are 3 bar and 2 bar, respectively. In addition, the

air inlet flow rate and hydrogen inlet flow rate are 1500 scc/min and 1400 scc/min, respectively. Figure 6.2 depicts the dynamic response of the cell output voltage as a result of a sudden change of cell current density from 0.5 A/cm² to 0 A/cm². The simulation predicts almost exactly same response time and magnitude as the experimental results from the reference. From these comparisons between model predictions and experiments at steady state and dynamic operation, it can be concluded that the single PEM fuel cell model developed describes the characteristics of real PEM fuel cell fairly well. Note that in most of cases dynamic responses of cell voltage for a sudden cell current drops show overshoot generally but the overshoot does not appear in Figure 6.2 for these given operating condition. However, it can be more clearly observed in Figure 6.5 (see Figure 6.5).

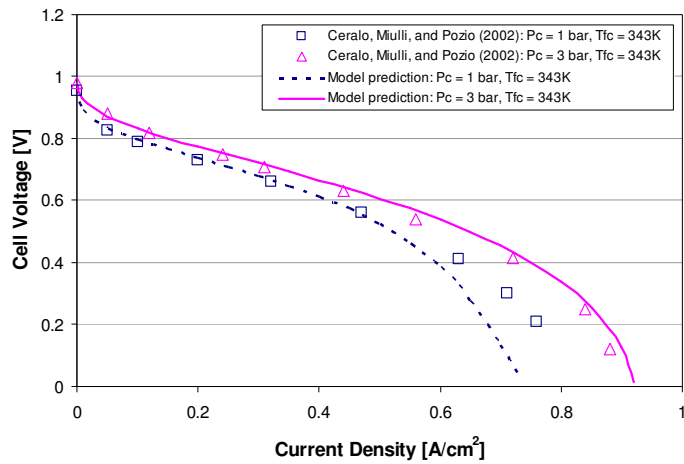


Figure 6.1 Comparison of the simulated and measured cell performance at steady-state.

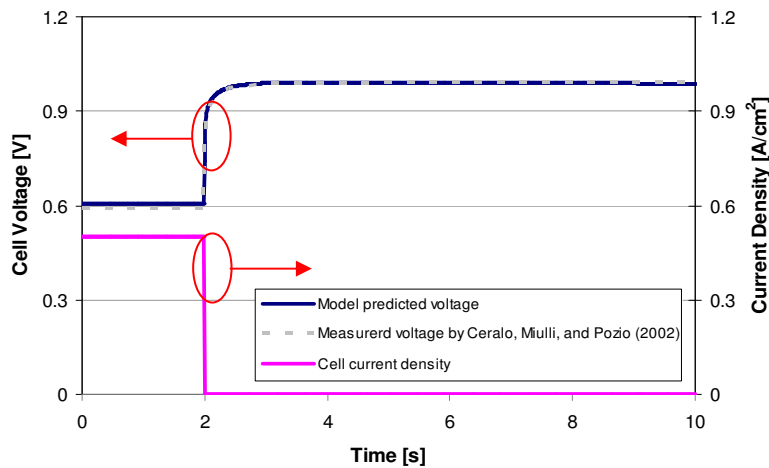


Figure 6.2 Comparison of the simulated and measured cell dynamic response.

There are several key parameters (e.g., cell temperature, pressure, humidity, hydrogen and air flow rates, fuel utilization, etc.) which determine the PEMFC response and cell efficiency. Among them, cell temperature and operating pressure are the most important parameters, and their effects on cell performance are described in Figure 6.3 and 6.4 in terms of polarization curve. For these curves, the cathode side and anode side pressures are fixed at 3 bar and 2 bar, respectively. Also, an air inlet flow rate to the cathode side of 1500 scc/min is assumed. As seen in Figure 6.3 and as expected, the higher temperature is, the higher cell current density that can be achieved for the same voltage.

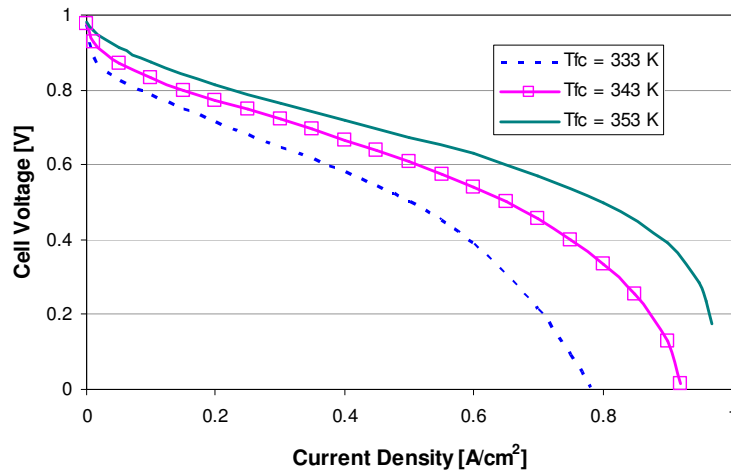


Figure 6.3 Influence of the cell temperature on the polarization curve.

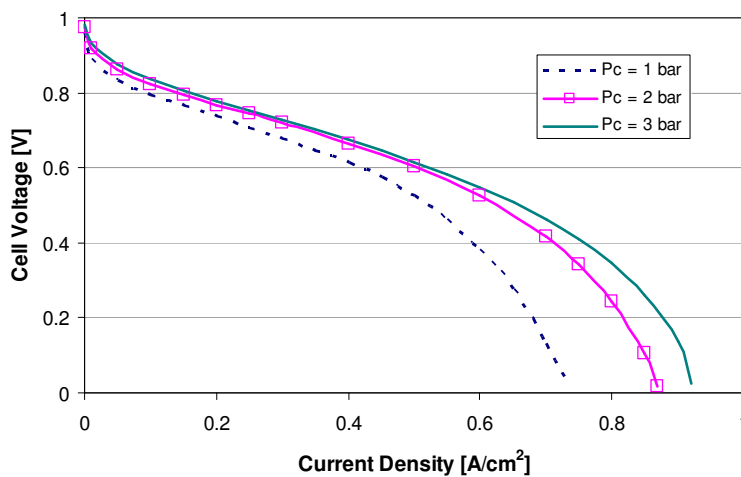


Figure 6.4 Influence of the operating pressure on the polarization curve.

Figure 6.4 presents the effect of operating pressure on cell performance. For this parametric study, cell temperature is fixed at 343 K; and the cathode side pressure is equal to the anode side pressure. As with the temperature effects on cell performance, the more the pressure increases, the greater the cell current density for the same cell output voltage. However, the increase from 2 bar shows much less of an improvement than from 1 bar to 2 bar.

The dynamic response of the single cell model developed to a sudden cell current change from 0.5 A/cm^2 to 0.35 A/cm^2 is shown Figure 6.5. The cell temperature is assumed to be 343 K, and the cathode side and anode side pressures are assumed to be 3 bar and 2 bar, respectively. For these given operating conditions, dynamic cell voltage shows overshoot for sudden cell current density drop as seen in the figure. Cell voltage can be expressed in terms of cell current density using the equation (3.37). Equation (3.23) describes the cell current density, and the charge storage term in the equation cause dynamic response behaviors including the overshoot. If electrolyte conductivity increases with the water contents the proton concentration also increases. Therefore, voltage overshoot appears to sudden current drops. The graph shows that it takes around 55 seconds to reach a steady-state output cell voltage of 0.705 V.

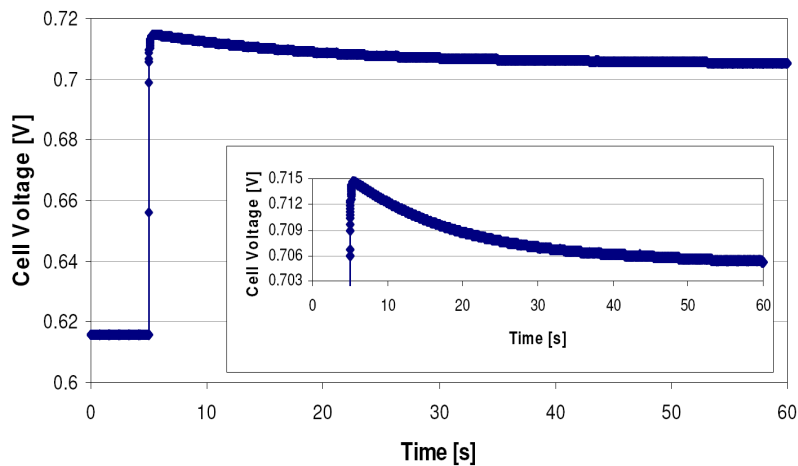


Figure 6.5 Voltage response due to a change of current density 0.5 A/cm^2 to 0.35 A/cm^2 .

From the validation and parametric study of the PEMFC model developed, it can be concluded that the stack model developed describes the behavior and characteristics of

the PEMFC at steady-state and even dynamic operation well enough for the purpose of the system simulation which are of important here.

6.1.2 FPS Model

A number of kinetic models and heat transfer models are used for developing the chemical reactors, a steam generator, and the heat exchangers in the FPS. In this section, validations of the SMR, HTSR/LTSR, PrOx, and the compact heat exchanger are presented and some characteristics of each is then discussed.

6.1.2.1 Validation of the FPS

SMR Model

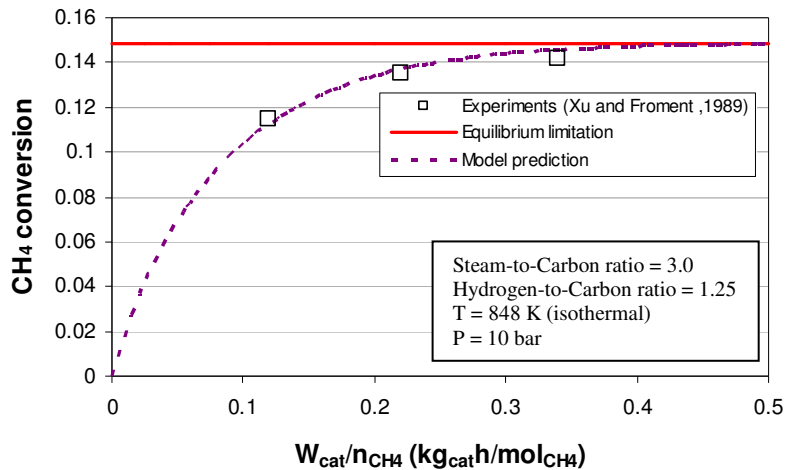


Figure 6.6 Conversion of methane according to variation in space time; the temperature (isothermal) is 848 K and the pressure at 10 bar.

The kinetic model of steam methane reforming by Xu and Froment (1989) is used for the SMR design. Xu and Froment developed the kinetic models (i.e. equation (3.46) and (3.44)) based on experimental data which is obtained in terms of conversion rate of each species and the space velocity. Figure 6.6 shows the validation of the SMR model with the reference. For this comparison, the SMR model developed is assumed to have the same operating constraints as the reference: the steam-to-carbon ratio is 3.0 and the hydrogen-to-carbon ratio is 1.25. As seen in Figure 6.6, the model predictions correspond

well to the reference data and shows that the methane conversion increases as space time increases and finally reaches the equilibrium limit. Note, that the term “space time” is used in the chemical engineering literature to designate the ratio between the fuel flow rate and the reactor size, the latter of which is represented here by the weight of the catalyst, W_{cat} . The inverse of this ratio is proportional to the reaction rate.

HTSR Model

As addressed in Section 3.3.3.1, Borgars and Campbell’s (1974) kinetic model obtained from Ettouney, Shaban, and Nayfeh (1991) has been used for the HTSR design. Ettouney, Shaban, and Nayfeh validate their model by comparing the simulation results with data collected from their pilot scale reactor, and the comparison shows good agreement between them. However, they do not provide values of the main parameters such as the amount of catalyst loaded and the operating pressure so that it is impossible to compare the HTSR model which is developed in this work with these references. Thus, in order to verify the HTSR model developed, Chen et al. (2006) is used as a reference, and a comparison of the results at steady-state are presented in Table 6.1. At the same inlet flow rate, pressure, and temperature as the reference, the differences between the outlet flow rates predicted by the model used here and the reference are less than 3.4%.

Table 6.1 Comparison of predicted outlet flow with those of Chen et al. (2006): Pressure=1 atm, T=675 K.

Constituent	Inlet flow rate (mol/s)	Outlet flow rate (mol/s)		Difference (%)
		Chen et al. (2006)	Model prediction	
CH ₄	2.500E-04	2.500E-04	2.500E-04	-
H ₂ O	1.497E-02	1.183E-02	1.159E-02	2.1
CO	4.567E-03	1.083E-03	1.120E-03	3.4
CO ₂	3.183E-03	6.667E-03	6.562E-03	1.6
O ₂	5.000E-04	5.000E-04	5.000E-04	-
H ₂	2.017E-02	2.350E-02	2.354E-02	0.2
N ₂	1.353E-02	1.353E-02	1.353E-02	-

LSTR Model

From a preliminary comparison of several different kinetic models of the low-temperature water-gas shift reaction listed in Table 3.6, the model of Choi and Stenger (2003, 2005) shows better performance than the other models. Therefore, their kinetic model with an effectiveness factor of 0.26, which is obtained by Lin et al. (2006)

empirically, is used for the LTSR model in this research. Figure 6.7 compares the predicted CO conversion by the LSTR developed here with those of Choi and Stenger (2003, 2005). As seen in the figure, the predicted CO conversion corresponds well to the experimental data of Choi and Stenger. From the figure, one can recognize a general characteristic of the water-gas shift reaction: as the feed-water flow rate increases, CO conversion performance increases as well.

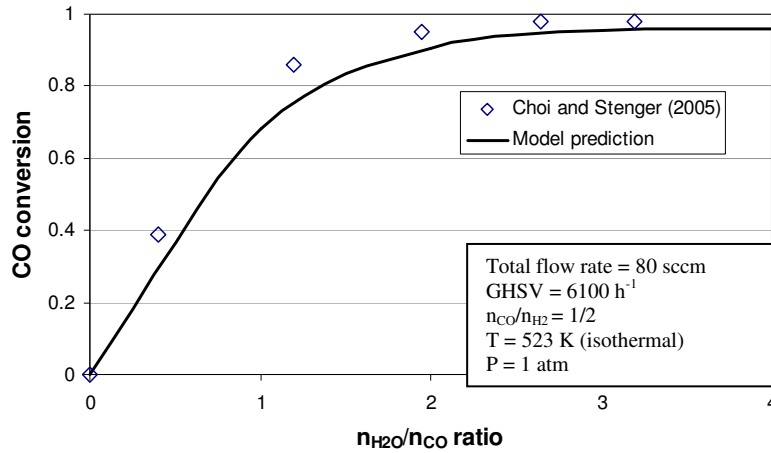


Figure 6.7 Comparison of predicted CO conversion with those of Choi and Stenger (2005): flow CO/H₂ ratio of 1/2, pressure of 1 atm, and operating temperature of 523 K.

PrOx Model

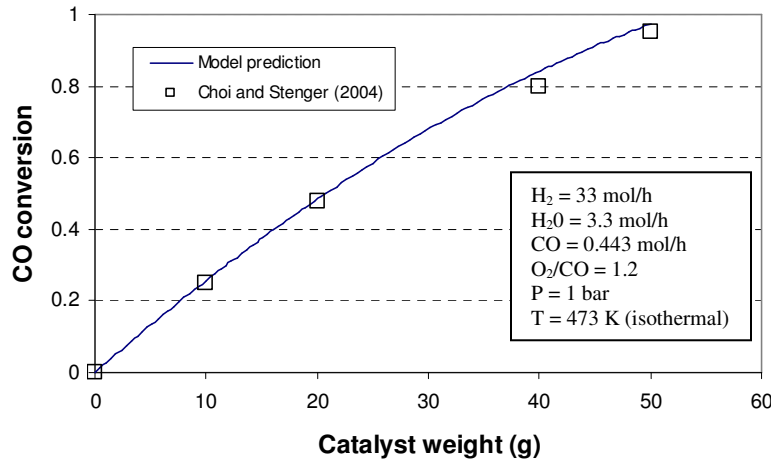


Figure 6.8 Comparison of the predicted CO conversion of the model with those of Choi and Stenger (2004) for different catalyst loadings; a O₂/CO flow ratio of 1.2, a pressure of 1 bar, and an operating temperature of 473 K.

For the PrOx reactor design, the kinetic model of Choi and Stenger (2004) has been used with one additional assumption, namely, that the effectiveness factor of 0.26 obtained and used by Lin et al. (2006) for the water-gas shift reaction. Figure 6.8 presents the comparison of predicted CO conversion with those of the reference (Choi and Stenger, 2004), and the comparison shows good agreement. The reference data is the simulation result of a reactor model developed by Choi and Stenger based on their kinetic model.

HX Model

A compact heat exchanger model developed here is based on the heat transfer models of Kim (2002) (equations (3.82) and (3.83)). Figure 6.9 compares the predicted heat transfer performance with those of Kim (2002) as a function of different face velocities which are inlet air flow velocities. UAF represents the heat transfer capacity or performance and it can be non-dimensionalized to the Nusselt number. U is the overall heat transfer coefficient (W/m^2K), A is the heat transfer surface area (m^2), and F is the correction factor (0.9 of correction factor is assumed). In particular, this comparison shows good agreement in the low face velocity range (a face velocity of 1m/sec corresponds to a Reynolds number of 1000 in this comparison). Because the general operating range of the PEMFC system developed here is in a range of 100~1000 Reynolds number, the heat exchanger model developed in this research has high accuracy for describing a real compact heat exchanger.

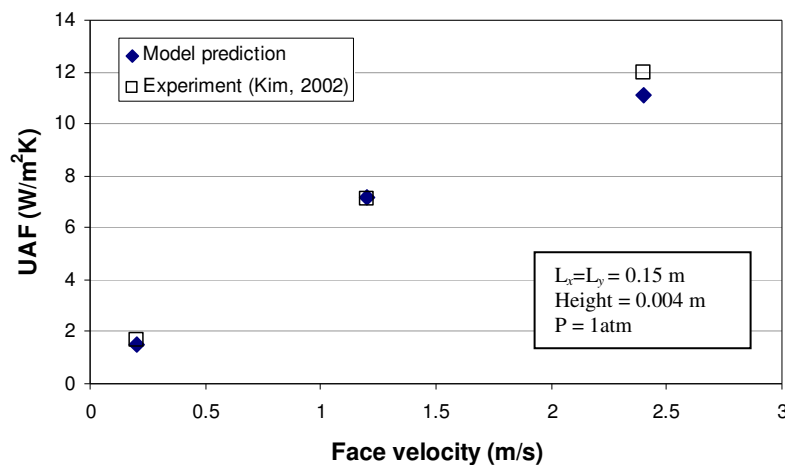


Figure 6.9 Comparison of the predicted heat transfer performance with those of Kim (2002).

6.1.2.2 Characteristics of the FPS

Some of the characteristics of each reactor are presented below. The given operating conditions and specifications of the each reactor are listed in Table 6.2. Chemical reactions are limited by stable chemical equilibrium. Of course, local thermodynamic conditions (temperature and pressure) as well geometry determine where this limit occurs or if it can even be reached. The effect of a change in conditions on chemical equilibrium is a consequence of the 2nd Law as described by Le Chatelier's principle i.e. when a system in a state of chemical equilibrium experiences a change in concentration, temperature, and/or pressure, the equilibrium shifts to minimize the change.

Table 6.2 Operating conditions and reactor specifications for the SMR, HTSR, LTS, and PrOx reactors.

SMR	Steam to methane ratio (S/C)	3.25
	Inlet temperature	936.5 K
	Inlet pressure	1.5 bar
	Fuel feed rate (methane)	70 mol _{CH₄} /h
	Tube length	1 m
	Tube number	10
	Tube diameter	0.025 m
HTSR	ϕ : 20 mm; length: 0.5 m; tube number: 12	
LTSR	ϕ : 20 mm; length: 1.0 m; tube number: 12	
PrOx	ϕ : 20 mm; length: 0.5 m; tube number: 12	
	Oxygen feed rate	O ₂ /CO = 1.5

SMR

It takes a long reaction time at the given conditions to reach stable chemical equilibrium. To overcome the slow reaction rate, catalyst is used in real reactors to improve the reaction performance. In this model, a nickel type catalyst, Ni/MgAl₂O₄, is selected and used in the kinetic modeling. The reaction characteristics for steam-methane reforming is a function of the operating conditions (temperature, steam-to-carbon ratio (S/C), and pressure) and the amount of catalyst loaded.

In particular, the steam-methane reforming reaction is favored with high temperature and low pressure conditions by Le Chatelier's principle. 3-D graphs, Figure 6.10 (a) and (b), show the effects of temperature, S/C ratio, and pressure on methane conversion for the given specification of the SMR as addressed in Table 6.2. The final (i.e. exit) methane conversion of the SMR is described as a function of S/C ratio and pressure in Figure 6.10 (a) and as a function of S/C ratio and temperature in Figure 6.10 (b). As seen in the figures, methane conversion increase as S/C, and/or temperature

increase(s). However, methane conversion decreases as operating pressure increases as predicted by Le Chatelier's principle.

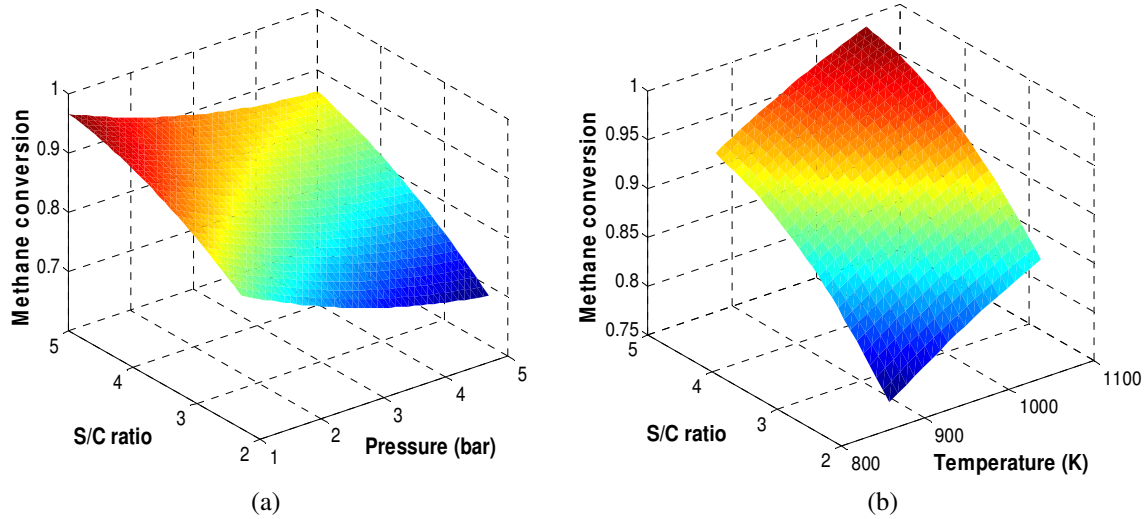


Figure 6.10 Steam-to-carbon (S/C) ratio, pressure, and reforming temperature effects on the steam reforming.

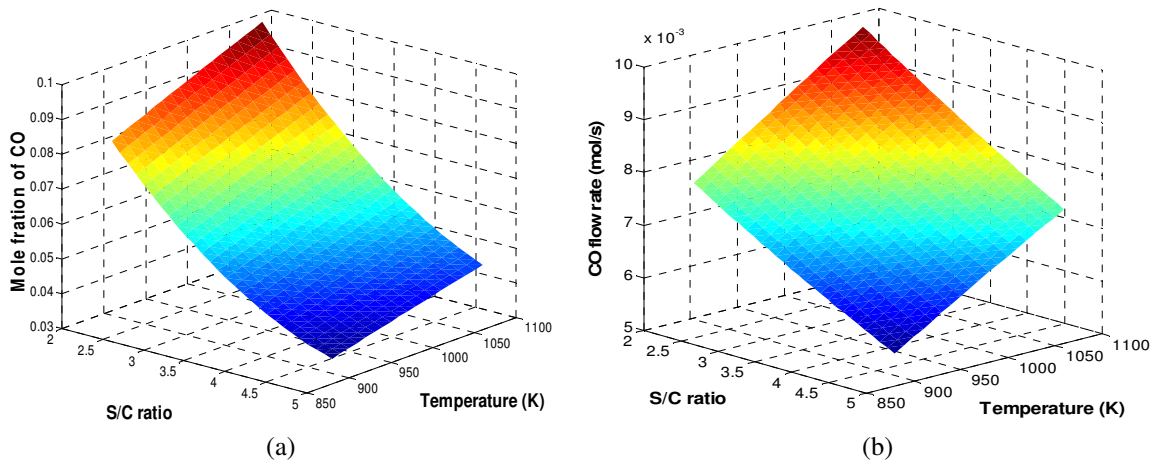


Figure 6.11 Steam-to-carbon (S/C) ratio and temperature effects on CO generation in the SMR.

The main objective of the FPS is to supply hydrogen rich gas to the SS, and the gas should be very low in CO concentration (i.e. less than 10 ppm). Therefore, CO generation in the SMR for different S/C ratios and temperatures is also evaluated and is presented in Figure 6.11 (a) and (b). As seen in Figure 6.11(a), the mole fraction of CO (i.e. CO generation) decreases as the S/C ratio increases. On the other hand, it increases as the operating temperature increases. One may think that the mole fraction of CO

decreases at higher S/C ratio because the un-reacted steam increases the total amount of the reformate gas. That is correct, but the more steam is supplied, the more the water-gas shift reaction advances which makes the mole fraction of CO decrease. Figure 6.11 (b) presents the molar flow rate of CO for same conditions as that of Figure 6.11 (a) and shows that the molar flow rate of CO decreases as the temperature decreases and the S/C ratio increases.

From Figure 6.10 and 6.11, one can conclude that the SMR favors high temperatures and S/C ratios and low operating pressures in order to maximize hydrogen production for a given set of conditions. However, lower temperatures favor minimizing CO generation. Thus, a system-level optimization should be carried out to determine the optimum S/C ratio, temperature, and pressure and is discussed later in this chapter.

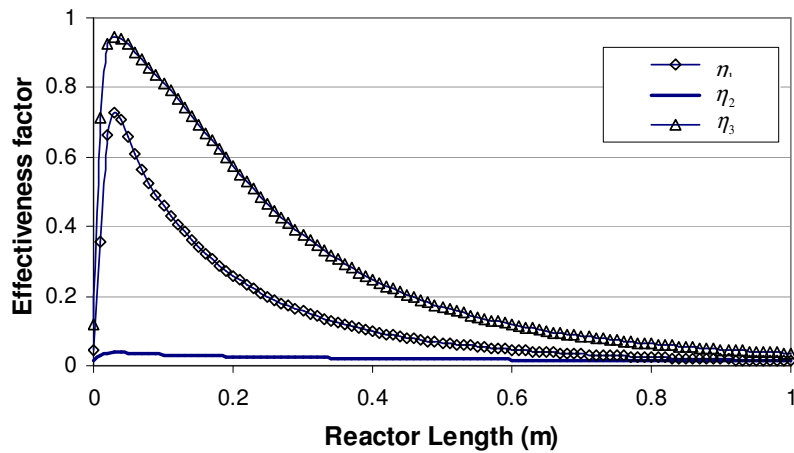


Figure 6.12 Effectiveness factors for each of the reaction mechanisms.

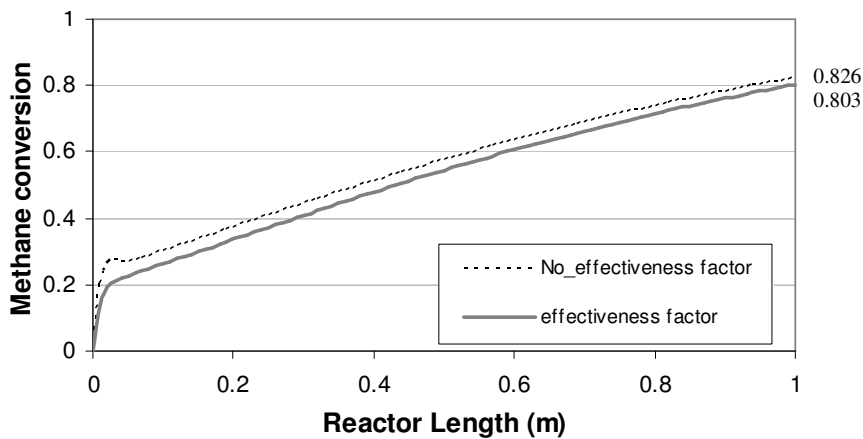


Figure 6.13 Effect of effectiveness factor on SMR performance.

The three effectiveness factors η_i (equation (3.58)) for the three SMR reaction mechanisms (equations (3.43) to (3.45)) are plotted as a function of axial position in Figure 6.12. The effectiveness factor of the third reaction, i.e. the overall reaction, shows the largest values while that for the water-gas shift reaction shows by far the least. The effectiveness factors are related to the mole fractions of each species and reduce the intrinsic reaction rate which is assumed to be 100% effective to something less than this due to diffusion limitations associated with each reaction mechanism. The influence of these factors on the chemical reaction rate and the conversion of methane in the SMR are shown in Figure 6.13. At 0.1 m, the difference in the methane conversion rates between the intrinsic reaction rate and that for which diffusion limitations are taken into account is around 20%, while that at the end of the reactor is around 2.9%.

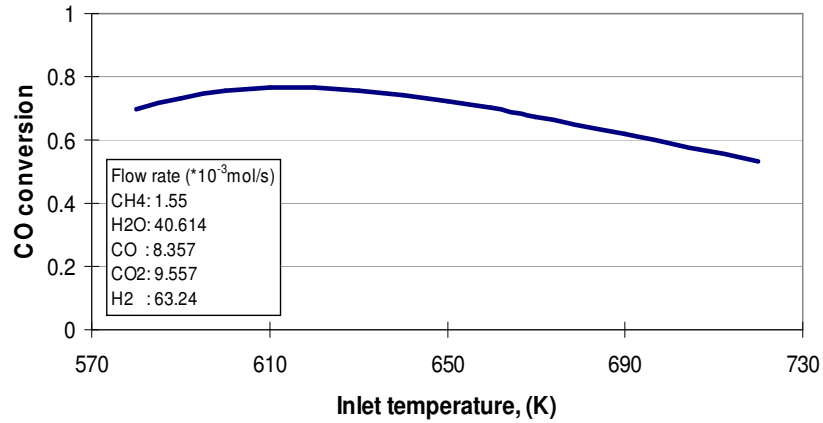
HTSR/LTSR and PrOx Reactors

The performance of the HTSR, LTSR, and PrOx reactor is shown in Figure 6.14 in terms of the conversion rate of CO versus the inlet reformat gas temperature. In order to verify the effect of the inlet temperature on CO removal performance, other factors inside the reactors (e.g., the reformat gas flow rate and pressure, the steam-to-methane ratio, the size of the reactors) are kept constant.

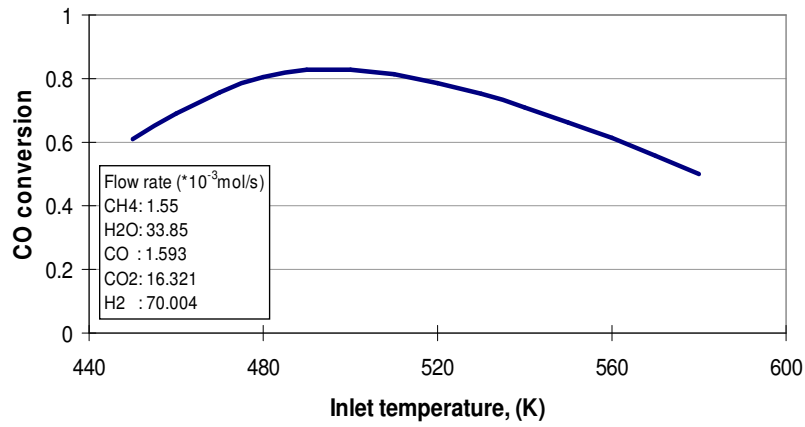
In the HTSR/LTSR, the reaction rate of the water-gas shift reaction increases as the temperature increases. However, the equilibrium limitation of the process is lower at higher temperature. Thus, there exists an optimal temperature range, which provides the highest CO conversion for which the reactors should be designed.

As shown in Figure 6.14(a), the maximum conversion rate of CO is less than 78% in the HTSR at around 620 K when the iron based catalyst mentioned earlier is used. In the LTSR model, the maximum conversion of CO (83%) occurs at around 495 K (Figure 6.14(b)), while, in the PrOx reactor, CO is removed almost completely over a range from 440 K to about 490 K for the given conditions. However, after the temperature reaches 490 K, CO is generated by the reverse water-gas shift reaction which dominates the whole reaction process. In fact, after about 590 K, the CO conversion drops to 0%. Thus, it is important to size the PrOx reactor properly in order to control the maximum conversion range. Of course, higher temperatures cause higher hydrogen oxidation.

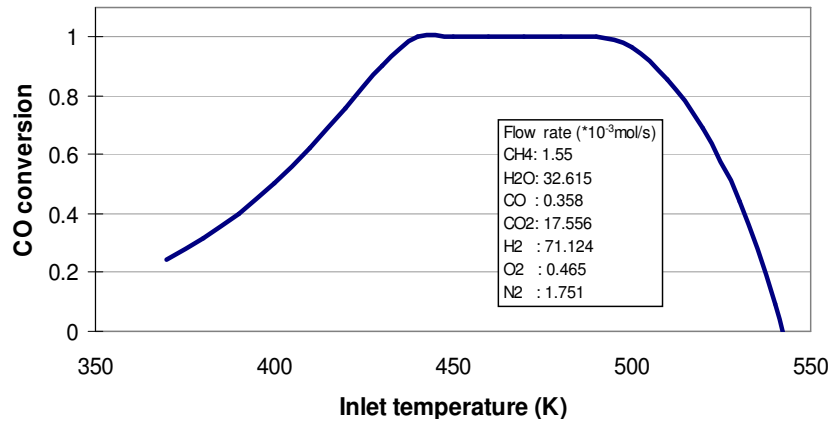
Therefore, the beginning point of complete CO conversion is the most favorable operating point for the PrOx reactor.



(a) HTSR



(b) LTSR



(c) PrOx reactor

Figure 6.14 Conversion of CO in the HTSR/LTSR/PrOx reactor as a function of the inlet temperature of the reformat gas.

6.1.3 WRAS Model

The fundamental concept of the WRAS is explained in Section 3.4 of Chapter 3. Un-optimized values for the 6 decision variables of the WRAS are assumed for validation of the WRAS, and they are listed in Table 6.3. In addition, a gear ratio (equation (3.102)) of 8 is assumed for coupling the motor and compressor shaft.

Table 6.3 Assumed decision variable values for the validation of the WRAS model developed here.

Compressor		Expander		Motor	
$p_{design}^{Compressor}$	2.2	$p_{design}^{Expander}$	2.2	Tq_{design}^{Motor}	1.0
$\dot{m}_{design}^{Compressor}$	0.1	$\dot{m}_{design}^{Expander}$	0.1	rpm_{design}^{Motor}	1000

Table 6.4 Comparison of predicted performance of the WRAS with those of Osscanson (2003).

		Osscanson (2003)	This work
Unit		Opcon OA 1050-1032	Off-designed WRAS
Application		Transportation (60 kW)	Residential (5 kW)
Max. compressor efficiency		71%	70% (70% of expander efficiency)
Comparison (at the max. compressor efficiency)	Compression ratio	2.8	
	Expansion ratio	2.3	
	Air mass flow rate (at the max. compressor efficiency)	60 g/s	6 g/s
	Net power consumption by the unit (parasitic power)	6 kW	595 W
	Parasitic power/Gross system power output	10%	11.1%
	Energy saving for the compressor work	33.3%	32.6%

Osscanson (2003) published results for Opcon Autorotor AB's twin screw compressor and expander units (i.e. an Opcon OA 1050 for the compressor and an Opcon OA 1032 for the expander) applicable to fuel cell application. Results predicted with the model developed here and the experiment results of Osscanson are compared in Table 6.4. This comparison is based on the maximum compressor efficiency point which corresponds to a mass flow rate of 60 g/s on the map of Osscanson (2003) and to 6 g/s on the map of the present research. At this condition, the compressor of Osscanson's system requires 9 kW; and 3 kW of that is recovery by the expander unit. Thus, 33.3% of the energy for the compressor can be saved by the expander, and as a result, there is a 5%

improvement in the overall fuel cell system efficiency. The preliminary test of the WRAS model developed here shows results similar to those of Osscarnson. At the given condition as addressed above, the compressor needs 881 W, and 287 W can be recovered by the expander unit. Thus, 32.6% of the energy to the compressor is saved by the expander.

6.2 FPS Synthesis/Design and Operation/Control Optimization under Uncertainty

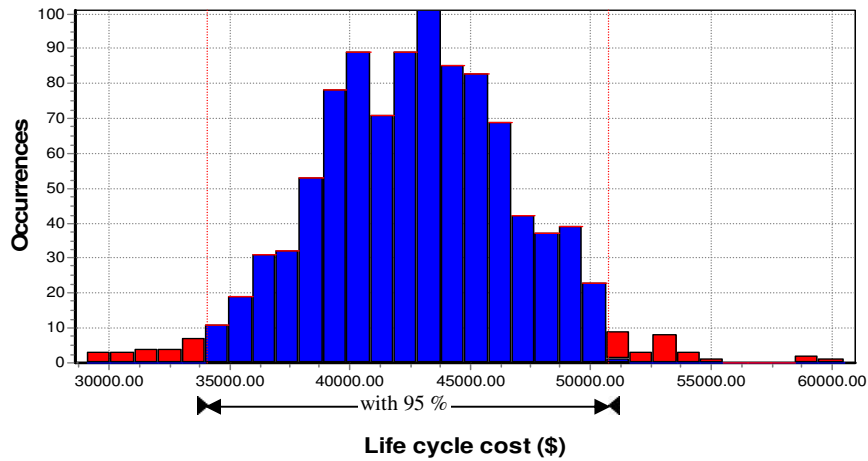
One of the main objectives of this doctoral research is to determine an appropriate strategy for describing uncertainty in the dynamic energy system synthesis/design and operation/control optimization problem. For this purpose, the response sensitivity analysis (RSA) method is chosen here after evaluating it and a number of other methods to determine which is the most suitable for describing uncertainties in energy system analysis and optimization problems. This was done in a preliminary way in Chapter 4 using the dynamic SMR synthesis/design problem. A more extensive evaluation of the RSA method is done here by applying it to the dynamic FPS synthesis/design and operation/control optimization problem. Results are presented in following sections showing its efficiency and accuracy. Because of this, the RSA method is also used as the uncertainty analysis method for the dynamic PEMFC system optimization problem for which results are presented later in this chapter. In addition, the multi-objective optimization for energy systems addressed in Chapter 5 is carried out here using the FPS optimization problem. These results are also presented and discussed in the following sections.

6.2.1 RSA Method Evaluation

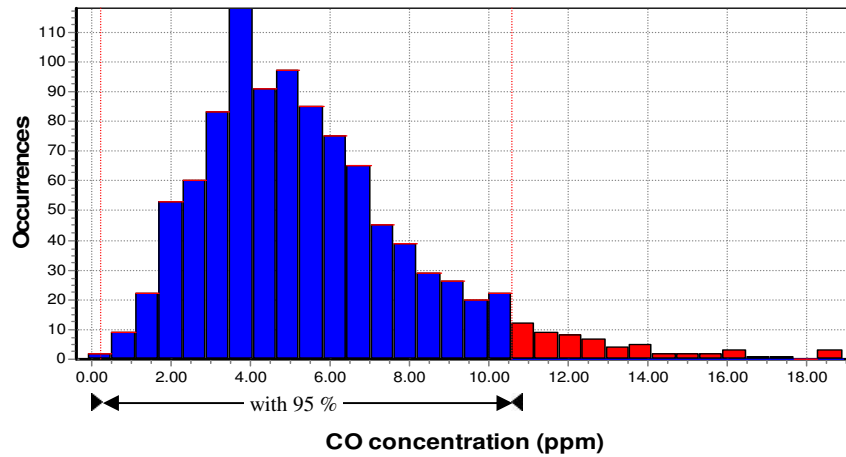
Indirect uncertainty sources (i.e. load profiles and cost functions) play an important role in a dynamic system synthesis/design and operation/control optimization, and both types of uncertainties are considered in this research. In order to validate the proposed RSA method, uncertainty analysis results of the FPS using the RSA method are compared to the results found by a MCS. This comparison is carried out at the optimum

solution which is presented in following section, and the uncertainty factors and their assumptions for the FPS are found in Table 5.4 of Chapter 5.

Figure 6.15 shows the uncertainty analysis results for the outputs of the FPS using a MCS. The uncertainties of the outputs, i.e. the total life cycle cost and the CO concentration of the reformate gas, are estimated at the optimal synthesis/design and operation/control point of the FPS. 1000 simulation are used to obtain the distributions. The total life cycle cost shows normal distribution characteristic while the CO concentration shows a left-skewed characteristic. The red area on the graphs represents a 95% confidence interval ($\pm 2\sigma_{M_j}$) for the system response M_j (i.e. the CO concentration or the total life cycle cost).



(a)



(b)

Figure 6.15 Probabilistic distributions of the total life cycle cost and the CO concentration of the FPS found by MCS.

Uncertainty analysis results from the RSA are compared to those from the MCS in Table 6.5. As seen in the table, there is little difference between the results from the RSA method and the MCS, i.e. less than 1%. The uncertainty analysis results found from the RSA method show significant fidelity to the more precise results from the MCS. Moreover, the RSA method finds this level of fidelity with only three simulations in parallel while the MCS requires at least 1000 simulations.

Table 6.5 Comparison of the uncertainty analysis results between by the MCS and the RSA method.

	Standard deviation		Number of simulations
	Life cycle cost (\$)	CO concentration (ppm)	
MCS	4402.0	2.776	1,000
RSA	4427.8	2.752	3 simulations in parallel
Difference (%)	0.59	0.86	-

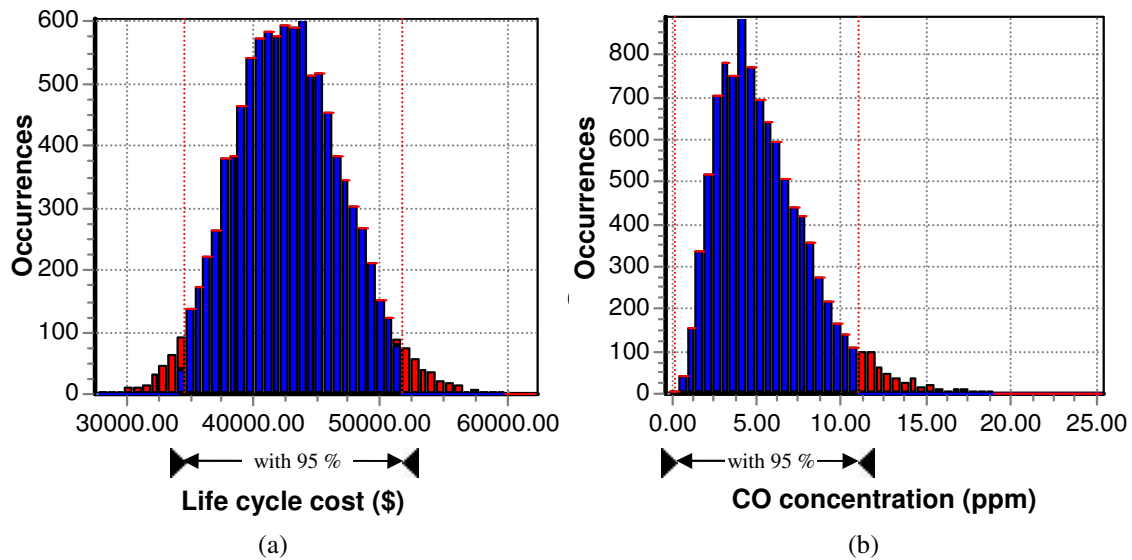


Figure 6.16 The probabilistic distributions of the total life cycle cost and CO concentration of the surrogate model of the FPS found by the MCS with a sampling of 10,000.

Using the MCS, it took around 30 hours using dual-core, 3.2 GHz 2G RAM PC, to develop the graphs in Figure 6.15, but even then they do not show the smoothness of the probabilistic distributions one would expect because the number of samples (i.e. 1,000) is not enough to describe the PDF exactly. In order to get more detail probabilistic distributions, two 2nd-order fully quadratic polynomial correlation equations for the CO concentration and life cycle cost (with a 99.99% coefficient correlations (R^2)) are obtained as a function of the uncertainty of the cost functions and the load profile using the

response surface methodology described in Chapter 4. The additional graphs in Figure 6.16 present the simulation results of the surrogate models of the CO concentration and life cycle cost using the MCS with 10,000 samples. One can confirm that life cycle cost shows highly normal distribution characteristics as seen in Figure 6.16 (a) and CO the concentration has left-skewed distribution characteristics as seen in Figure 6.16 (b).

If uncertainties with respect to the CO concentration are not considered in the FPS synthesis/design and operation/control optimization, the optimization results just satisfy the constraint placed on the CO concentration of less than 10 ppm, i.e. the CO concentration is at this upper limit of 10 ppm. However, this is simply a mean value which if placed in the context of a probability distribution such as given in Figures 6.15(b) and 6.16(b) would have the effect of shifting the PDF to be centered on 10.00 implying that the confidence level of actually meeting the value of 10 or less would be quite low. However, as seen in Figure 6.15 (b) and 6.16 (b), when uncertainties are considered at the outset a 95% confidence interval of the mean value is achieved so that the FPS satisfies the limit of less than 10 ppm with a high level of certainty since the mean of the CO concentration is around 5.15 in this case. Therefore, the FPS system synthesis/design and operation/control optimization can obtain a better solution which can avoid possible system failure by taking into account uncertainties in the constraints.

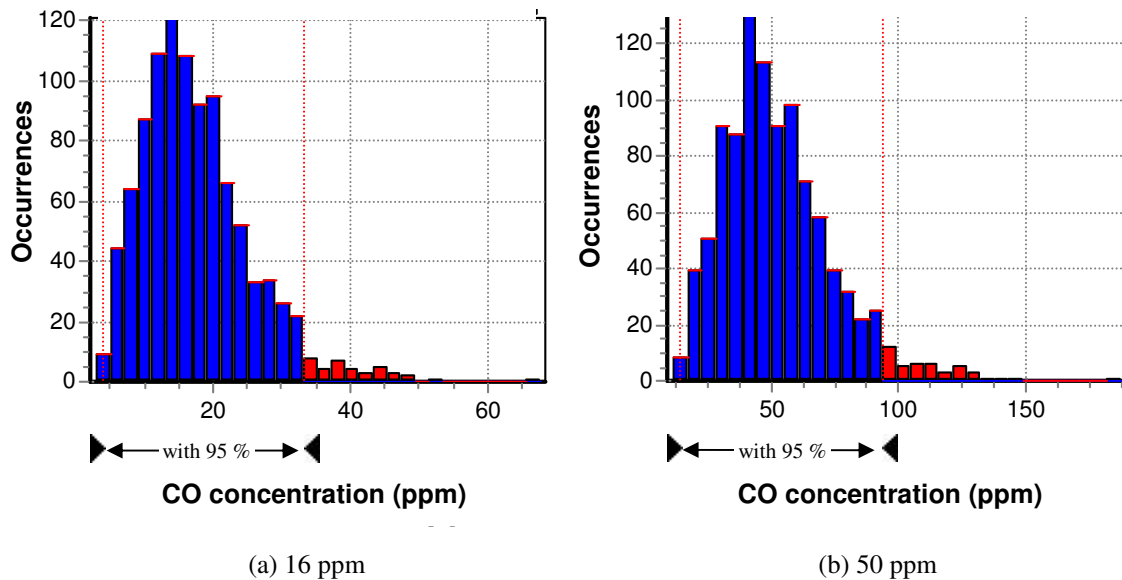


Figure 6.17 Probabilistic distribution for different mean values of the CO concentration for the FPS found by MCS.

To make sure of the distribution characteristics of the CO concentration, simulations as was done for Figure 6.15 have been carried out for two different cases have different mean values of the CO concentration. Figure 6.17 (a) is the result for the case of 16 ppm as the mean CO concentration, and Figure 6.17 (b) is for the case of 50 ppm as the mean CO concentration. For this comparison, all synthesis/design and operation decision variables are assumed equal to those of the simulation for Figure 6.15 except the length of the PrOx reactor. By adjusting the length of the reactor, different CO concentrations can be achieved for this comparison. As seen in Figure 6.15 (b) and Figure 6.17, the distribution of the CO concentration of the FPS shows the same trend regardless of the mean value. Standard deviations of Figure 6.17 (a) and 6.17 (b) are 7.69 ppm and 20.87 ppm, respectively, and the RSA method predicts standard deviations of 7.45 ppm and 20.49 ppm, respectively. These comparisons also show less than 3.2% of difference between that by the MCS and that of the RSA method. Thus, these results verify that the RSA method is a very efficiency and accurate method for describing the uncertainties of dynamic energy system analysis and optimization problems.

6.2.2 Multi-Objective Optimization

The synthesis/design and operation/control optimization of the FPS under uncertainty is carried out using a SMBO algorithm (i.e. the SEQOPT). All decision variables are listed in Tables 5.2 and 5.3 of Chapter 5, and the definitions of the uncertainty factors are listed in Table 5.4. The dynamic system optimization is conducted based on the configuration of the FPS proposed in Figure 5.6.

The total life cycle cost of the FPS (i.e. equation (5.18)) is generally used as a single objective function and is composed of capital cost, C_{FPS} , and operating cost, C_{oper} , which is directly proportional to the system efficiency. Thus, the total life cycle cost optimization problem of the FPS can be treated as a multi-objective function (i.e. C_{FPS} and C_{oper}) problem. In this section, this multi-objective approach for the dynamic FPS synthesis/design and operation/control optimization problem is investigated and compared to the results of the single-objective (C_{total}^{FPS}) approach. For the multi-/single-objective optimizations of the FPS, uncertainties in the objectives are ignored in order to facilitate the calculations. This assumption is reasonable for the FPS as shown in Chapter 5 because the mean values of the

optimum total life cycle cost of the FPS show little difference whether or not the uncertainty term (i.e. equation (5.21)) is considered in the objective functions, i.e. preliminary tests show less than a 0.2% difference between them and this small difference can be attributed to the fact that the distribution characteristic of the total life cycle cost distribution is highly normal as shown in Figures 6.15 (a) and 6.16 (a). Nonetheless, throughout the optimization process, uncertainties in the load profile, fuel cost, and cost functions are taken account in order to determine their effect on the inequality constraints (e.g., that on the CO concentration).

The two-/single-objective functions are defined as follow:

i) Multi-objective FPS Optimization Problem

$$\text{Minimize } C_1^{FPS} = C_{FPS} \quad (6.1)$$

$$C_2^{FPS} = C_{oper} \quad (6.2)$$

$$\text{w.r.t } \{ \vec{X}_{FPS}, \vec{Y}_{FPS} \}$$

$$\text{subject to } \vec{H}_{FPS} = 0 \quad (6.3a)$$

$$\vec{G}_{FPS} \leq 0 \quad (6.3b)$$

$$\text{and } G_{CO,95\%} = G_{CO} + 2G_{CO}^{SD} \leq 10 \text{ ppm} \quad (6.3c)$$

ii) Single-objective FPS Optimization Problem

$$\text{Minimize } C_{total}^{FPS} = C_{FPS} + C_{oper} \quad (6.4)$$

$$\text{w.r.t } \{ \vec{X}_{FPS}, \vec{Y}_{FPS} \}$$

$$\text{subject to } \vec{H}_{FPS} = 0 \quad (6.5a)$$

$$\vec{G}_{FPS} \leq 0 \quad (6.5b)$$

$$\text{and } G_{CO,95\%} = G_{CO} + 2G_{CO}^{SD} \leq 10 \text{ ppm} \quad (6.5c)$$

where expression (6.5b) includes all the FPS equality constraints except for that for the CO concentration, G_{CO} is the mean value of the CO concentration in the reformat gas after the PrOx reactor and G_{CO}^{SD} is the standard deviation of this concentration (see equation (5.27)).

In this doctoral research, SEQOPT, which is a kind of SMBO algorithm, has been employed as the optimization algorithm. As addressed in Chapter 5, SEQOPT is a less computationally expensive yet efficient optimization algorithm for complex problem like that

for the FPS. Using SEQOPT, the single-objective approach is carried out for the dynamic FPS synthesis/design and operation/control optimization problem based on the required hydrogen production profile shown in Figure 6.18. At the maximum load requirement (i.e. at 5 kWe), a 0.06 mol/s hydrogen flow rate to the SS is obtained based on roughly 80% fuel utilization at the stack an un-optimized value. Thus, the optimum solutions of this section may be different from those of the overall PEMFC system optimization addressed in the next section.

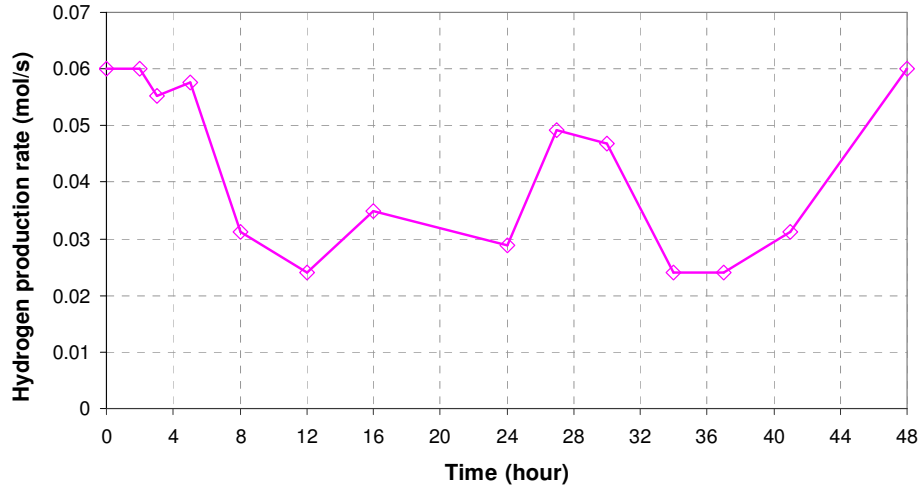


Figure 6.18 Approximate hydrogen demand profile for 48 hours.

The single-objective (i.e. total life cycle cost⁴) optimization results are depicted in Figure 6.19. The synthesis/design and operating decision variable ranges in Table 5.2 and 5.3 are used for the optimization, and the non-solid square in the figure represents the optimum total life cycle cost \$43,020 found. The optimization is repeated three times starting from significantly different initial points and each optimization predicts almost the same result as the first one.

Here, the question arises: does this point represent the global optimum of the FPS? The answer is that it may not. Because the SEQOPT algorithm uses a surrogate model which is generated for a given set of decision variable ranges, it may predict a different

⁴ In Sections 6.2.2 and 6.2.3, the total life cycle cost of the FPS, C_{total}^{FPS} , reported here is not given in present-value dollars and is, thus, not the total life cycle cost, $C_{total}^{LCC,FPS}$ as typically reported in the literature. To arrive at the latter, C_{total}^{FPS} must be divided by the product of N_{year} and C_{ratio} . For example, the optimum total life cycle cost of the FPS found here is $C_{total}^{FPS} = \$42,847$ which includes \$4,290 of capital cost and \$38,557 of operating cost. This cost in present-value dollars is $C_{total}^{LCC,FPS} = \$34,064$, a 20.5% difference.

solution if a different set of ranges is used. To verify this, the single-objective optimization is conducted for a different set of decision variable ranges. These results are also presented in Figure 6.19, and the solid square represents the optimum total life cycle cost, \$42,670, found. In the figure, the circles are possible outcomes or intermediate solutions of the FPS which satisfy all of the constraints (i.e. expressions (6.5)). The second optimization result (i.e. the solid square) for the total life cycle cost is a 0.8% improvement over the initial optimization result (i.e. the non-solid square): 1.65% of the operating cost is reduced but 7.3% of the capital cost of the FPS increases compared to the initial optimization result.

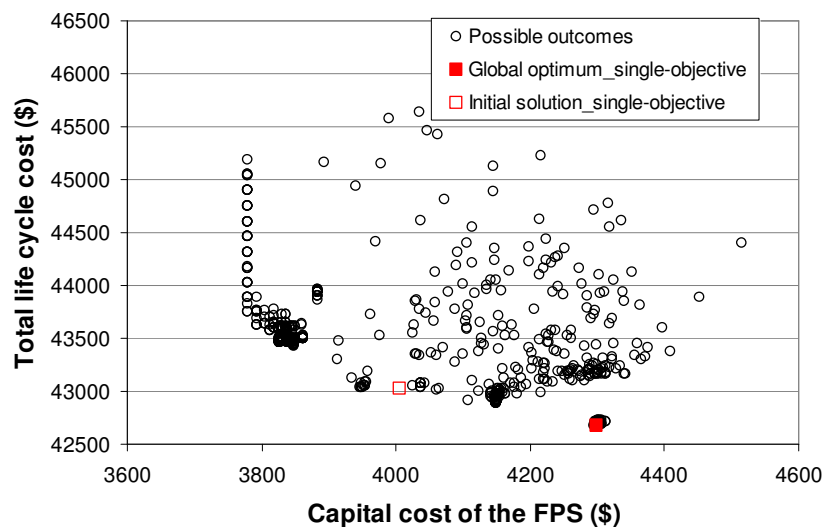


Figure 6.19 Single-objective results for the dynamic FPS synthesis/design and operation/control optimization.

However, has the question initially posed been answered, i.e. does the solid square may represent the global optimum solution of the dynamic PFS? To try to answer this, the single-objective optimization of the FPS is repeated 5 more times for different sets of decision variable ranges, and Figure 6.19 contains all possible outcomes from these 5 optimization processes. This procedure may nonetheless not be the best organized way to proceed because there is no rule for adjusting the range of the decision variables. This issue can be resolved by using the multi-objective optimization approach, i.e. equations (6.1) to (6.3). The basic procedure of the multi-objective optimization of the dynamic FPS and its results are given in Table 6.6.

Both cost based objective functions, equations (6.1) and (6.2), are minimized during the optimization process. The multi-objective optimization is carried out by

optimizing the objectives individually. When the optimization is conducted for one objective function, the other objective is treated as an inequality constraint as described in Table 6.6. Initially, the capital cost (i.e. sub-system size) of the FPS is set to some larger enough number (i.e. \$4,650 is chosen for that limit) so that the first optimization of the operating cost finds an optimum solution in the right-upper space in Figure 6.19. That is to make the optimization procedure converge from the first optimization solution in the direction of left-down in the figure, because it is not known where the global optimum point is. Once the first optimization finds an optimum solution, the optimization procedure continues trying to find an improved solution until changes in the operating cost, capital cost, and total life cycle cost form one step to the next is below the prescribed limit of 0.1%

Table 6.6 Multi-objective function optimization of the FPS.

Step	C_1^{FPS}	C_2^{FPS}	C_{total}^{FPS}	Improvement (%)			Optimization procedure
				C_1^{FPS}	C_2^{FPS}	C_{total}^{FPS}	
1	4673	38716	43390	-	-	-	Min C_2^{FPS} S.T. $G_{CO,95\%} \leq 10ppm, C_1^{FPS} > 4650$
2	4607	38617	43224	1.41	0.26	0.38	Min C_1^{FPS} S.T. $G_{CO,95\%} \leq 10ppm, C_2^{FPS} < 38716$
3	4333	38590	42903	5.95	0.07	0.74	Min C_2^{FPS} S.T. $G_{CO,95\%} \leq 10ppm, C_1^{FPS} < 4607$
4	4291	38576	42867	0.97	0.04	0.08	Min C_1^{FPS} S.T. $G_{CO,95\%} \leq 10ppm, C_2^{FPS} < 38590$
5	4290	38557	42847	0.02	0.05	0.05	Min C_2^{FPS} S.T. $G_{CO,95\%} \leq 10ppm, C_1^{FPS} < 4291$

The first optimization (step1) finds an optimum value of \$38,716 for the operating cost, and \$4,673 for the capital cost. In the second optimization or step, the capital cost is optimized, while the operating cost becomes a constraint. At the 5th optimization or step, the optimization process converged below the prescribed limit. Figure 6.20 shows the optimization process and each solid diamond represents the solution for each optimization in Table 6.6. As seen in the figure, there is only a 0.4% difference between the optimum total life cycle cost of the multi-objective optimization and that of the single-objective optimization. Circles in the figure are possible outcomes obtained from

the entire multi-objective optimization process. The optimization results of the multi-objective optimization shown in Figure 6.20 are zoomed in, and each step is depicted in Figure 6.21.

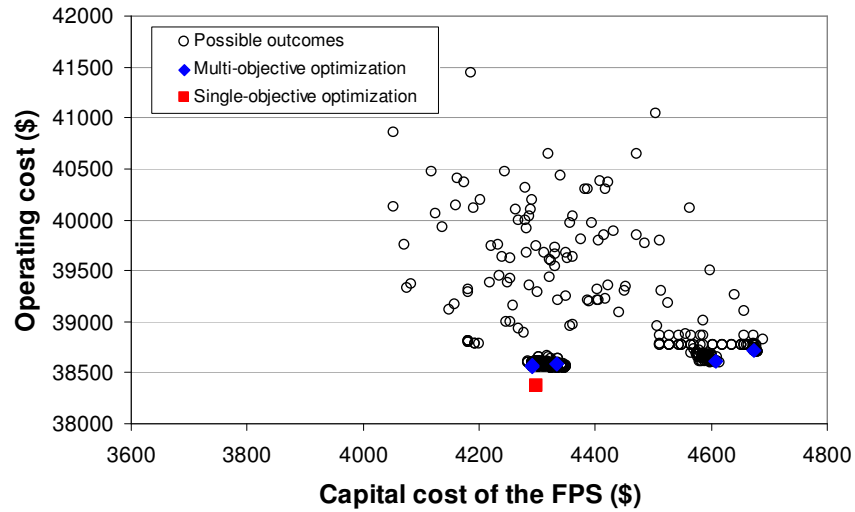


Figure 6.20 Result for the dynamic multi-objective FPS synthesis/design and operation/control optimization.

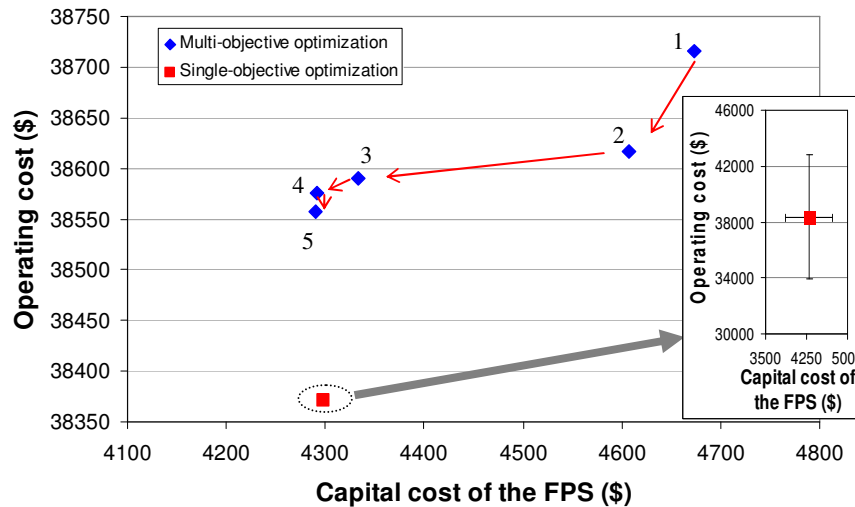


Figure 6.21 Zoom-in of the multi-objective optimization results in Figure 6.20.

For every point on Figures 6.19 to 6.21, uncertainty information in terms of standard deviations of the operating cost, capital, and total life cycle costs of the FPS can be generated, even though these uncertainties are not taken into account during the optimization process. In the zoomed-in figure inside of Figure 6.21, the global optimum

operating cost and capital cost of the FPS is depicted with uncertainties (i.e. \pm standard deviations) on them using error bars. The uncertainty on the global optimum total life cycle cost of the FPS is described in Figure 6.22 in terms of three uncertainty factors (i.e. the load profile, fuel cost, and capital cost) and their contributions. As seen in the table of Figure 6.22, the uncertainty from the load profile and that from the fuel cost are fairly equal around 50% while the capital cost contributes less than 1%. That is because the operating cost takes about 90% of the total life cycle cost and the remaining 10% is from capital cost. Therefore, the uncertainty on the total life cycle cost is mainly dominated by the fuel cost and the load profile.

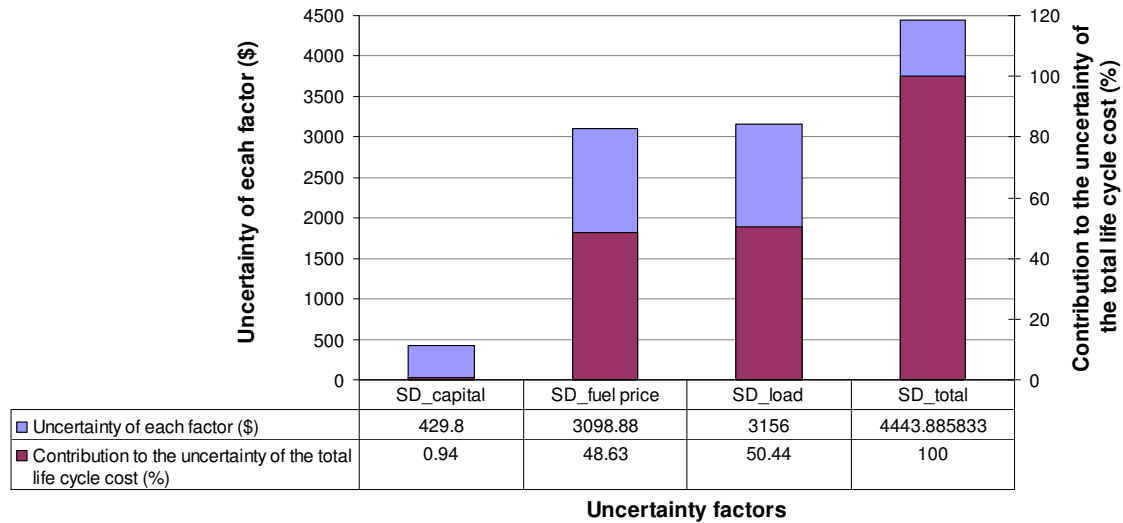


Figure 6.22 Uncertainty factors and their contributions to the uncertainty of the total life cycle cost of the FPS.

The dynamic FPS synthesis/design and operation/control optimization results, which are for the global optimum point in Figure 6.19, are summarized along with their initial values in Table 6.7. In the system configuration of the FPS as seen in Figure 5.6, the first pre-heater, P_HX1, and the third heat exchanger, HX3, in the system configuration are eliminated by the synthesis/design and operation/control optimization. The fuel and steam mixture is able to obtain enough thermal energy by increasing the size of the second pre-heater, P_HX2, so that the first pre-heater is eliminated. The LSTR and PrOx reactor show a similar operating temperature range of around 500~550 K at this optimum solution so that the outlet temperature of the reformate gas of the LSTR does not need to be decreased before entering the PrOx reactor.

The optimum tube diameter of the steam generator is almost unchanged from its initial diameter of 0.006 m so that the diameter is fixed at 0.006 m during the system-level optimization using DILGO. Optimizing the number of tubes in the steam generator makes the FPS simulation fail or get stuck fairly often because it is a very complex discontinuous problem to solve due to equations (3.78). Thus, the number of tubes is in the end fixed at 10 to facilitate the optimization process.

The dynamic characteristics of the FPS and the interactions between its components are discussed with the other subsystem optimums found by the system-level optimization in Section 6.3.

Table 6.7 Optimum synthesis/design and operation decision variable values of the FPS.

Synthesis/design decision variables							
Component	Decision variables	Initial value	Optimum value	Component	Decision variables	Initial value	Optimum value
SMR	L^{SMR} (m)	1.0	1.210	P_HX1*	$N_{P_HX1}^{HX}$	4	N/A
	d_{IN}^{SMR} (m)	0.02	0.025	P_HX2	$L_{P_HX2}^{HX}$ (m)	0.4	0.282
HTSR	L^{HTSR} (m)	0.5	0.589		$h_{P_HX2}^{HX}$ (m)	0.004	0.00365
	d_{IN}^{HTSR} (m)	0.09	0.066		$N_{P_HX2}^{HX}$	4	4
LTSR	L^{LTSR} (m)	0.6	0.630	HX1	L_{HX1}^{HX} (m)	0.25	0.490
	d_{IN}^{LTSR} (m)	0.09	0.071		h_{HX1}^{HX} (m)	0.004	0.00385
PrOx	L^{PrOx} (m)	0.5	0.549		N_{HX1}^{HX}	3	4
	d_{IN}^{PrOx} (m)	0.08	0.067	HX2	L_{HX2}^{HX} (m)	0.3	0.173
SG	L^{SG} (m)	1.0	1.410		h_{HX2}^{HX} (m)	0.004	0.00395
	d_{IN}^{SG} (m)	0.006	0.006		N_{HX2}^{HX}	3	4
	N^{SG}	10	10	HX3*	L_{HX3}^{HX} (m)	0.3	N/A
P_HX1*	$L_{P_HX1}^{HX}$ (m)	0.2	N/A		h_{HX3}^{HX} (m)	0.004	N/A
	$h_{P_HX1}^{HX}$ (m)	0.004	N/A		N_{HX3}^{HX}	2	N/A
Operation decision variables							
Variable	Initial value	Optimum value	Variable	Initial value	Optimum value		
$\xi_{S/C}$	3.5	2.8	ξ_{AIR}^{LTSR}	0.07	0.170		
ξ_{CH_4}	0.42	0.296	$\xi_{AIR}^{HX3^*}$	0.12	N/A		
ξ_{AIR}^{HTSR}	0.13	0.104	ξ_{AIR}^{PrOx}	0.40	0.453		
ξ_{AIR}^{HX2}	0.28	0.273	T_{inlet}^{HTSR}	610	605		

* Component has been eliminated by the optimization.

6.2.3 Uncertainty Effects on the FPS Synthesis/Design and Operation /Control Optimization

The single-objective optimization results in Figure 6.19 and those for the multi-objective optimization in Figure 6.20 are depicted together in Figure 6.23. In this figure, some synthesis/design results which violate the constraint (i.e. equations (6.3c) and (6.5c)) are also placed in the figure and are represented by the non-solid circles. The figure shows some interesting facts of the FPS synthesis/design. First of all, none of synthesis/design results satisfy the constraint below \$3,780 for the capital cost of the FPS. This means that the system size has a minimum requirement below which the 10 ppm of CO concentration with a 95% confidence cannot be satisfied. As seen in Figure 6.23, a number of outcomes which violate the constraint appear beginning at about \$3,550 for the capital cost and rarely show up for a capital cost over \$4,400. The total life cycle costs of all outcomes decrease as the capital costs (i.e. system size) of them increase until the capital cost of the global optimum point is reached. At this point, the total life cycle costs increase gradually, even though the capital costs increase. This tendency can be seen more clearly in Figure 6.24 which includes all the intermediate and final solution for the single- and multi-objective of the dynamic FPS synthesis/design and operation/control optimization results.

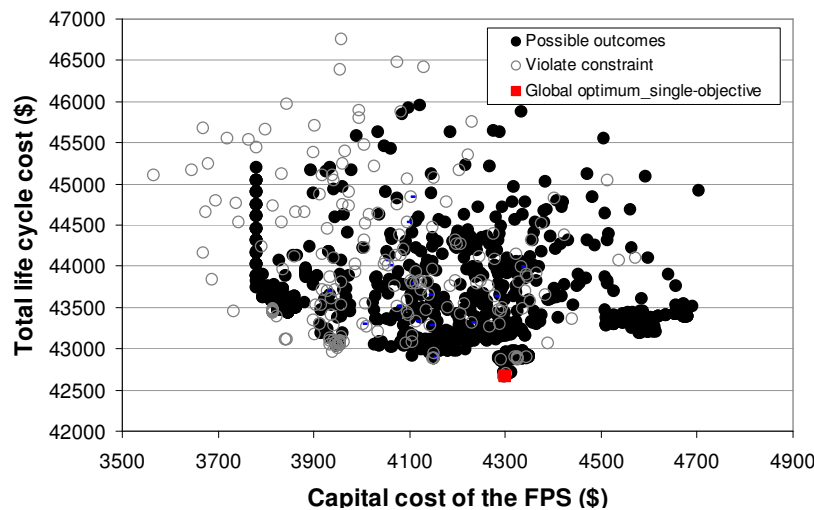


Figure 6.23 All the FPS result from the single-/multi-objective dynamic optimizations in Figures 6.19 and 6.20.

Among the outcomes which violate the constraint for the CO concentration of 10 ppm with a 95% confidence level, some are acceptable syntheses/designs if uncertainties are not

considered in the constraint. This uncertainty effect on the FPS synthesis/design is described using a Pareto set in Figure 6.24. The solid-line represents the Pareto set which takes into account uncertainty in the constraint, and the dotted-line describes the Pareto set in which uncertainty is not addressed in the constraint but satisfies the 10 ppm without knowledge of the confidence level. Furthermore, if the uncertainty effect is not considered in the FPS synthesis/design and operation/control optimization, the optimizer underestimates the operating cost when compared to that from the optimization under uncertainty for the same capital cost. This tendency only shows up for capital lower than \$4,120, since both Pareto sets describe the same line for capital costs as greater than this values as seen in Figure 6.24. As capital cost increases, optimizer allows sizes enough for the HTSR, LTSR, and PrOx reactor to remove the CO almost completely. For example, the optimum synthesis/design of the first optimization of the multi-objective optimization predicts being able to achieve a CO concentration of 2.5 ppm while a CO concentration with a 95% confidence level is able to achieve 4.5 ppm.

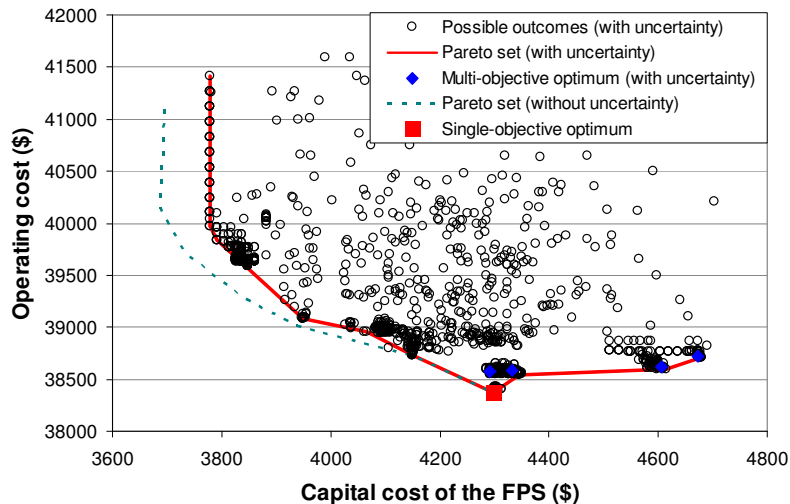


Figure 6.24 Uncertainty effects on the FPS synthesis/design and operation/control optimization.

Because the global optimum given in Figure 6.24 does not appear to be influenced much by uncertainty considerations, i.e. the global optimums with and without uncertainty are almost identical, one might draw the conclusion that there is no effect of uncertainty on this dynamic FPS synthesis/design and operation/control optimization. However, as seen above, the ability of the synthesis/design to meet certain critical constraints with any high degree of confidence is significantly affected. Furthermore, there is no way of knowing ahead of time to what extent the

optimum solution will be affected by uncertainties. Moreover, if there are system sizes or cost limitations on the system synthesis/design and operation/control, constraint uncertainties will significantly affect the system synthesis/design and operation/control optimization.

As addressed in Section 5.4.2, uncertainties on the objective function affect the synthesis/design and operation/control optimization results very little. However, as seen in Figure 6.24, uncertainties on the constraints can significantly influence the optimization results. In other words, among the indirect sources of uncertainty, those related to parameters which are tied to the operating conditions such as the load profile may greatly affect the constraints placed on these parameters. As is shown here, for example, the CO concentration is indeed greatly affected and leads to different synthesis/design and operation/control Pareto sets as indicated in Figure 6.24. In contrast, uncertainties in the purchase costs and fuel cost do not greatly influence these parameters and the constraints placed upon them. Figure 6.25 qualitatively illustrates the effect that uncertainties in the load profile have on the synthesis/design and operation/control results. As seen in the figure, if the uncertainties on the load profile are zero, then the optimization results predict the red line which represents the dotted-line in Figure 6.24. As the uncertainties in the load profile increase, the synthesis/design and operation/control space shrinks as described in Figure 6.25. Thus, it is evident that uncertainties on certain critical constraints play an important role in the energy system synthesis/design and operation/control optimization problem.

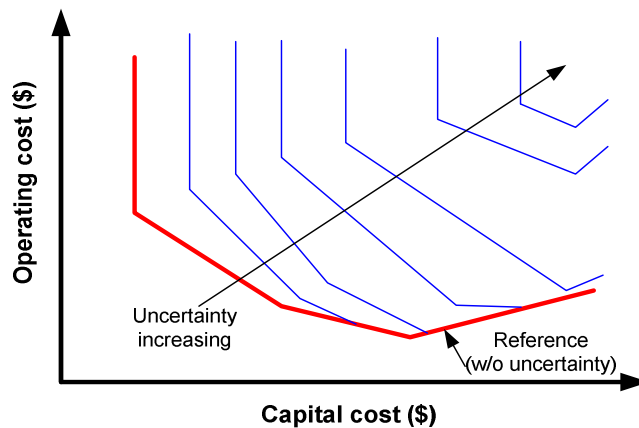


Figure 6.25 Effects of the magnitude of uncertainty on the FPS synthesis/design and operation/control optimization.

Two additional characteristics of the optimization results are presented in Figures 6.26 (a) and (b). As addressed above, the total life cycle cost on the Pareto set increases

gradually as the capital cost beyond the global optimum point increases. The reason for this can be explained by Figures 6.11 and 6.26 (a). As shown in Figure 6.11, the more CO that is generated in the SMR, the lower the steam-to-carbon ratio. To remove more CO in the reformat gas, a bigger CO removal unit (i.e. HTSR, LTSR, and PrOx reactor) is required. In the PrOx reactor, the H₂ oxidation reaction also occurs along with the CO oxidation reaction i.e. H₂ is also removed in proportion to how much the CO removal capacity of the PrOx reactor is enhanced. Therefore, more methane is required to produce the amount of H₂ required by the SS, which raises the operating cost.

Figure 6.26 (b) shows the optimum fuel ratio, which is the ratio between the methane flow rate to the combustor and that to the SMR, on the Pareto set. The fuel consumption for the combustor is a kind of parasitic energy which primarily raises the operating cost. As seen in Figure 6.26 (b), the fuel ratio keeps decreasing until the global optimum capital cost on the Pareto set is reached and then changes little after that. That is one of the main reasons why the operating cost (or total life cycle cost) decrease (i.e. decreases with decreasing fuel rates) as the capital cost increases.

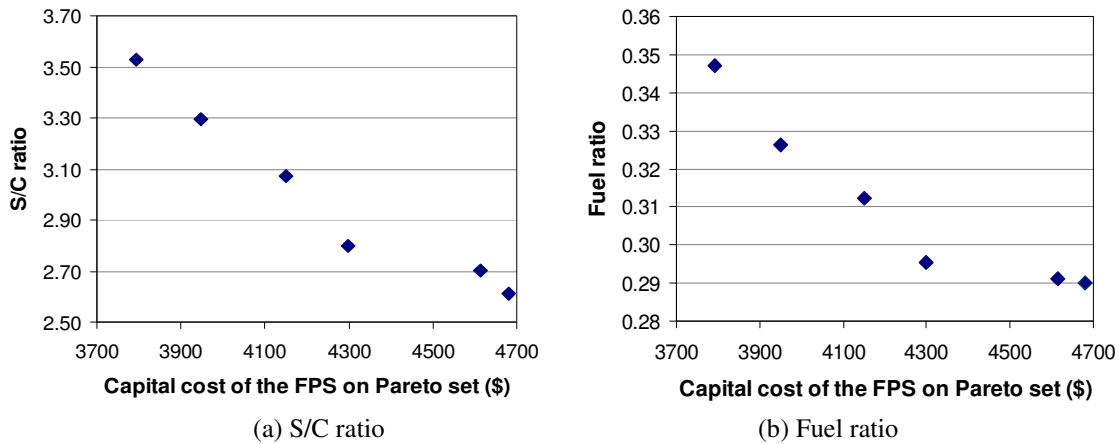


Figure 6.26 Optimum operating steam-to-carbon ratio and fuel ratio on the Pareto set.

6.3 Dynamic Synthesis/Design and Operation/Control Optimization of the PEMFC System using DILGO

The 5 kWe PEMFC system model developed here was validated in Section 6.1, and several methodologies proposed for uncertainty analysis and single-/multi-objective

optimizations of dynamic energy systems were evaluated in Section 6.2. These studies have proven the high fidelity of the system/subsystem/component models and the efficiency and accuracy of those uncertainty analysis and optimization methodologies for dynamic energy systems. Based on these preliminary studies, a system-level optimization of the dynamic PEMFC system is implemented using the DILGO physical decomposition strategy as discussed in Chapter 5. In the following sections, the system-level optimization results of the system synthesis/design and operation/control are discussed, and overall system performance and characteristics at the optimum design will be introduced as well.

6.3.1 Optimization Results

In Chapter 5, the system-level, unit based (SLUB) optimizations of the PEMFC system are defined using the ILGO strategy. Information on each subsystem and the coupling functions, objective functions, synthesis/design and operation decision variables, and the optimization procedure for DILGO are explained in detail.

As addressed in Chapter 5, the dynamic PEMFC system synthesis/design and operation/control optimization problem is decomposed into SLUB optimization sub-problems for the FPS, SS, and WRAS. Once the SS SLUB optimization is completed for a given DILGO iteration for the dynamic load profile (Figure 5.13), it generates the optimum dynamic air and hydrogen profiles required by the WRAS and FPS as shown in Figure 6.27. The FPS and WRAS SLUB optimizations for the next DILGO iteration are then carried out based on these dynamic profiles. According to the optimization results of the SS SLUB optimization, the dynamic profiles in Figure 6.27 are scaled down or up in each DILGO iteration, affecting the FPS and WRAS SLUB optimizations.

The results of the FPS, SS, and WRAS SLUB optimizations of the PEMFC system are implemented through the sequential DILGO scheme depicted in Figure 5.10 of Chapter 5. The PEMFC total life cycle cost and uncertainty (i.e. standard deviation) on the total life cycle cost for each iteration of the DILGO approach are summarized in Table 6.8, and Figures 6.28 and 6.29 present the optimization results for each DILGO iteration graphically.

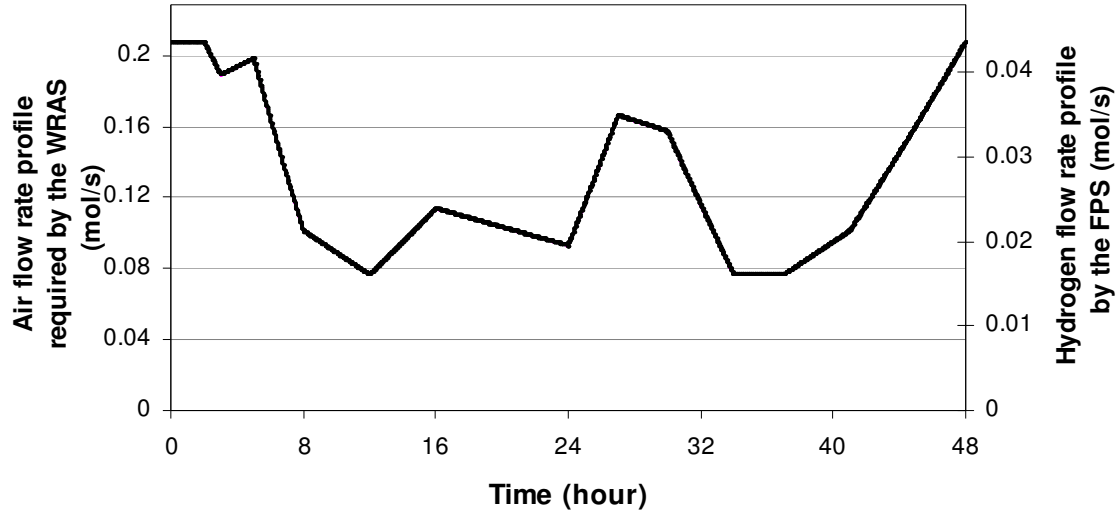


Figure 6.27 Optimum dynamic air and hydrogen profiles required by the FPS and WRAS SLUB optimizations during a given DILGO iteration.

The DILGO procedure continues until the improvement in the total life cycle cost⁵ of the PEMFC system is below 0.1%. The global optimum value for total life cycle cost of the PEMFC system is obtained during the 6th iteration of DILGO procedure is \$38,077 with a stand deviation of \$3,932. Thus, the optimum total life cycle cost of the PEMFC system is expressed as $\$38,077 \pm 7864 (2\sigma)$ with a 95% confidence level (i.e. interval). The uncertainty of the total life cycle cost in each IDLGO iteration is presented along with this cost using error bars in Figure 6.28. Uncertainties in the capital cost of each subsystem and the operating cost are presented in Figure 6.29.

Significant improvements in the system-level objective function and capital costs of the subsystems are observed up on completion of the second DILGO iteration as seen in Figures 6.28 and 6.29, and there are no significant improvements after the 4th iteration. The second DILGO iteration predicts the total life cycle cost of the PEMFC system to be \$38,199.6 which is a 18.44% improvement over the first DILGO iteration, but there is only a 0.26% improvement from the second to the 6th DILGO iteration.

⁵ As indicated in footnote 4 in Section 6.2, the total life cycle cost, C_{total}^{PEMFC} , reported here is also not given in present-value dollars and is, thus, not the total life cycle cost, $C_{total}^{LCC,PEMFC}$ as typically reported in the literature. To arrive at the latter, C_{total}^{PEMFC} must be divided by the product of N_{year} and C_{ratio} . For example, the optimum total life cycle cost of the PEMFC system found here is $C_{total}^{PEMFC} = \$38,077$ which includes \$10,364 of capital cost and \$27713 of operating cost. This cost in present-value dollars is $C_{total}^{LCC,PEMFC} = \$31,764$, a 16.6% difference.

Table 6.8 Optimum costs of the PEMFC system and its subsystems for each iteration of the DILGO procedure.

DILGO Iteration No.		<u>1</u>		<u>2</u>		<u>3</u>		<u>4</u>		<u>5</u>		<u>6</u>
FPS	C_{FPS}	4959.7		5052.3		5331.2		5321.6		5265.7		<u>5255.7</u>
	C_{opeer}	38736.0		28163.7		27822.4		27796.4		27704.5		<u>27712.8</u>
	C_{SS}^*	2300.0		3961.9		3915.7		4077.1		4049.4		4051.7
	C_{WRAS}^*	1300.0		865.5		1021.7		1065.0		1074.0		1061.1
	C'_{FPS}	47295.7		38043.4		38091.0		38260.2		38093.6		38081.3
	C_{UNC}^{FPS}	4450.8		4076.9		3910.2		3912.3		3893.2		3902.2
SS	C_{FPS}^*	5000.0	4959.7		5052.3		5331.2		5321.6		5265.7	
	C_{oper}^*	40000.0	38736.0		28163.7		27822.4		27796.4		27704.5	
	C_{SS}	2299.6	3961.9		3915.7		4077.1		4049.4		<u>4051.7</u>	
	C_{WRAS}^*	1300.0	865.5		1021.7		1065.0		1074.0		1061.1	
	C'_{SS}	48599.6	37366.7		37247.8		37614.4		37649.2		37679.0	
	C_{UNC}^{SS}	396.2	391.6		407.7		404.9		405.2		404.9	
WRAS	C_{FPS}^*	5000.0		4959.7		5052.3		5331.2		5321.6		5265.7
	C_{oper}^*	40000.0		38736.0		28163.7		27822.4		27796.4		27704.5
	C_{SS}^*	2300.0		3961.9		4193.8		4077.1		4049.4		4051.7
	C_{WRAS}	865.5		1021.7		1065.0		1074.0		1061.1		<u>1056.9</u>
	C'_{WRAS}	48165.5		48565.6		38353.5		38181.0		38036.2		38069.8
	C_{UNC}^{WRAS}	283.4		256.4		269.2		260.2		269.4		262.6
$C_{total,UNC}^{PEMFC}$	4477.3		4103.7		3940.6		3941.8		3923.4		3931.9	
Improvement (%)	-		8.34		3.97		- 0.03		0.40		-0.22	
C_{total}^{PEMFC}	46860.8		38199.6		38134.3		38269.2		38080.7		<u>38077.1</u>	
Improvement (%)	-		18.48		0.17		-0.35		0.49		0.01	

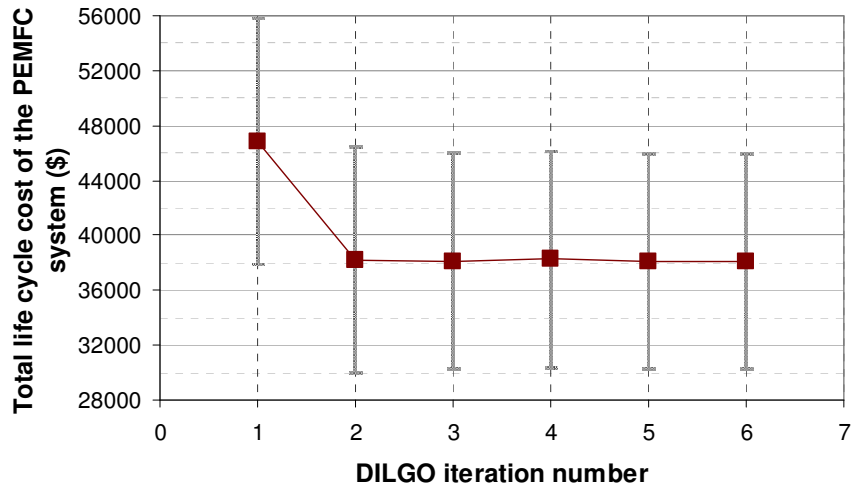
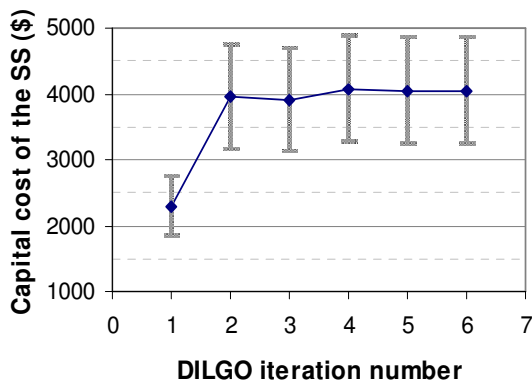
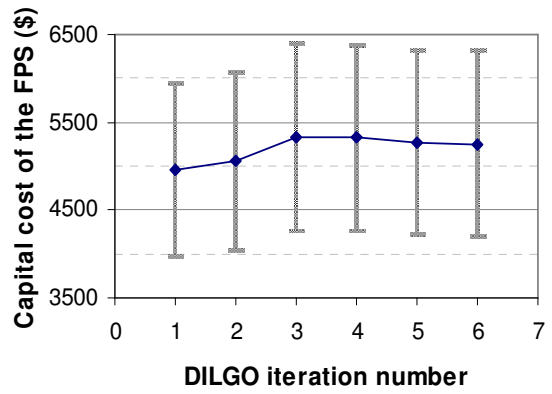


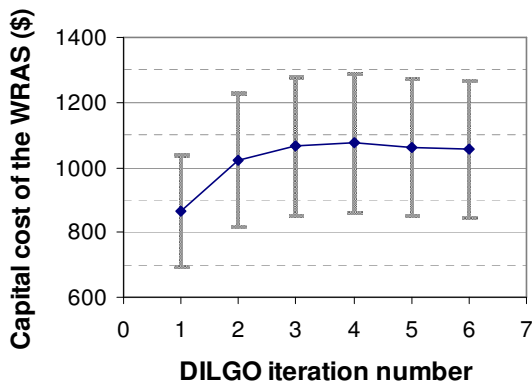
Figure 6.28 Changing total life cycle cost of the PFMEC during the DILGO procedure with a 95% confidence interval and the variance in the cost indicated by error bars.



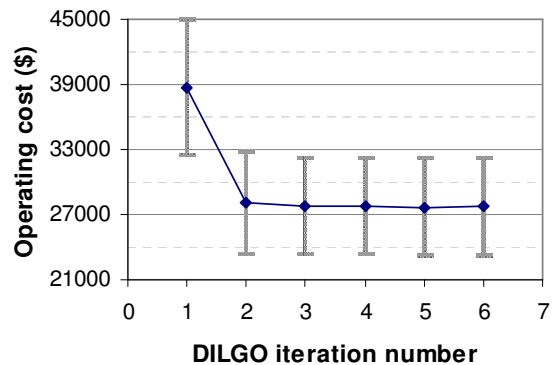
(a) Capital cost of the SS



(b) Capital cost of the FPS



(c) Capital cost of the WRAS



(d) Operating cost

Figure 6.29 Changing capital costs of the SS, FPS, and WRAS and operating cost during the DILGO procedure with a 95% confidence interval and the variance in cost indicated by error bars.

It may appear that the synthesis/design and operation/control optimization of the PEMFC is already complete after the second or the third DILGO iteration because there is little improvement after either iteration. Furthermore, it may appear that the predefined limit of 0.1% is too small. However, to determine whether or not the system-level optimization using DILGO is complete, the stabilizing of all coupling functions must be evaluated as well. Figure 6.30 depicts the stabilization of each coupling function graphically. Figure 6.30(a) and (b) present the required hydrogen and air flow rate by the SS at the full load condition. Each point in the graphs indicates the starting point of the dynamic profile in Figure 6.27. These two graphs show that the required hydrogen flow rate and the required air flow rate are stabilized at 0.0436 mol/s and 0.2078 mol/s at the full load condition, respectively.

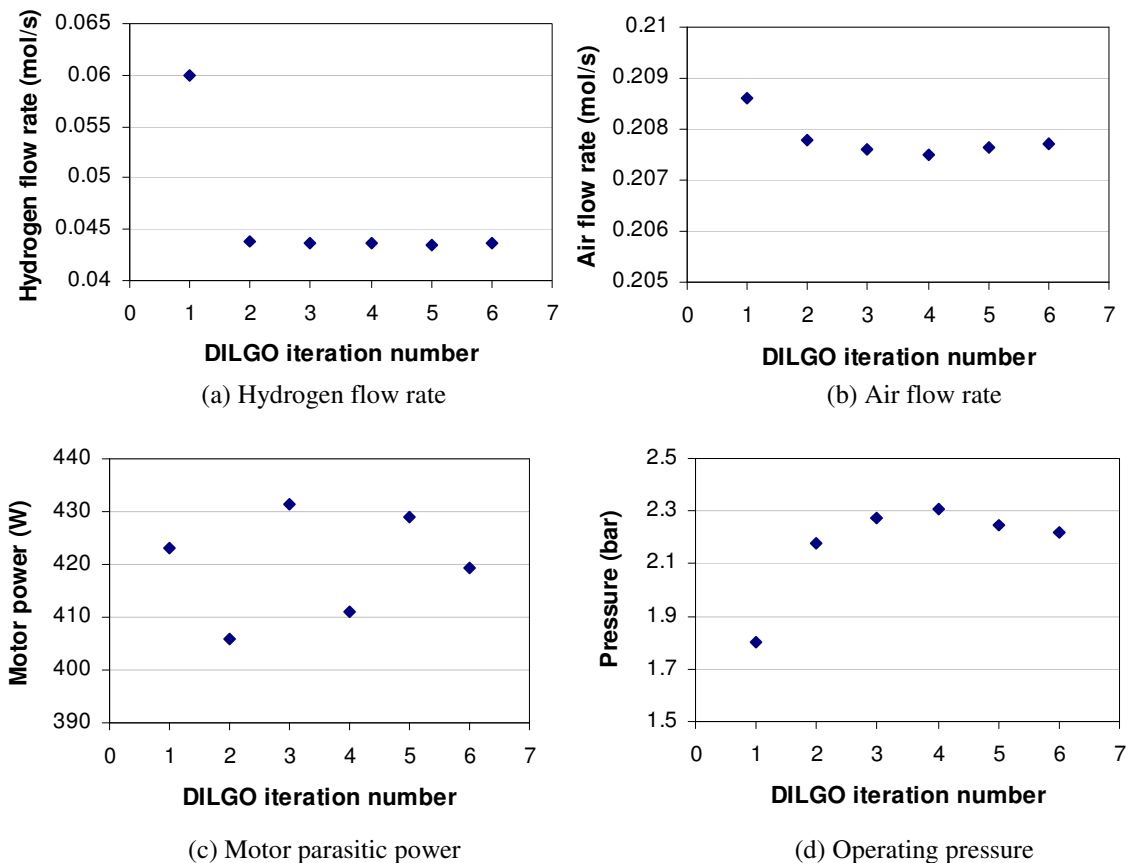


Figure 6.30 Changing the coupling functions during DILGO iteration.

Another coupling function, i.e. the motor parasitic power at the full load condition, is presented in Figure 6.30(c). The motor parasitic power oscillates with DILGO iteration

number begins to stabilize at around 420 W after the 6th DILGO iteration. As to the stack operating pressure, it is one of the coupling functions as well as one of the operating decision variables. The pressure plays an important role in the PEMFC system operation because it significantly affects PEMFC system performance and also determines the operating pressure of the FPS and WRAS. A final optimum operating stack pressure appears to begin stabilizing 2.22 bar in the 6th DILGO iteration as seen in Figure 6.30(d). Thus, it can be inferred from the figures that stabilized coupling functions may be obtainable after one or two more DILGO iterations.

The global optimum synthesis/design and operation decision variable values of the PEMFC system appear in Table 6.9. As indicated in Section 6.2, the number of tubes and tube diameter in the steam generator are fixed at 10 and 6 mm during the FPS SLUB optimization process, but other FPS decision variables are the same as in Tables 5.2 and 5.3. Furthermore, the FPS SLUB optimization results are not much different from the unit-level FPS optimization results as seen in Tables 6.7 and 6.9. The FPS SLUB optimization also eliminates the first pre-heater, P_HX1, and the third heat exchanger, HX3 as did the unit-level optimization of the FPS in the previous section. It should be noted that some of the cost functions (e.g., purchase cost, installation cost, and maintenance cost of the FPS) were corrected after the preliminary optimization study presented in Section 6.2, and the cost functions used in the system-level optimization are listed in Table 3.10. That is why the optimum capital cost of the FPS from the system-level PEMFC synthesis/design and operation/control optimization is higher than that from the unit-level FPS optimization presented in Section 6.2.

The optimal design of the SS predicts 0.1274 m² for the single cell active area (3.7 m² of total cell active area), while the initial design of the SS a single active area of 0.0475 m² (2.0 m² total cell active area). Furthermore, the PEMFC stack efficiency increases with increasing stack (active area) size because the stack can operate at lower current densities as seen in Figure 6.31. In this figure, the relationships between cell active area and cell current density and hydrogen consumption rate at the full load condition of 5 kWe. For this comparison, all decision variables are fixed at the optimal values which are in Table 6.8, while cell size is varied. As seen in the figure, cell current density and hydrogen consumption rate decrease with increasing cell active area. Less

cell current density produces higher cell voltage to generate the same amount of power. Thus, the larger size fuel cell stack consumes less hydrogen. This in turn reduces the operating cost of the PEMFC system. However, as the fuel cell stack size increases, the

Table 6.9 Optimum synthesis/design and operation decision variable values of the PEMFC system.

Synthesis/design decision variables							
Component	Decision variables	Initial value	Optimum value	Component	Decision variables	Initial value	Optimum value
FPS							
SMR	L^{SMR} (m)	1.0	1.15	P_HX2	$L_{P_HX2}^{HX}$ (m)	0.4	0.300
	d_{IN}^{SMR} (m)	0.02	0.0237		$h_{P_HX2}^{HX}$ (m)	0.004	0.0038
HTSR	L^{HTSR} (m)	0.5	0.590		$N_{P_HX2}^{HX}$	4	4
	d_{IN}^{HTSR} (m)	0.09	0.0663	HX1	L_{HX1}^{HX} (m)	0.25	0.540
LTSR	L^{LTSR} (m)	0.6	0.680		h_{HX1}^{HX} (m)	0.004	0.0039
	d_{IN}^{LTSR} (m)	0.09	0.0708		N_{HX1}^{HX}	3	4
PrOx	L^{PrOx} (m)	0.5	0.540	HX2	L_{HX2}^{HX} (m)	0.3	0.197
	d_{IN}^{PrOx} (m)	0.08	0.0670		h_{HX2}^{HX} (m)	0.004	0.0039
SG	L^{SG} (m)	1.0	1.71		N_{HX2}^{HX}	3	4
P_HX1	$L_{P_HX1}^{HX}$ (m)	0.2	N/A	HX3	L_{HX3}^{HX} (m)	0.3	N/A
	$h_{P_HX1}^{HX}$ (m)	0.004	N/A		h_{HX3}^{HX} (m)	0.004	N/A
	$N_{P_HX1}^{HX}$	4	N/A		N_{HX3}^{HX}	2	N/A
WRAS							
Motor	Tq_{design}^{Motor}	3	2.10	Expander	$p_{design}^{Expander}$	2.0	2.17
	rpm_{design}^{Motor}	2400	1457		$\dot{m}_{design}^{Expander}$	0.1	0.076
Compressor	$p_{design}^{Compressor}$	2.2	2.18	<u>Unit:</u> $\dot{m}_{design}^{Compressor}$ & $\dot{m}_{design}^{Expander}$ (kgT ^{0.5} /s bar)			
	$\dot{m}_{design}^{Compressor}$	0.1	0.083	Tq_{design}^{Motor} (Nm)			
SS							
	L^{SS} (m)	0.218	0.357		N^{SS}	42	29
Operation decision variables							
Variable	Initial value	Optimum value	Variable	Initial value	Optimum value		
$\xi_{S/C}$	3.5	2.92	ξ_{AIR}^{HX3}	0.12	N/A		
ξ_{CH4}	0.42	0.305	ξ_{AIR}^{PrOx}	0.40	0.300		
ξ_{AIR}^{HTSR}	0.13	0.186	T_{inlet}^{HTSR} (K)	610	612		
ξ_{AIR}^{HX2}	0.28	0.365	p^{SS} (bar)	1.8	2.2		
ξ_{AIR}^{LTSR}	0.07	0.149					

* Component has been eliminated by the optimization.

capital cost of the SS increases as well. Therefore, a compromise between the operating cost of the PEMFC system and the capital cost of the SS with regard to the stack size must be determined by the system-level optimization process. As seen in Table 6.9, this compromise results in a cell active area of 0.1274 m^2 (0.357 m length) with the optimum number of cells 29. Even though the larger cell size may cause some technical difficulties in terms of stack assembly, thermal management, and uniform fuel distribution in the cell, these are not considered in this work because there is no available information about size limitations on stack design in the literature. If it becomes available, it must be taken into account as a constraint in future work.

As mentioned above, two heat exchangers are eliminated from the initial configuration (see Figure 5.6), and Figure 6.32 depicts the optimally determined 5 kWe PEMFC system configuration.

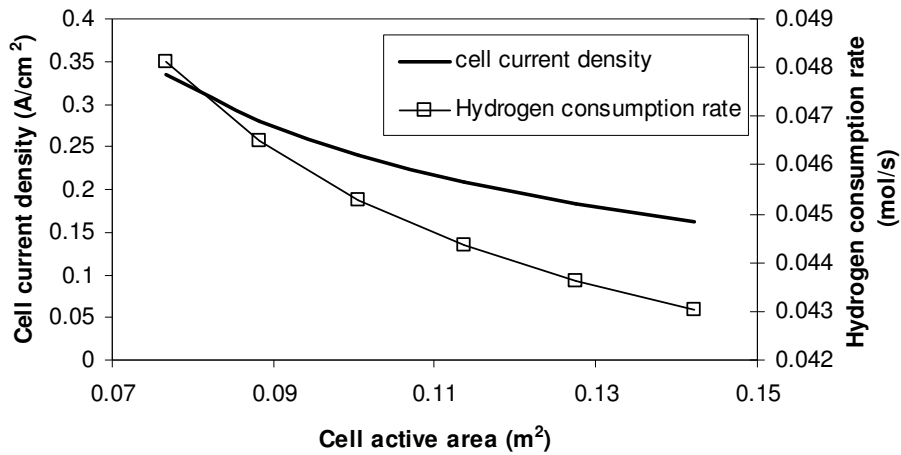


Figure 6.31 Relationships between the single cell active area and cell current density and hydrogen consumption rate at the full load condition of 5 kWe.

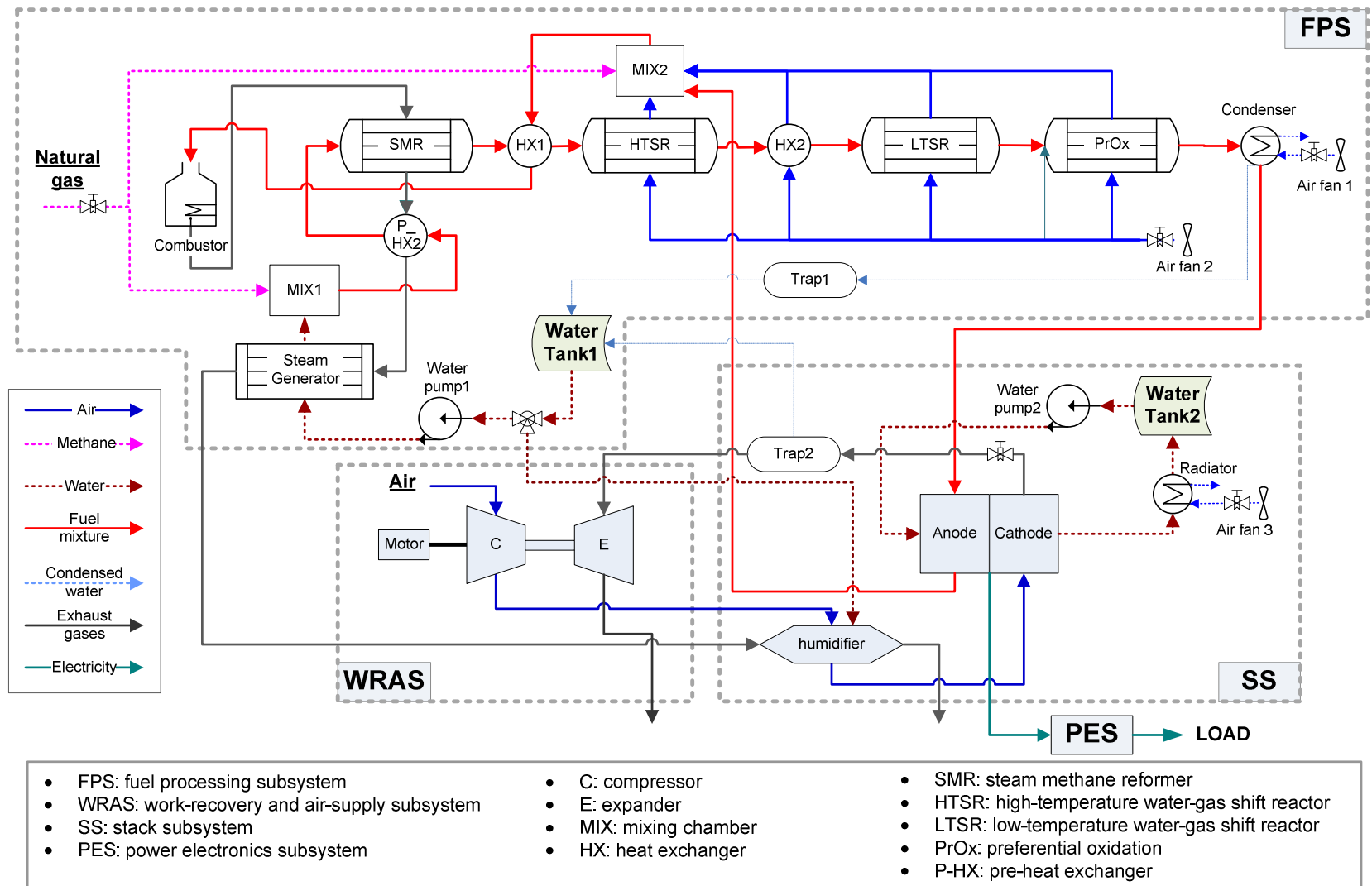


Figure 6.32 Optimum configuration of the PEMFC system.

6.3.2 Cost Evaluation

Synthesis/design and operation/control optimization of the 5 kWe PEMFC system is carried out based on a production volume of 500,000 units per year, and the detailed cost models and the economic assumptions for the PEMFC system cost analysis are presented in Tables 3.10 to 3.16. The total life cycle cost of the PEMFC system consists of operating cost and capital cost which includes purchase cost, indirect cost, installation cost, amortized cost, and maintenance cost. System-level, unit-based optimizations of the PEMFC result in a global optimum operating cost of \$27,704.5 and the global optimum capital cost each subsystem and the overall system appear in Table 6.10. The optimum total capital cost of the PEMFC system is \$10,363.9 and represents 27.2% of the optimum total life cycle cost of the PEMFC system.

Table 6.10 Optimum capital cost for the proposed PEMFC system based on 500,000 units per year.

	FPS	SS	WRAS	PEMFC
Purchase cost (\$)	1,886.5	1,454.4	379.2	3,720.1
Indirect cost (\$)	190.5	146.9	38.3	375.7
Installation cost (\$)	377.3	290.9	75.8	744.0
Amortized cost (\$)	3,178.8	2,450.5	638.8	6,268.1
Maintenance cost (\$)	2,077.0	1,601.2	417.6	4,095.8
Capital cost (\$)	5,255.8	4,051.7	1,056.4	10,363.9

The optimum purchase cost of each subsystem and its cost breakdown are presented in Table 6.11 and Figure 6.33. The optimum purchase cost of the PEMFC system is \$3,720.1, and the optimum purchase costs of the FPS, SS, and WRAS take 51%, 39%, and 10% of the system purchase cost, respectively. The optimum purchase cost of the FPS breakdown is given in Figure 6.33 (b). Of this cost, the cost of the reactors (the SMR, HTSR, LSTR, and PrOx reactor) is around 62% of the optimum purchase cost of the FPS, that of the three heat exchangers (P_HX2, HX1, and HX2) is 19%, and that of the auxiliary parts (e.g., valves, pipes, controllers, etc.) is 17%. The remaining 2% is the steam generator.

As seen in Figure 6.33 (c), the stack purchase cost takes 82% of the optimum purchase cost of the SS, and 89% of that is for purchasing the electrodes which include the anode, cathode, and gas-diffusion-layers. The purchase cost of the auxiliary parts

such as pipes, valves, and controllers for the SS represents 8% of the SS purchase cost. It should be noted that the some of auxiliary parts for the SS (e.g., valves and controllers) are also in common with the WRAS because both subsystems are coupled with each other via these valves and controllers. Thus, the purchase cost of these parts for the SS and WRAS is not considered in the purchase cost of the WRAS but in that of the SS.

Table 6.11 Optimum purchase cost of each subsystem based on 500,000 units per year.

SS			FPS	
Stack	Membrane (\$)	81.1	Reactors (\$)	1164.9
	Bipolar Plate (\$)	46.2	Steam Generator (\$)	41.4
	Electrode (\$)	1,046.7	Heat exchangers (\$)	365.7
	Assembly (\$)	31.5	Auxiliary parts (\$)	314.4
	Stack purchase (\$)	1,205.5	FPS purchase (\$)	1886.5
Humidifier (\$)	57.5	WRAS		
Cooling cycle (\$)	76.6	Compressor (\$)	225.6	
Auxiliary parts (\$)	114.8	Expander (\$)	108.5	
SS purchase (\$)	1454.4	Motor (\$)	45.1	
		WRAS purchase (\$)	379.2	

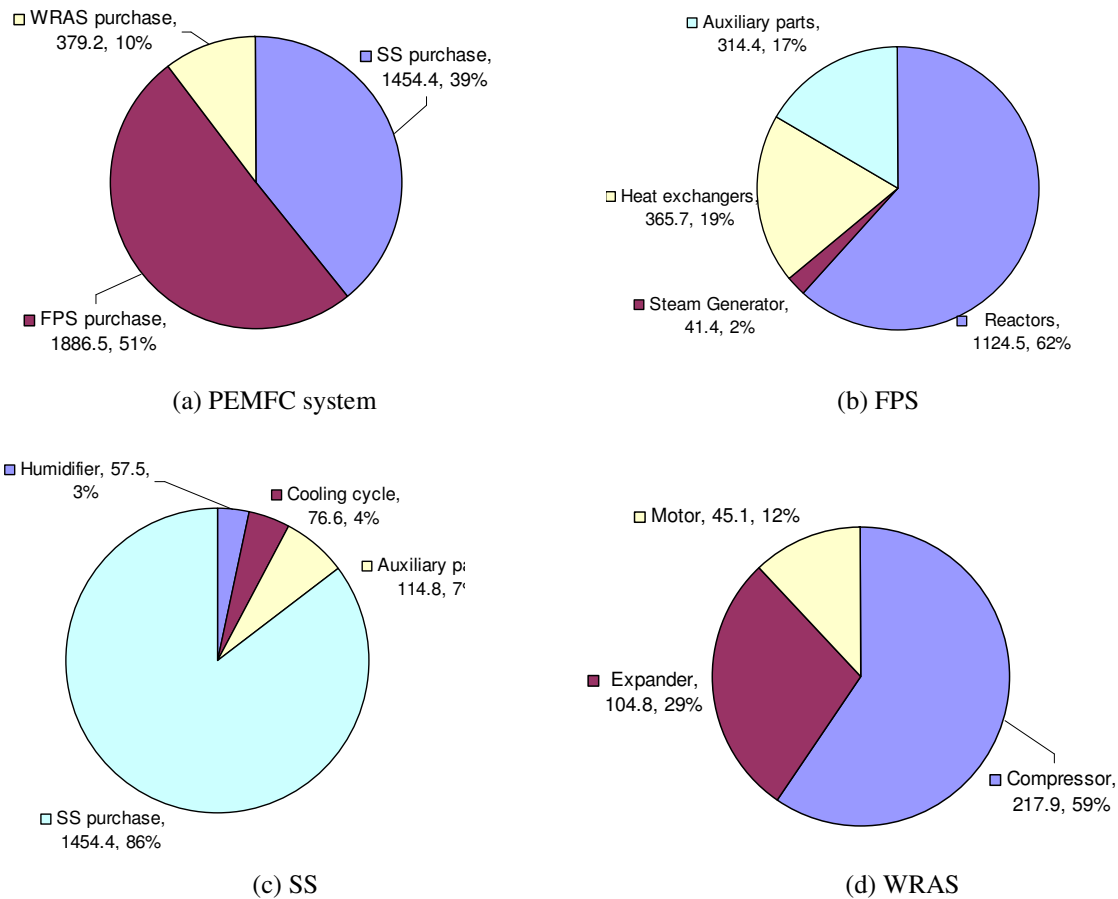


Figure 6.33 PEMFC system and its subsystems' purchase cost breakdown based on 500,000 units per year.

As to the WRAS, the larger size compressor is required than expander for fuel cell systems because more air flows through the compressor than the expander (Osscarson, 2003). The system-level optimization results show that fact appropriately. The compressor purchase cost is 59% of the optimum purchase cost of the WRAS, while the expander purchase cost is 29% of this cost.

It should be emphasized that the system optimization of the 5 kWe PEMFC system is conducted based on 500,000 production units per year. Changing this number significantly increases the system purchase cost significantly. The effects of the number of production units on the optimum capital cost of each subsystem and the operating cost are presented in Table 6.12. With a decreasing number of production units, the capital cost of each subsystem increases as seen in the table. The optimum total life cycle cost of the PEMFC system is \$38,077.1 based on 500,000 production units, while it is \$70,819.1 for 10,000. That is because the capital cost based on 10,000 production units increases \$32,742 and dominates the optimum total life cycle cost, i.e. it represents around 60.0% of this cost. Thus, the system optimization based on the economic objective function is affected more and more as the number of production units decreases.

Table 6.12 also shows that the system purchase cost per kWe is \$744.0/kWe for 500,000 production units and goes up to \$3,094.3/kWe for 10,000. The relationship between the number of production units and capital cost of each subsystem is depicted with operating cost as a percentage of the total life cycle cost in Figure 6.34 and graphically shows the decreasing influence of operating cost with decreasing in the number of production volume. Figure 6.35 shows the increasing influence of the system purchase cost per kWe as the production volume decreases. Thus, one can conclude that at 500,000 units per year, the PEMFC system is competitive with more conventional technologies in many small-scale stationary power markets (see Ellis and Gunes, 2002) and even at a production volume of 100,000 units per year remains competitive but in a small number of markets. At a production volume of 10,000 unit, however, this competitiveness which points to the need for finding ways of decreasing the cost of these systems that are not just based on the number of units produced per year.

Table 6.12 Effect of the number of production units per year on the optimum total life cycle cost and the system purchase cost per kWe for the proposed PEMFC system.

# of units	Life cycle cost									\$/kWe
	SS (\$, %)		WRAS (\$, %)		FPS (\$, %)		Operating (\$, %)		Total (\$)	
10000	16913.8	23.9	4285.5	6.1	21907.0	30.9	27712.8	39.1	70819.1	3094.3
100000	7349.2	15.8	1862.1	4.0	9518.8	20.5	27712.8	59.7	46442.9	1344.5
500000	4051.7	10.6	1056.4	2.8	5255.8	13.8	27712.8	72.8	38077.1	744.0

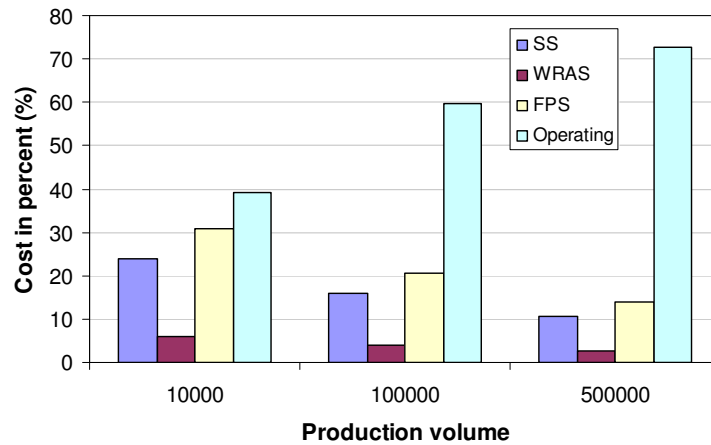


Figure 6.34 Relationship between the number of production units and the capital cost and operating costs as a percentage of total life cycle cost.

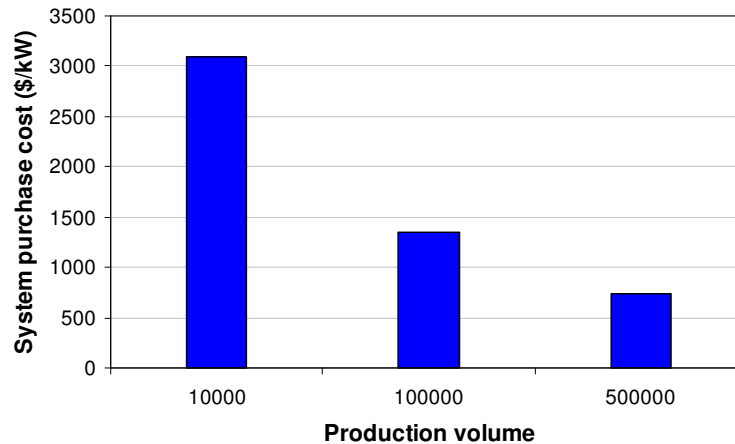


Figure 6.35 Relationship between the number of production units and the system purchase cost per kWe.

6.3.3 Sensitivity Analysis

A sensitivity analysis of a system model shows how the system model outputs vary with variations in the input values. For example, it gives the direction and magnitude of a system response due to variations in a decision variable value. If a system is non-linear, the sensitivity of a given synthesis/design and specified operating conditions may

be different from another synthesis/design at the same operating conditions. Thus, a sensitivity analysis provides useful information to engineers for developing a system as well as appropriate system operating strategies and control characteristics.

As briefly introduced in Chapter 4, $\partial g_{M_j} / \partial Z_i$ represents the system response sensitivity for a system output, M_j , and system input, Z_i . It can be non-dimensionalized by multiplying by nominal input and output values such that

$$Sensitivity = \frac{\partial g_{M_j}}{\partial Z_i} \cdot \frac{Z_{i,nom}}{g_{M_j,nom}} \approx \frac{\Delta g_{M_j}}{\Delta Z_i} \cdot \frac{Z_{i,nom}}{g_{M_j,nom}} \quad (6.6)$$

where the subscript *nom* indicates a nominal value of M_j or Z_i . By comparing the non-dimensionalized sensitivity of a system response for each decision variable, one can evaluate the contribution which each decision variable makes to the system response.

The sensitivities of the global optimum total life cycle cost of the PEMFC system and of the final CO concentration of the FPS are evaluated and the results given in Figures 6.36 and 6.37, respectively. Figure 6.36 shows the sensitivities of the optimum total life cycle cost to changes in all of the optimum decision variable values and these are compared to the sensitivities of the total life cycle cost for the initial synthesis/design point. The initial/optimum values in Table 6.9 are used for the nominal values of the decision variables, and \$51,508.1 and \$38,077.1 are used as nominal values for the total life cycle cost of the initial and optimum syntheses/designs, respectively.

For the initial synthesis/design of the PEMFC system, the total life cycle cost is very sensitive to the number of cells, cell length (all length squared is the active area), HX1 length, fuel ratio, PrOx reactor diameter, steam-to-carbon ratio, and inlet reformat gas temperature of the HTSR, while it shows high sensitivity to the cell length, PrOx reactor diameter and length, fuel ratio, and inlet reformat gas temperature of the HTSR for the optimum synthesis/design as seen in Figure 6.36. In particular, the optimum total life cycle cost shows the highest sensitivity to the fuel ratio because it is directly associated with the fuel consumption rate and the operating cost is the major contributor to the total life cycle cost of the PEMFC system. The optimum total life cycle cost is also very sensitive to the size of the PrOx reactor due to the hydrogen oxidation reaction in this reactor. A larger size requires more fuel to produce the hydrogen in the SMR required by SS, and this increases operating cost.

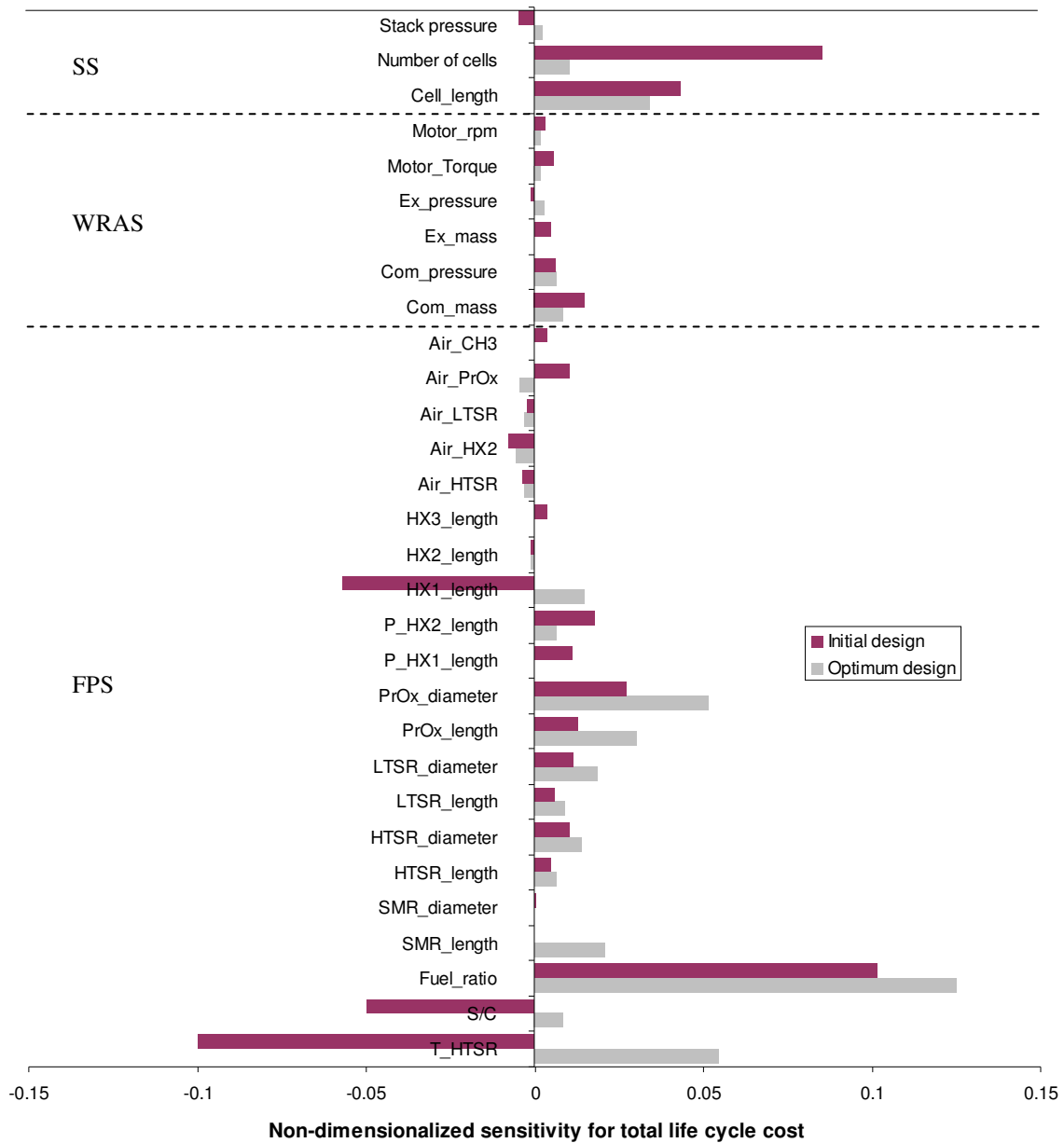


Figure 6.36 Non-dimensionalized sensitivity (magnitude and direction) of the optimum total life cycle cost for each decision variable.

In case of the SS, the sensitivity of the total life cycle cost associated with the number of cells is more significant than due to the cell length (active area) for the initial synthesis/design, while for the optimum synthesis/design it is just the opposite. In the case of the WRAS, the decision variables do not affect the total life cycle cost of the system much because the purchase cost of the WRAS is much less than that for the other subsystems and certainly much less than the operating cost.

Figure 6.36 illustrates the non-linearity of the PEMFC system developed. As seen in the figure, some decision variables (e.g., the stack operating pressure, HX1 length, steam-to-carbon ratio, and inlet reformat gas temperature of the HTSR) show different directions for different syntheses/designs. Some of other decision variables would probably also show different directions if the sensitivity analysis were carried out for another synthesis/design point. These non-linear behaviors of the system responses due to the decision variables make the system optimization problem highly difficult to solve. In addition, this figure also shows why the non-linear system control is difficult. The typical control architecture of an energy system is designed based on a linearized model of the system, and this linearized model is obtained from a sensitivity analysis of the initial synthesis/design of the system. That controller may not work correctly for other syntheses/designs or operating conditions because of the system non-linearity. Therefore, stability of the controller must be evaluated and updated during the controller design and system optimization process. Wang (2008) focuses on this issue in his dissertation and develops an advanced controller architecture design method for the non-linear system based on the state-space control of multi-inputs and multi-outputs.

One of the important issues in the operation of PEMFC system is to control the CO concentration for all operating conditions and transients to less than a certain limit (e.g., 10 ppm). However, controlling the CO concentration directly is not practical, because it makes the system control architecture more complex and also requires very expensive instruments such as for gas chromatography which can detect the constitution of the flowing gas. Therefore, system synthesis/design and operating conditions should satisfy the CO concentration limitation without a controller by taking this limit into account as a constraint under uncertainty during the synthesis/design and operation/control optimization of the PEMFC system. Uncertainty considerations are important in order that one can have a high degree of confidence that the final system can meet this limitation for all conditions and transients.

Figure 6.37 compares the non-dimensionalized sensitivity of the CO concentration of the outlet gas of the PrOx reactor for each decision variable in the FPS and shows that the CO concentration is very sensitive to the diameter and length of the PrOx reactor, the steam-to-carbon ratio, and the inlet reformat gas temperature of the

HTSR. Increasing the size of the PrOx reactor and inlet reformat gas temperature of the HTSR decreases the CO concentration, while this same concentration increases as the steam-to-carbon ratio increases. In Section 6.1, Figure 6.11 shows that for the SMR, the CO generation decreases with increasing steam-to-carbon ratio. However, the sensitivity study on the PEMFC system above indicates that it increases with increasing steam-to-carbon ratio. As shown in Figure 6.11, the higher the steam-to-carbon ratio is, the less CO is produced in the SMR. Moreover, the water-gas shift reaction in the HTSR and LTSR also favors a higher steam-to-carbon ratio. However, more steam in the reformat gas makes the gas temperature decrease, which causes less CO oxidation in the PrOx reactor. The next effect is that the CO concentration increases with increasing steam-to-carbon ratio.

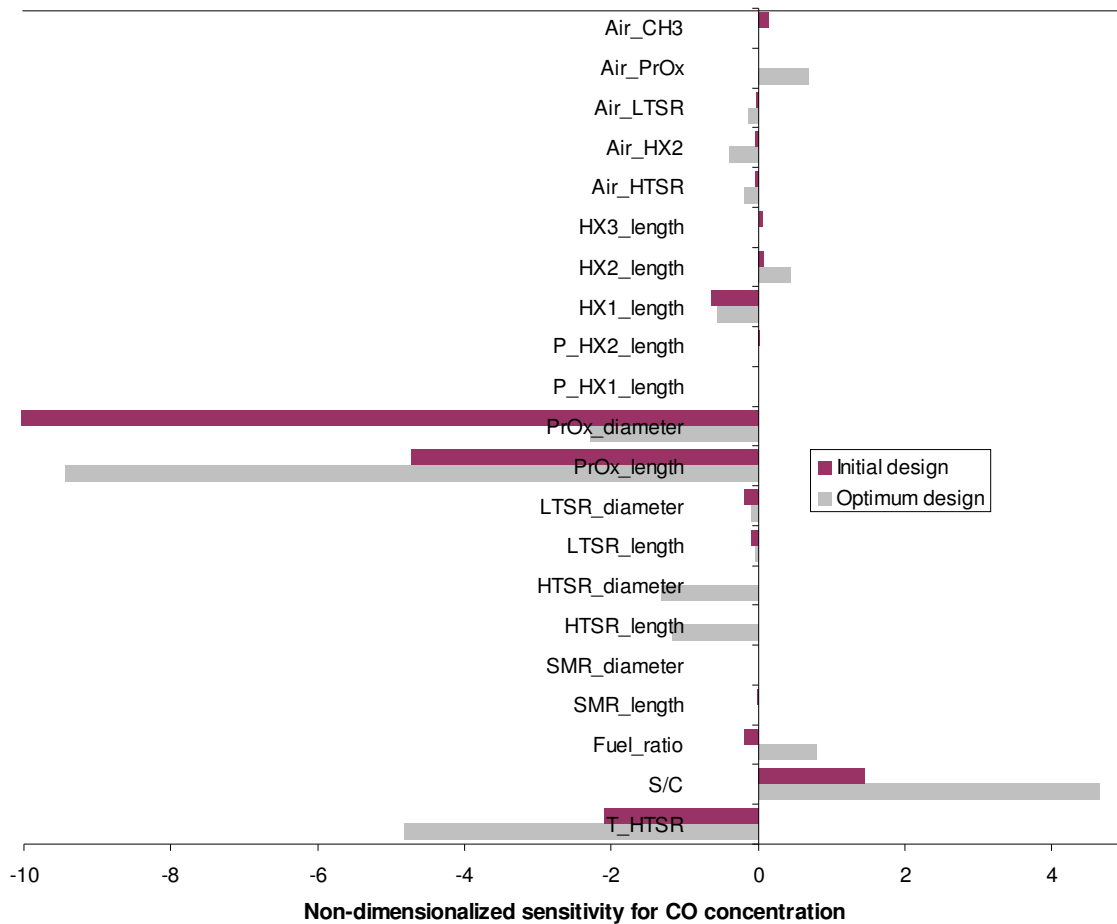


Figure 6.37 Non-dimensionalized sensitivity (magnitude and direction) of the CO concentration of the outlet gas of the PrOx reactor for each decision variable in the FPS.

As seen in Figure 6.37, the PrOx reactor plays an important role in removing CO from the reformat gas. A larger size PrOx reactor can remove more CO, but it also increases the operating cost as depicted in Figure 6.36. Thus, the optimum size of the PrOx reactor must be determined by a system-level optimization, and for the optimization concluded here results in a 0.54 m length and 0.067 m diameter.

6.3.4 Dynamic Responses

6.3.4.1 FPS

The optimum temperature profile of the reformat gas in each reactor over the 48 hour operation is depicted in Figure 6.38. Figure 6.38(a) shows the transient temperature profile of the reformat gas in the SMR. The inlet temperature range of the steam-methane mixture is 950 ~ 1140 K and the outlet temperature range of the reformat gas temperature is 1110 ~ 1200 K. The temperature of the steam-methane-reformat mixture drops drastically at first and then increases gradually through the reactor length. The drastic drop at the start results because a lot of thermal energy is required at the beginning of the reactor where the reaction rate is highest. Furthermore, in order to avoid high temperature gradients (i.e. those between the combustion gases and the steam-methane-reformat mixture), which may cause catalyst sintering problems, a parallel flow configuration is selected in order to supply the thermal energy the most effectively at the start of the reactor while minimizing the radial temperature gradient along the axis of the reactor. Of course, due to the same reason, all the other reactors (i.e. the HTSR, LTSR, and PrOx reactor) also have a parallel configuration.

The transient reformat gas temperature profile in the HTSR increases rapidly at first due to the exothermic reaction, and then decreases gradually as shown in Figure 6.38(b). The inlet temperature of the reformat gas is controlled to 612 K which is determined via the system-level optimization, and the outlet temperature a range of about shows around 635 ~ 640 K.

The transient reformat gas temperature profile in the LSTR is depicted in Figure 6.38(c), and this case reformat gas temperature drops suddenly at the entrance and then continues decreasing along the reactor length. This contrasts with the HTSR where the temperature raises sharply at the inlet to the reactor. In both cases, the reaction

mechanism is exothermic. The difference in behavior, can, however, be explained by the fact that at the lower temperatures of the LTSR, the energy release is much lower than in the HTSR and the cooling air flow in the LTSR absorbs all this energy release and more so that the reformate gas temperature drops suddenly at the start and then continues to decrease the length of the reactor. As seen in the figure, the inlet reformate gas temperature ranges from about 512 ~ 517 K, and the outlet temperature from about 501 ~ 503 K.

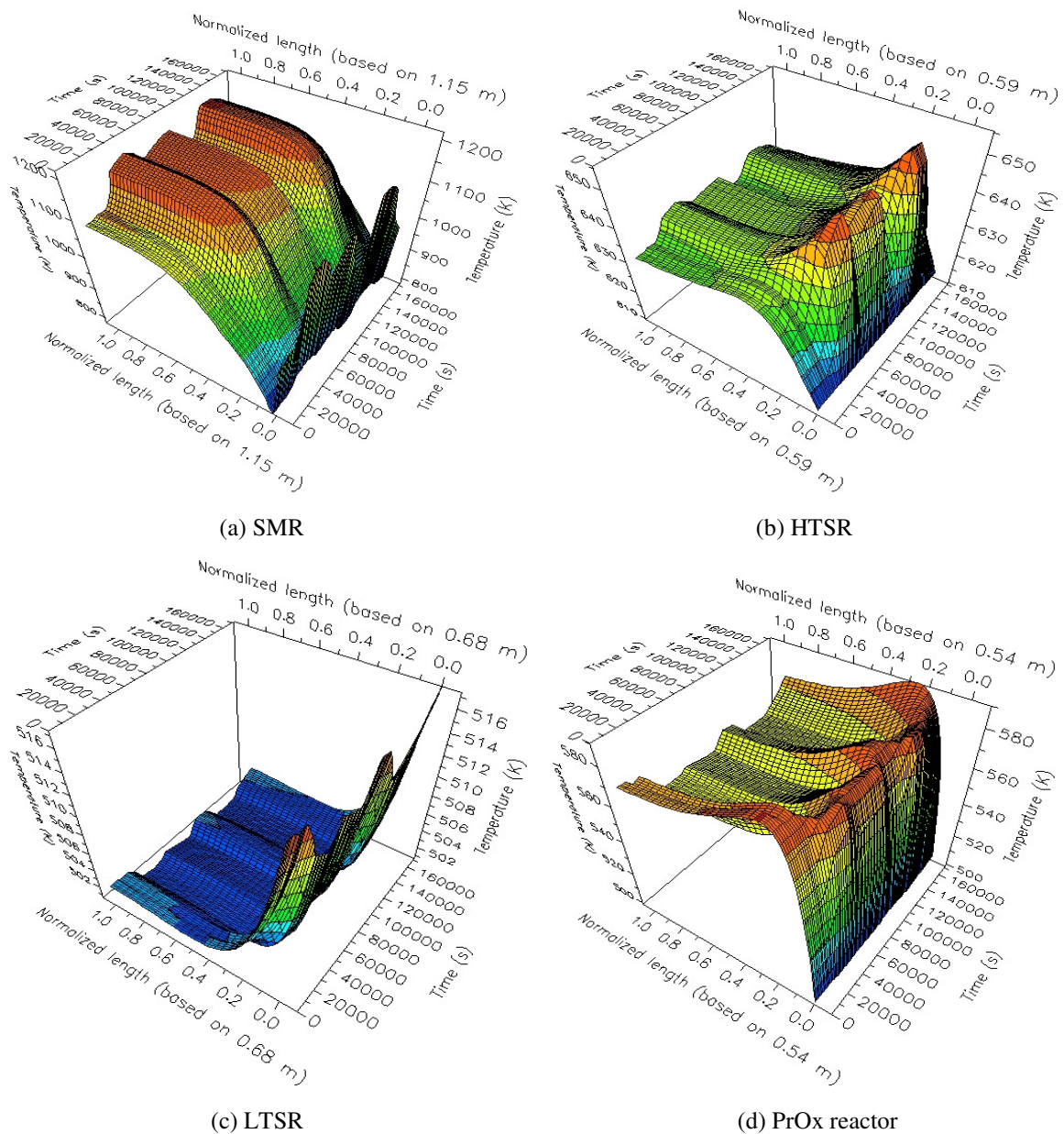


Figure 6.38 3D depiction of the transient reformate gas temperature profile in each reactor.

Like the transient temperature profile in the HTSR, the transient reformate gas temperature profile in the PrOx reactor increases suddenly at the inlet. This increase, however, is almost double that in the HTSR. As seen in Figure 6.38(d), the reformate gas temperature increases swiftly at the beginning of the PrOx reactor because the CO and H₂ oxidation reactions are highly exothermic. The inlet reformate gas temperature is same as the outlet reformate gas temperature of the LTSR, and the outlet temperature of the PrOx reactor ranges from about 560 ~ 570 K.

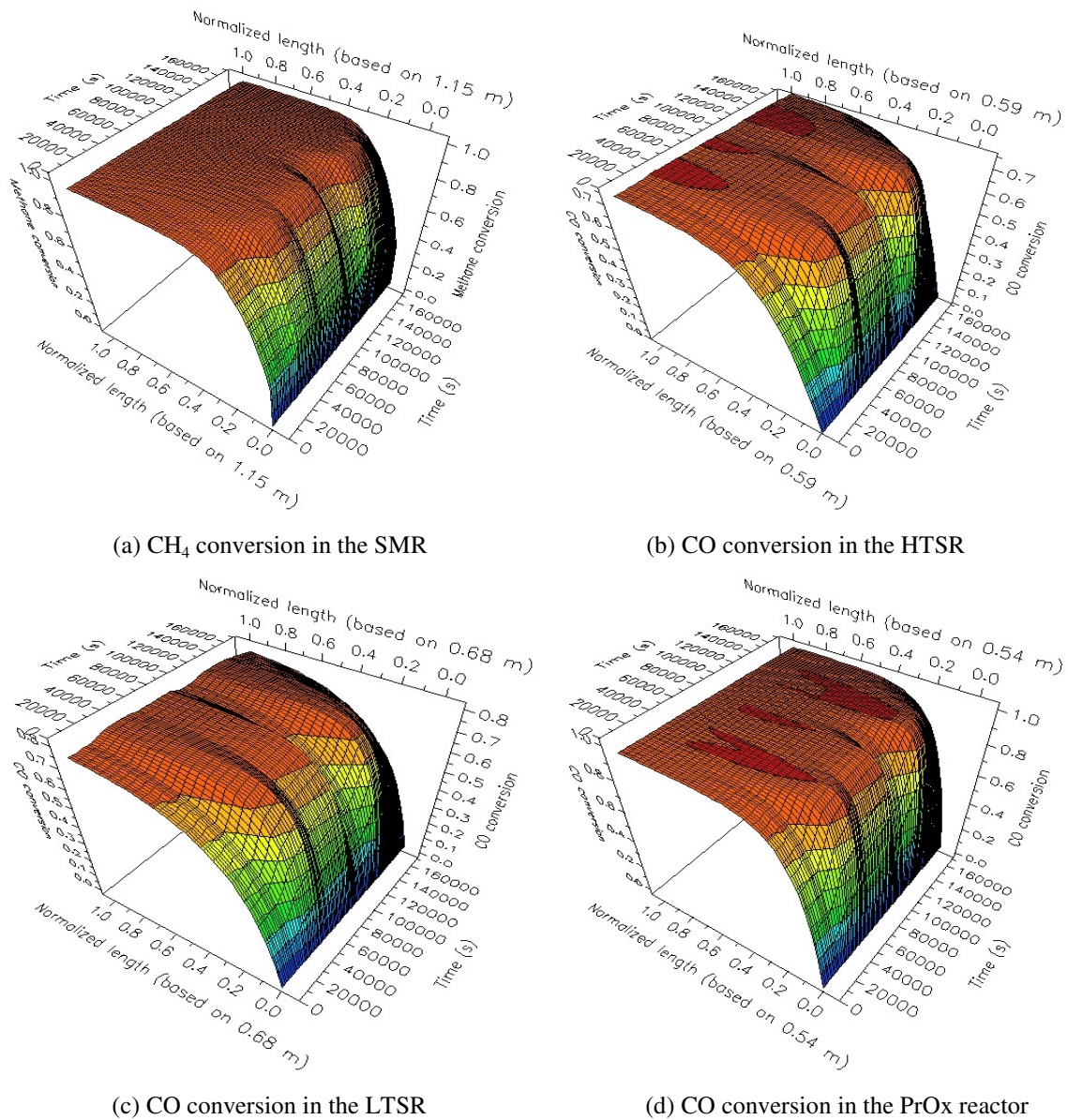


Figure 6.39 3D depiction of CH₄ conversion in the SMR and CO conversion in the HTSR, LTSR, and PrOx reactor.

Performance of each reactor is evaluated in terms of methane conversion for the SMR and CO conversion for the HTSR, LTSR, and PrOx reactor. Figure 6.39 shows these profiles along the reactor length over 48 hours of operation. Methane conversion in the SMR is depicted in Figure 6.39(a). The optimum SMR shows over a 99% methane conversion for the optimum operating conditions through the entire operating regime. The final CO conversions in the HTSR and LTSR show 76% and 78 ~ 81%, respectively, while almost complete conversion of CO (over 99.9%) is achieved by the PrOx reactor as shown in Figure 6.39(d).

In particular, the CO generation (in the SMR) and conversion (in the HTSR, LTSR, and PrOx reactor) are depicted for three different operating points (i.e. at 0 sec - full load, at 43,200 sec - 40% of full load, and at 97,200 sec - 80% of full load) in Figure 6.40. As seen in the figure, CO removal performance in each of the latter three reactors is fairly equal for the three different load conditions, while CO generation in the SMR shows a 2.6% of difference between full load and 40% of full load. CO is generated through the reforming process and the outlet reformat gas from the SMR contains around 14.5% CO in the gas, of which 76% is removed by the HTSR. About 80% of the remainder is eliminated through the LTSR, and the PrOx reactor gets rid of other 20%. The zoomed-in graph on Figure 6.40 shows the CO conversion along the reactor length in the PrOx reactor.

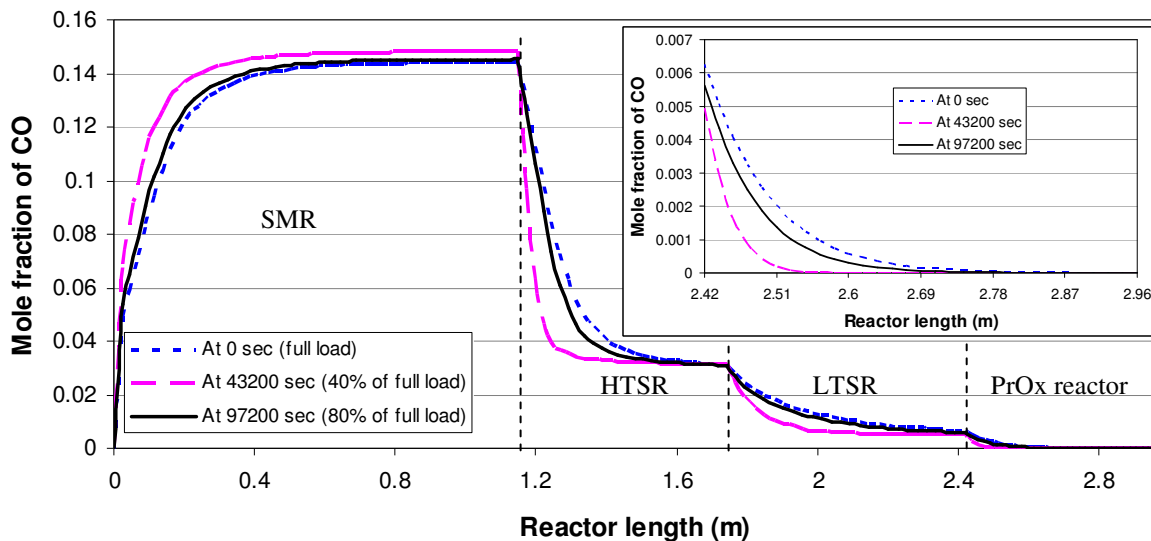


Figure 6.40 CO generation and conversion through reactors for different operating points.

6.3.4.2 SS

The dynamic responses of the cell current density and cell voltage over the 48 hours of operation are depicted in Figure 6.41. In the figure, the optimum responses are compared to the non-optimum (i.e. initial synthesis/design and operating conditions) responses. As seen in the figure, the optimum cell current density is lower than the non-optimum cell current density. Thus, the optimum cell voltage is higher than the non-optimum cell voltage to generate the same amount of electrical power. As explained in Section 6.3.1, the larger size fuel cell consumes less hydrogen, so operating costs are reduced. Through the system-level optimization, about 47% of the initial cell current density is predicted as the optimum cell current density. The optimum dynamic cell current density at the full load condition (at 0 sec) is 0.18 A/cm^2 as compared to 0.38 A/cm^2 for the initial synthesis/design. A 40% of full load (at 43,200 sec), it is about 0.07 A/cm^2 as opposed to the about 0.14 A/cm^2 for the initial system.

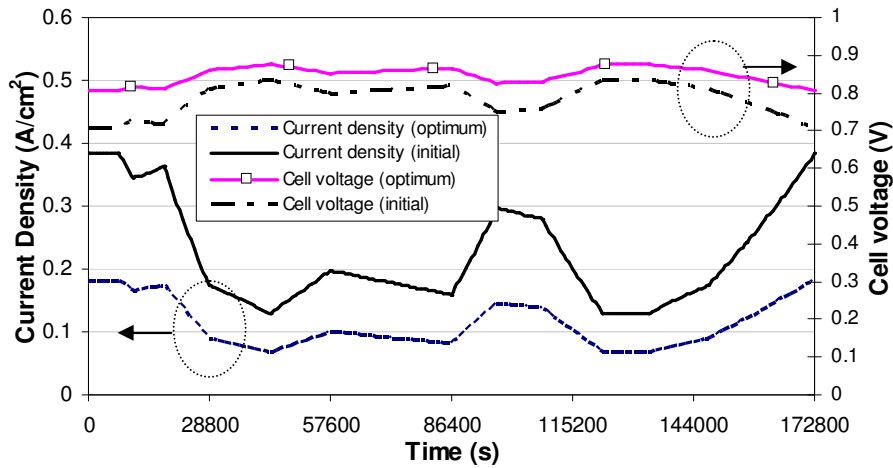


Figure 6.41 Dynamic responses of the cell current density and cell voltage of the optimum and initial syntheses/designs over the 48 hours of operation.

6.3.4.3 WRAS

The optimum dynamic responses of the compressor, expander, and motor work rate are compared in the Figure 6.42 with the dynamic responses of the initial design over the 48 hours of operation. The un-optimized initial design of the compressor requires 95 W of more work rate at the full load condition (at 0 sec) and 40 W more at 40% of full load (at 43,200) than the optimum compressor. In the case of the expander unit, the un-

optimized initial design of the expander recovers 35 W more at full load and 9 W more at 40% of full load than the optimum design. Therefore, taking into account the initial un-optimized motor design, the un-optimized initial design of the compressor needs an additional 61 W of work at full load and 42 W more at 40% of full load. This is the case because for the initial motor, which is un-optimized (i.e. the optimum motor performance is better than that of the un-optimized one), the additional motor work rate is slightly higher than the difference between the additional work for the compressor (i.e. 95 W at full load and 40 W at 40% of full load) and additional work recovered by expander (i.e. 35 W at full load and 9 W at 40% of full load).

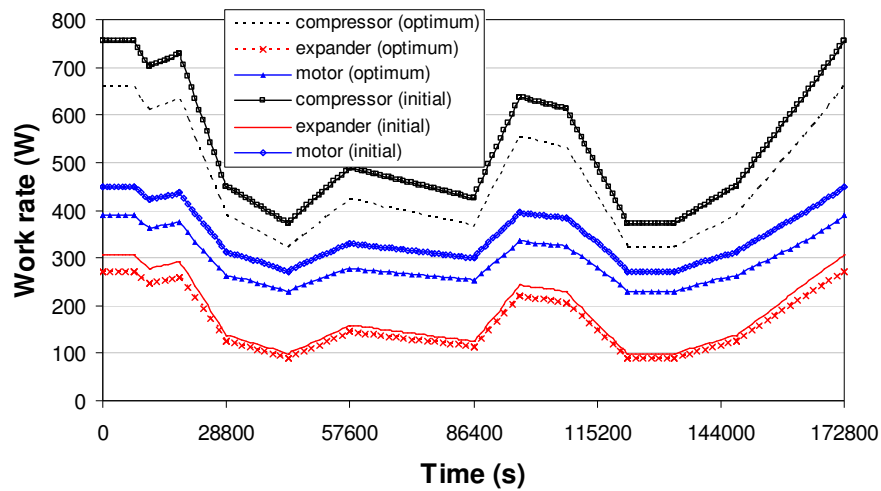


Figure 6.42 Dynamic responses of the compressor, expander, and motor work rate for the optimum and initial designs over the 48 hours of operation.

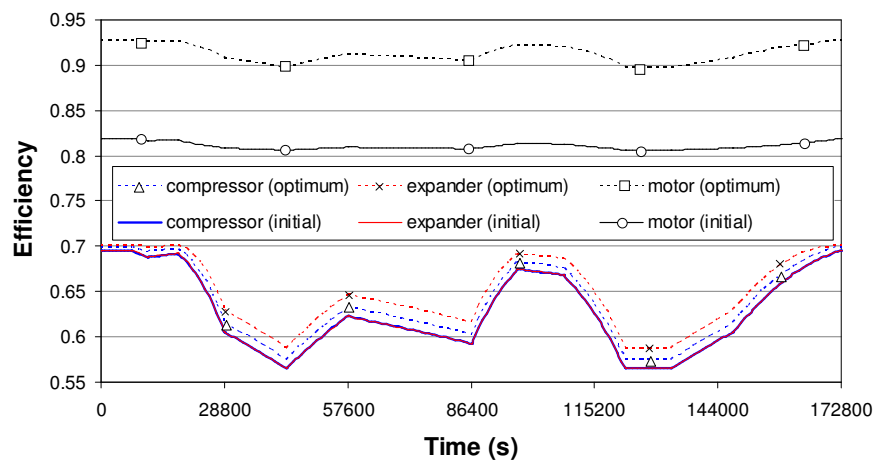


Figure 6.43 Dynamic responses of the compressor, expander, and motor operating efficiency for the optimum and initial designs over the 48 hours operation.

The optimum and un-optimized operating efficiency of each component is compared in Figure 6.43 over the 48 hours of operation. In particular, the optimum motor efficiency ranges from about 89 ~ 92% through the entire operating regime, while the un-optimized initial motor efficiency ranges from about 81 ~ 82%. Initial designs of the compressor and expander show less than a 0.1% difference between both dynamic efficiencies over the 48 hours, because the un-optimized performance maps for both units are derivatives of each other. However, the optimum efficiencies of the compressor and expander, which are higher than those of the un-optimized initial compressor and expander, show more of a difference since that of the expander is a little bit higher than that of the compressor as seen in the figure.

The performance of the WRAS can also be expressed in terms of the work recovery rate which is the rate of the work recovered by the expander for the required work of the compressor. This is described in Figure 6.44 which compares the work recovery rate of the optimum design and that of the un-optimized initial design. The optimum WRAS recovers about 41% with the required compressor work by the expander unit at full load, and about 28.5% at 40% of full load. The work recovery rate of the optimum WRAS is from 0.5% (at full load) to 1.5% (at 40% of full load) higher than that of the un-optimized initial WRAS as seen in the figure.

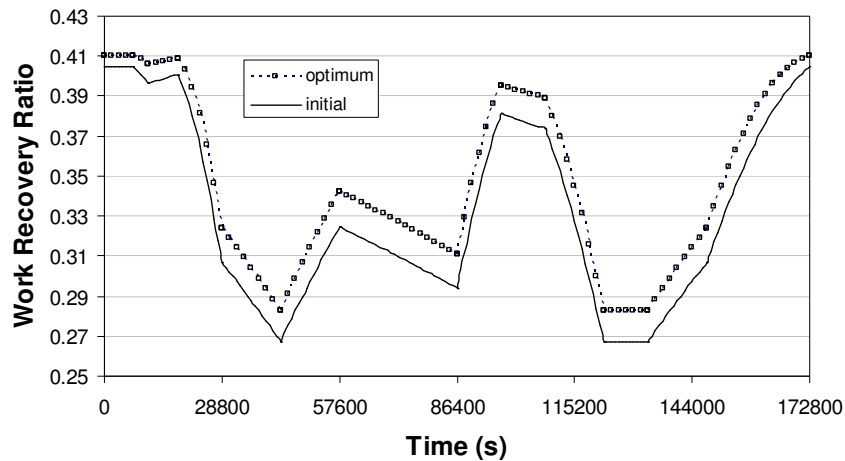


Figure 6.44 Comparison of the optimum and initial work recovery ratio by the expander.

The optimum performance maps of the compressor, expander, and motor are illustrated in Figures 6.45 to 6.47, and Table 6.13 shows the operating characteristics of

the optimum WRAS at the full load and at part load (40% of full load). The inside axes on each map represent the original map and the outside axes the optimum one determined by the system-level optimization. The symbol u and l on the x-axis indicate the full load point and the part load point of 40% of full load. The bold line on each map indicates the operating line which all the operating factors (e.g., the rotor speed factor, pressure ratio, mass flow factor for the compressor and expander, and the motor torque and rotational speed for the motor) follow. Thus, the efficiency of each component for a certain set of operating factors can be determined on the map and is used for determining the dynamic behavior of the WRAS.

Table 6.13 Operating characteristic of the optimum WRAS.

Unit	Rotational speed (rpm)		Mass flow rate factor ($\text{kgT}^{0.5}/\text{s bar}$)		Motor torque (Nm)		Pressure ratio
	Max	Min	Max	min	max	min	
Compressor	15332	7977	0.10395	0.04148	-	-	2.22
Expander	15332	7977	0.1032	0.041775	-	-	2.176
Motor	1916	997	-	-	2.303	2.129	-

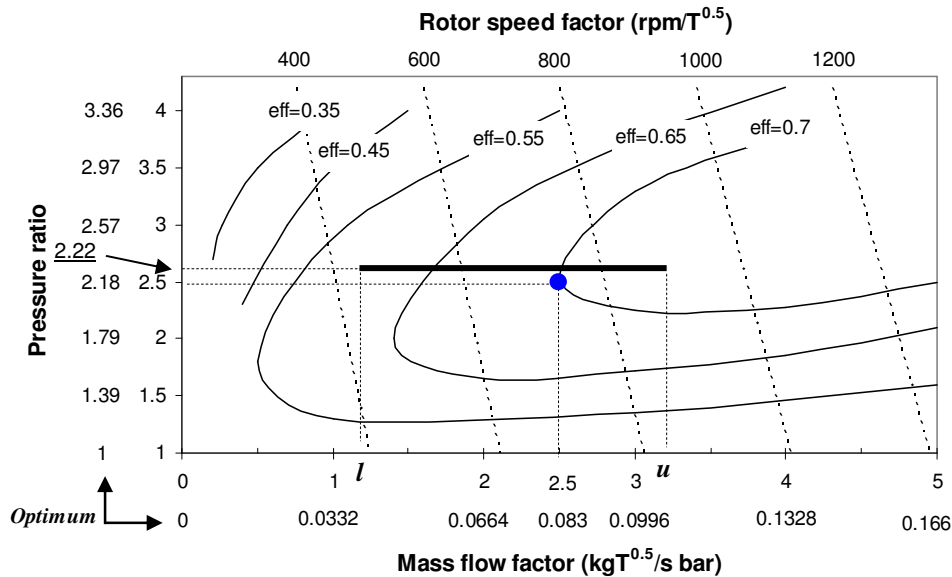


Figure 6.45 Optimal performance map of the compressor for the 5 kWe PEMFC system.

As seen in Figures 6.45 and 6.46, the pressure ratio of the compressor is assumed as a constant operating condition, and the optimum pressure ratio 2.22 is obtained by the

system-level optimization of the PEMFC system. As a result of this, the pressure ratio in the expander is also constant. However, the optimum torque-rotational speed line on the motor map shows a slight curvature because the motor torque varies according to the required torque and speed of the compressor-expander unit. As described in Figure 6.48, the maximum motor torque appears at 40% of full load, while the minimum motor torque occurs at 80% of full load.

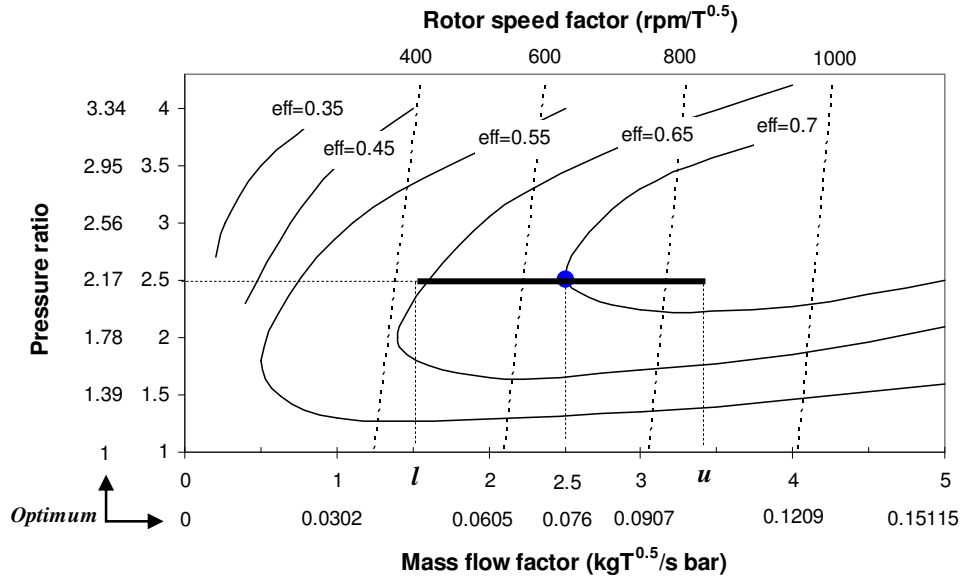


Figure 6.46 Optimal performance map of the expander for the 5 kW PEMFC system.

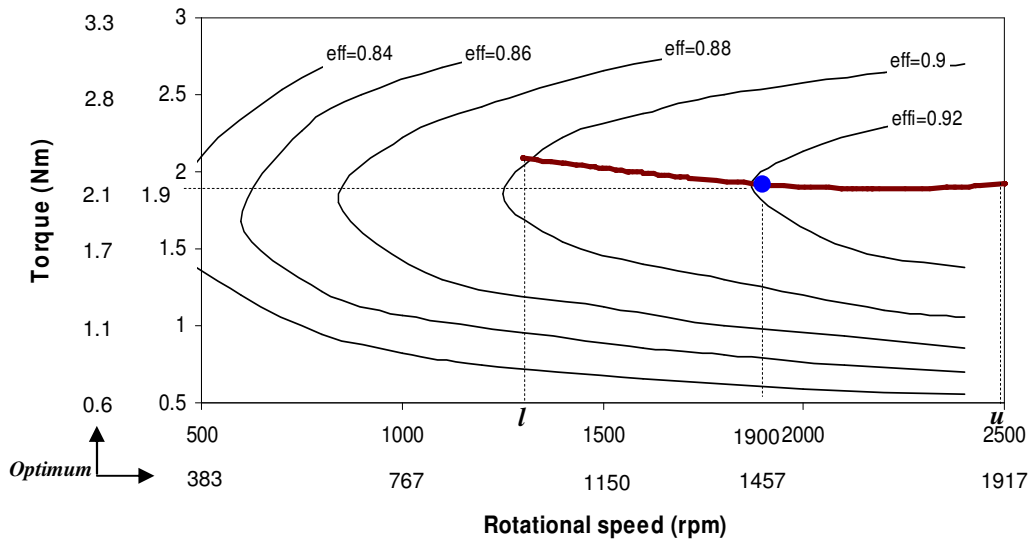


Figure 6.47 Optimal performance map of the motor for the 5 kW PEMFC system.

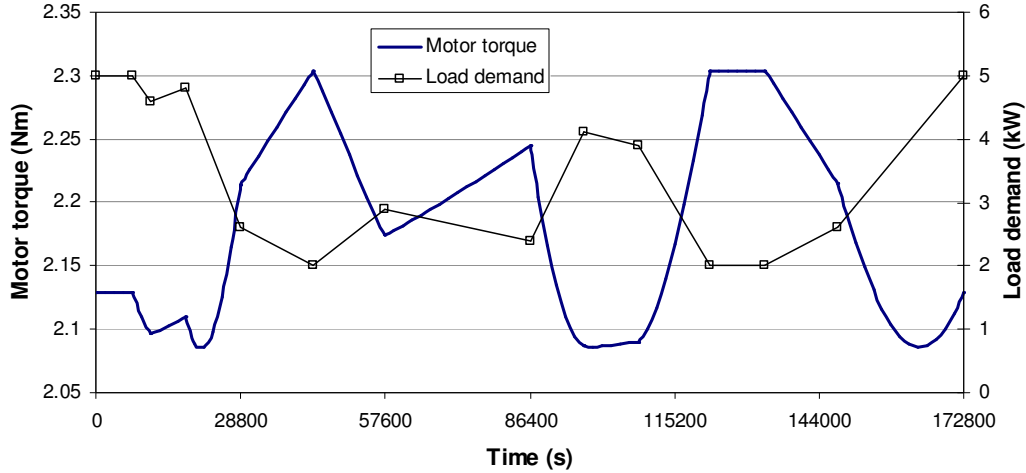


Figure 6.48 Optimum dynamic responses of the motor torque.

6.3.5 System Efficiencies

The efficiencies of the FPS and the PEMFC system are evaluated in this section and are defined as follow:

$$\eta_{FPS} = \frac{\dot{m}_{H_2} LHV_{H_2}}{(\dot{m}_{CH_4}^{SMR} + \dot{m}_{CH_4}^{BR})LHV_{CH_4} + \dot{m}_{H_2}^{BR} LHV_{H_2}} \quad (6.7)$$

$$\eta_{PEMFC} = \frac{\dot{E}_{net}}{(\dot{m}_{CH_4}^{SMR} + \dot{m}_{CH_4}^{BR})LHV_{CH_4}} \quad (6.8)$$

where η_{FPS} and η_{PEMFC} are the FPS and PEMFC system efficiencies. $\dot{m}_{CH_4}^{SMR}$, $\dot{m}_{CH_4}^{BR}$, and $\dot{m}_{H_2}^{BR}$ are the methane flow rates to the SMR and burner and the hydrogen flow rate to the burner, respectively. LHV_{CH_4} and LHV_{H_2} are the lower heating values of the methane and hydrogen, and \dot{E}_{net} is the system net power. Un-reacted hydrogen in the stack is fed into the burner. As a result of this, the overall system efficiency is improved.

Figure 6.49 shows the dynamic optimum FPS efficiency over the 48 hours of operation and compares with that for the un-optimized initial FPS. The optimum FPS efficiency ranges from about 85.6 ~ 86.1% through entire operating regime, while that for the un-optimized initial FPS varies from about 77.9 ~ 78.5%. Initially, a 0.42 fuel ratio is assumed and 0.305 is obtained from the optimization, which principally leads to an 8% efficiency enhancement of the FPS.

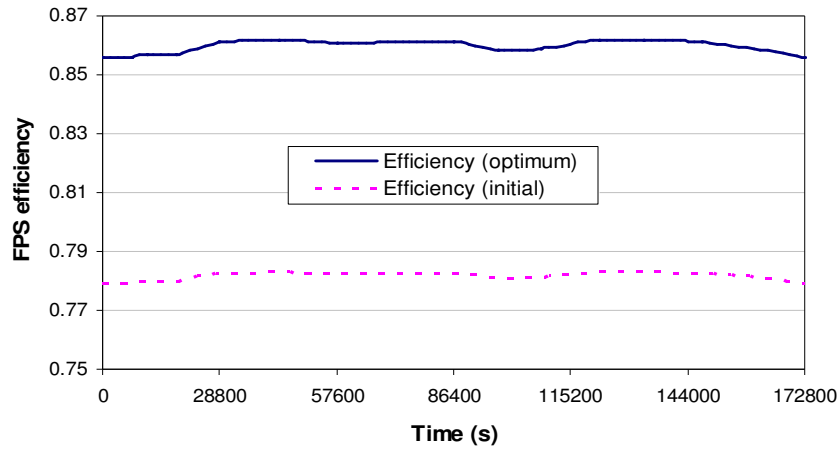


Figure 6.49 Comparison of the optimum and un-optimized initial FPS efficiencies.

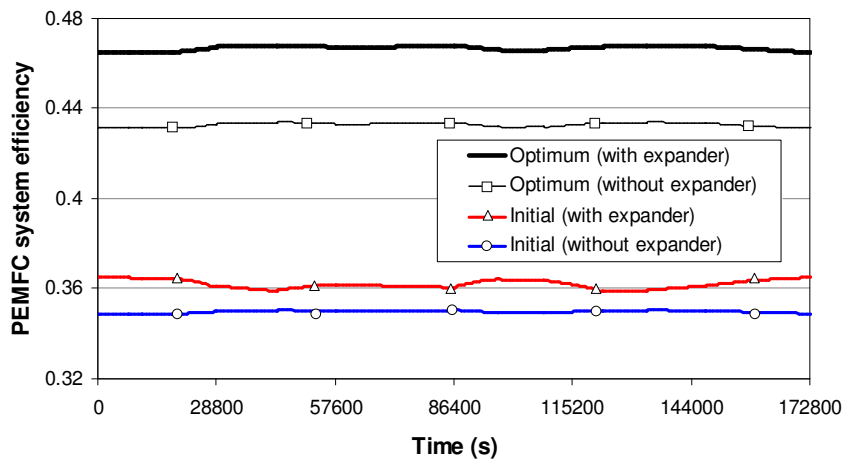


Figure 6.50 Comparison of the optimum and un-optimized initial PEMFC system efficiencies with/without the expander unit.

The optimum overall system efficiency of the PEMFC system is described in Figure 6.50 is compared with that of the un-optimized initial PEMFC system. The optimum efficiency of the PEMFC system remains fairly steady at 46.5% throughout the operating regime, while that for the un-optimized initial system ranges from about 36 ~ 36.5%. Thus, the overall system efficiency increased by 10 percentage points through the optimization process, a 27.4% improvement which is huge. The main reason for the improvement is that the hydrogen fuel consumption of the optimum PEMFC system is reduced a lot compared to the un-optimized initial PEMFC system. The initial design of the stack requires 0.0496 mol/s of hydrogen at full load but only 0.0436 mol/s for the optimum stack.

The effects of the work recovery unit using the expander are evaluated in terms of the PEMFC system efficiency in Figure 6.50 as well. As seen in the figure, the system efficiency is enhanced by 3.4 percentage points by using the work recovery unit for the optimum PEMFC system, and by only 1.2 percentage points for the un-optimized initial PEMFC system.

6.3.5 Comparison with Gradient-based Optimization Results of Wang (2008)

The synthesis/design and operation/control optimization of the 5 kWe PEMFC system developed is carried out for the same system in two different ways. Wang (2008) conducts the dynamic system optimization using a gradient-based optimization algorithm (i.e. SQP) in his doctoral research, and a hybrid heuristic/gradient-based optimization algorithm (i.e. SEQOPT which is a kind of SMBO algorithm) is used in this doctoral research. One additional difference is that in Wang (2008), the gains are treated as decision variables while in the present research they are fixed at values determined by Wang in a preliminary analysis. Thus in this present doctoral research, they are un-optimized. However, this difference cannot be the reason for the significant difference in operating costs observed here because the given load profile does not have sudden changes on it which can increase the operating cost at the transition regime. Thus, it is assumed that the difference in operating costs is due primarily to the different optimization algorithms used.

Both optimization algorithms have different characteristics as mentioned in Chapter 5. The gradient-based optimization algorithms are simple to apply and have a lower computational burden but easily get stuck at local minima points. In contrast, the SMBO algorithms (e.g., the SEQOPT) are somewhat more computationally expensive than the gradient-based algorithms but much less computationally expensive than, for example, GAs. Furthermore, they show good characteristics for finding global optimum for non-linear system optimization problems.

The optimization results from both approaches are compared in Table 6.14. An optimum total life cycle cost of \$42,445 is obtained by Wang, while this work \$38,077 is found. Most of the difference between them is due to the optimum operating cost, i.e. \$32,826 and \$27,713, respectively. However, there is only a \$745 difference in the total capital costs between the two.

Operating cost is directly related to the hydrogen consumption rate by the stack and to the methane consumption rate by the combustor. Table 6.15 helps to understand why there is such a big difference between both optimum operating costs. Three decision variables which affect significantly the fuel and hydrogen consumption rate are compared in the table. First of all, the optimum fuel ratio of 0.305 is obtained in this work, while the gradient-based optimization finds 0.351 as the optimum value. If 0.351 is used for the optimum system found in this work, the operating cost is increased by \$1,450. As addressed in the previous section, the bigger size of stack is favored because it reduces the hydrogen consumption rate. As seen in the table, the gradient-based optimization finds a smaller size stack (i.e. 0.0784 m² for the single cell active area and 3.2928 m² for the total stack active area) than in this work (i.e. 0.1274 m² for the single cell active area and 3.6960 m² for the total stack active area). As a result, in this work, 0.0436 mol/s of hydrogen consumption rate is required at full load, while 0.0442 mol/s is needed at full load in the gradient-based optimization. This difference adds an additional \$750 to the operating cost. Thus, about \$2,200 difference are added to the operating costs just by the optimum values of these three decision variables, i.e. ξ_{CH_4} , L^{SS} , and N^{SS} .

Table 6.14 Comparison the optimum total life cycle cost of the 5 kWe PMEFC system obtained by Wang (2008) and this work.

	Capital cost (\$)			Operating cost (\$)	Total life cycle cost (\$)
	FPS	SS	WRAS		
Non-gradient-based (this work)	5256	4052	1057	27713	38077
Gradient-based (Wang, 2008)	4705	3693	1222	32826	42445
Difference (\$)	551	359	-165	-5113	-4368

Table 6.15 Comparison optimum values of some major decision variables obtained by Wang (2008) and this work.

Major decision variables	ξ_{CH_4}	L^{SS} (m)	N^{SS}
Non-gradient-based (this work)	0.305	0.357	29
Gradient-based (Wang, 2008)	0.351	0.28	42

The remaining \$2,913 difference between the two solutions can be attributed to the different size of the FPS. As shown in Figure 6.23, the smaller FPS consumes more

fuel, if it is located on the left side of the global optimum point. The optimum FPS determined by this work is placed close to the global optimum point, but the optimum FPS of Wang is located on the left-upper side of the global optimum point in the figure. That is why the optimum FPS determined by the gradient optimization consumes much more fuel. This comparison shows that the SEQOPT shows better search capabilities for finding the global optimum than the gradient-based optimization.

CHAPTER 7

CONCLUSIONS

A 5 kWe PEMFC system for a residential application is developed in this doctoral research, and the system synthesis/design and operation/control optimization under uncertainty is carried out using a physical decomposition strategy (i.e. the dynamic iterative local-global optimization (DILGO) approach). This study leads to a number of conclusions and these are summarized as follow:

1. Several uncertainty analysis methods (i.e. Monte Carlo simulation (MCS), fast probability integration (FPI), and response sensitivity analysis (RSA)) have been evaluated. As seen in Chapter 4, the RSA method is the most appropriate way to describe the uncertainties in the dynamic simulation of energy systems due to its efficiency in computation. However, the RSA method is an approximate method so that the uncertainty analysis results generated must be evaluated by comparisons with the MCS which can provide exact uncertainty results. In this research, the RSA method shows high accuracy when compared to the MCS, showing a difference of less than 1%. Therefore, it is a useful approach for uncertainty analysis in dynamic energy system optimization problems.
2. Sensitivity analysis of the PEMFC system has been carried out and it shows highly non-linear characteristics of the system. Non-linear behaviors of the system responses due to the decision variables make the system optimization problem and control architecture design highly difficult to solve. The typical control architecture of an energy system is designed based on a linearized model of the system, and this linearized model is obtained from a sensitivity analysis of the initial synthesis/design of the system. That controller may not work correctly for other syntheses/designs or operating conditions because of the system non-

- linearity. Therefore, stability of the controller must be evaluated and updated during the controller design and system optimization process.
3. A hybrid heuristic/gradient-based optimization algorithm, Sequential Approximate Optimization (SEQOPT), has been used during this doctoral research, and its efficiency for finding the global optimum point is proven by comparing with the gradient-based optimization algorithm used by Wang (2008). Gradient-based optimization algorithms easily get stuck at local minima as demonstrated by the fuel processing subsystem (FPS) optimization results of Wang which result in a local optimum point which causes a big difference in the operating costs between Wang's result and the result in this study. Therefore, if a gradient-based algorithm is used for highly non-linear system optimization problems, a number of optimizations from a different set of initial points must be carried out in order to develop confidence in the globality of the solution. However, even with multiple optimizations this may not be achievable.
 4. Uncertainty effects on the energy system synthesis/design and operation/control optimization have been assessed using the FPS by taking the uncertainties into account in the objectives and constraints. As seen in Sections 5.4.2 and 6.2, there is little effect on the objective (the operating cost and capital cost), while the constraints (e.g., on the CO concentration) may be significantly affected during the synthesis/design and operation/control optimization. These can be depicted by using the Pareto set as shown in Figure 6.24.
 5. The multi-objective optimization for the energy system synthesis/design provides a number of benefits. Most of all, multi-objective optimization provides a range of possible synthesis/design solutions which can be traded off against one another. Multi-objective optimization also offers a logical procedure for searching for the global optimum solution. The multi-objective optimization for the FPS synthesis/design and operation/control is carried out by optimizing the objectives individually, and it finds the global optimum in the 5th iteration.
 6. The proton exchange membrane fuel cell (PEMFC) systems promises higher system efficiencies compared to conventional power generation systems such as

internal combustion engines and steam and gas turbine systems. The optimum synthesis/design of the PEMFC system developed here shows a fairly steady and remarkably high overall system efficiency at 46.5% throughout the operating regime (i.e. full load to 40% of full load). This system efficiency is the highest of the PEMFC system efficiencies reported in the literature. The reason is that all design issues (i.e. synthesis/design and operation/control) are taken into account in one optimization problem so that all the optimum values are achievable.

7. Decomposition techniques are a very useful strategy for large-scale energy system optimization as demonstrated in previous chapters. In particular, the overall system model with its complex control architecture and very detailed component models causes a large computational burden and quite often simulation failure during a dynamic optimization. Fortunately, the optimization of the complex system model and control architecture can be treated as a set of approximate smaller unit(subsystem)-level optimization problems via a decomposition strategy which minimizes the loss of system-level information. A physical decomposition approach (i.e. DILGO) is successfully applied to the synthesis/design and operation/control optimization of the dynamic PEMFC system, and the global optimum solution is found within 6 iterations by DILGO.
8. The operating cost dominates the life cycle cost of the energy system (fuel cell system) during the optimizations. Thus, minimizing the fuel consumption rate by the system is of great importance. The optimum synthesis/design of the FPS plays a very important role in the entire PEMFC system synthesis/design and operation/control optimization problem because most of the additional fuel consumption in the PEMFC system occurs during the fuel processing (e.g., the hydrogen oxidation reactions in the CO preferential oxidation (PrOx) reactor, fuel for the combustor, poor reforming performance, etc.). The large cell active area also favors the reduction in the fuel consumption rate as seen in Chapter 6.
9. The system efficiency is enhanced by 3.4 percentage points by using the work recovery unit for the optimum PEMFC system. In the WRAS synthesis/design and operation/control optimization problem, finding the optimum design of the

motor is more important than those of the compressor and expander because there is significant improvement in the motor design while little improvement occurs in the compressor and expander designs (see Figure 6.42).

10. The optimum purchase cost of the PEMFC is highly dependent on the production volume per year and \$744.0/kWe for 500,000 production units per year is competitive with conventional technologies in many small-scale stationary power markets. Even at 100,000 production units per year, the fuel cell system remains competitive in a number of markets, \$1,344.5/kWe. Therefore, mass production of fuel cell systems will be required for commercialization.
11. Finally, this doctoral work provides an effective way to deal with a dynamic fuel cell system synthesis/design and operation/control optimization under uncertainty into a single problem. This proposed paradigm can be applied to any other energy system development tasks.

References

- Adams, B.M., April 2006, Uncertainty Quantification and reliability analysis-based design optimization capabilities in DAKOTA, *9th Copper Mountain Conference on Iterative Methods*.
- Ahluwalia, R., Wang, X., and Kumar, R., 2003, Fuel cell systems analysis, *Hydrogen, Fuel Cell, and Infrastructure Technologies*, DOE Progress Report.
- Amadeo, N.E. and Laborde, M.A., 2006, Hydrogen production from the low-temperature water-gas shift reaction: Kinetics and simulation of the industrial reactor, *International Journal of Hydrogen Energy*, Vol. 20, No. 12, pp 949-956.
- Amphlett, J.C., Mann, R.F., and Peppley, B.A., 1996, On board hydrogen purification for steam reformation/PEM fuel cell vehicle power plants, *International Journal of Hydrogen Energy*, Vol. 21, No. 8, pp 673-678.
- Ang, A.H-S and Tang, W.H., 1984, Probability concepts in engineering design, Vol. 2: Decision, risk, and reliability, Wiley, New York.
- Arsie, I. and Domenico A., 2005, Transient analysis of PEM fuel cell for hybrid vehicle application, Proceedings of FUELCELL2005, 3rd International Conference on Fuel Cell Science, Engineering and Technology, May 23-25, 2005, Ypsilanti, Michigan.
- Arthur D. Little, Inc., 2001, Conceptual Design of POX/SOFC 5kW net system, The final report for the Department of Energy Technology Laboratory.
- Audet, C., Dennis, J.E., Moore, D., Booker, A., and Frank, P., 2000, A surrogate-model-based method for constrained optimization, Proceedings of the eighth AIAA/USAF/NASA/ISSMO symposium on multidisciplinary analysis & optimization, Long Beach, CA, Paper no. 2000-4891, AIAA.
- Bansal, V. and Perkins, J.D., Piskikopoulos, E.N., Ross, R., van Schijndel, J.M.C.,

2000, Simultaneous design and control optimization under uncertainty, *Computer and Chemical Engineering*, Vol. 24, pp 261-266.

Baratto, F., Diwekar, U., and Manca, D., 2005a, Impacts assesment and trade-offs of fuel cell-based auxiliary power units Part I: System performance and cost modeling, *Journal of Power Sources*, Vol. 139, pp 205-213.

Baratto, F., Diwekar, U., and Manca, D., 2005b, Impacts assesment and trade-offs of fuel cell-based auxiliary power units Part II: Environments and health impacts, LCA, and multi-objective optimization, *Journal of Power Sources*, Vol. 139, pp 214-222.

Bird, R.B., Stewart, W.E., and Lightfoot, E.N., 1960, Transport phenomena, John Wiley & Sons, New York.

Bissett, E.J. and Oh, S.H., 2005, PrOx reactor model for fuel cell feedstream processing, *Chemical Engineering Science*, 60, pp 4722-4735.

Borgas, D.J. and Campbell, J.S., 1974, Design and operation of CO shift, naphtha and natural gas, Marcel Dekker, Inc., New York.

Bowers, B.J., Zhao, J.L., Ruffo, M., Khan, R., Dattatraya, D., Dushman, N., Beziat, J.C., and Boudjemaa, F., 2007, Onboard fuel processor for PEM fuel cell vehicles, *Hydrogen Energy*, Volume 32, Issues 10-11, pp 1437-1442.

Calise, F., Accadia, M., Vanoli, L., and von Spakovsky, M., 2007, Full load synthesis/design optimization of a hybrid SOFC-GT power plant, *Energy*, Vol. 32, pp 446-458

Calise, F., Accadia, M., Vanoli, L., and von Spakovsky, M., 2006, Single-level optimization of a hybrid SOFC-GT power plant, *Journal of Power Sources*, Vol. 159, pp 1169-1185

Ceraolo, M., Miulli, C., and Pozio, A., 2002, Modeling static and dynamic behavior of proton exchange membrane fuel cells on the basis of electro-chemical description, *Journal of Power Sources*, Vol. 113, pp 131-144.

Carlson, P., Kopf, P., Sinha, J., Sriramulu, S., and Yang, Y., 2005, Cost analysis of

PEM fuel cell system for transportation, Subcontract report NREL/SR-560-39104, TIAX LLC, Cambridge, Massachusetts.

Chemical Power Plant Cost Index, *Chemical Engineering*, September, 2006.

Chen, Y.H., Yu, C.C., Liu, Y.C., and Lee, C.H., 2006, Start-up strategies of an experimental fuel processor, *Journal of Power Sources*, Vol. 160, pp 1275-1286.

Choi, D., Lee, J., Kwon, O., Kim, J., and Kim, K., 2007, Sulfonated poly(fluorinated arylene ether)s/poly(N-vinylimidazole) blend polymer and PTFE layered membrane for operating PEMFC at high temperature, *Journal of Power Sources*, doi:10.1016/2007.08.054.

Choi, Y. and Stenger, H.G., 2003, Water gas shift reaction kinetics and reactor modeling for fuel cell grade hydrogen, *Journal of Power Source*, 124, pp 432-439.

Choi, Y. and Stenger, H.G., 2004, Kinetics, Simulation and insights for CO selective oxidation in fuel cell applications. *Journal of Power Source*, Vol. 129, pp 246-254.

Choi, Y. and Stenger, H.G., 2005, Kinetics, simulation and optimization of methanol steam reformer for fuel cell applications, *Journal of Power Source*, 142, pp 81-91.

Chin, S.Y., Alexeev, O.S., and Amiridis, M.D., 2005, Preferential oxidation of CO under excess H₂ conditions over Ru catalyst, *Applied Catalysis A: General*, 286, pp 157-166.

Choi, Y. and Stenger, H.G., 2004, Kinetics, Simulation and insights for CO selective oxidation in fuel cell applications. *Journal of Power Source*, Vol. 129, pp 246-254.

Couper, J.R., Penny, W.R., Fair, J.R., and Walas, S.M., 2005, *Chemical Process Equipment: Selection and Design*, 2nd edition, Elsevier.

Diwekar, U., Rubin, E.S., and Frey, H.C., 1997, Optimal design of advanced power systems under uncertainty, *Energy Conversion and Management*, Vol. 38, No. 15-17, pp1725-1735.

Eills, M.W. and Gunes, B., 2002, Status of fuel cell systems for combined heat and power applications in buildings, *ASHRAE Transactions*, Vol. 108, No. 1, pp 1032-

1044.

Energy Information Administration, 2006, "U.S. Natural Gas Prices", <http://www.eia.doe.gov>.

Energy Nexus Group., 2002, Technology characterization-micro-turbines.

Energy Nexus Group., 2002, Technology characterization-fuel cells.

Etouney, H.M., Shaban, H.I., and Nayfeh, L.J., 1995, Theoretical analysis of high and low temperature shift converters, *Chemical Engineering Community*; Vol. 134, pp 1-16.

Feehery, W.F., Tolsma, J.E., and Barton, P.I., 1997, Efficiency sensitivity analysis of large-scale differential-algebraic, *Applied Numerical Mathematics*, Vol. 25, pp 41-54.

Fogler, H.S., 1997, Element of chemical reaction engineering, Prentice-Hall International, Inc.

Fuel cell report to congress, 2003, Department of Energy.

Fuel Cell Handbook, 2004, 7th edition, Office of Fossil Energy, National Energy Technology Laboratory, Morgantown, West Virginia.

Galambos, J.D. and Holmes, J.A., 1997, Efficient treatment of uncertainty in numerical optimization, *Risk Analysis*, Vol. 17, No. 1, pp 93-96.

Gamou, S., Yokoyama, R., and Ito, K., 2002, Optimal unit sizing of cogeneration systems in consideration of uncertainty energy demands as continuous random variables, *Energy Conversion and Management*, 43, pp 1349-1361.

Georgopoulos, N., 2002, Application of a Decomposition Strategy to the Optimal Synthesis/Design and Operation of a Fuel Cell Based Total Energy System, M.S. thesis, Department of Mechanical Engineering, Virginia Polytechnic Institute and State University, Blacksburg, VA.

Goerke, O., Pfeifer, P., and Schubert, K., 2004, Water gas shift reaction and selective oxidation of CO in microreactors, *Applied Catalysis A: General*, 263, pp 11-18.

- Giunata, P., Amadeo, N., and Laborde, M., 2006, Simulation of a low temperature water gas shift reactor using the heterogeneous model/application to a PEM fuel cell, *Journal of Power Source*, 156, pp 489-496.
- Gorke, O. and Schubert, P.P.K., 2004, Water gas shift reaction and selective oxidation of CO in microreactors, *Applied Catalyst, General* 263, pp 11-18.
- Gorla, R., 2004, Probability analysis of a solid oxide fuel cell based hybrid gas turbine system, *Applied Energy*, 78, pp 63-74.
- Haldar, A. and Mahadevan, S., 2000, Probability, reliability, and statistical methods in engineering design, John Wiley & Sons, New York.
- Haslego, C. and Polley, G, September 2002, Compact Heat Exchanger – Part I: Designing plate-and-frame heat exchangers, *Chemical Engineering Progress*.
- Hasofer, A.M. and Lind, N.C., 1974, Exact and invariant second moment code format, *Journal of Engineering Mechanics Division*, ASCE, Vol. 100, No. EM1, pp 111-121.
- Hiskens, I.A., Pai, M.A., and Nguyen, T.B., 2000, Bounding uncertainty in power system dynamic simulations, *IEEE Power Engineering Society Winter Meeting*, Vol. 2, pp 1533-1537.
- Hiskens, I.A. and Alseddiqui, J., 2006, Sensitivity, approximation and uncertainty in power system dynamic simulation, *IEEE Transactions on Power System*, Vol. 21, No. 4, pp 1808-1820.
- Hubert, C., Achard, P., and Metkemeijer, R., 2006, Study of a small heat and power PEMFC system generator, *Journal of power sources*, Vol.156, pp 64-70.
- IEA Energy Technology Essentials, Fuel Cells, No. 6, April 2007.
- Ishida, M., Shiga, N., and Sadahiro, K., 2003, Improvement of motor performance by use of high-efficiency electrical steels, *Kawasaki Steel Technical Report*, No. 48.

Jansson, N., Wakeman, W.D., and Manson, J., 2007, Optimization of hybrid thermoplastic composite structures using surrogate models and genetic algorithms, *Composite Structure*, Vol. 80, pp 21-31.

Jee, H. and Bae J., 2005, Modeling and simulation model for PEMFC/solar panel hybrid vehicle with solar water electrolysis system, Proceedings of FUELCELL2005, 3rd International Conference on Fuel Cell Science, Engineering and Technology, May 23-25, 2005, Ypsilanti, Michigan.

Jimenez, S., Soler, J., Valenzuela, R.X., and Daza, L., 2005, Assessment of the performance of a PEMFC in the presence of CO, *Journal of Power Source*, 151, pp 69-73.

Kakac S. and Liu H., 2000, Heat Exchangers Selection, Rating, and Thermal Design, CRS press.

Kamarudin, S.K, Daud, W.R.W, Som, A.MD., Takiff, M.S., and Mohammard, A.W., 2006a, Technical design and economic evaluation of a PEM fuel cell system, *Journal of Power Sources*, Vol. 157, pp 641-649.

Kamarudin, S.K., Daud, W.R.W., Som, A.Md., Takriff, M.S., and Mohammard, A.W., 2006b, Synthesis and optimization of a PEMFC system via reactor-separation network (RSN), *Journal of Power Sources* Vol. 159, pp1194-1204.

Kim, D.H. and Lim, M.S., 2002, Kinetics of selective CO oxidation in hydrogen-rich mixtures on Pt/alumina catalysts, *Applied Catalysis A: General*, 224, pp 27-38.

Kim, K., 2002, A study on the performance of plastic plate heat exchanger, Master thesis, Chungnam National University, Daejeon, South Korea.

Kolavennu, P., Telotte, J., and Palanki, S., 2004, Modeling of a fuel cell power system for automotive applications, Fuel Cell Science, Engineering and Technology, June 14-16, 2004, Rochester, New York.

Larminie, J. and Dicks, A., 2003 Fuel cell systems explained 2nd edition, John Wiley & Sons, New York.

Lobato, J., Canizares, P., Rodrigo, M.A., Linares, J.J., and Aguilar, J.A., 2007,

Improved polybenzimidazole films for H₃PO₄-doped PBI-based high temperature PEMFC, *Journal of Membrane Science*, doi:10.1016/2007.08.028.

Lee, D.K., Baek, I.H., and Yoon, W.L., 2004, Modeling and simulation for the methane steam reforming enhanced by in situ CO₂ removal utilizing the CaO carbonation for H₂ production, *Chemical Engineering Science*, Vol. 59, pp 931-942.

Li, C.H. and Finlayson, B.A., 1977, "Heat transfer in packed-beds – A reevaluation", *Chemical Engineering Science*, Vol. 32, pp 1055-1066.

Lin, S., Chen, Y., Yu, C., Liu, Y., and Lee, C., 2006, Dynamic modeling and control structure design of an experimental fuel processor, *International Journal of Hydrogen Energy*, 31, pp 413-426.

Lommerts, B.J., Graaf, G.H., and Beenackers, A.A.C.M, 2000, Mathematical modeling of internal mass transport limitations in methanol synthesis, *Chemical Engineering Science*, Vol. 55, pp 5589-5598.

Mavris, D.N. and DeLaurentis, D.A., 2000, A probabilistic approach for examining aircraft concept feasibility and viability, *Aircraft Design*, Vol. 3, pp 79-101.

Milburn, S.M., Cronin, J., and Cohen, B., 1996, A variable displacement compressor/expander for vehicular fuel cell air management, *SAE Technical Paper*, 961713, pp 63-69.

Moe, J.M., 1962, *Chemical Engineering Progress*, 58, 33.

Mohideen, M.J., Perkins, J.D., and Pistikopoulous, E.N., 1996, Optimal synthesis and design of dynamic systems under uncertainty, *Computers and Chemical Engineering*, Vol. 20, pp. 895-900.

Muñoz, J.R., 2000, Optimization strategies for the synthesis/design of highly coupled, highly dynamic energy systems, Ph.D. Dissertation, Virginia Polytechnic Institute and State University, Blacksburg, VA.

Muñoz, J.R. and von Spakovsky, M.R., 2000a, An Integrated Thermo-economic Modeling and Optimization Strategy for Aircraft / Aerospace Energy System Design,

Efficiency, Costs, Optimization, Simulation and Environmental Aspects of Energy Systems (ECOS'00), Twente University, ASME, Netherlands, July 5-7.

Muñoz, J.R. and von Spakovsky, M.R., 2000b, The Use of Decomposition for the Large Scale Synthesis/ Design Optimization of Highly Coupled, Highly Dynamic Energy Systems: Part I - Theory, 2000 ASME International Mechanical Engineering Congress and Exposition, Orlando, FL, Nov 5-10.

Muñoz, J.R. and von Spakovsky, M.R., 2000c, The Use of Decomposition for the Large Scale Synthesis/ Design Optimization of Highly Coupled, Highly Dynamic Energy Systems: Part II - Applications, 2000 ASME International Mechanical Engineering Congress and Exposition, Orlando, FL, Nov 5-10.

Oei, D., Adams, J. A., Kinnelly, A. A., Purnell, G. H., Sims, R. I., Sulek, M. S., and Wernette, D. A., 1997, "Direct-Hydrogen-Fueled Proton-Exchange-Membrane Fuel Cell System for Transportation Applications", Final Report for the U.S. Department of Energy, Report No. DOE/CE/50389-503, Dearborn, Michigan, July.

O'Hayre, R., Cha, S., Colella, W., and Prinz, F., 2006, Fuel cell fundamentals, John Wiley & Sons, New York.

Oosterkamp, P. and Bruijn, F., 2005, Fuel specification for fuel cell, EU workshop on regulations, codes, and standards for H₂/FC technologies.

Osscarson, J., 2003, Power recovery by a twin screw expander in a fuel cell application, *2003 SAE International*, 2003-01-0411.

Oyarzabal, B., 2001, Application of a decomposition strategy to the optimal synthesis/design of a fuel cell sub-system, M.S. thesis, Department of Mechanical Engineering, Virginia Polytechnic Institute and State University, Blacksburg, VA.

Oyarzabal, B., von Spakovsky, and M., Ellis, M., 2004, Optimal synthesis/design of a PEM fuel cell cogeneration system for multi-unit residential applications – Application of a decomposition strategy, *Journal of Energy Resources Technology*, Vol. 126, pp 30-39.

Palazzi, F., Autissier, N., Marechal, F., and Favrat, D., 2007, A methodology for thermo-economic modeling and optimization of solid oxide fuel cell systems, *Applied*

Thermal Engineering, Vol. 27, pp 2703-2712.

Pan, C., Li, Q., Jensen, J., He, R., and Cleemann, L., 2007, Preparation and operation of gas diffusion electrodes for high-temperature proton exchange membrane fuel cells, *Journal of Power Sources*, Vol. 172, pp 278-286.

Papalambros, P., 2002, The optimization paradigm in engineering design: promises and challenges, *Computer-Aided Design*, Vol. 34, pp 939-951.

Perna, P., 2007, Hydrogen from ethanol: Theoretical optimization of a PEMFC system integrated with a steam reforming processor, *International journal of Hydrogen energy*, Vol. 32, No. 12, pp. 1811-1819.

Perry, R., Green, D., and Maloney, J., 1997, Perry's Chemical Engineers' Handbook, 7th Edition, McGraw-Hill, New York.

Peter, M., Timmerhaus, K., and West, R., 2003, Plant design and economics for chemical engineers, 5th Edition, McGraw-Hill, New York.

Quantum Fuel System Technologies Worldwide, Inc, 2005, Annual progress report for the DOE hydrogen program.

Queipo, N., Haftka, R., Shyy, W., Goel, T., Vaidyanathan, R., and Tucker, P., 2005, Surrogated-based analysis and optimization, *Progress in Aerospace Sciences*, Vol. 41, pp 1-28.

Rackwitz, R., 1976, Practical probability approach to design, Bulletin No. 112, Comite European du Beton, Paris, France.

Rackwitz, R. and Fiessler, B., 1978, Structural reliability under combined random load sequences, *Computer and Structures*, Vol. 9, No. 5, pp 484-494.

Rancruel, D., 2003 "A Decomposition Strategy Based on Thermoeconomic Isolation Applied to the Optimal Synthesis/Design and Operation of an Advanced Fighter Aircraft System", Master thesis, Virginia Polytechnic Institute and State University, Blacksburg, VA.

Rancruel, D., 2005, Dynamic synthesis/design and operation/control optimization

approach applied to a solid oxide fuel cell base auxiliary, Ph.D. Dissertation, Virginia Polytechnic Institute and State University, Blacksburg, VA.

Rancruel, D. and von Spakovsky M.R., 2003, Decomposition with Thermo-economic Isolation Applied to the Optimal Synthesis/Design of an Advanced Fighter Aircraft System, *International Journal of Thermodynamics*, Vol. 6, No.3, pp. 93-105.

Rikards, R., Abramovich, H., Kalnins, K., and Auzins, J., 2006, Surrogate modeling in design optimization of stiffened composite shells, *Composite Structures*, Vol. 73, pp 244-251.

Sacks, J., Schiller, S.B., and Welch, W.J., 1989a, Designs for computer experiments, *Technometrics*, Vol. 30(1), pp 41-47.

Sacks, J., Welch, W.J., Michell, T.J., and Wynn, H.P., 1989b, Design and analysis of computer experiments, *Statistical Science*, Vol. 4(4), pp 409-435.

Sahinidis, N.V., 2004, Optimization under uncertainty: state-of-art-and opportunities, *Computers and Chemical Engineering*, Vol. 28, pp 971-983.

Saraf, D.N. and Singh, C.P.P., 1977, Simulation of high-temperature water-gas shift reactors, *Industrial Engineering and Chemistry Process*, Vol. 16, No. 3, pp 313-319.

Satyapal, S., Petrovic, J., Read, C., Thomas, G., and Ordaz, G., 2007, The U.S. Department of Energy's National Hydrogen Storage Project: Progress towards meeting hydrogen-powered vehicle requirements, *Catalysis Today*, Vol. 120, 246-256.

Seo, Y.T., Seo, D.J., Jeong, J.H., and Yoon, W.L., 2006, Design of an integrated fuel processor for residential PEMFCs applications, *Journal of Power Sources*, Vol. 160, pp 505-509.

Shooman, M.L., 1968, Probabilistic Reliability: An engineering approach, MacGraw-Hill, New York.

Slack, A.V. and James, G.R., 1974, *Ammonia, Part 2*, Marcel Dekker, Inc, New York.

Sommer, M., Lamm, A., Docter, A., and Agar, D., 2004, Modeling and dynamic simulation of a fuel cell system with an autothermal gasoline reformer, *Journal of Power Sources*, Vol. 127, pp 313-318.

Springer, E.T., Zawodzinski, T.A., Wilson, M.S., and Gottesfeld, S., 1996, Characterization of polymer electrolyte fuel cells using AC impedance spectroscopy, *Journal of The Electrochemical Society*, Vol. 143, pp 582-586.

Stiller, C., 2006, Design, operation, and control modeling of SOFC/GT hybrid system, Ph.D. Dissertation, Norwegian University of Science and Technology, Norway.

Subramanyan, K., Diwekar, U., and Goyal, A., 2004, Multi-objective optimization for hybrid fuel cells power system under uncertainty, *Journal of Power Sources*, Vol. 132, pp 99-112.

Subramanyan, K. and Diwekar, U., 2005, Characterization and quantification of uncertainty in solid oxide fuel cell hybrid power system, *Journal of Power Sources*, Vol. 142, pp 103-116.

Subramanyan, K., and Diwekar, U., 2007, Optimizing model complexity with application to fuel cell based power systems, *Chemical Engineering and Processing*, Vol. 46, pp 1116-1128.

Thome, J.R., 2004, Engineering data book 3, Wolverine Tube, Inc.

Toffolo, A. and Lazzaretto, A., 2002, Evolutionary algorithms for multi-objective energetic and economic optimization in thermal system design, *Energy*, Vol. 27, pp 549-567.

Union Gas Limited, 2006, "Chemical composition of natural gas", <http://www.uniongas.com/>

von Spakovsky, M., Nelson, D., Leo, D., Mazumder, S., Herbison, D., and McIntyre, C., 2006, Optimal-control strategies based on comprehensive modeling and system-interaction analysis for energy-efficient and reduced-emission fuel-cell-energy-conversion technologies for hybrid stationary and non-stationary applications, *EPA Annual Report*.

Wang, F.S., 1985, First-order, second-moment methods, *Computer and Structure*, Vol. 20, No. 4, pp 779-791.

Wang, J.F., Periaux, J., and Sefrioui, M., 2002, Parallel evolutionary algorithms for optimization problems in aerospace engineering, *Journal of Computational and Applied Mathematics*, 149, pp 155-169.

Wang, M., 2008, Integration of state-space into the dynamic synthesis/design and operational/control optimization of a PEMFC system, Ph.D. Dissertation, Virginia Polytechnic Institute and State University, Blacksburg, VA.

Webb, R.L., 1994, Principles of enhanced heat transfer, John Wiley & Sons, New York.

Xiu, G., Li, P., and Rodrigues, A.E., 2003, Adsorption-enhanced steam-methane reforming with intraparticle-diffusion limitations, *Chemical Engineering Journal*, Vol. 95, pp 83-93.

Xu, J. and Froment, G.F., 1989, Methane steam reforming and water gas shift: I. Intrinsic kinetics, *AIChE Journal*, Vol. 35, No. 1, pp 88-96.

Xu, J. and Froment, G.F., 1989, Methane steam reforming: II. Differential limitations and reactor simulation, *AIChE Journal*, Vol. 35, No. 1, pp 97-103.

Youn, B.D., Choi, K.K., and Du, L., 2005, Adaptive probability analysis using an enhanced hybrid mean value method, *Structural and Multidisciplinary Optimization*, Vol. 29, pp 134-148.

Vita

Kihyung Kim received a Bachelor of Science degree with the highest honors from Department of Mechanical Design Engineering at Chungnam National University, South Korea, in February 2000. He joined graduate program for a master degree in the area of heat transfer at the same school and completed his mater degree in February 2002. After graduation, he worked for Energy Policy Research Center at Korea Institute of Energy Research until 2003. In 2003, he was selected to a scholarship program of the Ministry of Commerce, Industry, and Energy of Korea. He has studied in Mechanical Engineering at Virginia Polytechnic Institute and State University with the fellowship program since 2004. Upon completion of his Ph.D. he will launch his career as a plant systems analysis engineer at General Electric Energy.